UNIVERSIDAD AUTÓNOMA DE NUEVO LEÓN
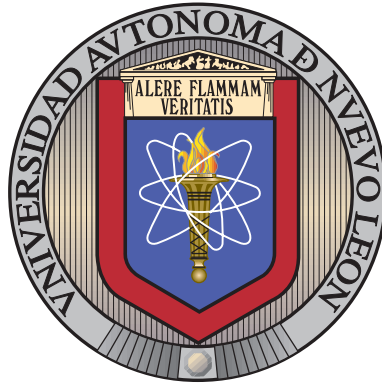
FACULTAD DE INGENIERÍA MECÁNICA Y ELÉCTRICA

"STUDY ON THE PROPERTIES OF $CuSbS_2$ AND $CuSbSe_XS_{2-X}$ THIN FILMS FOR PHOTOVOLTAIC AND PHOTODETECTOR APPLICATIONS"

THESIS SUBMITTED BY

VINEETHA VINAYAKUMAR

IN PARTIAL FULFILLMENT OF THE REQUIREMENTS FOR THE DEGREE OF

DOCTOR OF PHILOSOPHY IN MATERIALS ENGINEERING

SAN NICOLÁS DE LOS GARZA, NUEVO LEÓN   NOVEMBER 2019

UNIVERSIDAD AUTÓNOMA DE NUEVO LEÓN

FACULTAD DE INGENIERÍA MECÁNICA Y ELÉCTRICA

SUBDIRECCIÓN DE ESTUDIOS DE POSGRADO

"STUDY ON THE PROPERTIES OF $CuSbS_2$ AND $CuSbSe_XS_{2-X}$ THIN FILMS FOR PHOTOVOLTAIC AND PHOTODETECTOR APPLICATIONS"

THESIS SUBMITTED BY

VINEETHA VINAYAKUMAR

IN PARTIAL FULFILLMENT OF THE REQUIREMENTS FOR THE DEGREE OF

DOCTOR OF PHILOSOPHY IN MATERIALS ENGINEERING

SAN NICOLÁS DE LOS GARZA, NUEVO LEÓN   NOVEMBER 2019

UNIVERSIDAD AUTÓNOMA DE NUEVO LEÓN
FACULTAD DE INGENIERÍA MECÁNICA Y ELÉCTRICA
SUBDIRECCIÓN DE ESTUDIOS DE POSGRADO

Los miembros del Comité de Tesis recomendamos que la Tesis **"Study on the properties of CuSbS$_2$ and CuSbSe$_X$S$_{2-X}$ thin films for photovoltaic and photodetector applications"**, realizada por la alumna **Vineetha Vinayakumar,** con número de matrícula 1831368, sea aceptada para su defensa como opción al grado de **"Doctor en Ingeniería de Materiales".**

El Comité de Tesis
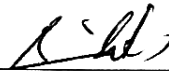
_____
Dra. Bindu Krishnan
Directora

_____
Dr. David Avallaneda Avallaneda
Revisor

_____
Dr. Sadasivan Shaji
Revisor

_____
Dr. Manuel García Méndez
Revisor

_____
Dr. Jorge O. González Garza
Revisor

Vo. Bo.

_____
Dr. Simon Martínez Martínez
Subdirección de Estudios de Posgrado

San Nicolás de los Garza, Nuevo León, México   Noviembre, 2019

Dedicated to my beloved parents,

V.R. VINAYAKUMAR

ANITHA VINAYAKUMAR

ACKNOWLEDGEMENTS

First and foremost, I would like to thank the almighty for his love and uncountable blessings showered upon me. Without his blessings, this doctoral study wouldn't have completed successfully.

I am thankful to Facultad de Ingeniería Mecánica y Eléctrica (FIME), Universidad Autónoma de Nuevo León (UANL) for accepting me to the Ph.D. program, giving me the opportunity to make my dreams to become a researcher come true and for providing all the experimental and characterization facilities. I am also thankful to Centro de Innovación, Investigación y Desarrollo en Ingeniería y Tecnología (CIIDIT) and Centro de Investigación e Innovación en Ingeniería Aeronáutica (CI-IIA), UANL for the laboratory facilities provided. My sincere gratitude to Consejo Nacional de Ciencia y Tecnología (CONACYT), Mexico for the financial assistance through research fellowship during the entire Ph.D. program as well as during the research stay at National Renewable Energy Laboratory (NREL), Colorado, USA. Special thanks to Centro Mexicano para la Innovación en Energía Solar (CEMIE-sol: project No.35) for all the financial support during the program.

My sincerest acknowledgment goes to Dr. Bindu Krishnan for accepting me as a Ph.D. student, for all the support and guidance during the entire time frame of the Ph.D. Her advice helped me to stay on track and to improve my practical as well as writing skills, which are mandatory for a researcher. I would like to thank Dr. Sadasivan Shaji and Dr. David Avallaneda Avallaneda for their help in corrections and improvements of the thesis during the entire period of the program. My gratitude also goes to my thesis revisers Dr. Manuel García Méndez and Dr.

Jorge O. González Garza for their time and effort to review this thesis and for the valuable comments. My sincere thanks to Dr. Josué Amilcar Aguilar Martínez for his continuous motivation and collaboration especially for helping me with a number of X-Ray diffraction measurements. A special thanks to Dra. Marla Berenice Hernández Hernández for all the help with in-situ XRD measurements and for all the supports during this time. Many thanks to Dr. Selene Sepulveda Guzman for putting her helping hand towards me with financial support at the last stage of the Ph.D. and for the unlimited support. I would like to thank Dr. Marco Antonio Loudovic Hernández Rodríguez, for all his help as a program coordinator and Dr. Simón Martínez Martínez for the financial support during my research stay. A special thanks to Dr. Tushar Kanti Das Roy for all the support and for the kind and supportive words. My sincere thanks to Dr. Manju T, for helping me to find a Ph.D. position in Mexico and for continuous motivation.

I am forever grateful to National Renewable Energy Laboratory and Dr. Andriy Zakutayev, for providing me a platform for an exchange program and special thanks to Dr. Andriy for the uncountable helps that he had done during my exchange visit. My sincere thanks to Dr. Imran S. Khan, Dr. Sage Bauers, Dr. Karen Heinselman, Kevin Talley and all the group members who had supported me during my research stay at NREL. Special thanks to Bobby To, Karen Bowers, Dr. Eric Colegrove for their technical supports. A very special thanks to Dr. Paul Ndoine for his friendship and countless support done during my research stay at NREL. Thanks to Sathya and Ram for your friendships and supports. My sincere gratitude to Mrs. Anju and Mr. Ligish, for their great help during my hard time in the USA.

A special thanks to all my friends and colleagues from Mexico and India for their help and support during my Ph.D. journey. I would like to thank especially, Jacob, Dorian, Vanessa, Daniel, Lucio, Ivan, Cesar, Jesus, Arturo, Eleazer, Loura, Anjali, Sreed, Ernesto, Joseph, Franco, Anahi, Katia, Grisel, Linda, Isabel, Augustine, Alan, Mariano, Fernando, Gabriel, Paloma, Ilse, Susan, Erik, Paola, Dr. Mario, Dr. Oscar, Dr. Fernando, Lineth, Libin, Archana, Sebin, Aiswarya and

Paulosukutty. A special thanks to Jacob, for inspiring me to come to Mexico for pursuing a Ph.D. Special thanks to Dr. Aijo John and Dr. Anitha Abraham, Dr. Mercy Mathews and all the teachers in Sree Sankara College and K.E college mannanam for their supports. I'm grateful to the family of Paloma for considering me as a member of her family and for all the supports given.

Thanks to my dear Mary teacher and her family members, Lulu, Aminta, Santiago, Juanjo, Emmanuel, Raul and the teacher's mom for all the care and love and for considering me as a member of her family. I am thanking Mary teacher from the bottom of my heart for all the care and support that she gave me during my whole stay in Mexico and especially for considering me as her own daughter.

Thanks to the whole Malayali community in Monterrey for their support.

To all my family relatives, cousins and especially to my grandparents and my sister Anulakshmi who showed their support and love.

Last but not least, to the most important personalities in my life, my parents (Mr. V.R. Vinayakumar and Mrs. Anitha Vinayakumar), thank you for everything. Without their support, it was impossible to even dream a Ph.D. abroad. Thank you so much for all the care, love and support and for being with me at every single moment of my life's ups and downs.

Contents

CHAPTER 5:   CuSbSe$_x$S$_{2-x}$ THIN FILMS: SYNTHESIS, CHARACTER-
IZATION AND DEVICE APPLICATIONS 152

ABSTRACT

The photovoltaic (PV) technology is of great interest in the present scenario owing to renewable energy production from natural resources such as solar light. At present, the PV technology markedly deals with the solar cells based on single crystalline Silicon. However, the production cost involved in the single crystalline Si-based solar cells accelerated the research towards much cheaper materials for a cost-effective technology. In this aspect, thin film solar cells are of great importance especially solar cells based on chalcogenide semiconductors without compromising much in the device performance due to their versatile properties. $CuInGaSe_2$ and CdTe have come up with conversion efficiencies up to 21.7% and 21.5% which is comparable with the highest reported efficiency of 25.6% for a single-crystalline Si-based cell. Nevertheless, the price and inadequacy of In and Ga, as well as the toxicity of Cd, serves as barriers towards their practical applications. The research was then focused on other semiconducting materials having earth-abundant, low cost and non-toxic constituents. Different material systems were studied as a result including the Cu-based compounds such as copper zinc tin sulfo selenide (CZTSSe) and copper zinc tin sulfide (CZTS). Due to issues such as complex structural polymorphism and cation stoichiometry of CZTSSe materials also face problems while incorporated as absorber layers in solar cells.

Copper antimony sulfide ($CuSbS_2$) is a novel chalcogenide semiconductor featuring suitable chemical and physical properties for being an absorber layer in solar cells as Antimony preserves the same chemistry as that of Indium and Gallium due to the similarities in their oxidation states as well as ionic radii. Addition-

xiv

ally, $CuSbS_2$ exhibits an optical band gap of 1.5 eV for direct transition, a high absorption coefficient of 10^4 cm^{-1} and Spectroscopic Limited Maximum Efficiency (SLME) of 22.9% which are some characteristic features required for an ideal photovoltaic absorber layer. This material has gained intense attention in the scientific community since it was first introduced by P.K. Nair et al. via heating of Sb_2S_3 and Cu_2S layers. A lot of attempts have been made thereafter towards developing this material through different physical and chemical methods and subsequently integrating the same in PV devices. In the majority of the attempts, the conversion efficiency of the fabricated cells, however, remained very low compared to the present commercial PV technologies. The highest reported efficiency of a $CuSbS_2$ based solar cell up to date is 3.22% where $CuSbS_2$ was spin-coated using its precursor ink. In this thesis, we make a strong effort towards understanding different properties and device performance associated with this material. We used chemical bath deposition to prepare Sb_2S_3 thin films onto which the Cu layer was evaporated followed by heating to form the ternary $CuSbS_2$ phase. The effects of different Cu thicknesses, heat treatments (rapid thermal processing, conventional vacuum oven annealing or both at different temperatures durations), were studied in detail on the semoconducting properties of $CuSbS_2$ for PV applications. The structure, morphology, chemical composition and optoelectronic properties of the thin film formed at different conditions were analyzed using various characterization techniques such as XRD, Raman, SEM-EDX, XPS, UV-Vis spectroscopy, I-V and photocurrent response measurements. Device applications of the films which showed comparatively better properties were tested by incorporating them in solar cells as absorber layers. The best solar cell based on $CuSbS_2$ showed an efficiency of 0.6% for the substrate p-n configuration, glass/ITO/n-CdS/p-$CuSbS_2$/Ag. To further improve the efficiency, we alloyed $CuSbS_2$ with selenium solid solution to fabricate quaternary $CuSbSe_XS_{2-X}$. Our assumptions for alloying it with Se was ground on the fact that incorporation of Se can shift the bandgap of $CuSbS_2$ from 1.5 to 1.2 eV depending on the Se content for much efficient solar light absorption. The champion cell featuring the quaternary $CuSbSe_XS_{2-X}$ as the absorber displayed a conversion efficiency of

0.91%, higher than the $CuSbS_2$ based cells. In addition to the PV device application, we also explored the capability of the $CuSbS_2$ in optoelectronic applications where it was tested as a photodetector for a wide range of wavelengths. For the first time ever, we found that $CuSbS_2$ has great potential as a photodetector as well owing to its high sensitivity towards detection of different wavelength light. The synthesis procedure, characterizations, and device applications are explained in detail in different chapters of the thesis which can be really useful in understanding the distinct properties of both $CuSbS_2$ and $CuSbSe_XS_{2-X}$ and towards further optimization to improve the conversion efficiencies where these compounds are used as absorbers.

HYPOTHESIS

The Sb_2S_3-Cu, Sb_2S_3-Se-Cu precursor layer composition variations influence the optoelectronic properties of $CuSbS_2$ and $CuSbSe_XS_{2-X}$ photovoltaic absorber thin films.

OBJECTIVES

GENERAL OBJECTIVE

To control the optoelectronic properties of $CuSbS_2$(CAS), $CuSbSe_XS_{2-X}$ (CASeS) thin films by varying Sb_2S_3-Cu , Sb_2S_3-Se-Cu precursor layer thicknesses respectively, for their applications in solar cells.

SPECIFIC OBJECTIVES

- Preparation of $CuSbS_2$thin films by thermal treatment of Sb_2S_3/Cu layered precursor

- Preparation of $CuSbSe_XS_{2-X}$ thin films by heating glass/Sb_2S_3/Se/Cu layers.

- To determine the influences of individual layer thicknesses of Sb_2S_3 and Cu to form the ternary $CuSbS_2$ and quaternary $CuSbSe_XS_{2-X}$ phase

- Study the effect of post thermal treatments on the formation of phase pure $CuSbS_2$

- Analyze the structure, elemental and chemical composition, morphology, optical as well as electrical properties of $CuSbS_2$ and quaternary $CuSbSe_XS_{2-X}$ films

- Fabrication and characterization of solar cell devices in superstrate configuration: glass/FTO/(n)CdS/(p)$CuSbS_2$/Ag

- Study the effects of different thermal treatments such as conventional vacuum oven annealing, RTP and both (vacuum oven annealing followed by RTP)

- Fabrication and characterization of solar cell device in superstrate configuration using p-n junction: glass/FTO/(n)CdS/(p)CuSbS$_2$/Ag and glass/FTO/(n)CdS/(p)CuSbSe$_X$S$_{2-X}$ /Ag for comparing photovoltaic performances.

- Fabrication and characterization of solar cell device in superstrate p-i-n junction configuration: glass/FTO/(n)CdS/(i)Sb$_2$S$_3$/(p)CuSbS$_2$/Ag

JUSTIFICATION

The increasing demand for photovoltaics in the present scenario leads the researchers to identify the earth-abundant and environment-friendly new visible light absorbers for the PV device applications.$CuSbS_2$ thin films gained special interest from the past few decades as a photovoltaic absorber material due to the environmentally benign and cost-effective constituent elements unlike current commercialized $Cu(In,Ga)Se_2$ (CIGS) and CdTe-based technologies which encounter scarcity of raw materials (In, Ga, Te) and toxicity (Cd, Te). As one of the most promising candidates for emerging thin film solar cells, there are various techniques such as chemical bath deposition (CBD), spray pyrolysis, spin coating, electrodeposition, thermal evaporation, sputtering, etc., are available for the fabrication of $CuSbS_2$ thin films. Based on the available reports on these materials, $CuSbS_2$ possesses great potential such as an optimal direct band gap of 1.5 eV satisfying the criteria for Shockley-Queisser limit, the high optical absorption coefficient of over 10^5 cm^{-1} and low melting point of 551 °C. $CuSbS_2$ shows such promising properties to be used as an absorber layer in PV devices. Only a few reports discuss the properties of $CuSbS_2$ thin films with special focus to photovoltaic application till date. Most of the available reports are limited to basic thin film synthesis and its characterization. Hence, this thesis is focused on detailed characterization of $CuSbS_2$ thin film synthesized by combining chemical bath and thermal evaporation techniques followed by vacuum annealing or/and rapid thermal processing and also the effects of incorporation of Se. This work opens up a new window for the development of thin film solar cells based on $CuSbS_2$ and $CuSbSe_XS_{2-X}$ absorbers with better solar cell parameters.

LIST OF PUBLICATIONS

INTERNATIONAL JOURNALS

1. Vinayakumar, V., Shaji, S., Avellaneda, D. A., Martinez, J. A., & Krishnan, B. (2019). Highly oriented $CuSbS_2$ thin films by rapid thermal processing of pre-annealed Sb_2S_3-Cu layers for PV applications. Materials Science in Semiconductor Processing, 91, 81-89.

2. Vinayakumar, V., Shaji, S., Avellaneda, D., Aguilar-Martínez, J. A., & Krishnan, B. (2018). Copper antimony sulfide thin films for visible to near infrared photodetector applications. RSC Advances, 8(54), 31055-31065.

3. Vinayakumar, V., Hernández, C. O., Shaji, S., Avellaneda, D. A., Martinez, J. A., & Krishnan, B. (2018). Effects of rapid thermal processing on chemically deposited antimony sulfide thin films. Materials Science in Semiconductor Processing, 80, 9-17.

4. Vinayakumar, V., Shaji, S., Avellaneda, D., Roy, T. D., Castillo, G. A., Martinez, J. A. A., & Krishnan, B. (2017). $CuSbS_2$ thin films by rapid thermal processing of Sb_2S_3-Cu stack layers for photovoltaic application. Solar Energy Materials and Solar Cells, 164, 19-27.

5. S, Shaji, V. Vinayakumar, B. Krishnan, J. Johny, S. Sharma Kanakkillam, J. M. Flores Herrera, S. Sepulveda Guzman, D. A. Avallaneda, G. A. Castillo Rodriguez, J. A. Aguilar Martinez, Applied Surface Science 476, (2019) 94-106

BOOK CHAPTER

1. Vinayakumar, V., Shaji S., Avellaneda, D., Krishnan, B. (2017) Cu-Sb Based Chalcogenide Thin Films: An Alternative Absorber Material for Photovoltaic Applications. Advances in Materials Science Research, 31, Nova Science Publisher

PRESENTATIONS IN INTERNATIONAL CONFERENCES

1. Paper Presentation at 21 st International Conference on Ternary and multinary compounds (ICTMC-21) at Colorado, USA

2. Paper presentation at the 4 th international conference on advanced nanoparticle generation and excitation by lasers in liquids (ANGEL-2018), France.

3. Paper presentation at XXVI International Materials Research Congress 2017 at Cancun, Mexico.

LIST OF FIGURES

LIST OF TABLES

ABBREVIATIONS

AFM	:	Atomic Force Microscopy
BE	:	Binding Energy
CAS	:	Copper Antimony Sulfide
CASe	:	Copper Antimony Selenide
CASeS	:	Copper Antimony Seleno Sulfide
CB	:	Conduction Band
CBD	:	Chemical Bath Deposition
CdTe	:	Cadmium Telluride
CIGS	:	Copper Indium Gallium Selenide
CIS	:	Copper Indium selenide
CV	:	Cyclic Voltammetry
CZTS	:	Copper zinc tin sulfide
CZTSSe	:	Copper zinc tin sulfo selenide
EDX	:	Energy Dispersive X-Ray
FESEM	:	Field Emission SEM
FF	:	Fill Factor
FTO	:	Fluorine-doped tin oxide
GIXRD	:	Grazing Incidence XRD

ITO	:	Indium Tin Oxide
I-V	:	Current-Voltage
JCPDS	:	Joint Committee on Powder Diffraction Standards
J-V	:	Current density – Voltage
LED	:	Light Emitting Diode
Mo	:	Molybdenum
NIR	:	Near Infrared
PV	:	Photovoltaic
RTP	:	Rapid Thermal Processing
SEM	:	Scanning Electron Microscopy
SLME	:	Spectroscopic Limited Maximum Efficiency
UV-Vis-NIR	:	Ultraviolet-Visible-Near Infrared
XPS	:	X-Ray Photoelectron Spectroscopy
XRD	:	X-Ray Diffraction
XRF	:	X-Ray Fluorescence spectroscopy
VB	:	Valence Band

Chapter 1

THIN FILM SOLAR CELLS: EMERGING

MATERIALS

1.1 INTRODUCTION

The concept of energy is fascinating due to the rapid growth in world energy demand for the last few decades. Fossil fuels such as coal, oil, and gas are the world´s dominant energy sources [1–3]. However, fossil fuels have negative impacts, being a dominant source of carbon dioxide, a greenhouse gas that contributes to a series of environmental problems such as air pollution, climate change, global warming, and acid rain [4, 5]. These concerns are triggering the world to look at renewable energy such as solar, wind, geothermal, biomass, hydropower and wave energy, in order to deal with both economic and environmental challenges [6, 7].

According to "Renewable Energy Policy Network for the 21st Century by the year 2050, solar energy will be the highest energy source with a production of approximately 11,941 EJ/yr. Effectively, solar energy can be harvested in three ways, solar thermal, photovoltaics and solar fuels. Among these three, the potentially suitable strategy is photovoltaics which involves photovoltaic effect, the conversion of sunlight directly into electricity, which was first discovered by a French scientist Edmond Becquerel while experimenting with an electrolytic cell made up of two electrodes placed in a conductive solution in 1839. William G. Adams and Richard

E. Day discovered photovoltaic effect by illuminating a junction between selenium and platinum producing an electromotive force, without the addition of heat or any moving parts in 1876. These two discoveries were the founding stones for the first solar cell made of selenium thin sheets coated with gold by Charles Fritts in 1882. Daryl Chapin, Calvin Fuller, and Gerald Pearson developed a crystalline silicon photovoltaic (PV) cell having conversion efficiency of 4% at Bell Labs in 1954, which was the first solar cell capable of converting enough of the sunlight into power to run every day electrical equipments and is considered as the cutting edge in energy technology [8–10]. By early 20´s global warming awareness and the importance of renewable energy in the science community, lead to potential researches on silicon solar cells and achieved an efficiency of 24%. At present, modern Si PV devices are operated with 26% electricity return [6, 7, 11]. Another aspect to consider solar energy over other energy sources is the economy. Between the years 2010 and 2015, the price of PV devices has declined by nearly 58% compared to the past years. According to the estimation of the International Renewable Energy Agency, it will further reduce up to 57% by 2025 [12]. Hence the research on solar cells and efforts to improve efficiency by limiting the fabrication cost of the cell is progressing day by day. This chapter of the thesis will introduce the solar cell devices, the theory on which these cells convert light into electrical energy and current status of solar cell research.

1.2   FUNDAMENTALS OF PHOTOVOLTAICS

The photovoltaic (PV) effect is the process of direct conversion of solar radiation to electricity, occurring in solar cells constituted by semiconducting materials and metallic layers. This section will describe briefly about semiconductors, different types of junctions and the mechanisms behind the working of the PV devices.

1.2.1 Semiconductors

A semiconductor is a crystalline or amorphous solid material with intermediate electrical conductivity between that of a metal and an insulator. The conductivity of the semiconductors can be changed significantly by altering the temperature or the impurity content of the material, or by illumination with light. The band gap of semiconductors (energy gap between the maximum of the valence band and minimum of the conduction band) usually lies between 0.1-3 eV; those for which the gap is very small or absent are conductors, materials with a filled valence band and a large energy gap (>3 eV) are electrical insulators (see Figure 1.1). At temperature T = 0 K, a pure semiconductor becomes an insulator with a fully filled valence band with electrons (E_v) and an empty conduction band (E_c). Si and Ge are the most commonly used semiconductor materials [13].
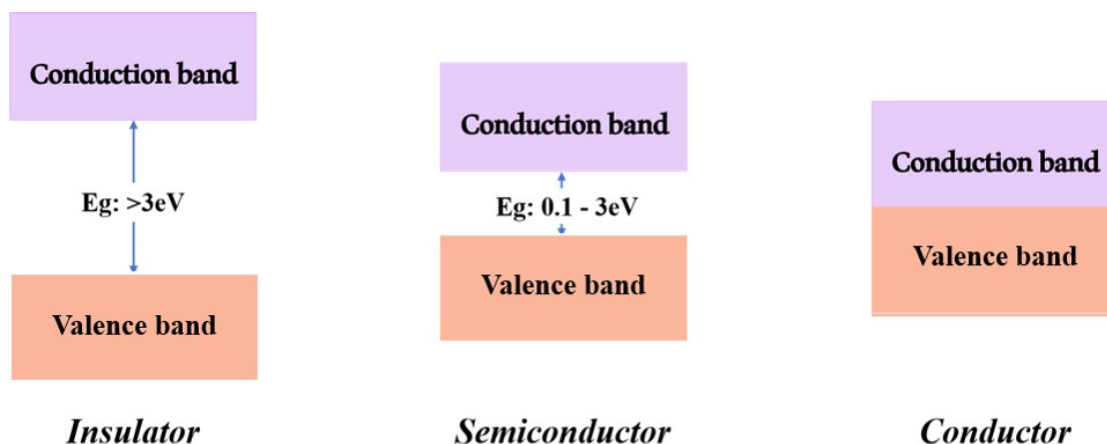
Figure 1.1: Energy band diagram for Insulator, Semiconductor and Conductor

Semiconductors can have either direct or indirect band gaps depending on the positions of the valence band (VB) maximum and the conduction band (CB) minimum. Direct band gap semiconductors (e.g. GaAs) can absorb light much easier since an electron in the VB can be promoted directly to the CB without a change in momentum. Absorption of the photon's energy takes place without any lattice interaction, and there is a sharp absorption band transition with relatively large values of the extinction coefficient. In indirect band gap semiconductors (e.g.

Silicon), the CB minimum and the VB maximum occurs at different k vectors, and hence for an electron to move from the VB to CB, a phonon must be involved. Figure 1.2 [14, 15]. shows the E-k diagram of direct and indirect band gap materials (GaAs and Si). Each PV device contains a p-n junction for producing the photovoltaic effect and thereby converting the light energy into electricity. Different types of semiconductor junctions used in solar cells and the behavior of the junction when illuminating with light are described in the following sections [13, 16, 17].

1.2.2 Semiconductor-Semiconductor junction

1.2.2.1 p-n junction

The classical model of the solar cell is the p-n junction. Typically, all PV devices are based on the development of a photovoltage incorporating a semiconductor p-n junction [17–19]. The p-n junction is created by differently doping the semiconductor's different regions so that an interface between the n-type and p-type layers is created (Figure 1.3) [19]. On the n side of such a junction, the electrostatic potential must be smaller than that on the p side since the work function of the n-type material is less than the work function of the p-type material. An electric field is thus established at the junction which moves the photogenerated holes towards the p region and electrons towards the n region. The center junction region is depleted of both holes and electrons (hence called the depletion region) and exhibits a low resistance path towards the minority charge carriers and a barrier towards the majority charge carriers. The photogenerated minority charge carriers throughout the p and n regions reach the junction by diffusion. At the point where the Fermi levels of the n and p layers are the same, the difference in the work functions of both is taken up by a step in the edges of the valence and conduction bands. This step is called the built-in bias where the junction region is depleted of charge carriers. Built-in potential can be expressed mathematically as in eq. (1.1):
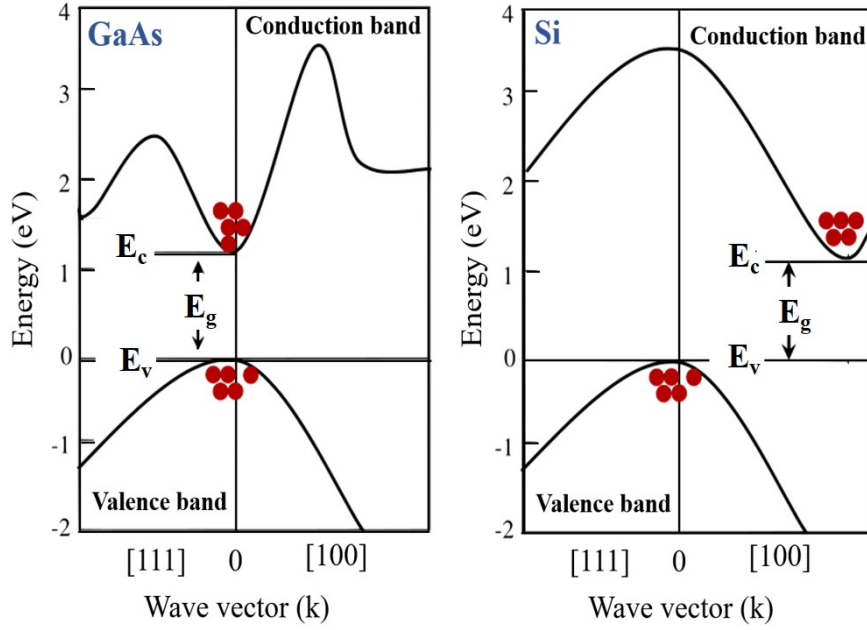
Figure 1.2: E-k diagram of direct and indirect band gap materials (GaAs and Si), where E_c, E_v are the conduction band and valance band energy, E_g is the energy band gap.

$$V_{bi} = \frac{1}{q}(\Phi_n - \Phi_p) = \frac{1}{q}\left((E_i - E_F)|_{p\ side} - (E_i - E_F)|_{n\ side}\right) \tag{1.1}$$

where Φ_n and Φ_p are the work functions of n and p regions respectively and $(E_i - E_F)$ is the difference in the Fermi level. Far from the junction, $E_i - E_F$ can be expressed in terms of the doping levels and hence the equation can be rewritten as:

$$V_{bi} = \frac{K_B T}{q} ln\left(\frac{N_d N_a}{n_i^2}\right) \tag{1.2}$$

when an electrical field is applied on one side, the Fermi level is raised on one side and the potential drop across the $p - n\ junction$ becomes:

$$V_i = V_{bi} - V \tag{1.3}$$

Almost all solar cell devices contain a p-n junction for the generation of electricity from solar light. The conversion is achieved due to different mechanisms happen in the p-n junction when the junction is irradiated by light. Characteristics of the p-n junction under dark and illumination are thus crucial to understand the working mechanisms of solar cells and will be described later in the thesis. In addition to the p-n junction formed by doping the same material differently, there are p-i-n junction and p-n heterojunction.
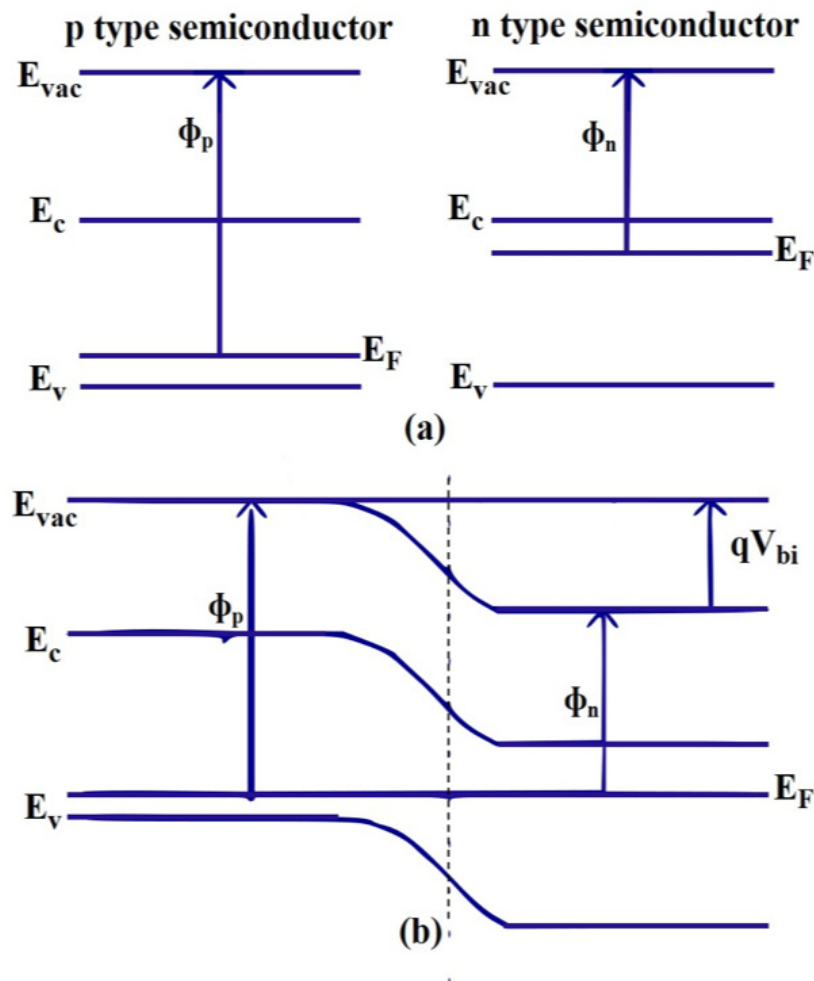
Figure 1.3: (a) Band profiles of p-type and n-type semiconductor in isolation (b) band profile of the p-n junction in equilibrium.

1.2.2.2 p-i-n junction

A p-i-n junction is formed when a small layer of undoped (or intrinsic) semiconductor is inserted between the p and n layers. The impact of the addition of the intrinsic layer on the built-in bias is the same as that of a normal p-n junction, but the electric field is extended over a wider region. The p-i-n junction is preferred over p-n junction when the minority carrier diffusion lengths of the material is short and hence the photogenerated carriers are unlikely to contribute to the photocurrent [17].

1.2.2.3 p-n heterojunction

As the name indicates, a p-n or p-i-n junction is called as a heterojunction when the materials forming up the p and n regions are different. In such a junction, a discontinuity in the valence and conduction band edges can be noticed due to the difference in the band gap of the materials. Different effective fields for the electrons and holes by assisting the electrostatic fields for one carrier and opposing the other are introduced due to this potential step. The overall effect of a p-n heterojunction on the photovoltaic performance is enhanced recombination in the junction region [17].

1.2.3 Photovoltaic effect

The basic concept of photovoltaics is the generation of free electrons and holes in a semiconductor due to optical excitation in the semiconductor when light having photon energy greater than the band gap of the semiconductor falls on it. For the photovoltaic effect to take place, the semiconductor material should possess some kind of internal electric field due to different reasons such as variations in doping in different regions, surfaces, contacts, etc. which is able to separate the generated electrons and holes into the external circuit without recombining with one another. The photogenerated electron moves towards the n-side of the junction whereas the hole moves towards the p-side. In case if the carriers are generated outside of the

depletion region of the p-n junction, they may reach the depletion region by thermal diffusion. The minority charge carriers from the n-side (holes) will move towards the p-region leaving an electron (negative charge) and the minority carriers from the p-side (electrons) will move towards the n-side leaving a hole(positive charge) in the p-region. Hence, a potential difference is created between the p and n regions of the junction and the entire process is termed as the photovoltaic effect. Such a flow of carriers into the external circuit forms up a reverse electrical current density, which is called short circuit current density (J_{sc}) under short-circuit conditions [20].

1.2.4 Photovoltaic parameters

A solar under dark conditions cell exhibits I-V characteristics of a diode. The behavior of a solar cell can be thus better understood considering an electrically equivalent circuit made of discrete electrical components whose behavior is well defined [21–24]. Figure 1.4 [25] depicts the equivalent circuit of a solar cell containing both series and parallel resistors.
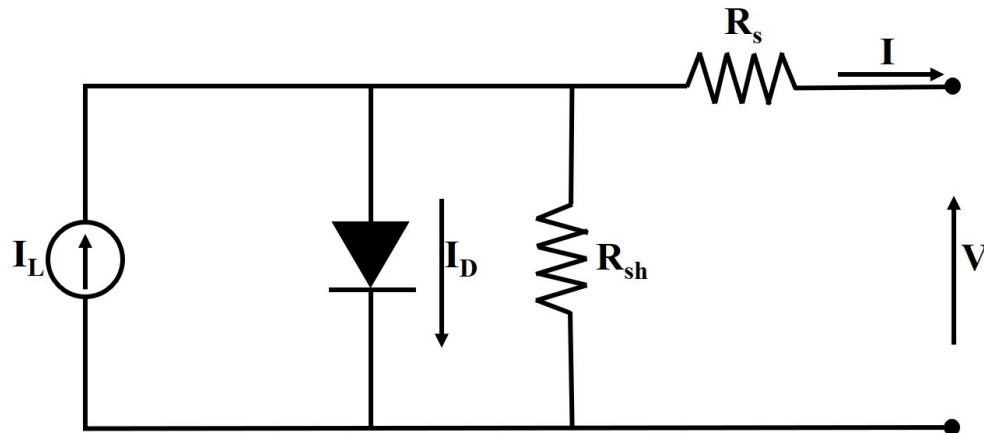
Figure 1.4: The equivalent circuit of a solar cell with series and parallel resistance

The photocurrent source I_L is the reverse current whose amplitude is linearly proportional to the solar irradiance $G(Wm^{-2})$. The current and voltage of the cell in dark are related by the Shockley equation as follows:

$$I_D = I_0 \left[exp \left(\frac{eV}{kT} \right) - 1 \right] \tag{1.4}$$

where k is the Boltzmann constant, e is the charge of an electron, I_0 is the inverse saturation current of the diode and T is the temperature in Kelvin. The I-V curve is displaced from the origin when the cell is illuminated due to the generation of the photocurrent I_L. Hence the above equation becomes:

$$I = I_L - I_0 \left[exp \left(\frac{eV}{mkT} \right) - 1 \right] \tag{1.5}$$

where m is the factor of ideality which is defined as how closely the diode follows the equation of an ideal diode. Generally, its value is in between 1 and 2 respectively for high and low voltages. The ohmic voltage drop at the contacts and through the layers of the materials is represented by a series resistance and the maximum power of a solar cell to the open-circuit voltage is related by this series resistance. On the other hand, a parallel resistor represents the leakage of the current around the cell, the small short circuits and the diffusion path along dislocations in the cell.

The I-V characteristics of a solar cell consisting of parallel and series resistances can be represented as:

$$I = I_L - I_0 \left\{ exp \left[\frac{e}{mkT} (V + IR_s) \right] - 1 \right\} - \frac{V + IR_s}{R_{sh}} \tag{1.6}$$

where R_s and R_{sh} are the series and shunt resistances respectively. The maximum power of the solar cell can be achieved when the voltage and current are at their maximum or in other words when the derivative of the power with respect to voltage is zero. The solar cell maximum power can be represented as:

$$I = I_m V_m \approx I_L \left[V_{oc} - \frac{kT}{e} ln \left(1 + \frac{eV_m}{kT} \right) - \frac{kT}{e} \right] \tag{1.7}$$

where V_{oc} is the open-circuit voltage of the cell. Figure 1.5. shows the I-V curve of a solar cell under illumination indicating the maximum power obtained [19].
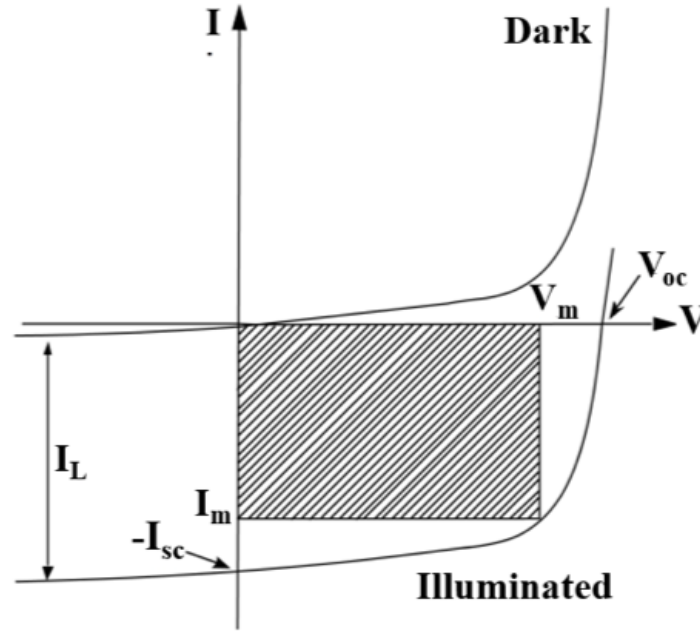
Figure 1.5: I-V curve for a solar cell with maximum power indicated by the shared area. The corresponding voltage and current are V_m and I_m. The value depends on the external load applied. Adapted from physics of semiconductor devices – S. M Sze.

The maximum current that flows in a solar cell when the terminals are short circuited is called the short circuit current I_{sc}, which imply a zero voltage across the contacts. This means, from eq. (1.5), I_{sc} = -I_L. When the short circuit current is divided by the area, we obtain current density (J_{sc}) in terms of mA/cm^2

The open circuit voltage V_{oc} is the maximum voltage generated across the contacts while the external circuit is in open condition (I = 0). The expression for open circuit voltage is:

$$V_{oc} = \frac{K_B T}{e} ln \left(\frac{I_L}{I_0} + 1 \right) \approx \frac{K_B T}{e} ln \left(\frac{I_L}{I_0} \right), \text{if } I_L \gg I_0 \qquad (1.8)$$

The ratio of maximum power $P_m = V_m \times I_m$ of a solar cell to the ideal power $P_0 = V_{oc} \times I_{sc}$, is called the fill factor FF which is given by:

$$FF = \frac{V_m I_m}{V_{oc} I_{sc}} \tag{1.9}$$

The efficiency of a solar cell, η is defined as the ratio of the power output (P_m) to power input $(P_{in} = 100 \ mW/cm^2)$ according to standard AM 1.5, and can be written as:

$$\eta = \frac{V_m I_m}{P_{in}} = \frac{V_{oc} I_{sc} FF}{P_{in}} \tag{1.10}$$

1.3 PHOTOVOLTAIC TECHNOLOGIES

All photovoltaic technologies require a light-absorbing material, present within the solar cell structure to absorb photons and generate electrons and holes via the photovoltaic effect. Using different types of materials, a wide variety of photovoltaic technologies are there in the market today and will be increased in the near future. Depending on the level of commercial maturity and raw materials used, PV cell technologies are generally classified into three generations [7, 26].

I. First-generation photovoltaic systems (fully commercial), which uses the wafer-based crystalline silicon (C-Si) technology, both in its single crystalline (sc-Si) as well as multi-crystalline (mc-Si) form.

II. Second generation photovoltaic systems (early market development) are based on thin-film PV technologies and generally include three main families: (i) Amorphous (a-Si) and micro morph silicon (a-Si/μc-Si); (ii) cadmium telluride (CdTe); and (iii) copper indium selenide(CIS) and copper indium gallium diselenide (CIGS)

III. Third generation photovoltaic technologies such as organic photovoltaic technologies are still under investigation or have not been widely marketed yet.

Even though there are three different generations of PV cell technologies, cost-effective production of high conversion efficiency cells is one of the major challenges that the photovoltaic technology faces [27]. The cost projections versus the efficiency of different PV technologies are shown in Figure 1.6 [28].
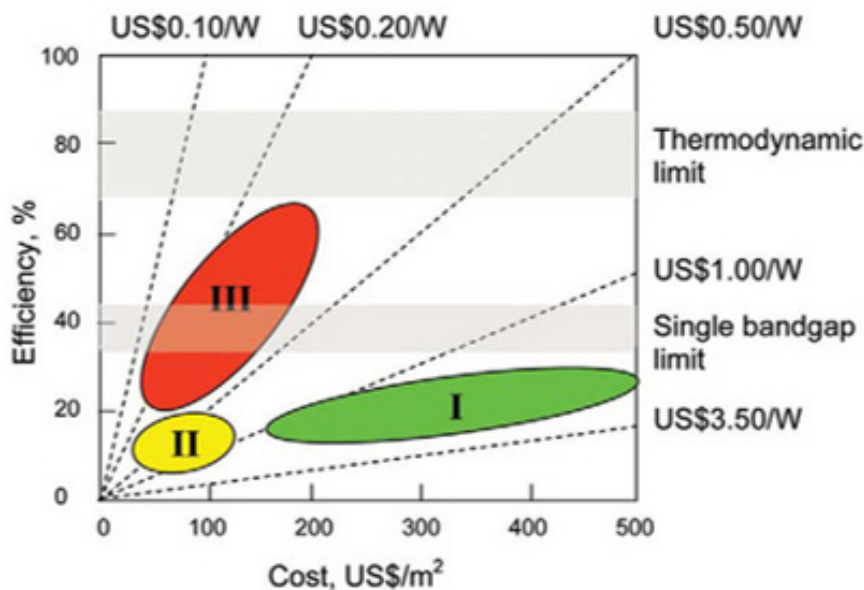
Figure 1.6: Efficiency and cost for first, second and third generation PV technologies. Reprinted with kind permission from John Wiley and Sons.

Crystalline silicon based solar cells are the first generation solar cells also referred to as traditional or conventional solar cells due to the beneficial characteristics of Si such as non-toxicity, abundancy, high stability and suitable optical band gap. There been a strong effort by the research community in fabricating single crystalline and multi crystalline Si based solar cells and enhancing the conversion efficiency of the same [29]. In fact, the high production cost, brittle nature of Si and wastage of huge amounts of Si while using in large scale applications function as barriers towards the production of cost-effective PV devices based on monocrystalline Si despite the relatively high conversion efficiency of monocrystalline Si based solar cells

over 26%. Consequently, the concept of polycrystalline/multi-crystalline solar cells appeared. Multicrystalline silicon is more attractive over monocrystalline because of its low manufacturing costs and feedstock tolerance even though these cells are somewhat less efficient than that of monocrystalline cells. The decreased efficiency of monocrystalline cells has resulted from the border defects occur at silicon cast blocks by hardening. The lab efficiency of this material is ranging from 18-23% and product range is from 14-17%. The high cost of Si and wafer wastage by slicing, driven the research towards second-generation solar cells which is based on thin films [30].

1.3.1 Thin film solar cells: A brief review

Thin film solar technology (second generation solar cells) has gained special attention in recent years in photovoltaics research which requires an absorber layer of a few micrometers thickness and low-temperature processability. Compared to crystalline silicon solar cells, thin film solar cells require much less material of the semiconductor to harvest the same amount of light. The material can be less even up to 99%. Due to its high flexibility, the diffuse light efficiency of $\sim$12%, easy installation and lifetime of approximately 25 years, the thin film technology has gained much attention in recent years. Thin-film PV technologies already developed generally include three main families, (i) Amorphous (a-Si) and micro morph silicon (a-Si/μc-Si); (ii) cadmium telluride (CdTe); (iii) copper indium selenide (CIS) and copper indium gallium selenide (CIGS).

1.3.1.1 Amorphous silicon

Amorphous silicon materials have been targeted as promising candidates for the fabrication of solar cells particularly in thin film form, in an effort to produce low-cost solar cells while still retaining the advantages of silicon (relative abundance, reliability, stability) and the backlog of information and experience in silicon cell manufacturing technology [31]. Amorphous silicon material is composed of ran-

domly oriented Si atoms in a homogenous layer rather than a crystal structure and which has an important effect on electronic properties and possesses a direct band gap of 1.7 eV. The absorption of light is higher in a-Si than that of c-Si, leading to the use of thin layers which makes the use of less material than crystalline silicon and for this same reason a-Si is also among the thin film solar cells. In 1976 Carlson and Wronski reported the first p-i-n amorphous silicon (a-Si) solar cells with a conversion efficiency of 2.4%, where the estimated theoretical efficiency of the same cell structure was ∼15% and within a year they were able to improve the efficiency by 4%. Willem in 1978 reported Schottky barrier amorphous-silicon solar cell (which is constructed with a metal-to-N junction rather than a p-n semiconductor junction) with an efficiency of 4.8%. The introduction and discovery of hydrogenated amorphous silicon (α-Si:H) by Tawada (1982) account for the growth of a-Si based solar cells. Hydrogenation is a process of incorporates of a significant percentage of H_2 atoms ∼(20-30)% bonded into a-Si structure and which help in improving the electronic properties. However, it improved the electrical properties, efficiency of a-Si based solar cells is declined during their first few hundred hours of illumination, known as Staebler-Wronski effect was the main problem of all the a-Si cells that are discovered. In order to reduce recombination losses, in the early 1990s research efforts were placed on the development of multi-junction cells and modules, which have multiple band gaps to allow response at multiple wavelengths [32]. The energy that would normally be lost in single-junction solar cells can be captured and converted in multijunction technologies by readily adjusted band gap via varied alloying. In addition to its multijunction exhibits less light-induced degradation. Guha et al. [33] demonstrated a multijunction having an efficiency of ∼11%. Later on, 1996 Yang et al. (United Solar Systems Corporation) achieved stabilized conversion efficiencies of 13% using a triple-junction structure [34]. Soohyun Kim et al. [35] recently reported triple-junction a-Si solar cell (a-Si:H/a-SiGe:H/μc-Si:H stack : hydrogenated amorphous silicon (a-Si:H) in the top cell, hydrogenated amorphous silicon-germanium (a-SiGe:H) or hydrogenated microcrystalline silicon (μc-Si:H) in the middle cell, and hydrogenated microcrystalline silicon (μc-Si:H) in the bottom) with a stabilized effi-

ciency of 13.4% (Figure 1.7) [35]. Further researches are currently going on with p-i-n stacked amorphous thin film solar cells for improved efficiency by further developments in novel light trapping technology and high-quality wide-band gap materials.

V_{oc} = 1.9627 V I_{max} = 8.4657 mA
I_{sc} = 9.5823 mA V_{max} = 1.5978 V
J_{sc} = 9.5237 mA/cm^2 P_{max} = 13.527 mW
Fill Factor = 71.92 %   Efficiency = 13.44 %
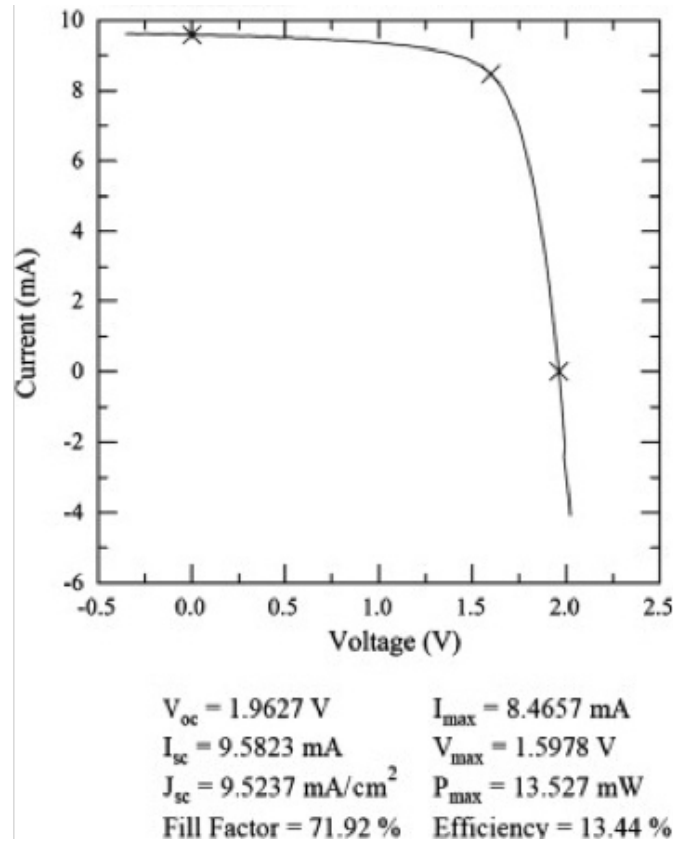
Figure 1.7: Solar cell performance of the a-Si:H/μc-Si:H/μc-Si:H triple-junction solar cell after 1000 h light soaking. Reprinted with permission from Elsevier.

1.3.1.2   Cadmium telluride (CdTe)

Cadmium telluride (CdTe) solar cells serve as a prime candidate for all thin film solar cells and it is the second most common photovoltaic (PV) technology in the world marketplace after crystalline silicon. CdTe is a direct-band gap material with a band gap energy of about 1.45 eV (which is well matched to the solar spectrum and nearly optimal for converting sunlight into electricity using a single junction) with a large absorption coefficient. CdTe is a stable compound and cells based on

CdTe thin-film can be manufactured quickly and inexpensively, providing a lower-cost alternative to conventional silicon-based technologies [32, 36]. If both bulk and surface recombination are curbed, a thin film of CdTe is adequate for producing high-efficiency cells. When look back to the history of CdTe solar cells, in 1972 Bonnet and Rabnehorst developed the first significant laboratory CdTe solar cell (CdTe - CdS p-n heterojunction solar cell) with 6% efficiency, where the cell was created in a three-step process involving high-temperature vapor phase deposition of CdTe and high vacuum evaporation of CdS [37]. The problems involving the back contact between pure Mo and CdTe lead to considerably high series resistances and low FF, reported by them. Variety of different fabrication methods (close-spaced sublimation, vapor-transport deposition, physical-vapor deposition, sputter deposition, electrodeposition, metal-organic chemical-vapor deposition, spray deposition, and screen-print deposition) were employed for the fabrication of CdTe due to the rapid interest in the CdTe field. Nakayama et al. [38] developed ceramic thin film CdTe solar cell (glass/In_2O_3/CdS/CdTe/Cu_2Te/Ag) by screen-printing method in 1976 where CdS layer served as an ohmic contact transparent electrode to the CdTe layer (prepared by mixing n-CdTe powder and $CdCl_2$ with a binder in a mixer was printed on the substrate by screen printing method), which reduced both series resistance and surface recombination at the n-CdTe layer. The reported solar conversion efficiency of the above-described cell was 8.1% . In 1981, Kodak used close-spaced sublimation (CSS) and made the first 10% CdTe cells. 1987 was the revolutionary year for CdTe solar cell industry. Meyers and others at Ametek introduced a novel n-i-p design, where i-layer assisted in the collection of charge carriers [39]. Because of CdTe´s large work function, it is always difficult to create a successful ohmic contact to it. But, by using p-ZnTe as a buffer layer, the minimal discontinuity in the valence band edge at the CdTe/ZnTe interface permits the free flow of holes from the CdTe into the ZnTe which lead to the formation of high efficiency solar cell. Even though these cells gave higher efficiency, the cost was a major concern for the commercialization of the CdTe solar cells. Unlike in previous attempts, many researchers were tried to achieve high-efficiency CdTe solar cells using low-cost simple high throughput

processing. As a result, Matsushita PV Research and Development Center developed CdTe solar cells having 16% efficiency where the CdS layer was deposited by a metal-organic chemical vapor deposition (low temperature and economic method) and CdTe by CSS method [40]. Wu et al. [41,42] at NREL reported a CdTe solar cell with 16.5% efficiency where they modified the conventional $SnO_2/CdS/CdTe$ device structure to glass/Cd_2SnO_4/$ZnSnO_X$/CdS/CdTe form. Cd_2SnO_4 (CTO) replaced the SnO_2 TCO and $ZnSnO_X$ (ZTO) buffer layer was placed between the TCO and the CdS film and oxygenated nanocrystalline CdS:O was used as the window layer in order to improve the FF. The oxygen present in the nano-crystalline CdS:O resulted in increasing the band gap (2.5 - 3.1 eV) and suppressed the formation of $CdS_{1-Y}Te_Y$ alloy by controlling the interdiffusion of Te from the CdTe to CdS film which led to the achievement of 75.5% FF. The US photovoltaics giant, the first solar has dominated in the past decade, with reported efficiencies of 18-21% with a heavier focus on commercialization. The latest record efficiency for a laboratory CdTe solar cell is 22.1% [43]. Even though CdTe cells got efficiency near to the Si-based solar cells, the toxicity of Cd and issue of Te availability are the main obstacles for the incorporation of these materials in to the PV devices as an absorber layer in a larger extent.

1.3.1.3 Copper Indium Gallium Selenide (CIGS) and Copper Indium Selenide (CIS)

Copper Indium Gallium Selenide (CIGS or $Cu(InGa)Se_2$) is a highly promising material for PV application owing to its high absorption coefficient (10^5 cm^{-1}), direct optical band gap in the range $\sim$1-1.2 eV and less material wastage. The lattice parameter ratio (c/a) of tetragonal CIGS is around 2 and any lattice distortion comes from the In-Se, Cu-Se or Ga-Se bonds. Indium in CIGS can be replaced by Ga to match its band gap to the solar spectrum [44–50]. For device fabrication using CIGS, a thin layer of thickness $\sim$2.0-2.5 μm is sufficient since CIGS can absorb most of the sunlight within 1 μm thickness thereby significantly reducing the ma-

terial usage in device fabrication. Usually, CIGS is deposited using techniques such as sequential deposition, co-evaporation, and some non-vacuum techniques [50]. In 1976, Kazmerski et al. fabricated the first CIGS based solar cell having a conversion efficiency of 4.5%. The CIGS based solar cell contained p-type CIGS, n-type CdS layer, an intrinsic ZnO layer above the CdS layer and an n-type ZnO:Al layer as the top contact. The back contact was molybdenum. The total thickness of the semi-conductor layers was less than 5 μm which is very less compared to that of 170-200 μm thick crystalline Si layers [32]. A 5.7% efficient cell was fabricated by Mickelsen and Chen in 1980 employing a CdS/CuInSe$_2$ heterojunction. The CuInSe$_2$(CIS) layer, in that case, was deposited using elemental evaporation technique [51]. The CIS based cell exhibited high J$_{sc}$ which was attributed to the combination of band bending and Fermi position in the CIS. Later in 1982, the same authors used a mixed Zn$_X$Cd$_{1-X}$S and obtained a record efficiency of 10.6%. Thereafter, many different authors attempted to improve the CIS based cell efficiency and as a result, solar cells having conversion efficiencies of 12.2% were generated. CIS was then replaced by CIGS owing to the possible band gap engineering by altering the In percentage in CIGS. The higher band gap of CIGS compared to CIS led to the fabrication of solar cells with 12.5% efficiency. Since then, the CIGS based cell efficiency was improved to above 20% by improving the interface between the absorber and buffer layers, optimizing the window layer and by using different deposition techniques. The highest lab efficiency of CIGS solar cell has reached up to 22.6% [52]. The certified efficiencies of solar cells of various photovoltaic technologies by NREL is shown in Figure 1.8 [53]. Even though the CIGS based cells have achieved efficiencies comparable with crystalline Si solar cells, they possess some disadvantages/ challenges as follows. Midgap defect states/ dangling bonds/ recombination and band discontinuities at the interface in CIGS have a bad impact on cell efficiency since the defects in CIGS are associated with increased band gap. When applied in solar cells using CdS as the window layer, due to discontinuity in the conduction band, recombination occurs at the CdS/CIGS interface. Furthermore, in the economic point of view, In and Ga are relatively more expensive and less abundant elements compared to many other

materials suitable for PV applications.
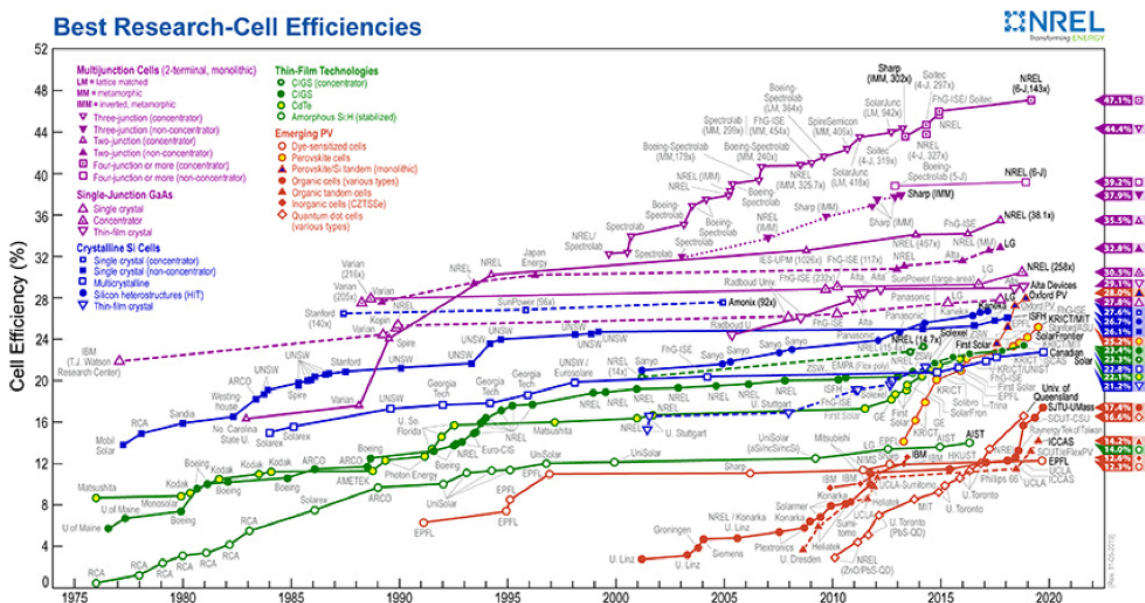
Figure 1.8: Certified efficiencies of solar cells of various PV technologies by NREL in 2019. This plot is courtesy of the National Renewable Energy Laboratory, Golden, CO (https://www.nrel.gov/pv/cell-efficiency.html).

1.3.1.4   Emerging materials

The present obstacles of photovoltaic devices based on CIGS and CdTe absorber layers have led the research on the development of other semiconducting materials which is easily available, cost-effective and non – toxic for the application in PV devices. As a result of this, in recent years, environmentally benign and economic friendly novel materials such as $Cu_2ZnSn(S,Se)_4$ (CZTS) [54], Cu_2S [55,56], Cu_2SnS_3 [57], Cu_2O [58,59], Sb_2S_3 [60,61], SnS [62,63], FeS_2 [64–66], $CuSbSe_2$ [67] and $CuSbS_2$ [68] gained special attention as an absorber layer for solar cell applications. Organic perovskite-based solar cells are notable due to the rapid rise in their published efficiencies and showing comparable performance to that of second generation inorganic cells. Although the perovskite based solar cells have achieved efficiencies more than 20%, these materials are very sensitive to the atmosphere (oxygen, moisture, and ultraviolet radiations) and perovskite structure degrades when exposed to air [69,70].

Therefore, these materials cannot be used in commercial solar cells unless somehow their degradation is hindered. Owing to the above facts, chalcogenide (solar cells based on sulfide, selenide and telluride semiconductors) based materials for PV applications are of significant importance in the present scenario. This thesis work focuses on the development of Cu-Sb chalcogenide absorber layers for solar cell application. The important features and advantages of this material as a solar cell absorber are explained in detail in the following chapter.

CHAPTER 2

Cu-Sb CHALCOGENIDES FOR PHOTOVOLTAIC APPLICATIONS

2.1 INTRODUCTION

In the past few decades, Cu-Sb based chalcogenides gained special interest as photovoltaic absorber materials due to earth-abundant and cost-effective constituent elements [71–76]. Compared to Ga and In, Sb and Cu are far less expensive according to the US geological survey reported in 2014 [77–79]. Sb is approximately 60 times less expensive than In and possesses almost the same chemistry as that of In (Sb has the same +3 oxidation state as that of In or Ga). The chemical and economic advantages make the Cu-Sb based chalcogenides as an effective alternative of $CuInS_2$ [80, 81]. The practical and scientific motivations behind the use of the Cu-Sb materials for solar cell application supported by the optoelectronic properties, moderate hole doping and grain growth at relatively low temperatures of this material. $CuSbS_2$ possesses a direct optical band gap of 1.5 eV which is the optimum band gap for PV absorbers to achieve maximum device performance [80, 82–84]. It also exhibits much steeper absorption onset compared to $CuInS_2$, specifically due to the non-bonding lone pair electrons in the Sb atom [85–87]. Even though among the Cu-Sb based compounds $CuSbS_2$ is the most studied and applied material in PV application with a maximum reported photoconversion efficiency of 3.22% [88], other

ternary phases such as Cu_3SbS_3 [89–94], $Cu_{12}Sb_4S_{13}$ [95–99] and Cu_3SbS_4 [100–104] have been also reported. Less PV efficiency of $CuSbS_2$ reported so far indicates that much research must be done on this material including better control of the device parameters and tuning its absorption composition since the theoretical efficiency of the compound is 23%. In the same way $CuSbS_2$ substitutes $CuInS_2$, $CuSbSe_2$ can replace $CuInSe_2$ due to the similar chemical nature of $CuSbSe_2$ compared to $CuInSe_2$ and simultaneously having a different structure due to the low-valent state of antimony [105–107]. Sb is in the same +3 oxidation state in $CuSbSe_2$ like for In in $CuInSe_2$. Owing to the suitable optical band gap (1.1-1.2 eV) and electrical properties, $CuSbSe_2$ has also the potential to be a good solar absorber [106–117]. Though it has been less investigated than $CuSbS_2$, photoconversion efficiency comparable to that of $CuSbSe_2$ has been achieved [88, 106].

This thesis is mainly focused on exploring the PV application of $CuSbS_2$, however taking the combination of the properties of both $CuSbS_2$ and $CuSbSe_2$, a quaternary $CuSbSe_XS_{2-X}$ as solar cell absorber layer is also investigated. The following sections of this chapter will describe in detail the structure, optical and electrical properties that make these materials suitable for PV device applications as well as the commonly used synthetic approaches to produce them.

2.2   STRUCTURE

The crystal structure of chalcostibite $CuSbS_2$ is orthorhombic with space group *pnma* no: 62, lattice constants, a = 6.045 Å, b = 3.807 Å and c = 14.545 Å, as described by Mukesh Kumar and Clas Persson [105]. The unit cell of $CuSbS_2$ contains 16 atoms with 4 atoms of Cu, 4 atoms of Sb and 8 atoms of S. Cu and Sb atoms occupy the cation sites where the Cu atoms are coordinated by four chalcogen atoms and the Sb atoms are coordinated by three chalcogen atoms. The structural stability, better charge transport properties and the ability to form interface structures are some of the adventures of having a layered crystal structure (as that of $CuSbS_2$) compared with other structural forms according to J.T Dufton et al [118]. $CuSbSe_2$

also exhibits a similar crystal structure as that of $CuSbS_2$ with the same *pnma* space group, no 62 (reported by Koji Takei et. al.) [82]. In $CuSbSe_2$ structure, Sb and Cu cations are 3 and 4 coordinated respectively with Se anions. The calculated lattice parameters of $CuSbSe_2$ are a = 6.2990 Å, b = 3.9734 Å and c = 15.0050 Å (ICSD #418754). The crystal structure of $CuSbS_2$ as reported by Koji Takei et.al. is schematically presented in Figure 2.1 [82]. As a newly emerging quaternary Cu-Sb based chalcogenide material, $CuSbSe_XS_{2-X}$ also exhibit orthorhombic crystal structure [82, 119].
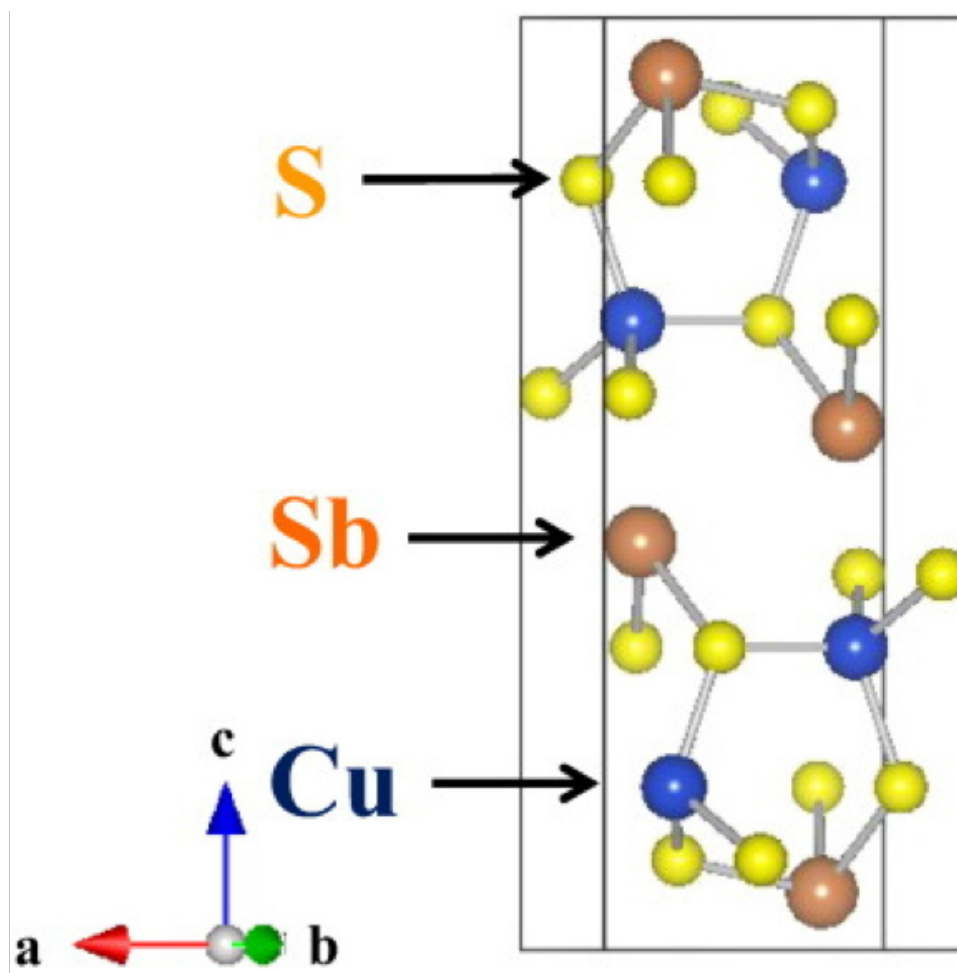
Figure 2.1: Crystal structure of chalcostibite $CuSbS_2$, orthorhombic crystal system with *pnma* space group, no:62. Reproduced with kind permission from Elsevier.

2.3   PROPERTIES

2.3.1   Optical Properties

According to theoretical studies, both $CuSbS_2$ and $CuSbSe_2$ possess reliable optical properties better than $CuInSe_2$ (CIS) and ideal for PV applications. Optical properties of Cu-V-VI (V = P, As, Sb, Bi; VI = S, Se) materials were explored theoretically by Libing Yu et al. [107], with special focus to photovoltaic applications. They presented a fundamental analysis of the controlling factors of absorption strength in compound semiconductors [86]. Considering the Cu-V-VI (V = P, As, Sb, Bi; VI = S, Se) system, the group V elements can exist in two oxidation states, +5 or +3 having respective valence electron configurations $s^\circ p^\circ$ and $s^2 p^\circ$. These configurations mirror the Tl^{3+} $s^\circ p^\circ$ and Tl^+ $s^2 p^\circ$ configurations of group III elements. Hence the Cu-III-VI_2 elements can be effectively replaced by Cu-V-VI system for similar or better photovoltaic performance. The Cu-V-VI system consists of four different element sets such as Cu-As-S, Cu-As-Se, Cu-Sb-S, Cu-Sb-Se each having compositions with both high valence V^{5+} and low valence V^{3+}. Moreover, calculations based on GW approximation show that the absorption coefficient of both $CuSbS_2$ (CAS) and $CuSbSe_2$ (CASe) are as high as 10^5 cm^{-1} and possess optical band gap in the range 1-1.5 eV satisfying the criteria for Shockley-Queisser criterion. In addition to this, CAS and CASe chalcostibite systems are found to exhibit higher or similar spectroscopic limited maximum efficiency (SLME > 20%) compared to the $CuInSe_2$ chalcopyrite system [108].

Owing to the suitable optical band gap, high absorption coefficient, and high SLME, CAS, CASe materials can replace the ongoing absorbers in PV application. In the present thesis work, in addition to the ternary $CuSbS_2$, quaternary $CuSbSe_X S_{2-X}$ has been also investigated for its photovoltaic performance. Although less investigated, $CuSbSe_X S_{2-X}$ also possess direct band gap in the range of 0.9-1.1 eV [119]. The calculated optical absorption spectra of Cu-Sb based chalcogenides using first principles is shown in Figure 2.2 [120].
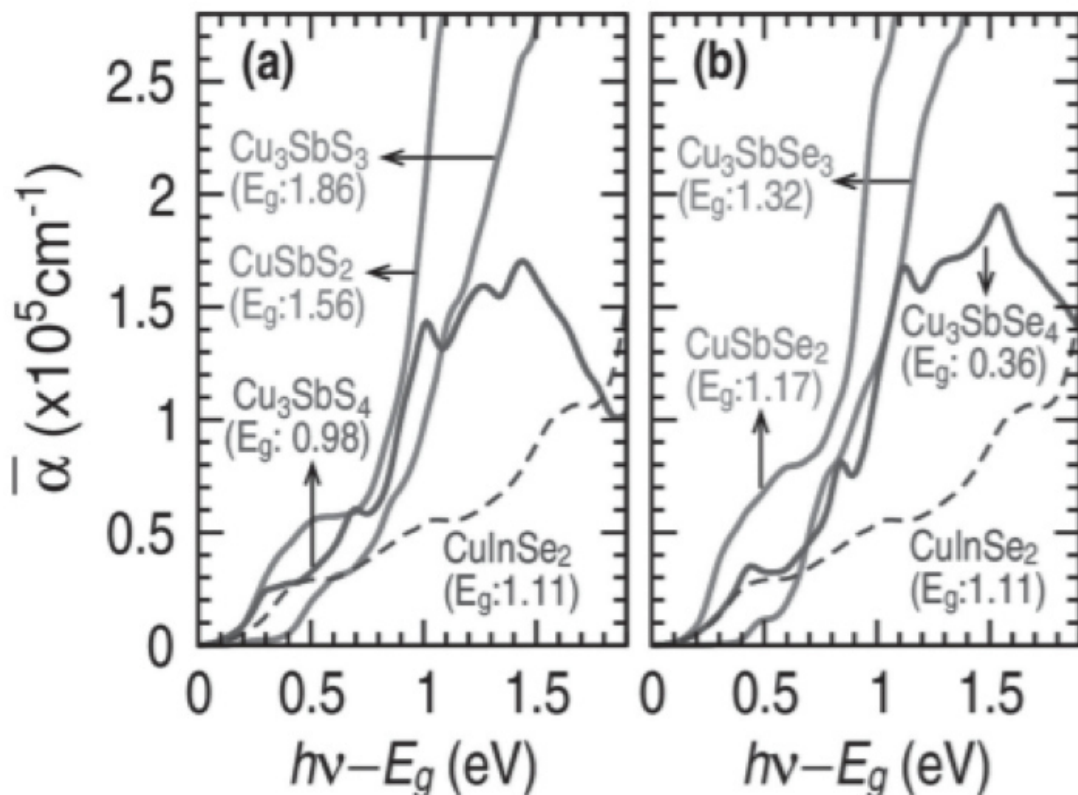
Figure 2.2: Calculated optical absorption spectra for Cu-V^{5+}-VI compounds and Cu-V^{3+}-VI compounds within the element sets of (a) Cu-Sb-S, (b) Cu-Sb-Se, using the first principles quasi-particle GW method based on wavefunctions generated from hybrid functional HSE06. CuInSe$_2$ (dashed) is shown as reference. Minimum band gaps (E_g) are aligned at E = 0. The energy differences (Δ) between E_g and dipole-allowed direct gaps for the indirect materials are CuSbS$_2$ (0.05 eV), Cu$_3$SbS$_3$ (0.13 eV), CuSbSe$_2$ (0.09 eV), and Cu$_3$SbSe$_3$ (0.26 eV). Adapted with kind permission from John Wiley and Sons.

2.3.2   Electrical Properties

Both CAS and CASe possess p-type conductivity. The p-type conductivity in $CuSbS_2$ originates due to the shallow defects of Cu vacancy with low ionization energy. According to Yang et al., $CuSbS_2$ thin films possess electrical conductivity of 10^{-3} to 10^{-4} ($\Omega\,cm^{-1}$). Since the acceptor defects such as Cu_{sb} and donor defects such as Sb_{cu} and Cu_i exhibit high formation energy in comparison with V_{cu}, they have no significant effect on the electrical conductivity of $CuSbS_2$. Like in $CuSbS_2$, the higher population of shallow accepter (V_{cu}) contributes to the p-type conductivity of $CuSbSe_2$. However, when the chemical potential goes from Se rich condition to Se poor, p-type conductivity of $CuSbSe_2$ can be switched to intrinsic. When doped with extrinsic elements weak n-type conductivity can be achieved in $CuSbSe_2$ due to the shift of the Fermi energy upward to the 1 eV above VBM.

To confirm the p-type conductivity of thin films, often, hall effect measurements using the van der pauw method is used. $CuSbS_2$ and $CuSbSe_2$ are proved to have p-type conductivity according to the above-mentioned characterization technique.

2.4 $CuSbS_2$ PHOTOVOLTAIC ABSORBER: A REVIEW

Taking the economic and chemical advantages of CAS and CASe over chalcopyrite into account, they have been mostly used as photovoltaic absorbers. This section of the thesis summarizes the literature survey on synthesis and PV applications.

2.4.1   Material synthesis

Various chemical, as well as physical depositions techniques, are available for the synthesis of CAS and CASe chalcostibite thin films. Physical deposition techniques include thermal evaporation and co sputtering. Moreover, there have been reports on combining chemical and physical deposition techniques such as a combination of chemical bath and thermal evaporation deposition techniques.

2.4.1.1 Chemical deposition techniques

Chemical methods mainly include chemical bath deposition, spin coating, spray pyrolysis, and electrode deposition.

(a) Chemical Bath Deposition (CBD)

For the fabrication of cost-effective, large area thin films for photovoltaic applications, CBD is a good choice among the other synthetic chemical approaches. In a typical chemical bath deposition, cations and anions contained in a bath are precipitated in a controlled manner on the substrates kept inside the bath for the formation of the respective thin films [121–123]. Using this technique, thin film deposition can be carried out as a single or multi-step process [124, 125] of the same material or different.

In a pioneering work reported by Nair et al. [126] deposition of $CuSbS_2$ thin film was demonstrated through sequential deposition of Sb_2S_3 and CuS layers followed by thermal annealing. The films were having p-type conductivity and optical band gap of 1.52 eV. In a follow-up work, the same group applied CBD deposited $CuSbS_2$ in thin film photovoltaics as an absorber layer. The growth of $CuSbS_2$ thin films on glass substrates was reported by César Macías et al. via a single step CBD technique where the bath containing $SbCl_3$, $C_2H_6O_2$, $C_4H_8Na_2O_8$, $Na_2S_2O_3$, 1,3-dimethyl-2-thiourea, $CuCl_2.H_2O$, deionized water was kept at 35 °C for 16 h [127]. Even though the obtained films were phase pure $CuSbS_2$, long deposition time can be considered as a barrier towards the device application of these films.

(b) Spin coating

Spin coating is a simple and low-cost technique as CBD to deposit thin films on flat substrates. A typical spin coating involves the deposition of a small amount of coating material on to the substrate by rotating the substrate holder at a high speed in order to spread the coating material by centrifugal force. The final thickness of the resultant thin films usually depends on the viscosity, concentration of the solution

and angular speed of the spinning [128–130]. Synthesis of CuSbS$_2$ thin films and their application on PV devices by this method was reported by S. Banu et al. [88] where the thin films were fabricated on Mo coated soda-lime glass substrates using spin-coating of hybrid inks with and without the nanoparticles (type A hybrid ink: Cu-S nanoparticles and the Sb precursor and type B hybrid ink: a Cu precursor with an Sb precursor without Cu-S nanoparticles) followed by a sulfurization process. Phase pure CuSbS$_2$ resulted in the hybrid ink containing no nanoparticles which enhanced the photovoltaic performance of the cell: Mo/CuSbS$_2$/CdS/i-ZnO/n-ZnO/Al with highest ever reported efficiency of 3.22%. As an attempt towards fabrication of low-cost PV devices, CuSbS$_2$ thin films were prepared by spin coating method by Bo Yang et al. [86]. The experimental results were compared with theoretical studies and the optical, electrical and chemical properties of CuSbS$_2$ and its potential applications in PV devices were investigated. The theoretical studies reveals that CuSbS$_2$ has intrinsically p-type conductivity with shallow V$_{Cu}$ defects being the dominant acceptors. For the experimental studies, a hydrazine-based solution process was used for the fabrication of phase pure and highly crystalline CuSbS$_2$ thin films with large grain size. Five layers were subsequently deposited to obtain a thickness of $\sim$1 μm. After deposition of each layer, it was dried on a preheated hotplate at 100 °C for 10 min followed by thermal annealing at 250 °C for 3 min. The resultant films showed a direct optical band gap of 1.4 eV with a hole concentration of $\sim$10^{18} cm^{-3} and hole mobility of 49 cm^2/(Vs). This work paved way for further photovoltaic research on this material. The formation of CuSbSe$_2$ is also possible by spin coating technique. A systematic theoretical and experimental studies on the fundamental properties of CuSbSe$_2$ and its application as an absorber material for PV devices reported by Ding-Jang Xue et al. [108]. Theoretical studies revealed that the higher population of shallow accepter (V$_{Cu}$) contributes to the p-type conductivity of CuSbSe$_2$ as same as CuSbS$_2$. But the conductivity can be turned to intrinsic or even weakly n-type under Se poor conditions similar to CuSbS$_2$. The fabrication of CuSbSe$_2$ thin films using hydrazine method, a systematical study on its properties (optical, electrical) and its incorporation in solar cell in a substrate (FTO/CuSbSe$_2$/CdS/ZnO/ITO/Al)

configuration described in their work. The best solar cell device showed a conversion efficiency of 1.32% with an open circuit voltage of 0.274 V, short-circuit current density 11.84 mA cm^{-2} and fill factor of 40.51%. The observed low efficiency of the cell was attributed to the less optimization done to the device. The authors suggested that passivation of interfacial defects, optimization of the band alignment, enhancing the quality of CuSbSe$_2$ film and ZnO/ITO layer, addition of an antireflection coating and optimization of device configuration could improve the device performance.

(c) Spray pyrolysis

Spray pyrolysis is an easy and relatively cost-effective technique for the fabrication of thin films of any composition as well as multi-layered and of large area. Moreover, scalability, coatings of complex geometry, high-quality layers, uniformity of thin film and non vacuum highlight its applications to a great extent [131–133]. There are a few reports available on the fabrication of CuSbS$_2$ thin films by spray pyrolysis technique. Manolache et al. reported the synthesis and characterization of CuSbS$_2$ thin films and evaluated the response of 3D solar cell: TCO/dense TiO$_2$/CuSbS$_2$/graphite, where the TiO$_2$ and CuSbS$_2$ thin films were obtained via spray pyrolysis deposition technique [134]. Their reports revealed that the presence of an impure Sb$_2$S$_3$ phase, porous structure and band gap values of the resulted CuSbS$_2$ thin films lower the photovoltaic response of the cells to a very low value. Later on, the formation of the ternary crystalline chalcostibite (CuSbS$_2$, Cu$_3$SbS$_4$, and Cu$_3$SbS$_3$ phases) on FTO substrate using a spray pyrolysis deposition technique using polymeric additives were reported by Ionut Popovici et al. The resultant films showed varied morphologies such as multigrain, fiber-like aggregates and worm-like surface features depending on the parameters used in the deposition process and the use of polymeric additives resulted in a densification of the films and a decrease in the grain size [135]. The influence of substrate temperature on the growth and properties of spray-deposited CuSbS$_2$ thin film was investigated by S. Thiruvenkadam et al. Their optical properties revealed that the band gap of all the films deposited at various condition were between 1.35-1.50 eV which is closes to the ideal band

gap for the highest conversions efficiency of solar cell and the optical absorption coefficient more than 10^6 cm^{-1} [136]. The formation of CuSbS$_2$ thin films with a minor phase of Cu$_2$S using precursor solutions containing SbCl$_3$, CuCl$_2$, CS(NH$_2$)$_2$ on glass substrates at 200 °C was reported by Ramos Aquino et al. The obtained films showed a direct optical band gap of 1.45 eV and possessed carrier concentration 5×10^{20} cm^{-3} respectively [137]. Even though there are a few reports available for the formation of CuSbS$_2$ thin films by spray pyrolysis technique as mentioned above, more investigation is needed to produce high-quality films for the application in photovoltaics.

(d) Electrodeposition

Electrodeposition is a well-established chemical technique in which thin films are deposited by applying an opposite charge of the particles to an electrode where the particles get attracted and deposited [138]. For a successful deposition by electrodeposition, the particles should possess a net surface charge to get attracted by the oppositely charged electrode. Hence, metal sheet or glass substrates having conductive coating are usually used as the electrodes (substrates for deposition) for establishing the electric field by applying a voltage [139]. Fabrication of CuSbS$_2$ thin film by sulfurization of an electrodeposited metallic stack composed of Cu and Sb on a Mo-coated glass (Mo/glass) substrate was reported by Wilman Septina et al. [140] where the sulfurization process was carried out at various temperatures (450 and 510 °C) for the formation of phase pure ternary CuSbS$_2$. CuSbS$_2$ film with a dense structure and good adherence to the Mo substrate were obtained by preheating the stacked-layer under Ar prior to sulfurization process. Solar cells (Al:ZnO/CdS/CuSbS$_2$/Mo/glass) having a maximum conversion efficiency of 3.13% was achieved using this approach by them. Later on A.C. Rastogi et al. reported the fabrication of CAS films using single-step electrodeposition in choline chloride–urea eutectic ionic liquid medium [141]. Highly crystalline single phase CuSbS$_2$ was demonstrated by potentiostatic electrodeposition in choline chloride-urea eutectic ionic liquid medium. However, the deposited films showed 3 order

less conductivity compared to the films obtained by other deposition methods and which resulted in the failure in the fabrication of the PV device having the structure Ag/(n)ZnO/(p)CuSbS$_2$/FTO. The deposition of mesoporous films of the CuSbS$_2$ nanoplates on a conductive substrate by electrophoretic deposition (EPD) was recently reported by Michael E. Edley et al. [142]. In their typical EPD deposition, the setup consisted of two electrodes (two ITO) separated by a 2.5 mm channel that was filled with a nanoplate dispersion of 9 mg/mL and the voltage was applied to the electrodes for 20 min. The S^{2-} capped CuSbS$_2$ nanoplates were deposited using a bias voltage of 5 V due to the relatively higher electrophoretic mobility in comparison with those capped by oleylamine where the applied voltage was much higher (250 V). The resultant films turned in to phase pure CuSbS$_2$ by the post-heat treatment at 220 °C . CuSbSe$_2$ thin films also were synthesized using electrodeposition technique by Ding Tang et al. where the electrodeposition of CuSbSe$_2$ films were carried out in a stagnant three-electrode cell configuration at room temperature (25 °C) with a SnO$_2$-coated glass substrate as the working electrode, a pure graphite plate as the counter electrode and a saturated calomel electrode (SCE) as the reference electrode. Cu-rich and Cu-poor films with a high optical absorption coefficient larger than 7×10^4 cm^{-1} and the optical band gap of about 1.09 eV were reported [143].

2.4.1.2   Physical deposition techniques

Physical deposition technique is mainly classified into two. (i) Sputtering and (ii) Thermal evaporation. The following section discusses in detail about it.

(i) Sputtering

Sputtering is a physical vapor deposition process that includes knocking out and directing target material atoms towards a substrate by the bombardment of energetic ions. Sputtering is used to obtain high-quality thin films and thus used extensively in the semiconductor industry to deposit thin films of various materials

for the applications in different fields [144,145]. The fabrication and characterization of $CuSbS_2$ and $CuSbSe_2$ thin films and the incorporation of materials in photovoltaic devices using a high throughput combinatorial sputtering method was reported by Weltch et al. [106,146]. In this work, $CuSbS_2$ absorber material was developed using a three-stage self-regulated growth process to control the stoichiometry of the resulting absorber at elevated growth temperature. The high-throughput experiments indicated that 1.4 μm is the optimum thickness for $CuSbS_2$ on Mo and 0.8 μm on MoO_X for the best harvesting of the sunlight. Highest efficiency obtained was $\sim$1%, due to the poor short circuit current and open-circuit voltage. Their results indicated that the crystallographic orientation and morphology of $CuSbS_2$ played important roles in determining the solar cell parameters [146]. The deposition of $CuSbSe_2$ thin films was successfully reported by the same group using self-regulated sputter deposition. $CuSbSe_2$ thin film with a band gap of 1.1 eV was incorporated in solar cell and achieved a conversion efficiency of 3%. The authors reported that the less photocurrent was due to bulk recombination, poor fill factor due to issues of device engineering and photovoltage deficit originated from the non-ideal $CuSbSe_2$/CdS band offset are the limiting factors in increasing the device efficiency [106]. Fabrication of phase pure $CuSbS_2$ thin films by sequential deposition of the Sb_2S_3 and Cu_2S precursor layers by RF magnetron sputtering, followed by annealing in nitrogen environment was recently reported by M I Medina-Montes et al. [72]. The reported films showed properties such as a direct optical band gap of 1.5–1.62 eV, absorption coefficient close to 10^5 cm^{-1} and p-type conductivity.

(ii) Thermal evaporation

Thermal evaporation is a common technique for the fabrication of thin-film and which includes heating a source material over its melting point so that the evaporated particles travel through the vacuum chamber to the substrate where they condense back to form the thin film. The structural and electrical properties of the ternary chalcogenides $CuSbTe_2$, $CuSbSe_2$ and $CuSbS_2$ thin films by thermal evaporation (under a vacuum of about 1.3 mPa (10^{-5} Torr) and the rate of deposition

was 30 nm/min) on glass substrates [147]. Thermoelectric power and Hall voltage measurements indicated that the majority of carriers are holes for all the thin films (p-type conduction) and the temperature dependence of thermoelectric power of samples showed that the films were markedly non-degenerate semiconductors for $CuSbS_2$ thin films and partially degenerate for $CuSbSe_2$ thin films, while $CuSbTe_2$ thin films were degenerate. In 2009 Adel Rabhi et al. [148] reported the fabrication of $CuSbS_2$ thin films grown by thermal evaporation and the effects of substrate heating conditions on structural, optical and electrical properties. The crushed powder of an ingot of $CuSbS_2$ prepared using high purity Cu, Sb and S raw material was the source material for their evaporation. The formation of polycrystalline $CuSbS_2$ was obtained for the films annealed from 170 °C and above (upto 200 °C) even though starting annealing temperature was 100 °C. Strong absorption coefficients in the range of 10^5-10^6 cm^{-1} in the visible and near-infrared range and a direct band gap lie between 0.91-1.89 eV were found for the films annealed at various temperatures. Their overall results concluded that the band gap and resistivity of the films showed a direct dependence with annealed temperature. The same group reported the effect of post-growth treatments in air atmosphere in the range of 100 to 300 °C resulted in the formation of the films with high absorption coefficients and p-type conductivity [149]. The recent report on the synthesis of $CuSbS_2$ thin films by thermal evaporation technique was reported by R. Suriakarthick et al. [150] where the evaporant-source material was synthesized by the solvothermal method. However, the as-prepared film showed an optical band gap of 2.14 eV, a band gap tailoring was achieved by increasing the substrate temperature (at 400 °C) and the resulted films showed a band gap of 1.64 eV and p-type conductivity.

2.4.1.3 Combined chemical bath and physical deposition techniques

Exploring the advantages of each to form excellent quality thin films, combined chemical bath, and physical depositions techniques (thermal evaporation or sputtering techniques) can be used. The advantage of this method over the single CBD

technique is, the precise control of stoichiometry as well as duration of the process. The preparation of $CuSbS_2$ thin films by annealing sequentially deposited Sb_2S_3-Cu stacked layers using CBD and thermal evaporation was reported by our group [151] where the thin films of antimony sulfide (Sb_2S_3) were chemically deposited on various substrates (glass and TCO substrates) from a bath contains $SbCl_3$, acetone, $Na_2S_2O_3$ and distilled water and Cu layers were thermally evaporated [78, 152]. U. Chalapathi et al. reported the formation of $CuSbS_2$ thin films by annealing chemically grown Sb_2S_3 (by CBD method) and sputter-deposited $Cu(Sb_2S_3/Cu)$ stacks in a graphite box. Their results conclude that the Cu/Sb ratio from 0.85 to 0.97 resulted in a phase-pure $CuSbS_2$ films having orthorhombic crystal structure with a p-type electrical conductivity and an optical band gap of 1.52 eV [153].

2.4.1.4 Post heat treatment methods

For the formation of the desired ternary phase, most synthesis methods include deposition of the stacked layers of the desired elements/compounds followed by a post-heat treatment which leads to the reaction of precursors obtain the desired ternary phase. Annealing in a conventional vacuum oven, rapid thermal processing and/or sulfurization are the mainly used post-treatment methods for the formation of a pure ternary phase. The following section will give a detailed idea about these three main post-heat treatment methods.

a. Vacuum annealing and Rapid Thermal Processing (RTP)

The vacuum annealing is a process in which the films or precursors (stacked layers of the constituent elements/compounds (for example stacks of CuS/Sb_2S_3 in the case of $CuSbS_2$) are allowed to heat inside a vacuum furnace at a specific temperature to form the desired composition by reacting the precursors at the specified temperature in a vacuum atmosphere. Since the process is carried out in a vacuum, this annealing method offers less chance of reacting the precursors with either oxygen or any unwanted material. However, the long annealing time is a drawback of

this process. Often, this long annealing process can result in the formation of the impure secondary phases such as Cu_2S in the case of $CuSbS_2$ phase. So that to increase the production rate as well as the efficiency of the photovoltaic devices, cell fabrication time must be reduced. Rapid thermal processing (RTP) is an alternative to the conventional vacuum annealing process which helps to reduce effectively the cell fabrication time compared to the conventional heat treatment methods without sacrificing any thin film or device properties, using a bunch of halogen or long arc lamps. The high-temperature heat treatment for a short time in RTP makes the diffusion process faster and avoids the oxidation of the films that normally takes place in conventional slow heating process by slower annealing processes. The advantages such as excellent temperature control, gas control, improved ambient control, high gas switching speed and uniformity make RTP more attractive in thin film technologies compared to conventional vacuum annealing [154–160]. A detailed study on the formation of phase pure $CuSbS_2$ thin films with improved crystallinity using RTP heat treatment is of this thesis work.

b. Sulfurization

The thin films of $CuSbS_2$ have been successfully grown by a number of authors by the sulfurization of metal precursors stack comprising copper and antimony at appropriate temperatures where the deposition of the metal precursors for the sulfurization process was done by various techniques such as electrodeposition, thermal evaporation, and sputtering. Colombara et al. [161] produced single-phase $CuSbS_2$ films having a band gap of ~1.5 eV and p-type conductivity by annealing Cu-Sb layers (either by evaporation of a Cu/Sb stack or electrodeposition of Sb-Cu alloy) in presence of sulfur vapor at temperatures above $350\,°C$. The fabrication of layers of phase pure $CuSbS_2$ from a metallic precursor stack comprising Cu and Sb was grown by dc sputtering followed by a sulfurization at $400\,°C$ under nitrogen atmosphere inside a graphene box was reported by Enzo Peccerillo et al. [162]. A recent report by Yuanfang Zhang et al. [73] on the synthesis of $CuSbS_2$ thin films by a two-step process involved the co-Sputtering of Cu/Sb_2S_3 precursors over Mo coated soda-lime

glass substrates followed by the sulfurization in a rapid thermal processor at $380\,^{\circ}$C for 3 minutes. Their results revealed that post-annealing treatment could improve the electrical properties such as the minority carrier lifetime of $CuSbS_2$ devices.

2.4.2 Photovoltaic device performance

There have been many reports on the preparation of $CuSbS_2$ thin films with various chemical as well physical deposition techniques, among all these reports, a very few demonstrated $CuSbS_2$ and $CuSbSe_2$ based PV device fabrication. A summary of these published PV devices is shown in Table 2.1 below.

Table 2.1: Performance of the prototype devices based on the $CuSbS_2$ and $CuSbSe_2$ absorbers

Structure	V_{oc}(mV)	J_{sc} (mA/cm^2)	FF (%)	η (%)	Ref
SnO_2:F-nCdS:In-iSb_2S_3-p$CuSbS_2$/Ag	335	0.2	$\cong$25	$\cong$0.017	[126]
SnO_2:F/CdS/Sb_2S_3/$CuSbS_2$/C:Ag	382	5.32	32	0.66	[127]
FTO/$CuSbS_2$/CdS/ZnO/ZnO:Al/Au	440	3.65	31	0.5	[86]
MoO_X/ $CuSbS_2$/CdS/i-ZnO/ZnO:Al/Al	309$\pm$61	8.91$\pm$2.5	31$\pm$3.1	0.86$\pm$.34	[146]
SnO_2:F/n-CdS/i-Sb_2S_3/p-$CuSbS_2$/ C/Ag	405	7.54	32	1	[163]
Mo/ $CuSbS_2$/CdS/i-ZnO/ITO/Al	622	13	$\cong$32	2.55	[73]
Mo/ $CuSbS_2$/CdS/i-ZnO/n-ZnO/Al	430	15.42	41.52	2.75	[71]
FTO/BL-TiO_2/mp-TiO_2+ $CuSbS_2$ /HTM/Au	304	21.5	46.8	3.12	[81]
Al:ZnO/CdS/$CuSbS_2$/Mo	490	14.73	44	3.13	[164]
Mo/$CuSbS_2$/CdS/i-ZnO/n-ZnO/Al	470	15.64	43.56	3.22	[88]
FTO/ $CuSbSe_2$/CdS/ZnO/ITO/Al	274	11.84	40.51	1.32	[108]
Mo/ $CuSbSe_2$/CdS/i-ZnO/ZnO:Al/Al	350	20	44	3.5	[106]
Si_3N_4/Mo/ $CuSbSe_2$/CdS/i-ZnO/ZnO:Al	380	24.5	41	3.8	[114]

The maximum conversion efficiencies reported so far for CAS and CASe are 3.22 and 3.5% respectively for CAS thin films reported from a hybrid ink using spin coating by S. Banu et al. and CASe formed by self-regulated sputtering process reported by Welch.et.al. shown in Figure 2.3 [88, 106].
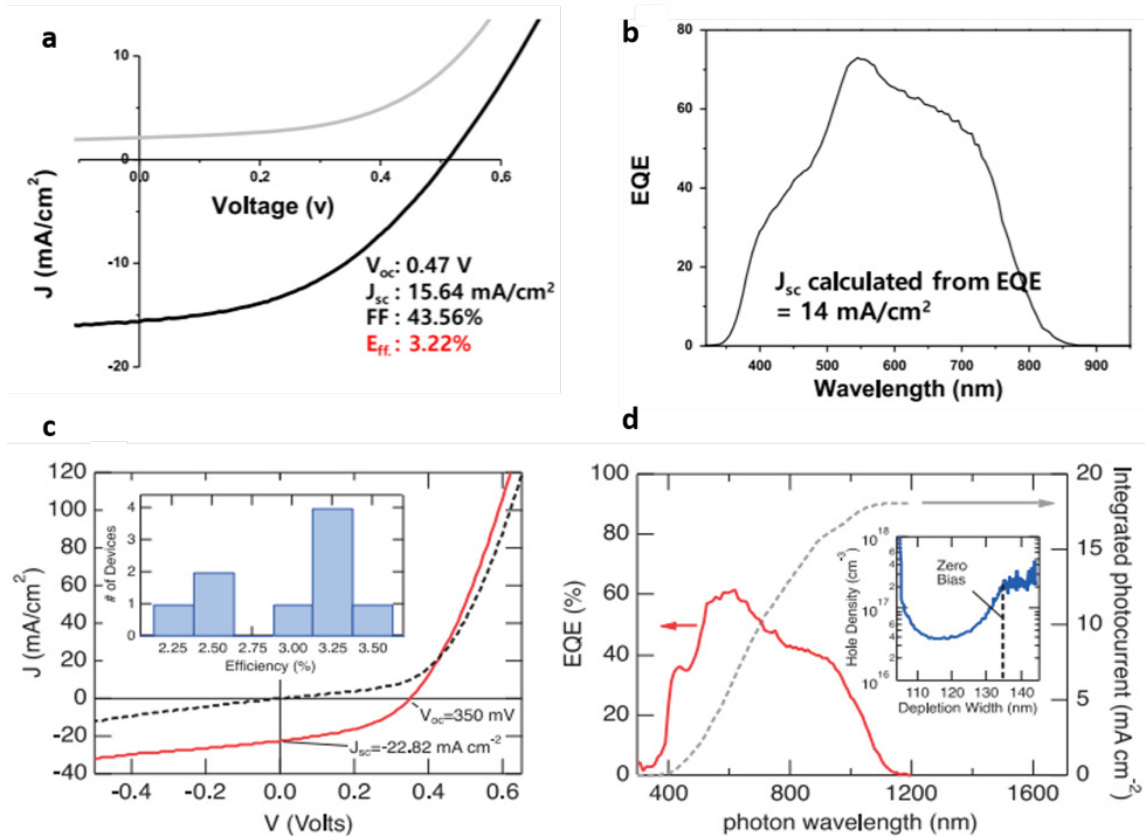
Figure 2.3: Light and dark J–V characteristics of the substrate CuSbS$_2$ cell (glass /Mo/CuSbS$_2$/CdS/ZnO/Al) fabricated using hybrid ink (b) EQE curve of the CuSbS$_2$ device (c) J–V results for the most efficient 3.5% CuSbSe$_2$ PV device and results of a histogram analysis of efficiency for 9 nominally equivalent, nonshunted devices from the first row on the combinatorial library as the inset. (b) EQE results for the 3.5% CuSbSe$_2$ PV device, including the integrated EQE × AM1.5G product, and results of C–V analysis in the inset. Reused with kind permission from Elsevier (a,b) and IOP science (c,d).

2.4.3 Current research issues

The current photovoltaic research is more towards developing PV devices using low-cost materials through cost-effective fabrication techniques without compromising much the conversion efficiency. Later, when these materials are really employed as commercial solar cells, their performance is also sometimes questioned because majority of the times the fabricated and reported cells are just in the laboratory aspects and would have large deviation from the expected performance if used commercially. $CuSbS_2$ and $CuSbSe_2$, both contain low cost and environment-friendly constituent elements and thus attract wide attention from the researchers worldwide based on the economic viewpoints. Even though researchers started to work on these materials a decades ago only a few demonstrated $CuSbS_2$ and $CuSbSe_2$ based PV device fabrication. Among those devices, usually reliable J_{sc} values are obtained but either the open-circuit voltage (V_{oc}) or the field factor (FF) or both are compromised. Hence, even though the cell has a higher short circuit current density, the overall performance is yet to be improved (refer to the Table 2.1). Many authors pointed out that the low efficiency of $CuSbS_2$ solar cells mainly arises from both the problematic absorber and unfavorable heterojunction configuration [165, 166]. Intense investigation is indeed to improve the devicel properties.

Chapter 3

CuSbS$_2$ thin films: synthesis and characterization

3.1 INTRODUCTION

This chapter deals with the synthesis and characterization of CuSbS$_2$ thin films and the results of the films as well. Here we used a combined chemical bath and thermal evaporation approach followed by heat treatments. Various characterizations techniques such as X-ray Diffraction (XRD), Raman Spectroscopy, X-ray photoelectron spectroscopy (XPS), X-ray fluorescence spectroscopy (XRF), Scanning electron microscopy (SEM), Atomic force microscopy (AFM), UV-Vis NIR Spectroscopy, I-V and Photoresponse measurement systems were used for the analysis of structure, elemental and chemical composition, morphology, surface roughness, optical and electrical properties of the films.

3.2 METHODOLOGY

CuSbS$_2$ thin films were synthesized by heating sequentially deposited Sb$_2$S$_3$/Cu stack layers. First, thin films of Sb$_2$S$_3$ were deposited using chemical bath deposition. Then, Cu was thermally evaporated on the Sb$_2$S$_3$ followed by heat treatment in a conventional vacuum oven, rapid thermal processing (RTP) system or both. The following sections describe in detail the deposition process.

39
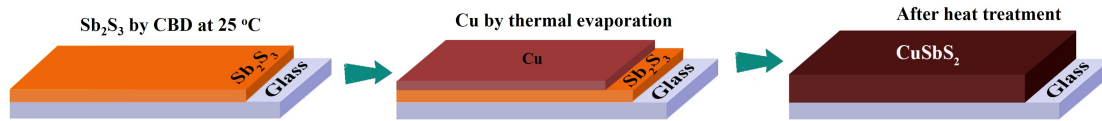
Figure 3.1: Schematic representation of CuSbS$_2$ formation

3.2.1 Preparation of Sb$_2$S$_3$/Cu layers

3.2.1.1 Chemical deposition of Sb$_2$S$_3$

Thin films of antimony sulfide (Sb$_2$S$_3$) were deposited on cleaned glass, molybdenum as well as TCO (ITO/FTO) substrates by chemical bath deposition [167] For that, 650 mg of SbCl$_3$ was dissolved in 2.5 ml of acetone in which 25 ml of Na$_2$S$_2$O$_3$·5H$_2$O (1 M) and 72.5 ml of deionized water were added and stirred. The glass substrates (75 mm × 25 mm × 1 mm) were cleaned with neutral soap solution followed by alcohol and isopropyl alcohol and dried in warm air. Such cleaned substrates were placed horizontally in a Petri dish and the solution was carefully poured into it without making bubbles. The bath was kept at room temperature (25 °C) for 2 h, 4 h, and 8 h. The films were deposited only on the lower side of the substrates facing the bottom of the Petri dish. The samples were washed gently with distilled water and dried. The resulted thin films were orange-yellow in color with good adhesion.

3.2.1.2 Thermal evaporation of Cu

Cu layer of different thicknesses (varied from 1 nm to 100 nm) on Sb$_2$S$_3$ thin films were deposited by thermal evaporation technique (Torr International, Model No: THE2–2.5 kW-TP). Cu wire of purity 99.99% was used as the source material for evaporation. The evaporation process was carried out in high vacuum (10^{-6} Torr) at a rate of 2 Å/s keeping the substrates rotating with 20 rpm speed. The copper film thickness was estimated in situ using a quartz crystal thickness monitor installed in the evaporation system.

3.2.1.3 Post heat treatments

In the present thesis work, the Sb$_2$S$_3$-Cu precursor layers with different Cu thicknesses were annealed in a vacuum oven (TM Vacuum Products, Model: V/IG-80314). The annealing process was carried out at 350 °C and 380 °C under 10^{-3} Torr for 30 min, 45 min, and 1 h. The annealed samples were labeled with prefix CAS. After identifying the copper thickness (Cu-50 nm) to form nearly phase pure films, glass/Sb$_2$S$_3$-Cu layers (Cu-50 and 100 nm) were heated in a rapid thermal processing (RTP) sysztem (Ecopia, Model: RTP-1300). The high temperature heat treatment for short time in RTP (Figure 3.2) makes the diffusion process fast and avoids the oxidation of the films that normally takes place in slower annealing processes which resulted the formation of phase pure thin films [168]. The samples were heated in the RTP system at 500 °C and 600 °C at a pressure 10^{-3} Torr for 5 min. Furthermore, 380 °C annealed Sb$_2$S$_3$/Cu layers (Cu-50 and 100 nm) were also subjected to RTP (pre-annealed RTP) at the same conditions as described above to examine the effect of further crystallization or grain growth on the CuSbS$_2$ films.

3.3 CHARACTERIZATION TECHNIQUES

The deposited CuSbS$_2$ thin films were subsequently characterized for their surface morphology and structure and for different properties such as optoelectronic, electrical, and optical. Each of these characterization techniques was chosen based on the thin film property being analyzed. Hence, it is relevant to briefly explain the mechanism behind each characterization method employed in the thesis to have a better understanding of the technique. This section of the thesis thus describes briefly the basic mechanism of the characterization techniques involved in the thesis for evaluating the properties of the CuSbS$_2$ thin films.
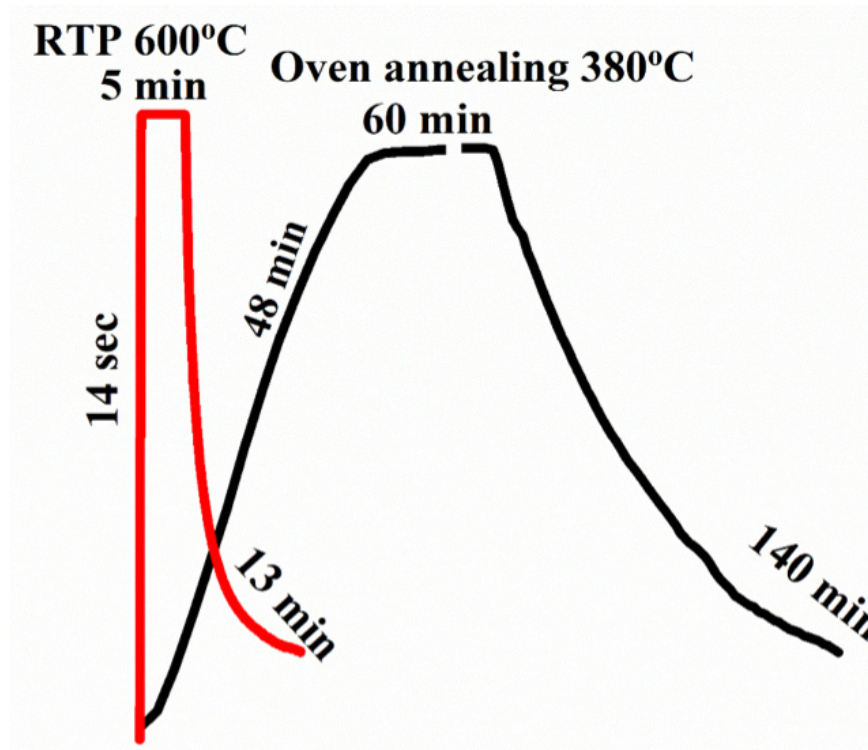
Figure 3.2: Graphical representation of duration of heating in vacuum oven as well as in RTP

3.3.1 X-ray Diffraction (XRD)

X-ray diffraction is widely used to characterize the structural properties of materials by measuring the scattering patterns produced by samples. X-rays will be scattered in all directions when it strikes atoms. If the sample is constituted by a periodic array of atoms, the scattered waves will reinforce in some specific directions and will cancel each other in other directions. The relation between the wavelength of the X-ray (λ), spacing between the lattice planes (d) and the angle of incidence (θ) is given by,

$$n\lambda = 2d \, \sin\theta \tag{3.1}$$

where n is the order of diffraction. The above equation is known as Bragg's

condition and serves as the principle behind X-ray diffraction technique. According to the Bragg's condition, as the interplanar distance of a crystal changes, the angle of incidence will also be changed accordingly at a given constant wavelength and thus the technique can be effectively used to identify the crystal structures of the analyzed samples given they are fully or partially crystalline.

In the present thesis work, the XRD technique was employed to analyze the structure of the deposited CuSbS$_2$ thin films. For the analysis, the diffractometer was operated in the normal mode for the preliminary prepared CuSbS$_2$ thin films using a Bruker D8 Advance diffractometer which employs a Cu-Kα radiation (λ=1.54056 $\mathring{A}$). Later on, grazing incidence mode (GIXRD) was used to reduce the background noise on the acquired diffractograms. A Panalytical Empyrean diffractometer employing Cu-Kα radiation of wavelength 0.154 nm was used for the XRD analysis and the acquired XRD patterns were compared with standard JCPDS values of the respective phases for identification of the phases and their crystal structures.

The average crystallite size can be estimated from the XRD patterns employing the Scherrer equation,

$$D = \frac{0.9\lambda}{\beta \cos\theta} \tag{3.2}$$

where D is the crystallite size, λ is the wavelength and β is the full width at half maximum (in radians, FWHM) of the peak analyzed. Even though XRD analysis is a powerful tool to characterize the crystalline properties of materials, it possesses a major limitation that amorphous samples cannot be identified using this technique [169, 170].

3.3.2 Raman spectroscopy

The structure and composition of materials can be analyzed by Raman spectroscopy based on the interaction between light and vibrational modes of the material (phonons).

Monochromatic light can interact with the samples in two different ways:

(i) Elastic scattering of photons where the energy is conserved (known as Rayleigh scattering)

(ii) Inelastic scattering where the photons exchange energy with crystal lattice (Raman scattering or Raman effect)

The Raman spectrum consists of two regions such as the stokes region (photons are scattered at lower energy than the Rayleigh energy) and the anti-stokes region (photons are scattered at higher energy than the Rayleigh energy). Depending on the molecular vibrations of each material, the peak positions observed in Raman spectra change due to the change in energy absorbed and thus can be used to identify the compounds [171,172]. Raman spectroscopy is used as a complementary technique to XRD in the present work to analyze and confirm the formation of the CuSbS$_2$ phase. It also served to identify any impurity phases present in the samples thus helping to control the deposition parameters to obtain phase pure CuSbS$_2$. Thermo Scientific DXR micro Raman spectrometer was used in the thesis for collecting the Raman spectra of the samples. The spectrometer was equipped with a 532 nm excitation line and the spectra were collected by scanning in the range 30 to 3500 cm^{-1}. As Raman spectra can be used to identify both crystalline and amorphous phases, it was effectively used to identify the presence of any phases present in the samples whether they were crystalline or amorphous.

3.3.3 X-ray photoelectron spectroscopy (XPS)

XPS is a surface characterization technique used to collect information on the elemental composition and chemical states of the samples. The working principle behind the technique can be explained as follows. When monochromatic X-rays of high energy interact with materials, they eject electron from the core energy levels which are called photoelectrons.The kinetic energy of these photoelectrons is ana-

lyzed using a detector and later converted into binding energies (BE's). Finally, the binding energy is plotted versus the number of photoelectrons emitted per second. Elemental composition analysis using XPS is usually done by scanning the spectrum in a wide range of BEs and then identifying each element present in the sample surface. Small BE ranges corresponding to the elements of interest are then scanned in high resolution to assign the chemical states associated with different phases present. In an XPS spectrum, peaks appear due to the emission of photoelectrons from specific binding energy states in the material. Quantification of the composition of the sample surface is also possible through measurement of the BE of the emitted photoelectrons. The p, d and f orbitals in the XPS spectra split into two peaks due to the coupling of the orbital angular momentum (l) with electron spin (s). The orbital "s" does not split since the orbital angular momentum associated with the "s" orbital is zero. On the other hand, type of bonding in compounds accounts for the chemical state of each atom. Changes in the potentials on the valence shell will influence the energy needed to remove the inner core electrons in a material and hence the BE will shift accordingly depending on the valence charge acquired. For instance, the BE energy will shift to lower values if the atom acquires a partial negative valence charge. This shift in BE can be identified by high-resolution scans in the specified energy ranges in XPS and hence can be used as a method to identify the different oxidation states associated with different phases. XPS machines also have the capability to carry out sample depth profiling by removing the surface atoms due to bombardment using energetic Ar$^+$ ions. In this way, the distribution of the elements through depth of the samples can be identified and hence the composition variations through the film thickness can also be tracked. Additionally, average thickness of thin-film samples can be estimated if the sputtering rate is known [169, 170, 172, 173].

In the present work, the elemental composition and chemical states of the CAS thin film samples were analyzed using a Thermo Scientific K-alpha X-ray photoelectron spectrometer equipped with monochromatic Al-Kα radiation of energy 1486.6 eV available in our laboratory. Typically, a low-resolution scan in a wide range

was used for identifying the elements and high-resolution core level scans were collected for further chemical state analysis. All the XPS peaks were corrected using BE of adventitious carbon at 284.6 eV; peak deconvolution was done by applying a Shirley-type background calculation and peak fitting using the sum of the Gaussian-Lorentzian function.

3.3.4 X-ray fluorescence spectroscopy (XRF)

The interaction of X-rays with matter below the electron-positron pair production threshold is dominated by three processes such as elastic scattering, inelastic scattering, and photoelectric effect. The elementally distinct or characteristic X-ray spectrum that is emitted from an atom as an inner-shell hole is filled is named as XRF. When such transitions occur, characteristic X-ray energies emitted serve as a "fingerprint" for the element being analyzed and are quite distinct. According to the electron-hole being filled and the strength of the decay channel, the fluorescence spectra are labeled. For instance, when an $L_{III}(2p_{3/2})$ electron fills a K hole, the emitted X-ray is termed as $K_{\alpha 1}$. A similar kind of nomenclature is used for the L holes and so on. Even though the X-ray absorption cross-sections, fluorescence yields, and characteristic X-ray spectra are virtually unchanged by the sample environment except very near threshold due to the chemical effects on inner-shell wavefunctions are small, the measured signal can strongly depend on absorption and secondary excitation. Characteristic X-ray lines usually have bandwidth of a few eV which is smeared by the resolution of the detector. The fluorescence signature corresponding to each element is distinct even when the analyzed elements are nearby in the periodic table and thus the technique can be effectively used for identifying the same [169, 174, 175].

The XRF technique was used in addition to the XPS to determine the elemental composition of the CAS thin films.

3.3.5 Scanning electron microscopy (SEM)

SEM is a microscopy method using a focused electron beam to image the surface morphology of samples. The energy of the electrons used in SEM may vary between 100 eV and 30 keV. When electrons interact with matter, different phenomena may take place as described below.

(i) Electron backscattering, where the energy of the electrons is comparable to that of the incident energy

(ii) Emission of secondary electrons which are low energy electrons emitted from the top sample surface

(iii) Production of characteristic X-ray radiation which can be used for elemental analysis

(iv) Emission of Auger electrons (not considered in SEM)

In the normal imaging mode in SEM, typically secondary electrons (SE) are characterized since these electrons contain the most information regarding the sample surface morphology. However, backscattered electrons (BSE) are also analyzed for phase-contrast information. The backscattered electrons are strongly influenced by the nuclei of atoms and thus differ when scattered by different elements that can be used for identifying different elements/ phases from the originating contrasts. The average energy of the backscattered electrons is much higher than that of the secondary electrons since the backscattered electrons are resulted due to elastic scattering. Heavier elements produce more BSE and appear brighter compared to lighter elements in the collected image. When electrons interact with matter, it may also strike out an inner electron that can be later occupied by an outer shell electron. While the transition from the outer shell to an inner shell takes place, to conserve energy, an X-ray is emitted which is a characteristic X-ray depending on the energies of the atomic orbitals of each element. Hence, by identifying the energy of the

emitted X-ray, the element from which it is emitted can be detected. SEM machines use different kinds of detectors for either analyzing the electrons or the X-ray radiations and digital set-ups for converting them into images or easily interpretable EDX spectra [176].

In the present thesis, SEM was used mainly to identify the surface morphology of the deposited CAS thin films. A Hitachi SU8020 field emission SEM was employed for the analysis. However, in some cases, elemental mappings were also acquired for information on the distribution of each element throughout the sample.

3.3.6   Atomic force microscopy (AFM)

Surface features with unprecedented clarity can be imaged using AFM. Any sufficiently rigid surface either in the air or with the specimen immersed in liquid can be examined using this technique. The data obtained using AFM can also be compared with the information acquired using low-resolution techniques since the field of view in AFM can be varied from the atomic or molecular scale up to sizes above 125 μm. In contrast to the electron microscopes, AFM can provide 3D images of the surface without expensive sample preparation protocols. There are different operation modes in AFM under these two categories among which contact mode, deflection or error mode, lateral force microscopy are the ones in the DC mode and non-contact mode, intermittent contact mode, phase imaging mode, and force modulation are some modes belong to the other category. Explaining each of these operation modes will be out of the context of the thesis. The ability of AFM to produce real 3D images of a sample surface can be considered as a major advantage of the technique over SEM which may help in detailed interpretation of the morphology and surface roughness of thin films [169, 177].

The surface morphology of the CAS thin films was characterized by AFM in addition to SEM. Most of the time the images were acquired in the contact mode unless otherwise specified. The AFM images provided a better understanding of

the topography of the thin films formed through CBD and thermal evaporation techniques.

3.3.7   UV-Vis NIR spectroscopy

Ultraviolet and visible near infrared (UV-Vis NIR) absorption spectroscopy deals with the measurement of the attenuation of a light beam after passing through a specimen or after reflection from a sample surface [169, 178]. Usually, for thin film samples of known thicknesses (t), the transmittance (T) and reflectance (R) spectra as a function of wavelength (λ) are recorded from which the absorption coefficient at each frequency ν of the material can be calculated as follows:

$$\alpha = \frac{1}{t} \ln \left[\frac{(1-R)^2}{T} \right] \tag{3.3}$$

From the absorption spectra, the optical band gap (E_g) of the materials, defined as the minimum energy required to excite an electron from the top of the valence band to the bottom of the conduction band, can be estimated from the Tauc plot:

$$(\alpha h\nu)^n = A(h\nu - E_g) \tag{3.4}$$

where $n = 2$, $1/2$ and $2/3$ for direct allowed, indirect allowed and direct forbidden transitions respectively and is the optical band gap, h is the planck's constant, ν is the frequency and A is a constant. The band gap was determined from $(\alpha h\nu)^n$ vs hν curve by drawing an extrapolation of the data point to the photon energy axis where $(\alpha h\nu)^n = 0$, gives the optical band gap E_g. For photovoltaic applications, the optical band gap is an important parameter since it will directly affect how much percentage of the incident light is absorbed. For solar cells, 1.5 eV is the optimum band gap for maximum photoconversion efficiency according to the

Shockley-Queisser limit which gives the peak power of the solar cell device, as mentioned in section 3.4.4

In this thesis, a dual-beam spectrophotometer (Jasco-V770) was used for the optical characterization of the CuSbS₂ thin films. Optical transmittance and reflectance of the films were measured for a wide range of wavelength covering the UV-Vis-NIR regions ($\sim$ from 250 to 2500 nm) and then the optical band gaps were estimated using the equations as described above. In each measurement, a plain substrate was used as the reference in the spectrophotometer while keeping the thin film sample on the sample holder. The baseline measurement was done by keeping two glass substrates simultaneously and scanning the entire region (one in the reference path and other in the sample path).

3.3.8 Electrical characterization

In this section, the electrical characterizations carried out on the thin film samples are briefly described.

The electrical characterization includes mainly D.C. conductivity and photoconductivity.

The conductivity of a material is the ability to conduct electrical current and can be determined as follows:

$$\sigma = \frac{1}{\rho} \tag{3.5}$$

where ρ is the resistivity of the material. The resistivity of thin films can be obtained if the resistance and physical dimensions of the electrodes and thin film thicknesses are known. According to Ohm's law, the resistance is given by:

$$\rho = \frac{Rwt}{l} \tag{3.6}$$

where ρ is the resistivity in Ω cm, R is the resistance measured using Ohm's law in Ω, w is the width of the electrodes, t is the thickness of the film and l is the distance between two electrodes [169].

In this thesis, typically a pair of electrodes having equal dimensions were painted on the film surface using colloidal silver to use as the terminals in the two-point probe technique. A keithley picoammeter/ voltage source (Model No. 6487) was employed for applying the voltage through the painted electrodes and simultaneously measuring the current. From the I-V curves, the average resistance was calculated and then the conductivities of the films were determined using the equations described above.

An increase in the electrical conductivity of a semiconductor due to the absorption of light of sufficient energy is called photoconductivity [179]. The photoconductivity measurements are usually realized by measuring the current at a constant applied voltage under dark and illumination for a specific interval of time. In this work, the photoconductivity measurements were done using the same keithley source while the sample was illuminated using a tungsten halogen lamp and under dark.

3.4   RESULTS AND DISCUSSIONS

CuSbS$_2$ thin films were fabricated by heating chemically deposited Sb$_2$S$_3$ and thermal evaporated Cu. Stack layers after heat treatments, thin films turned to dark brown. This section of the thesis describes the crystal structure, elemental composition, chemical state, morphology, optical and electrical properties of the films formed at different conditions. The first section of this discussion part focuses on the effect of precursor layer thickness such as Cu/Sb layer thickness on the formation of ternary

CuSbS$_2$ phase. The effect of heat treatments such as conventional vacuum oven annealing, rapid thermal processing (RTP) and both for the formation of phase pure CuSbS$_2$ is discussing on the 2nd part.

3.4.1 Crystal Structure

The crystal structure of the thin films formed at different conditions was analyzed from the XRD patterns and the chemical structure by Raman spectra.

3.4.1.1 Effect of precursor thickness

I Variation of Cu layer thickness

(a) X-ray Diffraction (XRD)

To study the effect of Cu layer thickness on the formation of the phase pure CuSbS$_2$ phase, the XRD patterns of samples formed on glass substrates by varying Cu layer thickness from 1 to 100 nm were analyzed.

XRD patterns of Sb$_2$S$_3$ and Sb$_2$S$_3$-Cu thin films annealed in the conventional vacuum oven at 380 °C for 1 h are shown in Figure 3.3 and Figure 3.4 [180]. The patterns of the Sb$_2$S$_3$ and the films with lower Cu thickness such as 1, 2, and 5 nm are shown in Figure 3.3. The diffractograms show peaks corresponding to the (020), (120), (130), (211), (140), (301), (240), (421) and (511) crystal planes of orthorhombic Sb$_2$S$_3$ according to the JCPDS file No. 42-1393 (also included in Figure 3.3). No additional peaks or change in the crystalline structure is observed for the films deposited using 1 nm Cu in comparison with that of Sb$_2$S$_3$. However, an additional peak is observed at $2\theta = 28.07°$ when the Cu thickness was increased to 2 nm corresponding to the (111) plane of CuSbS$_2$ thereby showing that the formation of the ternary phase started from Cu 2 nm onwards. While increasing the Cu thickness to 5 nm, the same kind of pattern was followed by diminishing more peaks corresponding to the Sb$_2$S$_3$ phase.
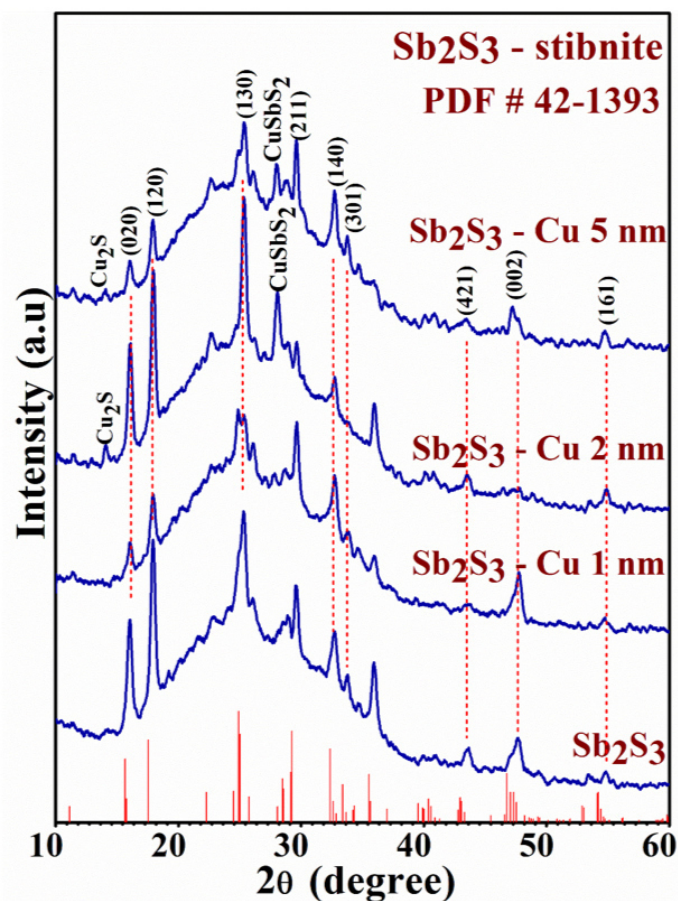
Figure 3.3: XRD patterns of Sb₂S₃-Cu thin films annealed at 380 °C for 1 h in vacuum oven (10^{-3} Torr) with varying Cu thickness: Sb₂S₃ (no copper), Sb₂S₃ with Cu 1 nm, Sb₂S₃ with Cu 2 nm, Sb₂S₃ with Cu 5 nm. The standard pattern corresponding to Stibnite Sb₂S₃ is included. Reprinted with kind permission from Elsevier (`https://doi.org/10.1016/j.solmat.2017.02.005`).

Figure 3.4 shows the XRD patterns of the annealed Sb₂S₃/Cu samples with varying Cu layer thicknesses 20, 50, and 100 nm. The major peaks marked by (200), (111), (410), (301), (501) and (800) are assigned to the orthorhombic CuSbS₂ according to JCPDS file # 44-1417 (also included in Figure 3.4) along with less intense peaks of Sb₂S₃ are present for 20 nm copper diffused films (CAS Cu20). These XRD peaks are coinciding with the reported results of CuSbS₂. Nair et al. [126] reported the formation of ternary CuSbS₂ films by annealing chemically deposited multilayer thin films and Yang et al. [86] by spin coating followed by a hot
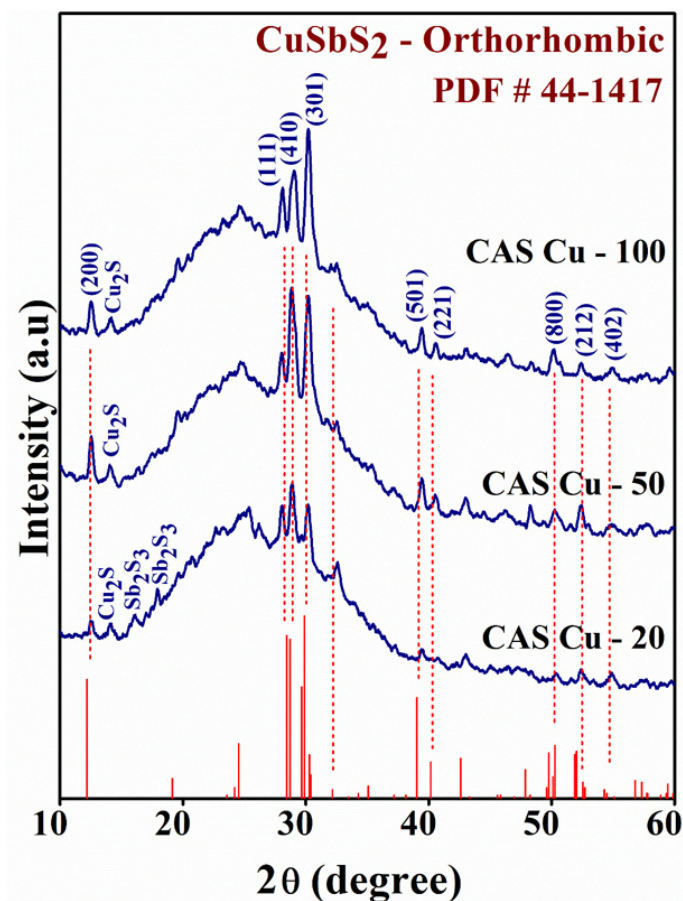
Figure 3.4: XRD patterns of Sb₂S₃-Cu(CAS) thin films annealed at 380 °C for 1 h in vacuum oven (10⁻³ Torr) with varying Cu thickness: Sb₂S₃/Cu with Cu 20 nm, Sb₂S₃ with Cu 50 nm, and Sb₂S₃ with Cu 100 nm. The standard pattern for orthorhombic CuSbS₂ (PDF#44–1417) is also included. Reprinted with kind permission from Elsevier (`https://doi.org/10.1016/j.solmat.2017.02.005`).

plate heat treatment. In both studies, the major XRD reflections are from the same planes as observed in the present work. Intensity of CuSbS₂ peaks increases for the films having Cu layer thickness of 50 (CAS Cu50) and 100 nm (CAS Cu100), with no Sb₂S₃.

The presence of a very feeble peak of Cu₂S was observed at $2\theta = 13.8°$ for the CAS films having Cu 20, 50 and 100 nm thicknesses. It might have originated due to the long-time conventional oven annealing.The presence of impurity Cu₂S peak was reported by Aquino et al. [137] and Acosta et al. [151] for the spray pyrolyzed

films as well as the films formed by combined chemical bath and thermal evaporation techniques respectively. CuSbS$_2$ films with binary CuS as minor phases were formed when Sb-Cu metal precursors were sulfurized at different temperatures as reported by Colombara et al. [161]. These results support the possible formation of feeble binary impurity phases (CuS and Cu$_2$S) while forming the CuSbS$_2$ phase involving a thermal annealing step. However, in this present work, for the Cu thickness of 50 nm and above, for the given thickness of Sb$_2$S$_3$ (200 nm), nearly phase pure CuSbS$_2$ thin films were formed as revealed by XRD analysis. On the other hand, the presence of the impurity phase in the thin films cannot be ruled out completely considering the 2% error limit of XRD.

For the photodetector application, the selected Cu layer thicknesses (20, 30 and 40 nm) were deposited on the Sb$_2$S$_3$ thin films coated on glass substrates. Structural characterization of CAS Cu 20 nm, CAS Cu 30 nm, and CAS Cu 40 nm thin films annealed at 380 °C for 1 h is shown in Figure 3.5. Here the diffraction patterns were collected in the grazing incident mode using PANalytical Empyrean Diffractometer in the range of $2\theta =$ 10-60 °C. For all these 3 samples, the diffraction patterns were collected at 0.5° incident angle in grazing incident mode. As observed in Figure 3.5 [181], for all of these samples the major reflections are originated from the planes (200), (101), (111), (410), (301), (501), (221), (321), (002), (800), and (212) that correspond to the orthorhombic crystal structure of CuSbS$_2$ (JCPDS#44-1417). For CAS Cu 20, Cu 30 nm thin films showed an additional reflection from the planes (020) and (120) and that corresponds to the stibnite Sb$_2$S$_3$ phase, which may arise from the unreacted chemically deposited Sb$_2$S$_3$ layer crystallized during heating. All the peaks in the reference JCPDS are identified in the CAS Cu 40 nm thin film without any reflections from the Sb$_2$S$_3$ plane. The above result implies that to form the complete ternary CAS phase there is a deficiency of Cu in the CAS 20 and CAS 30 thin films. Among the three samples, phase pure CAS with improved crystallinity was observed for the CAS 40 nm film from the diffraction pattern analysis. Compared to CAS 20 and 30 films, the intensity of the peak corresponds to the plane (111)
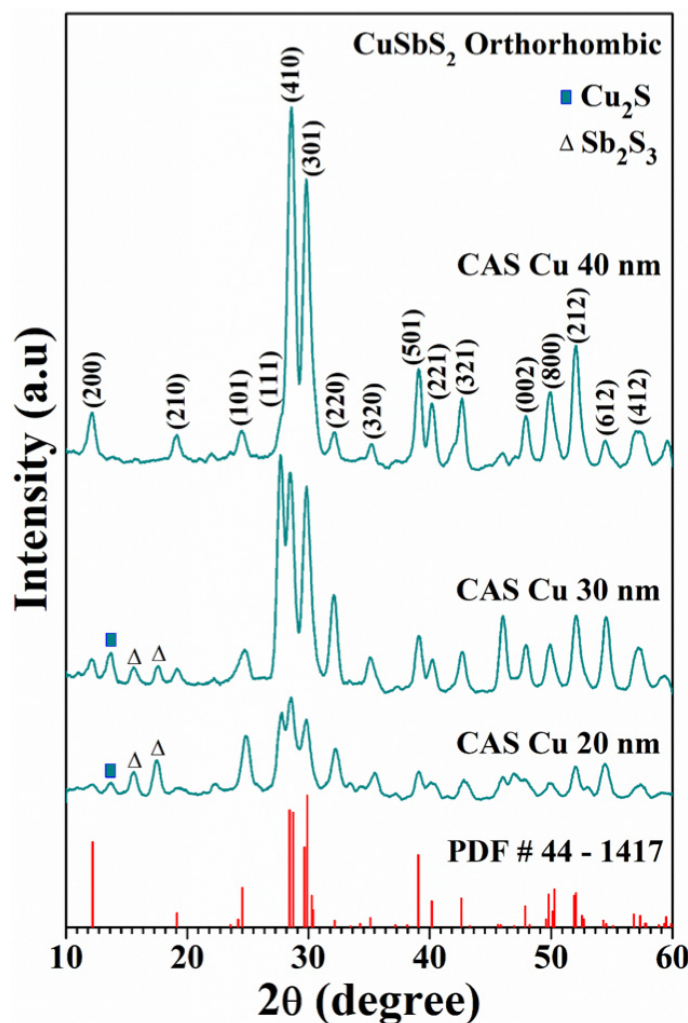
Figure 3.5: XRD pattern of CuSbS$_2$ thin films with varying Cu thicknesses 20, 30 and 40 nm annealed at 380 °C for 1 h in vacuum oven. The standard pattern corresponding to orthorhombic CuSbS$_2$ is included (PDF#44-1417) (DOI: 10.1039/C8RA05662E).

is diminished and the film gorwth tends to orient along (410) and (301) planes for CAS 40 sample. The crystalline size estimated for the CAS 20, CAS 30 and CAS 40 samples from the Scherrer equation (3.2) were 13, 13.6 and 14.6 nm respectively where the crystalline size increased with the increase in the Cu layer thickness.

(b) Raman analysis

The Raman spectra recorded using 532 nm laser excitation for identifying the

crystalline nature of thin films are shown in Figure 3.6 and 3.7 given below.
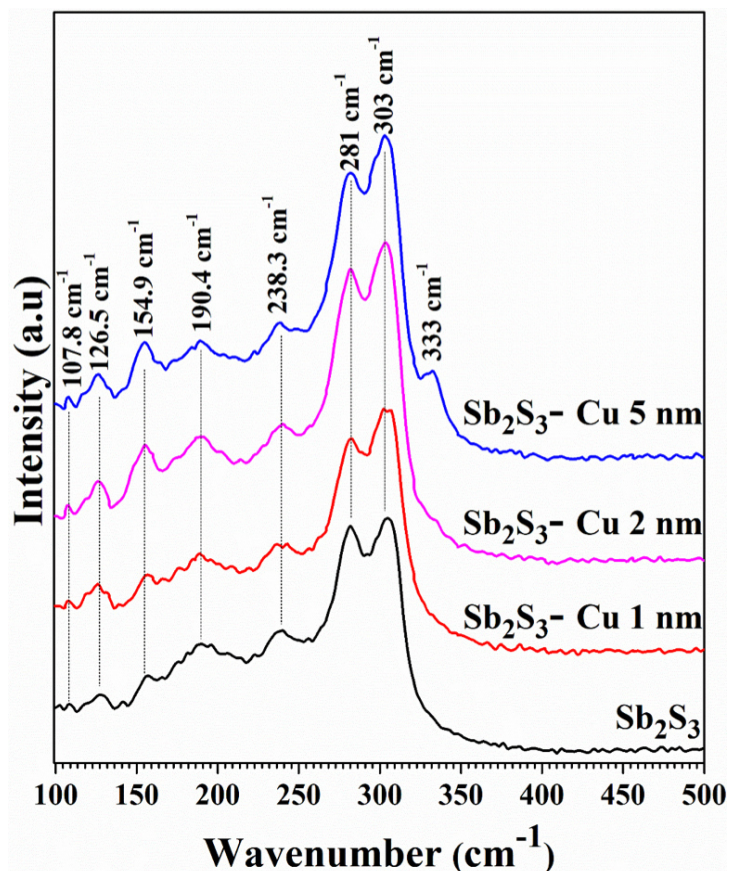
Figure 3.6: Raman spectra of Sb$_2$S$_3$-Cu thin films annealed at 380 °C for 1 h in vacuum oven (10^{-3} Torr) with varying Cu thickness: Sb$_2$S$_3$, Sb$_2$S$_3$ with Cu 1 nm, Sb$_2$S$_3$ with Cu 2 nm, Sb$_2$S$_3$ with Cu 5 nm.

Figure 3.6 shows the Raman spectra of Sb$_2$S$_3$, Sb$_2$S$_3$/Cu thin films annealed at 380 °C for 1 h in vacuum oven (10^{-3} Torr) with varying Cu thicknesses 1, 2 and 5 nm. All the samples were Raman active and the corresponding peaks are marked in the figure. As specified by Yun Liu et al. [182], the Raman and infrared (IR) modes of Sb$_2$S$_3$ are mutually exclusive and there are 60 phonon modes at zone center (Γ) where 3 are acoustic phonon modes (Γacoustic=B$_{1u}$+B$_{2u}$+B$_{3u}$), 30 are Raman active (ΓRaman=10A$_g$+5B$_{1g}$+10B$_{2g}$+5B$_{3g}$), 22 are IR active (ΓIR=4B$_{1u}$+9B$_{2u}$+9B$_{3u}$), and 5 are optically silent (Γ silent = 5A$_u$) modes. Experimentally they found only four Raman actives modes of A$_g$, B$_{1g}$, B$_{2g}$, and B$_{3g}$ at the wavenumbers 47.7, 50.8, 54.3, 69.1, 74.5, 99.1, 100, 124.1, 196.7, 208.2, 231.4, 251, and 257.9 cm^{-1}.
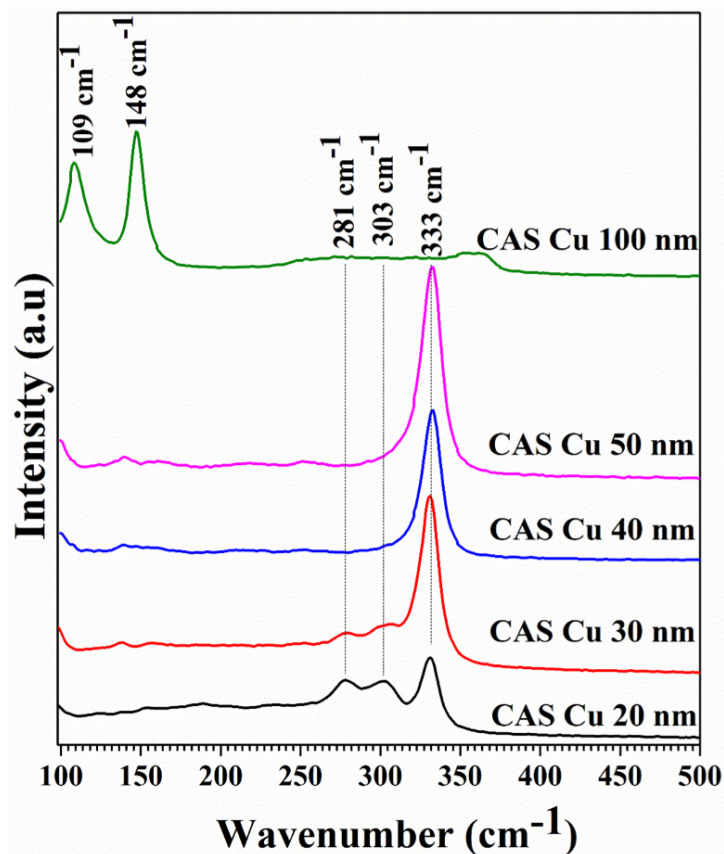
Figure 3.7: Raman spectra of Sb₂S₃-Cu(CAS) thin films annealed at 380 °C for 1 h in vacuum oven (10^{-3} Torr) with varying Cu thickness: Sb₂S₃/Cu with Cu 20 nm, Sb₂S₃ with Cu 30 nm, Sb₂S₃ with Cu 40 nm, Sb₂S₃ with Cu 50 nm and Sb₂S₃ with Cu 100 nm. Reproduced with kind permission from RSC advances (DOI: 10.1039/C8RA05662E).

Later on, Y A Sorb et al. [183] reported a few new Raman active modes A_{1g}, A_{2g} and A_{3g} at wavenumbers 195, 286 and 308 cm^{-1} and B_{3g}, B_{2g} modes at 241 and 314 cm^{-1} respectively. Here in the present spectra, all thin films show the Raman active modes at 107.8, 126.5, 154.9, 254, 190.4, 238.3, 281 and 303 cm^{-1} and which are attributed to the vibrational modes of Sb₂S₃ [182, 183]. A minor peak present at 333 cm^{-1} for Sb₂S₃ with Cu thicknesses 2 and 5 nm films are corresponding to the CAS phase. As specified by Baker et al. [184] in a study on pressure-induced structure transformation in orthorhombic CuSbS₂ (*Pnma* space group), the Raman active zone-center vibrational modes can be described with four Raman active modes

Table 3.1: Raman peaks for CuSbS$_2$ and Sb$_2$S$_3$

Wave number (cm^{-1})	Compound	Vibrational modes
107.8	Sb$_2$S$_3$	A$_g$ [182, 183]
109	CuSbS$_2$	[184]
126.5	Sb$_2$S$_3$	B$_{2g}$ [182, 183]
148	CuSbS$_2$	[184, 185]
154.9	Sb$_2$S$_3$	[186, 187]
190	Sb$_2$S$_3$	A$_{1g}$ [182, 183]
238.3	Sb$_2$S$_3$	B$_{3g}$ [182, 183]
281	Sb$_2$S$_3$	A$_{2g}$ [182, 183]
303	Sb$_2$S$_3$	A$_{3g}$ [182, 183]
333	CuSbS$_2$	[184, 185]

(A$_g$, B$_{1g}$, B$_{2g}$ and B$_{3g}$) and three infrared active modes (B$_{1u}$, B$_{2u}$ and B$_{3u}$). The Raman spectrum for an unoriented CuSbS$_2$ sample at 532 nm excitation wavelength published in RRUFF database [185] also supports the present findings. This implies that the ternary phase CuSbS$_2$ started to grow at Cu thickness 2 nm which is in good agreement with the observed XRD results for these same films. Raman spectra of Sb$_2$S$_3$-Cu(CAS) (CAS) thin films annealed at 380 °C for 1 h in a vacuum oven (10^{-3} Torr) with varying Cu thickness 20, 30, 40, 50 and 100 nm are shown in Figure 3.7 [181]. As seen in figure, all these samples characterize major Raman peaks corresponding to the CAS phase. For the samples having Cu thickness up to 50 nm, major Raman vibration is at 333 cm^{-1} whereas for the Cu 100 nm sample vibrations are at 148 and 109.5 cm^{-1} which is attributed to the CAS phase. When we compare these results with XRD, the CuSbS$_2$ and Cu$_3$SbS$_4$ possess a common peak at $2\theta = 50.2°$. It is evident from Figure 3.4, as the Cu layer thickness increased from 20 to 100 nm, an increase in the intensity of this peak was observed which supports the shift in Raman peaks and indicate the phase transition of CuSbS$_2$ to Cu$_3$SbS$_4$. The samples with 20 and 30 nm Cu thickness showed Raman bands

corresponding to impurity phase (Sb$_2$S$_3$) as marked by the peaks present at 281 and 303 cm^{-1} which also coincide with the XRD results of these samples. The Raman peaks of CuSbS$_2$ and Sb$_2$S$_3$ are tabulated in Table 3.1.

II Variation of Sb$_2$S$_3$ layer thickness
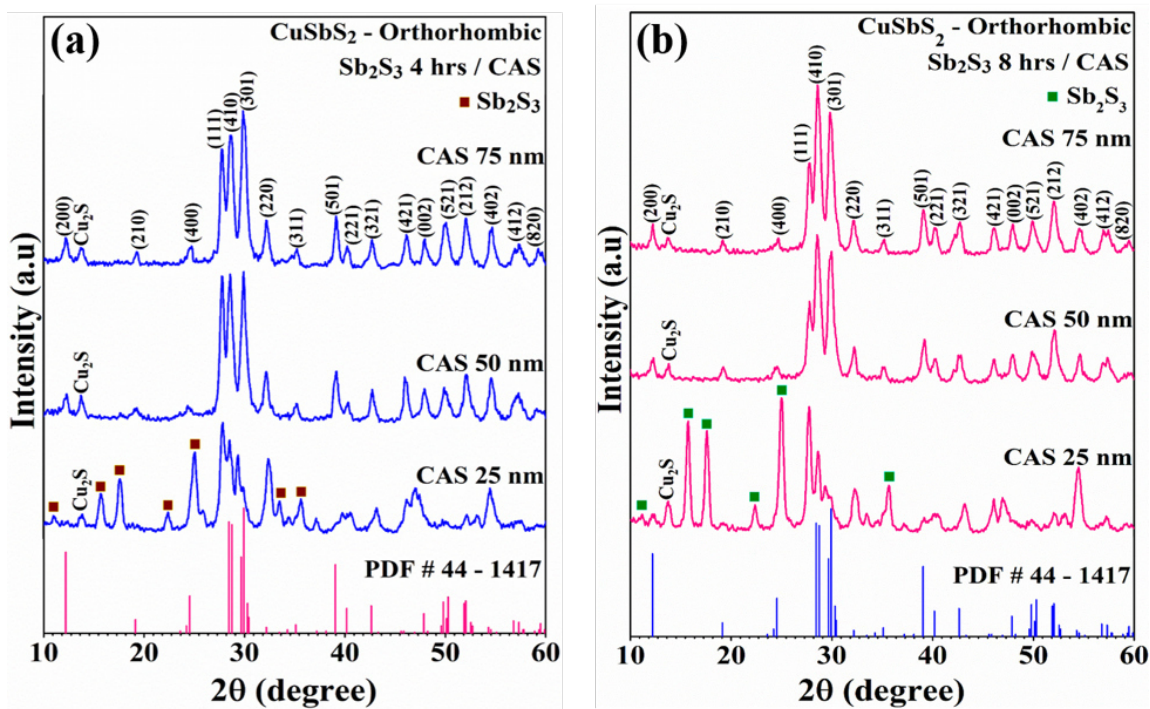
Figure 3.8: XRD patterns of Sb$_2$S$_3$-Cu(CAS) thin films annealed at 350 °C for 30 mins in vacuum oven (10^{-3} Torr) with varying Cu thickness: 25, 50 and 75 nm by keeping the CBD bath of Sb$_2$S$_3$ for (a) 4 h at 25 °C (b) 8 h at 25 °C. The standard pattern corresponding to orthorhombic CuSbS$_2$ is included in the same figure.

For the further improvement of the film properties, Sb$_2$S$_3$ CBD duration was changed from 2 to 4 and 8 h while simultaneously varying the Cu thickness. Figure 3.8 (a and b) shows the XRD patterns of the CAS 25, 50 and 75 nm samples deposited using 4 h and 8 h Sb$_2$S$_3$ bath durations respectively along with the JCPDS pattern corresponding to orthorhombic CuSbS$_2$. All the deposited Sb$_2$S$_3$/Cu samples in this case were annealed at 350 °C for 30 min in vacuum oven. For 4 h Sb$_2$S$_3$ films, the major reflections from the CAS 25 nm samples are from Sb$_2$S$_3$ phase due to the deficiency of Cu in these samples to form the ternary CuSbS$_2$. However,
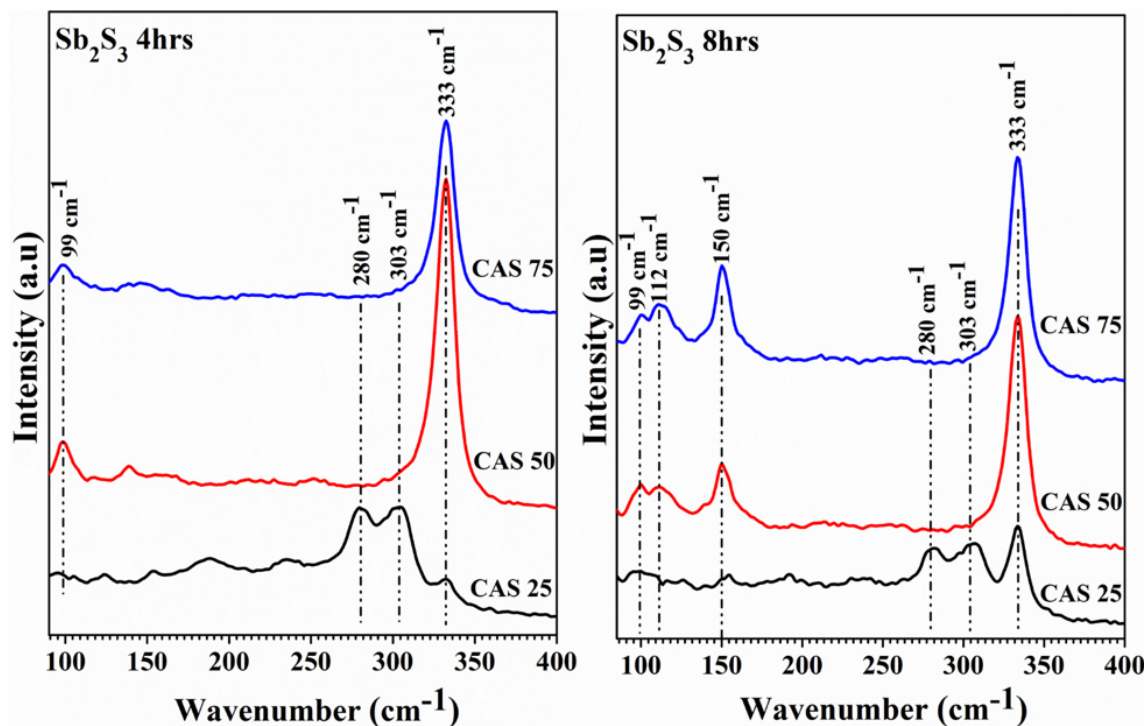
Figure 3.9: Raman spectra of Sb$_2$S$_3$-Cu(CAS) thin films annealed at 350 °C for 30 mins in vacuum oven (10^{-3} Torr) with varying Cu thickness: 25, 50 and 75nm by keeping the CBD bath of Sb$_2$S$_3$ for 4 h and 8 h at 25°C.

for Cu thickness 50 nm, the XRD pattern shows major peaks attributed to the CuSbS$_2$ phase. A similar diffraction pattern is observed for the CAS 75 nm sample as well with the difference that a better orientation along the (301) crystal plane of orthorhombic CuSbS$_2$ for the CAS 75 nm thin film sample. In addition to the Sb$_2$S$_3$ or CuSbS$_2$ phases, all the samples exhibit minor presence of the Cu$_2$S phase as denoted in the Figure 3.8. Similar results are observed for the 8 h Sb$_2$S$_3$ based CAS thin film samples where Sb$_2$S$_3$ is the major phase for the 25 nm Cu thickness and for higher Cu thicknesses (50 and 75 nm), CAS is the major phase.

Raman analysis on the CAS samples deposited using 4 and 8 h Sb$_2$S$_3$ supported the XRD results. The corresponding Raman spectra are given in Figure 3.9 for 4 h and 8 h Sb$_2$S$_3$ having varying Cu thicknesses. As evident from the figure, in both sets of samples, the CAS 25 nm sample showed Raman bands at 280 and 303 cm^{-1} originated from the vibrational modes of Sb$_2$S$_3$ along with a small peak at 333 cm^{-1}

due to the vibration mode of CuSbS$_2$. For 4 h CAS films, as Cu thickness increased to 50 or 75 nm, intensity of the 333 cm^{-1} peak increased and Sb$_2$S$_3$ vibrational peak 303 cm^{-1} completelety diminished. For the 8h CAS films the Raman spectra are characterized by two additional peaks located at 112 and 150 cm^{-1} which correspond to the CuSbS$_2$ vibration modes in addition to the peak at 333 cm^{-1}. The Raman shift at 112 cm^{-1} may contribute to the Cu$_2$S phase. This peak was observed only for the 8h Sb$_2$S$_3$ CAS films, which may be due to the higher thicknesses of Sb$_2$S$_3$ layer.

3.4.1.2   Rapid Thermal Processing (RTP)

RTP is the most commonly known post-treatment for the formation of the ternary chalcogenides which uses a bunch of halogen lamps or long arc lamps which help to effectively reduce cell fabrication time compared to conventional heat treatment methods without sacrificing film properties and device performance [188,189]. Based on the above results, effect of RTP at different temperatures on the crystalline nature of CAS 50 and 100 nm samples were studied and compared with that conventional vacuum oven treated samples. The RTP conditions: high temperatures (at 500 °C and 600 °C) and short time (5 min); conventional vacuum oven heating conditions: lower temperature (at 380 °C) and longer time (1 h). As evident from the diffraction patterns, the CAS 50 nm sample shows XRD patterns varying peak intensities upon conventional heating and RTP as given in Figure 3.10(a) [180]. The RTP 500 °C sample shows CuSbS$_2$ as the major phase along with Cu$_2$S as minor phase. When the RTP temperature was increased to 600 °C, phase pure CuSbS$_2$ with improved crystallinity is formed as seen in the figure, the presence of Cu$_2$S or Sb$_2$S$_3$ phases are not detected. Moreover, the film growth is likely to orient along (410) plane at 600 °C. To study the effect of RTP treatment on high copper content samples, the same analysis was done on CAS 100 nm thin films (Figure 3.10(b)) [180]. In this case, at 600 °C, Cu$_2$S peak intensity increases and also, new peaks corresponding to Cu$_3$SbS$_4$ is formed. To further improve the crystalline properties of the CAS 50
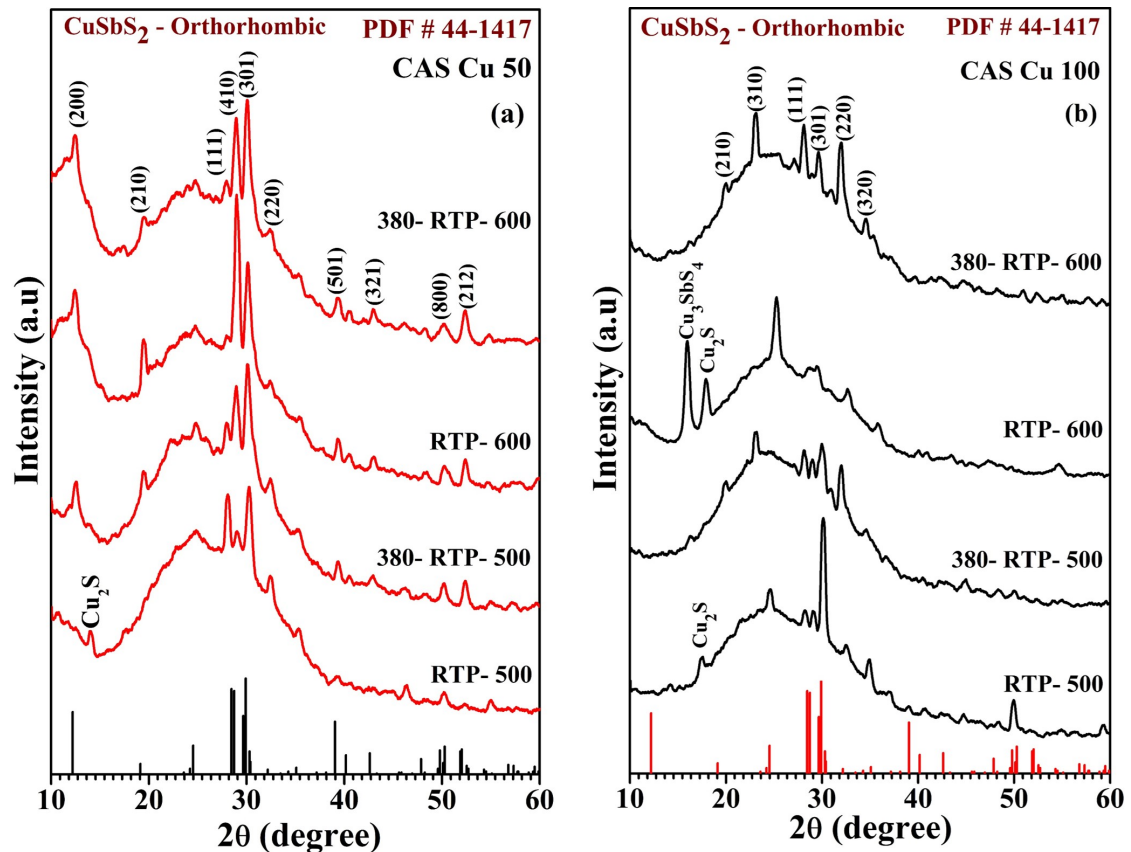
Figure 3.10: (a) XRD pattern of CuSbS$_2$ thin films thin films with Cu thickness 50 nm (CAS Cu50) formed at different heating conditions: conventional vacuum oven at 380 °C for 1 h, RTP at 500 °C for 5 min (RTP-500), pre-annealed RTP at 500 °C for 5 min (380-RTP-500), RTP at 600 °C for 5 min (RTP 600), pre-annealed RTP at 600 °C for 5 min (380-RTP-600) (b) CuSbS$_2$ thin films with Cu thickness 100 nm (CAS Cu100) formed by conventional heating at 380 °C for 1 h and RTP at 500 °C for 5 min (RTP-500), pre-annealed RTP at 500 °C for 5 min (380-RTP-500), RTP at 600 °C for 5 min, pre-annealed RTP at 600 °C for 5 min (380-RTP-600). The standard pattern corresponding to orthorhombic CuSbS$_2$ is also included in the same figure for reference. Reused with kind permission from Elsevier (`https://doi.org/10.1016/j.solmat.2017.02.005`).

and 100 nm samples, pre-annealed RTP (vacuum oven annealing at 380 °C for 1 h followed by RTP at 500 or 600 °C for 5 min) was done on both. Figure 3.10(a), Figure 3.10(b) present the corresponding XRD patterns of the CAS 50, 100 nm thin film

samples together with the samples annealed in vacuum oven for comparison. The pre-annealed RTP treated samples showed formation of phase pure CAS irrespective of the Cu thickness. However, the CAS 50 nm sample showed different crystalline behavior (peak intensity variations) compared to the CAS 100 nm thin films. Based on all of these results, it can be concluded that the thin films undergone RTP treatments after conventional vacuum oven annealing favors the formation of phase pure CuSbS$_2$ by excluding the formation of the impurity phases such as Cu$_2$S and Cu$_3$SbS$_4$ which can be attributed to the instant heating of the samples in RTP thereby improving the crystallinity and grain growth. But this effect was more prominent in the pre-annealed RTP samples probably due to the formation of the CAS phase on the first stage of vacuum annealing and then improving the crystalline properties of the same while later treated in RTP. Since the CAS 50 nm film showed the formation of phase pure CAS by direct and pre-annealed RTP treatments, further studies were carried out only on this sample. Crystallite size (D) was evaluated for CAS Cu 50 nm samples annealed at conventional vacuum oven, direct RTP and pre-annealed RTP at 600 °C using the Scherrer formula assuming the line broadening is merely due to the size effect. The average value of the crystallite size was ∼15 nm. For the calculation, the line broadening analysis of (301) peak was considered.

Phase structure of CAS samples formed at different conditions: annealing, pre-annealed RTP 600°C and direct RTP 600°C was analyzed using Raman spectroscopy (Figure 3.11) [180]. From the spectra, all the thin films show the Raman active modes at 100, 112,150, 254 and 332 cm^{-1} where the major peak located at 332 cm^{-1} and low intense peaks at 100 cm^{-1} and 150 cm^{-1} are assigned to the vibrational modes of the CuSbS$_2$ phase. The Raman shift at 254 cm^{-1} and 112 cm^{-1} are attributed to the Sb$_2$S$_3$ and Cu$_2$S phases respectively, where the intensity of these peaks diminished for the pre-annealed RTP sample. These results are in correlation with our XRD analysis of the same samples as discussed above.

Based on the XRD and Raman analysis it can be concluded that the Sb$_2$S$_3$ thin film with Cu thickness 50 nm pre-annealed RTP at 600 °C resulted the formation of
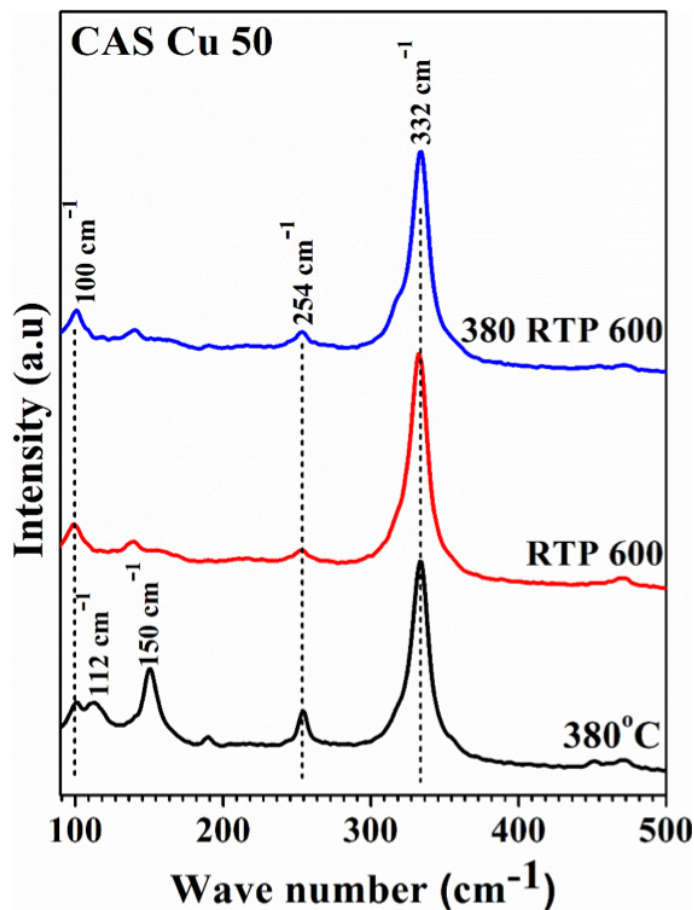
Figure 3.11: Raman spectra of the phase pure CuSbS$_2$ thin films (CAS Cu-50) formed at different conditions (a) annealed at 380 °C for 1 h in vacuum (b) RTP at 600 °C for 5 min (c) pre-annealed RTP at 600 °C for 5 min.(Reused with kind permission from Elsevier `https://doi.org/10.1016/j.solmat.2017.02.005`).

phase pure ternary CuSbS$_2$. These results encouraged us to do a systematic study on pre-annealed RTP at higher temperature for the formation of highly crystalline films having better properties. For that, the CAS 50 nm pre annealed films were heated in RTP at 625 °C for duration varying from 1 min up to 4 min 30 sec. Figure 3.12 [190]. shows the GIXRD (at $\omega = 0.5°$) patterns of CAS thin films deposited on glass substrates as prepared, annealed in conventional vacuum oven at 380 °C for 1 h and pre-annealed RTP at 625 °C for different time intervals from 1 to 5 minutes. From the figure, it is clear that as prepared films are completely amorphous. The observed reflections for CAS 380 °C sample from the planes were well matching with
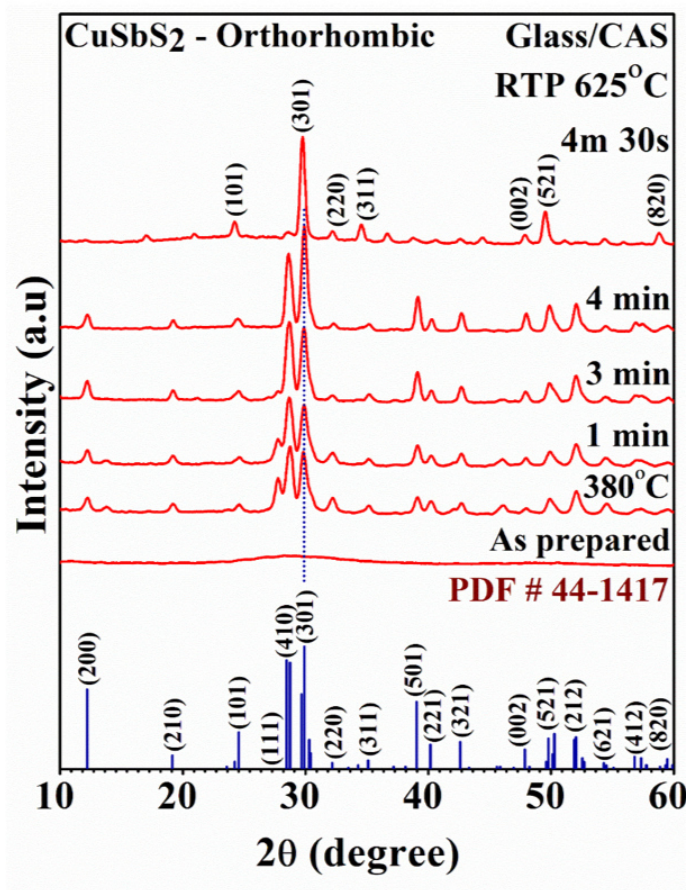
Figure 3.12: GIXRD patterns of CuSbS$_2$ (CAS) thin films as prepared, annealed at 380 °C for 1 h in vacuum oven (10^{-3} Torr) and pre-annealed RTP at 625 °C for 1 min, 2min, 4 min, 4 min 30 s and 5 minutes. The standard pattern for orthorhombic CuSbS$_2$ (PDF#44–1417) is also included. Reproduced with kind permission from Elsevier (`https://doi.org/10.1016/j.mssp.2018.11.007`).

the standard JCPDS for the orthorhombic CuSbS$_2$ phase. The feeble amount of an impurity phase Cu$_2$S presence is identified here also.

   The film pre-annealed RTP at 625 °C for 1 minute after the vacuum oven annealing shows the similar planes of CAS 380 °C samples which implies that the RTP treatment at higher temperature for 1 min duration is not sufficient to change the crystallinity. The Cu$_2$S peaks are absent in the pre-annealed RTP at 625 °C for 3-4.5 minutes sample and all the peaks are corresponding to the ternary CuSbS$_2$ phase. The 4 minutes and 30 s film shows a preferential orientation of (301) planes
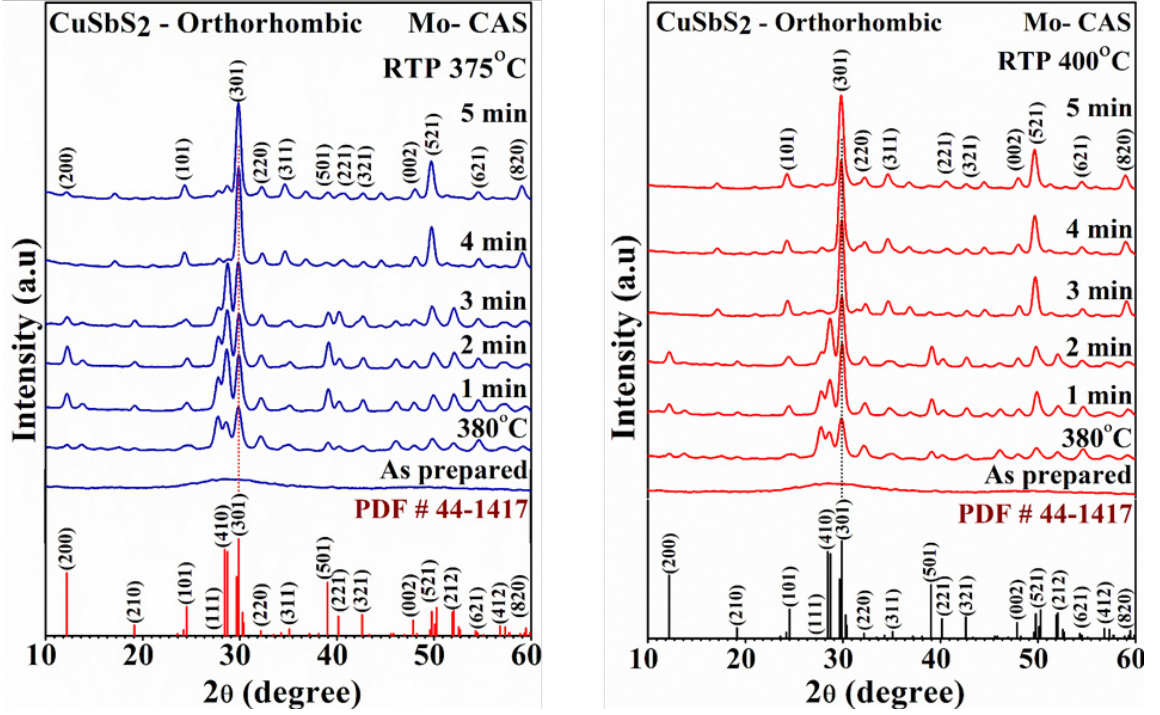
Figure 3.13: Raman spectra of the phase pure CuSbS₂ thin films (CAS Cu-50) formed at different conditions (a) annealed at 380 °C for 1 h in vacuum (b) RTP at 600 °C for 5 min (c) pre-annealed RTP at 600 °C for 5 min. Reused with kind permission from Elsevier (`https://doi.org/10.1016/j.solmat.2017.02.005`).

perpendicular to the substrate surface due to the high temperature supplied to the sample in short time. The preferential grain growth along (301) plane is further confirmed by the texture coefficient (TC) C_{hkl} by the equation:

$$C_{hkl} = \frac{N(I_{hkl}/I_{r,hkl})}{\sum_{i=1}^{N}(I_{hkl}/I_{r,hkl})} \tag{3.7}$$

where, N is the number of reflections in the XRD, I_{hkl} is the measured intensity of the plane under discussion, $I_{r,hkl}$ is the integral intensity for a sample with completely randomly oriented (hkl) plane taken from the JCPDS data file [191, 192]. In our analysis we considered major planes of (410) and (301), which are common in all the samples. The texture coefficient analysis confirmed that the TC (301) planes increased gradually with the pre-annealed RTP treatment. TC (301) of 380

°C, pre-annealed RTP at 1 min, 3 min, 4 min and 4 min 30 s CAS films were 1.7, 1.8, 1.8, 2.2, and 3.5 respectively. These results suggest the improved crystallinity and preferential gain growth along the plane (301).
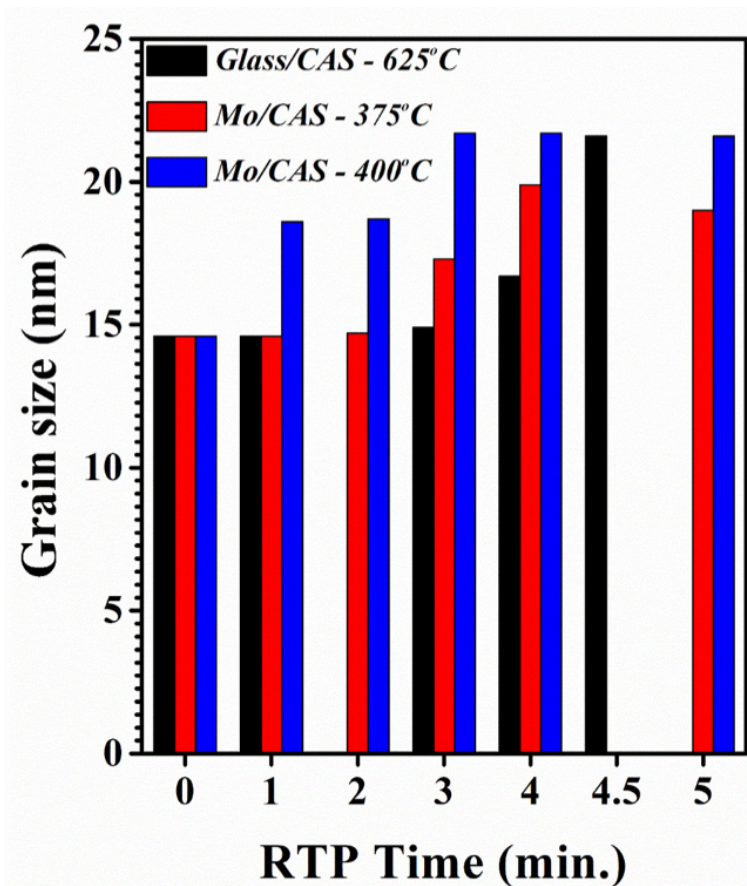
Figure 3.14: Grain size of CuSbS$_2$ (CAS) thin films on glass as well as on Mo substrates annealed at 380 °C (RTP time 0 min) in vacuum oven (10^{-3} Torr) and pre-annealed RTP at 625℃, 375 °C and 400 °C for 1 min, 2min, 3 min, 4 min 4 min 30 s (RTP time 4.5 min) and 5 min.

Further, we evaluated the crystallinity of CAS thin films grown on conductive substrates., the samples deposited on Mo coated glass substrates, for exploiting the properties of CuSbS$_2$ for the PV applications in the substrate configuration. Figure 3.13 [190]. shows the GIXRD patterns of CuSbS$_2$ thin films on Mo coated glass substrates subjected to post RTP at 375 °C and 400 °C for different durations, after annealed in conventional vacuum oven at 380 °C for 45 minutes. The patterns

corresponding to the samples as prepared and 380 °C annealed are also included for comparison. As the previous results obtained for glass/CAS films, no peaks are observed for glass/Mo/CAS as prepared sample which indicate that a heat treatment is required for the formation of ternary CuSbS$_2$ phase. The films annealed at 380 °C and pre-annealed RTP at 375 °C for 1 and 2 minutes show (101), (111), (410), (301), (220), (311), (501), (221), (321), (521) and (212) reflections with slight increase in the intensity of the peaks for RTP samples. The Cu$_2$S impurity phase is observed for these samples as well. This implies that the duration of heat treatment (2 min or less for 375 °C) in RTP is not enough to inter-diffusion Cu and Sb$_2$S$_3$ layer. Cu$_2$S impurity phase is disappeared when the pre-annealed sample is RTP treated for 3 min. The peaks corresponding to CAS are coinciding with the CAS peaks observed for the samples prepared on glass. The pre-annealed RTP for 4 min and 5min show a preferential orientation in (310) plane as same as observed for glass/CAS films treated in RTP at 625 °C for 4 min 30 sec. As the temperature was increased to 400 °C for the samples coated on Mo substrates, preferential orientation growth is achieved at a duration of 3 min which was less than the time required at 375 °C. All these results conclude that, either a moderate temperature for enough time or higher temperature for less time can make significant effect on the crystallinity of the CAS films. Preferential orientation of the films can improve the electrical properties of the films thereby enhancing their photovoltaic performances. The crystalline size of all the films deposited on glass as well as Mo substrates were calculated using Scherrer formula, increased from about 14.6 to 21.6 nm by the pre-annealed RTP treatment. As shown in Figure 3.14, conventionally annealed film on both the substrates show a grain size of 14.6 nm. Pre-annealed RTP treatment of 1 min didn't show a notable improvement in crystalline size. The crystalline size of the film on glass substrates increase to 21.6 nm by pre-annealed RTP treatment about 4 min 30 sec. The same crystalline size is observed for Mo/CAS 400 °C for 3, 4 and 5 min. Preferentially oriented film obtained by Mo/CAS pre-annealed RTP at 375 °C 4m show a crystalline size of about 19.9 nm which is less compared to the previously reported samples. It may be due to the insufficient post heating temperature. All the calculations are

carried out by the line broadening analysis of (301) peak. In general, the results suggest formation of CuSbS$_2$ films with preferential growth of (301) planes normal to the substrate surface by RTP.
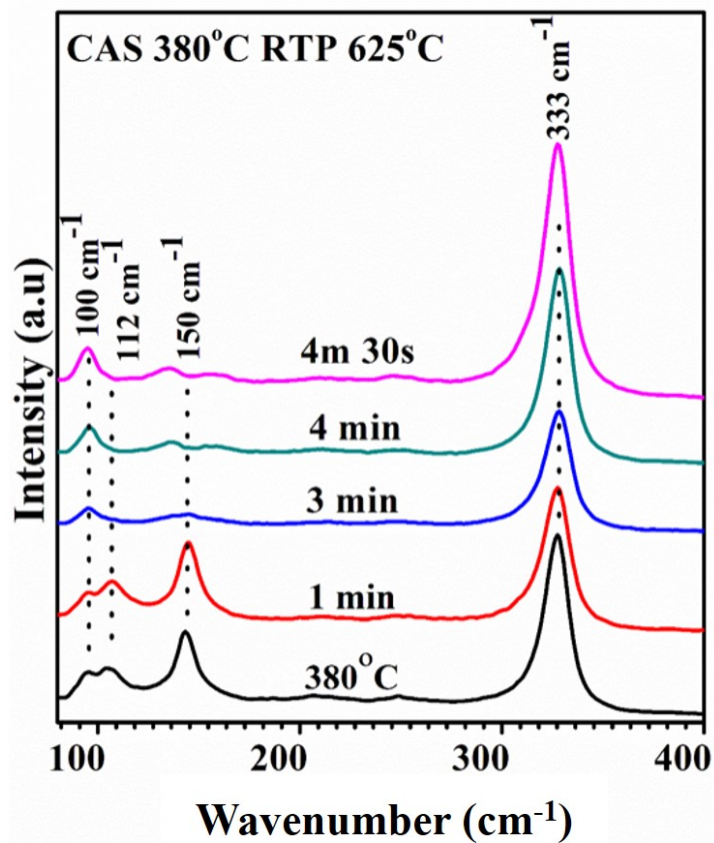
Figure 3.15: Raman spectra of CAS thin films with Cu thickness 50 nm annealed in vacuum oven at 380℃, Pre-annealed RTP at 1 min, 3 min, 4 min and 4 min 30 s after annealed in vacuum oven at 380 °C . Reproduced with kind permission from Elsevier (https://doi.org/10.1016/j.mssp.2018.11.007).

Figure 3.15 [190] shows the Raman spectra of CuSbS$_2$ thin films annealed in conventional vacuum oven at 380 °C for 1 hour and pre-annealed RTP at 625 °C for different durations (1 min, 3 min, 4 min, 4 min 30 s and 5 min). Raman spectra of all the films were measured using 532 nm laser excitation with power 5 mW. Here, all the films have Raman active modes. Films annealed only in vacuum oven and pre-annealed RTP for 1 min present same Raman peaks as shown in Figure 3.15. The peaks observed for these two samples at 100 cm^{-1}, 150 cm^{-1} and 333 cm^{-1}
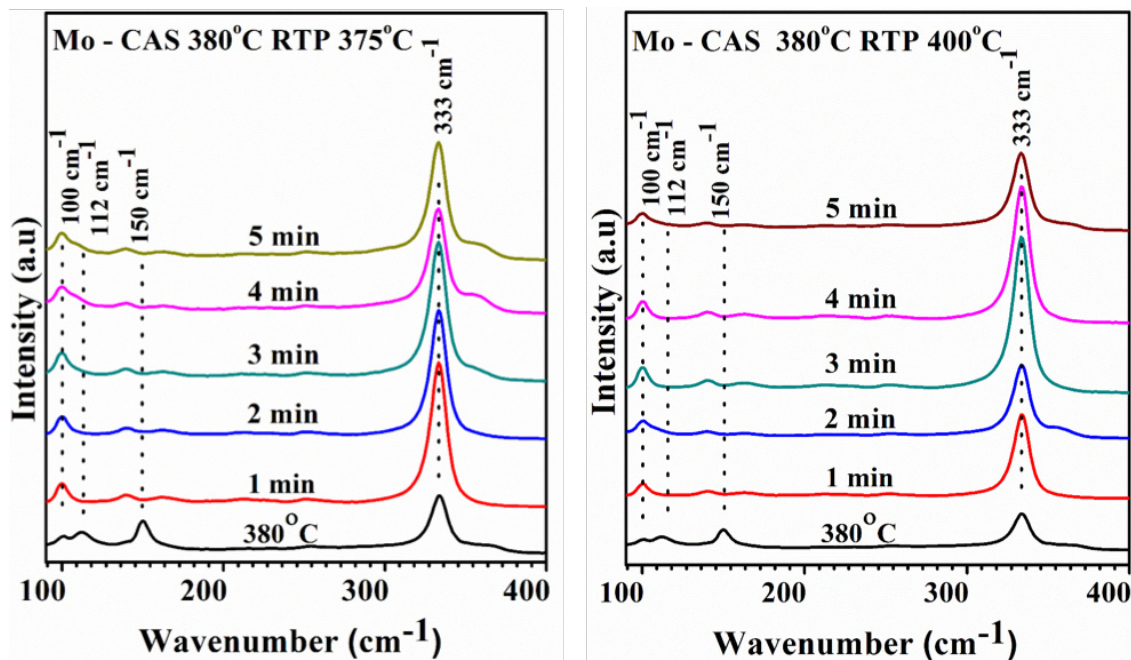
Figure 3.16: Raman spectra of CAS thin films on Mo with Cu thickness 50 nm annealed in vacuum oven at 380 °C , Pre-annealed RTP at (a) 375 °C and (b) 400 °C for varying durations 1 min, 2 min, 3 min, 4 min and 5 min after annealed in vacuum oven at 380 °C for 45 minutes. Reproduced with kind permission from Elsevier (https://doi.org/10.1016/j.mssp.2018.11.007).

correspond to Raman active modes for orthorhombic CuSbS₂ and a minor peak at 112 cm⁻¹ can be assigned to the presence of impurity phase Cu₂S. Samples annealed in RTP for longer duration (3 min, 4 min and 4 min 30 sec) show two peaks at 100 and 333 cm⁻¹, both corresponding to CuSbS₂ phase which implies that the higher temperature heat treatment in RTP removed the impurity phase and formed phase pure CuSbS₂. Even though, the intensities of these peaks are higher for the sample which heated in RTP for 4 mins 30 sec. The higher intensity indicates better crystallinity of the sample. Samples deposited on Mo substrates also showed same kind of Raman spectra like on glass (Figure 3.16) [190]. However, the maximum intensity was for the samples which post heated at 375 °C for 4 minutes and 400 °C for 3 minutes. Further increase in duration of heat treatment in RTP resulted in a reduced intensity of the strong peak at 333 cm⁻¹ due to the evaporation of the

sample during RTP. In conclusion, the major peak observed for CAS films prepared on the glass as well as Mo substrates at $333 \, \text{cm}^{-1}$ indicate the improved crystallinity of the films, which is consistent with the XRD results.

3.4.2   Composition analysis

3.4.2.1   X-ray photoelectron spectroscopy (XPS)

(a) Conventionally annealed samples

Having known the structural characteristics, the X-ray photoelectron spectroscopy was employed to determine the elemental composition and chemical states using a typical survey and high-resolution spectral analyses of the CAS thin film. Low-resolution survey spectra recorded from 0 to 1350 eV were used for the elemental analysis of each sample whereas high-resolution spectra of Cu, Sb, and S were used for the chemical states analysis. An extremely small amount of carbon and oxygen was present in the sample at the surface due to the surface contamination during exposure in the ambient atmosphere. After a small etch from the surface this impurity was totally removed from the sample surface.

Figure 3.17 shows the survey spectra of Sb_2S_3 and CAS 50 nm thin films. Both the spectra commonly display the peaks of C, O, Sb and S. In the case of the CAS 50 nm sample, additionally the Cu peaks are detected. The presence of C and O is due to the adventitious carbon and oxygen since the spectra were collected from the top surface of the thin films. Further, the Sb_2S_3 sample shows only peaks of Sb and S and in the CAS sample peaks of Sb, S, and Cu are seen. A typical survey spectrum of CAS 50 nm film collected after a smooth surface etching by Ar^+ ion sputtering is given in Figure 3.18 in which only the Sb, S and Cu peaks are detected. This supports the finding that the C and O present on the sample surface is due to the adventitious C and O and not from the sample composition. For the detailed analysis, a narrow scan was done for Sb and S, after one cycle of etching using
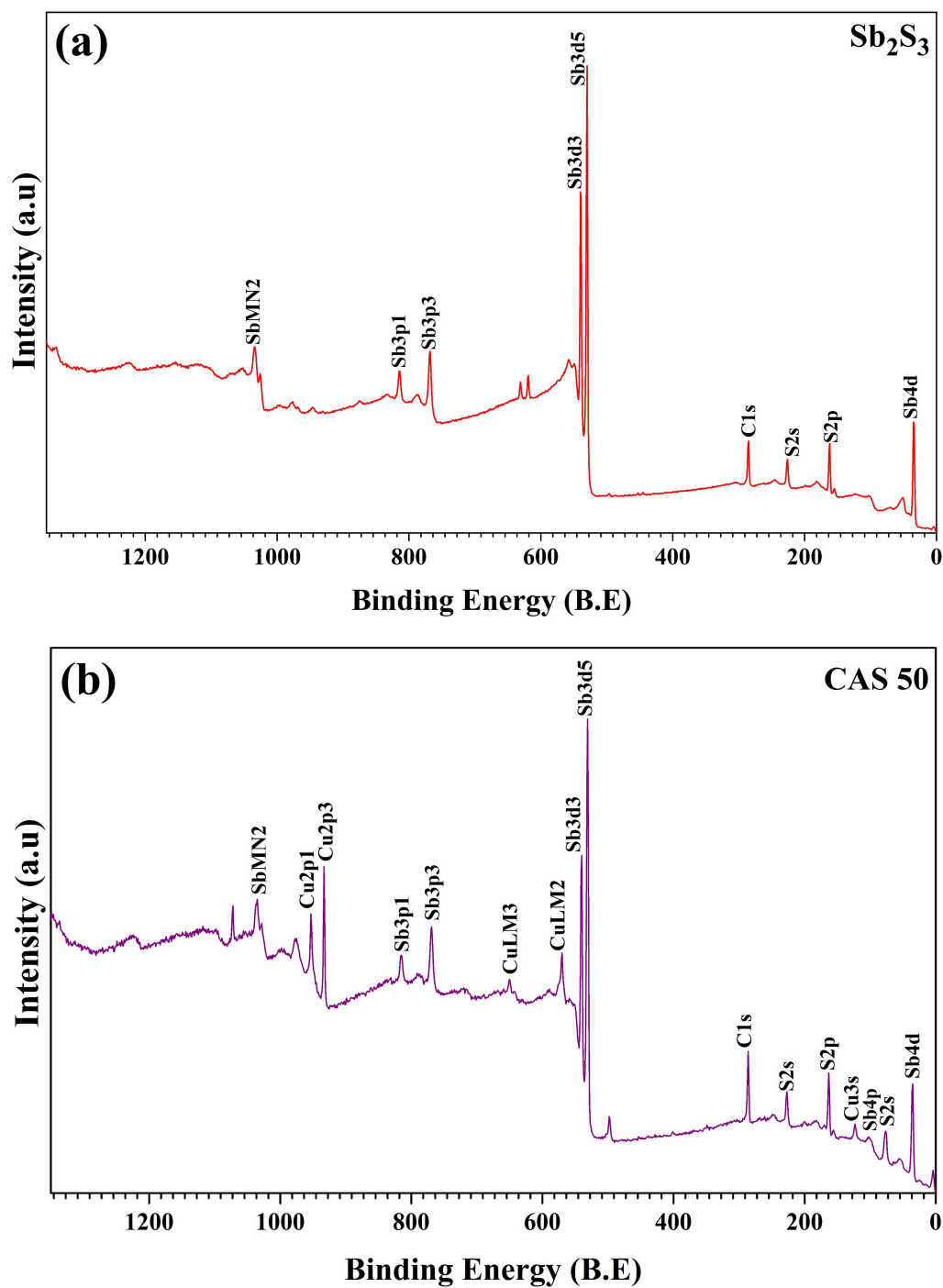
Figure 3.17: Survey spectrum of (a) glass/Sb$_2$S$_3$ (2 h at 25 °C) and (b) glass/Sb$_2$S$_3$ (2 h at 25 °C)/Cu 50 nm precursor thin film annealed at 380 °C for 1 h in vacuum oven (conventional annealing).
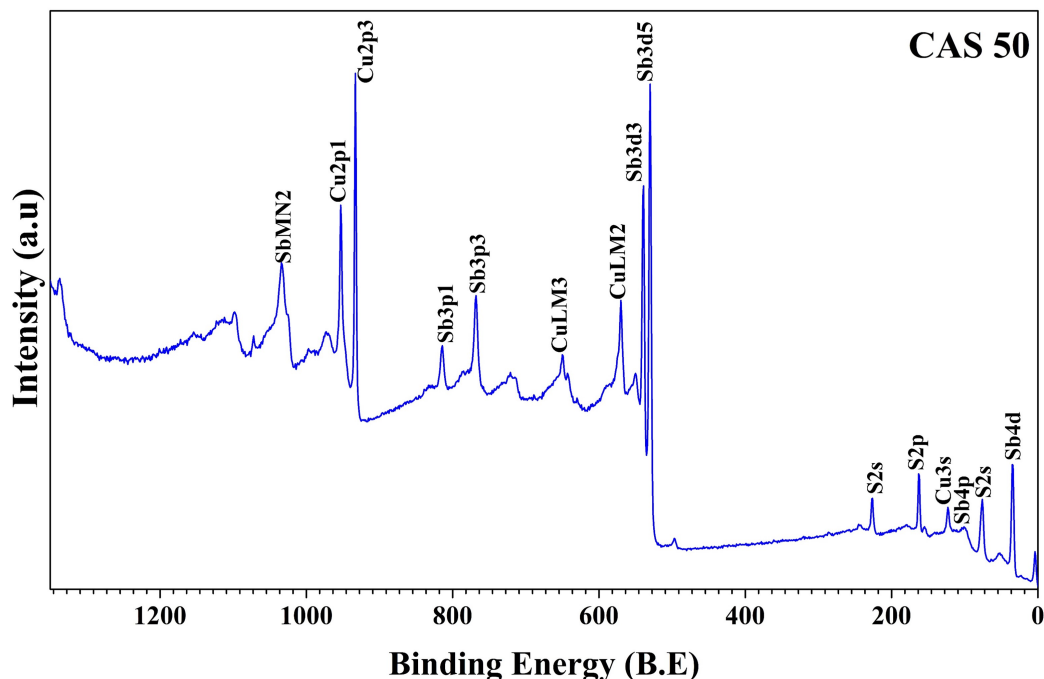
Figure 3.18: Survey spectrum of glass/Sb$_2$S$_3$ (2 h at 25 °C)/Cu 50 nm (CAS 50) precursor thin film annealed at 380 °C for 1 h in vacuum oven, after 30 s Ar$^+$ ion etching.

Ar$^+$ ions. Figure 3.19 shows the high-resolution core level spectra of Sb and S of conventionally annealed Sb$_2$S$_3$ after one etching (etching cycles were performed at a rate of 1.19 nm s^{-1} using 2 keV Ar$^+$ ions). A Shirley type background and a Gaussian–Lorentzian sum function were applied to the high-resolution spectra for deconvolution of the peaks, as shown in the Figure 3.19. From Figure 3.19(a) and Figure 3.19(b), the Sb3d$_{5/2}$, Sb3d$_{3/2}$, S2p$_{3/2}$ and S2p$_{1/2}$ peaks exhibit binding energy values (B.E) 529.2 eV, 538.59 eV, 161.2 eV and 162.36 eV respectively corresponding to Sb^{3+} and S^{2-} states in Sb$_2$S$_3$, with a peak separation of 9.34 and 1.16 eV for Sb and S respectively. The high-resolution photoelectron spectra of Cu, Sb, and S of annealed glass/Sb$_2$S$_3$/Cu samples after one etching (CAS 20, 30, 40 and 50) is given in Figure 3.20 [181]. Figure 3.20 (I-III) shows the Cu2p, Sb3d and S2p spectra of the CAS 50 sample. The Cu2p spectrum shows a 2p doublet corresponding to 2p$_{3/2}$ and 2p$_{1/2}$ due to spin orbit coupling at B.E. values 952.3 and 932.6 eV respectively
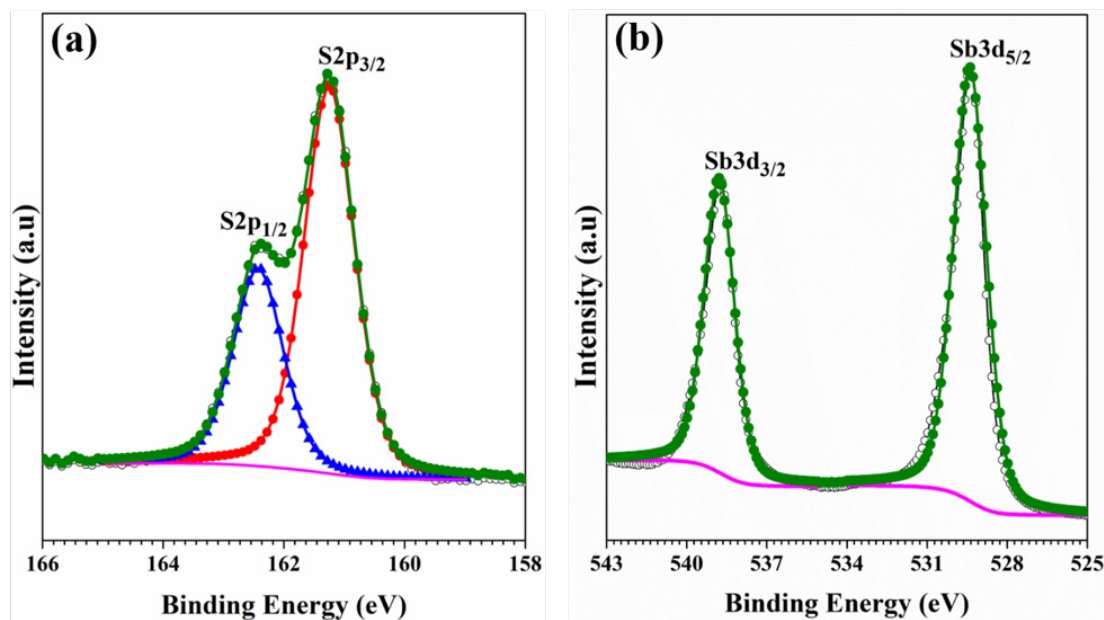
Figure 3.19: High-resolution spectra of (a) Sb3d core level and (b) S2p core level glass/Sb_2S_3 annealed at $350\,^{\circ}C$ after 30 s Ar^+ ions etching.

separated by $\Delta E = 19.7$ eV which is coinciding with the previously reported B.E. of Cu^+ in $CuSbS_2$ [163]. The XPS survey spectrum of Cu^{++} is different that of Cu^+. According to Haiyue Liu et al. [193] the high resolution XPS of $Cu^{2+}$and Cu^+ spectra shows peaks at 932.40 eV and 934. 69 eV, which results are also supporting the formation of $CuSbS_2$ phase in the present work.

Yang et al. and Mc Carthy et al. reported similar B.E. values for Cu2p peaks of $CuSbS_2$ thin films obtained by solution processing and spin coating [86]. The high-resolution spectrum of Sb is constituted by $Sb3d_{5/2}$ and $Sb3d_{3/2}$ peaks at B.E. of 539.82 and 530.43 eV respectively, match with the reported binding energies of antimony (Sb^{3+} state) from $CuSbS_2$.The B.E of the sulfur peaks also match with that of the reported values for $CuSbS_2$ where the $2p_{3/2}$ and $2p_{1/2}$ peaks are observed at 162.9 and 161.7 eV. The core level spectra of CAS 40, 30 and 20 samples present similar B.E. values as that of the CAS 50 thin film except for CAS 30 and 20 samples, extra peaks are observed in the spectra of S ad Sb peaks. In the case of CAS 30 and 20 samples, the smallest peaks observed in the S2p and Sb3d spectra
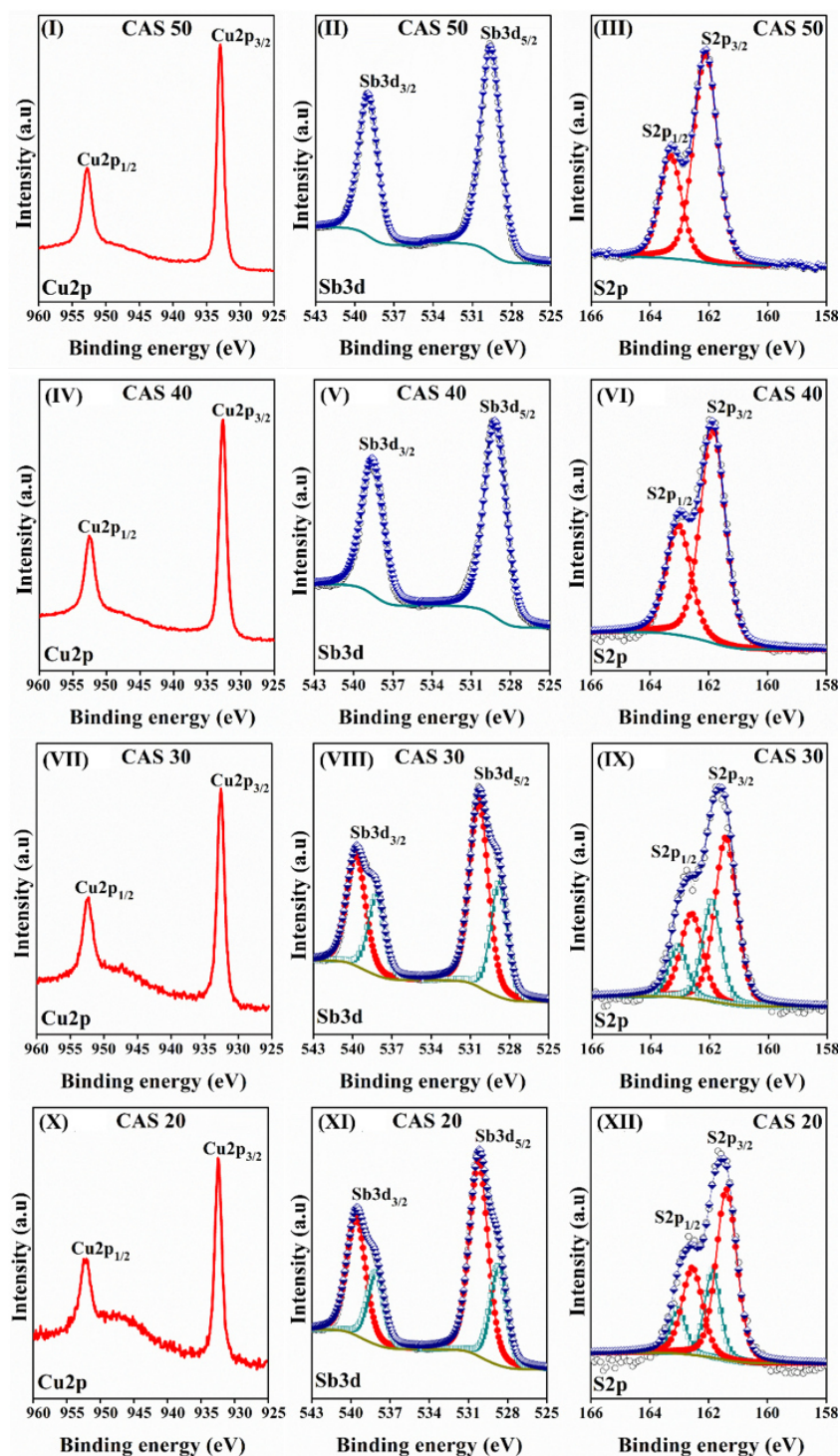
Figure 3.20: High resolution spectra of Cu2p, Sb3d and S2p of CAS 50 (I-III), CAS 40 (IV-VI), CAS 30 (VII-IX), CAS 20 (X-XII) (DOI:10.1039/C8RA05662E).

at 161.8 eV and 163 eV (for S2p$_{3/2}$ and S2p$_{1/2}$ respectively) and 528.8 and 538.19 eV (for Sb3d$_{5/2}$ and Sb3d$_{3/2}$ respectively) belong to the S and Sb from Sb$_2$S$_3$. This indicates the presence of unreacted Sb$_2$S$_3$ phase due to the insufficient Cu thickness for complete CAS phase formation, in consistent with the XRD and Raman results. Elemental composition and the respective chemical states of CuSbS$_2$ samples formed at different conditions are summarized in Table 3.2.

Table 3.2: Summary of elemental composition and the respective chemical states of CuSbS$_2$ samples formed at different conditions

Sample	High resolution Cu2p$_{3/2}$		High resolution Sb3d$_{5/2}$		High resolution S2p$_{3/2}$	
	Present work	Literature	Present work	Literature	Present work	Literature
CAS 20	932.4 eV	931.97 eV	530.1 eV	529.1 eV	161.4 eV	161.4 eV
CAS 30	932.5 eV	to	530.2 eV	to	161.5 eV	to
CAS 40	932.5 eV	932.8 eV	529.4 eV	530.6 eV	161.8 eV	162 eV
CAS 50	932.8 eV	[86, 151, 166]	529.7 eV	[86, 151, 166]	162.0 eV	[86, 151, 166]

The B.E profile montage and the respective composition analysis of the CAS 50 samples are shown in Figure 3.21 and Figure 3.22 respectively. Depth profile analysis showed the uniformity of Cu, Sb and S elements throughout the depth of the film. As observed in the Figure 3.21, the surface of the film is Cu, Sb and S rich and the presence of Si from the substrate is detected nearly the 15th etch level. The formation of the ternary CuSbS$_2$ phase by the interlayer diffusion of Sb$_2$S$_3$ and Cu is clearly understood from the composition.The atomic percentage of Cu, Sb and S is nearly equal after the first etch (30 sec).

XPS high resolution spectra of the CAS 25, 50 and 75 nm samples deposited using 4 h Sb$_2$S$_3$ bath durations are shown in Figure 3.23; CAS samples were formed by annealing at 350 °C for 30 min in vacuum oven. The spectra were recorded after first etching. The Cu2p spectra of all the three samples shows a 2p doublet corresponding to 2p$_{3/2}$ and 2p$_{1/2}$ at B.E. values 952.2 and 932.4 eV respectively, B.E. of Cu in CuSbS$_2$. The high-resolution spectra of Sb are constituted by Sb3d$_{5/2}$ and Sb3d$_{3/2}$ peaks located at B.E. values 538.79 and 529.4 eV respectively for CAS
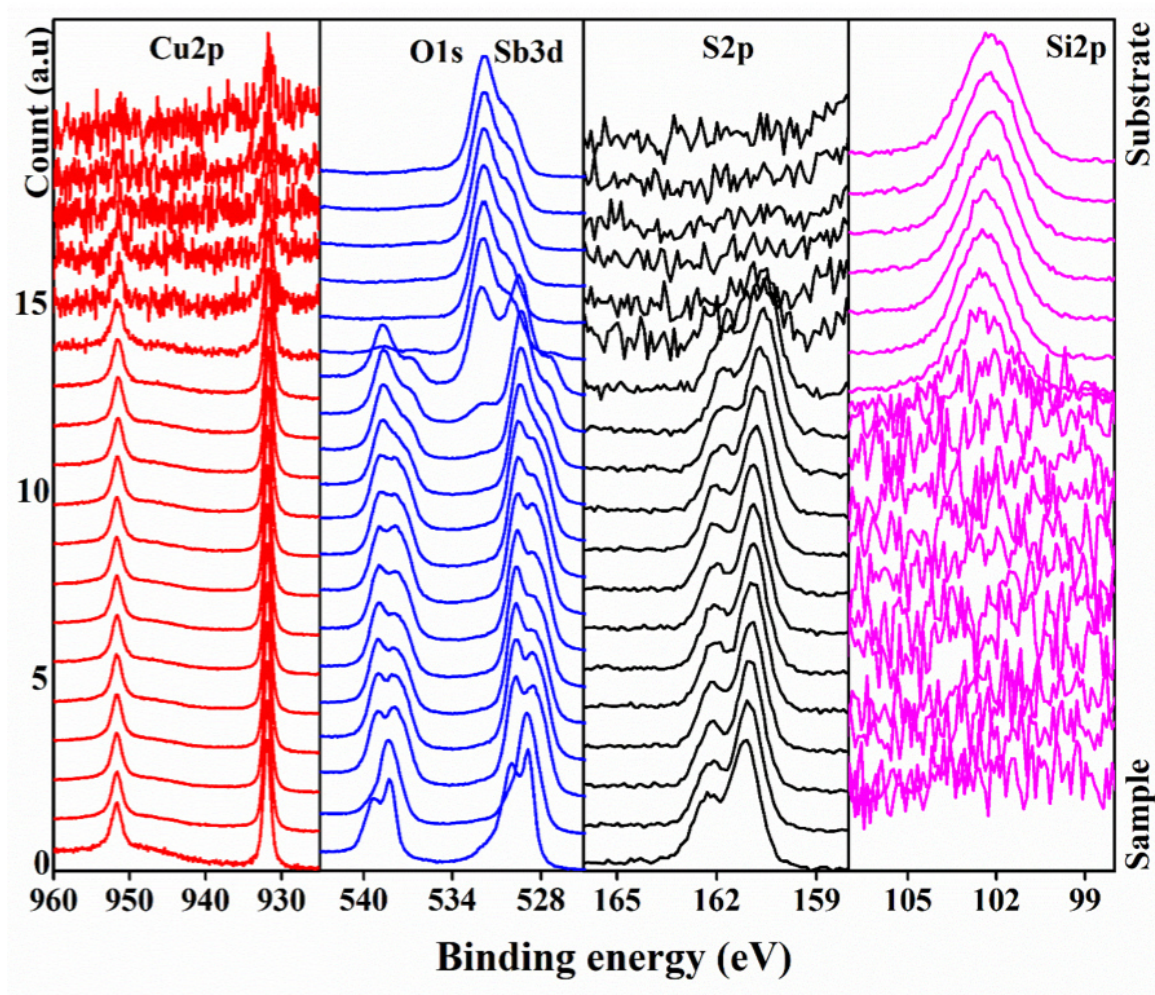
Figure 3.21: XPS depth profile of CuSbS$_2$ thin film formed by annealing Sb$_2$S$_3$/Cu-50nm annealed in conventional oven at 380 °C for 1 h

50, CAS 75 samples, which is also in close match with the reported binding energies of antimony from CuSbS$_2$. B.E of the sulfur peaks of these two same samples also match with the reported values for CuSbS$_2$, 162.9 and 161.7 eV. In the case of CAS 25, weak peaks of the S2p and Sb3d spectra at 161.8 eV and 163 eV (for S2p$_{3/2}$ and S2p$_{1/2}$ respectively) and 528.5 and 537.89 eV (for Sb3d$_{5/2}$ and Sb3d$_{3/2}$ respectively) indicate the presence of unreacted Sb$_2$S$_3$. Elemental composition and the respective chemical states of CuSbS$_2$ samples formed at different conditions are summarized in Table 3.3. The depth profile and the composition analysis of CAS 25, 50 and 75 nm samples are given in Figure 3.24. The depth profile data showed the uniformity of
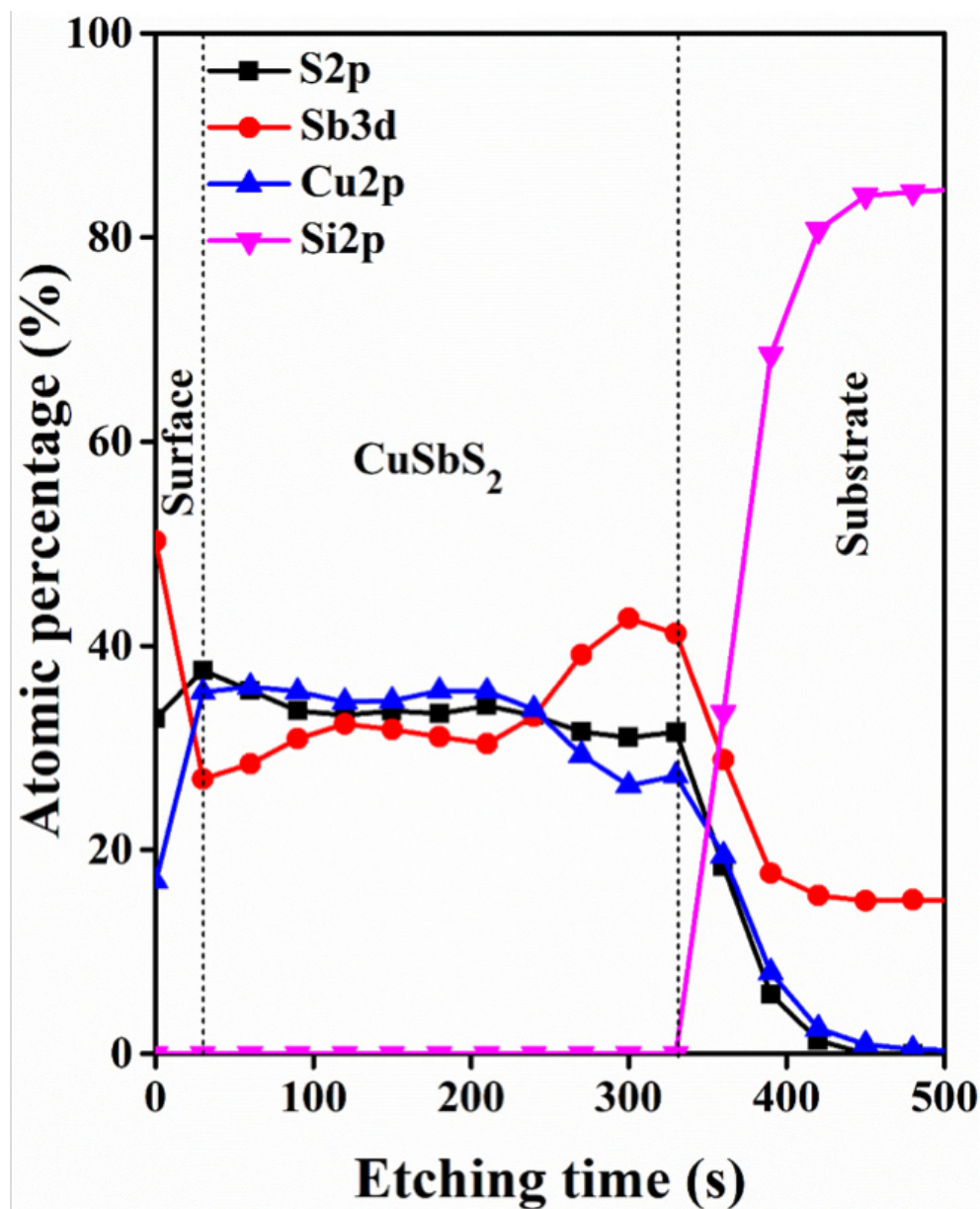
Figure 3.22: XPS profile montage of CuSbS$_2$ thin film formed by annealing Sb$_2$S$_3$/Cu-50nm annealed in conventional oven at 380 °C for 1 h.

the Cu, Sb and S elements throughout the depth of the films. In the case of CAS 25 nm sample, the presence of higher atomic percentage % of Sb represents that, for that particular thickness of Sb$_2$S$_3$, Cu thickness of 25 nm is not sufficiant to make the phase pure CAS.
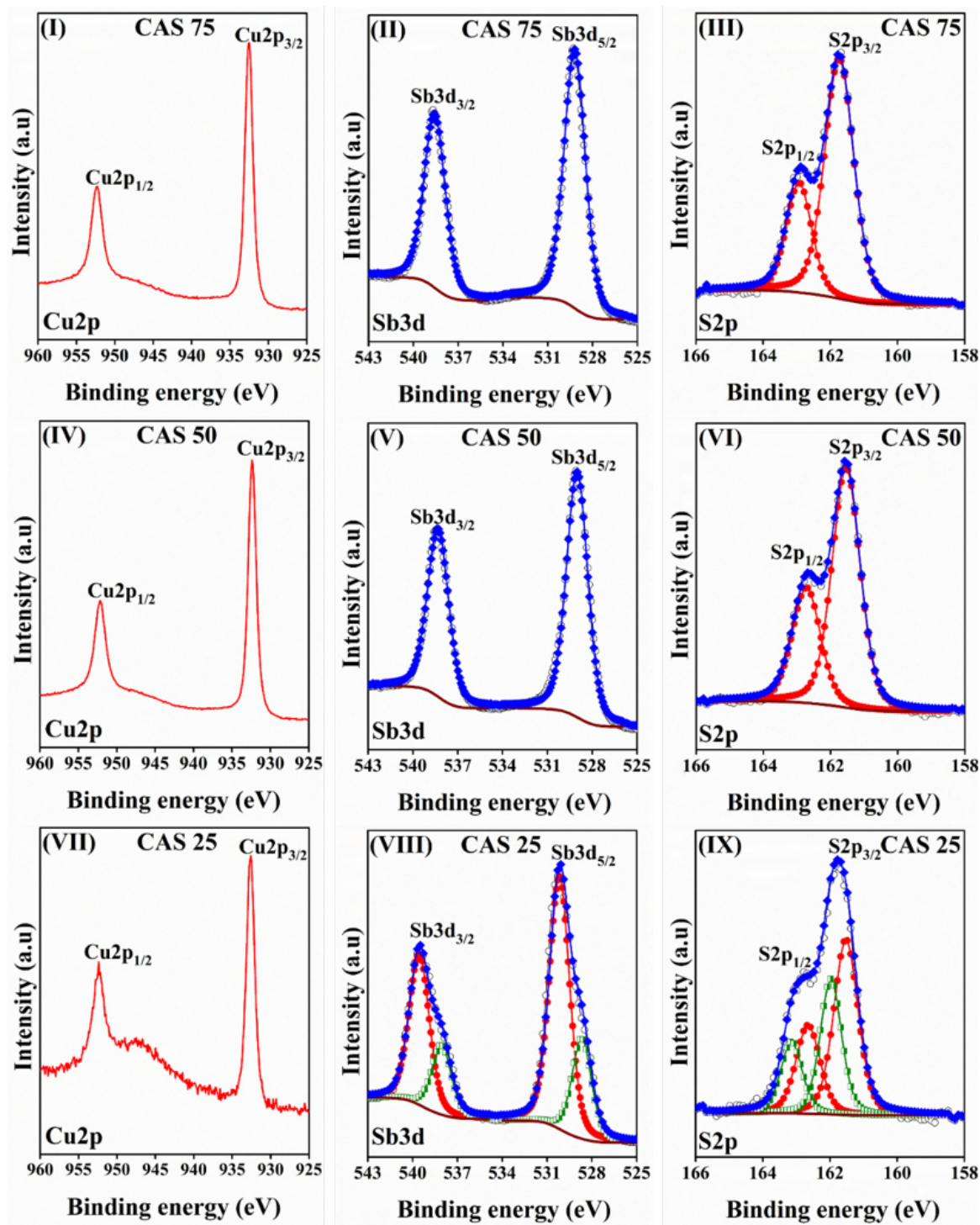
Figure 3.23: High resolution spectra of Cu2p, Sb3d and S2p of CAS 75 (I–III), CAS 50 (IV–VI), CAS 25 (VII–IX).

Table 3.3: Summary of elemental composition and the respective chemical states of CuSbS$_2$ samples formed at different conditions

Sample	High resolution Cu2p$_{3/2}$		High resolution Sb3d$_{5/2}$		High resolution S2p$_{3/2}$	
	Present work	Literature	Present work	Literature	Present work	Literature
CAS 25	932.4 eV	931.97 eV	530.6 eV	529.1 eV	161.4 eV	161.4 eV
CAS 50	929.4 eV	to	529.5 eV	to	161.7 eV	to
CAS 75	929.5 eV	932.8 eV	529.4 eV	530.6 eV	161.8 eV	162 eV
		[86, 151, 166]		[86, 151, 166]		[86, 151, 166]
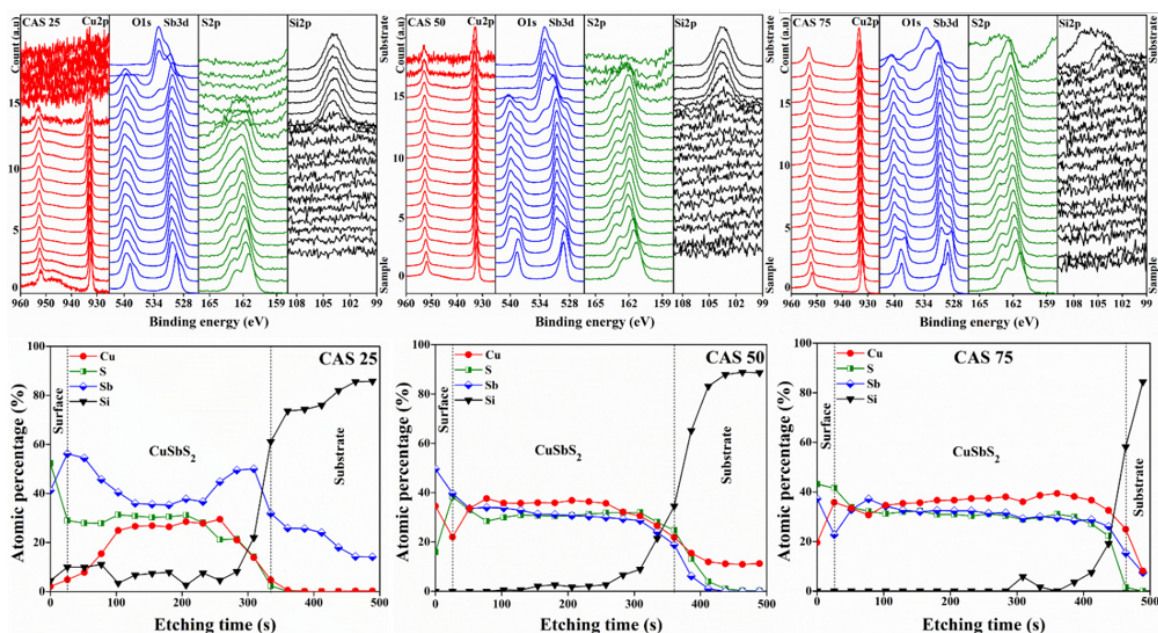
Figure 3.24: XPS depth profile and corresponding composition spectra of CuSbS$_2$ thin film formed by annealing Sb$_2$S$_3$/Cu (Sb$_2$S$_3$ by CBD at 25 °C for 4 h thermally evaporated Cu thicknesses on Sb$_2$S$_3$ of 25, 50, and 75 nm) layer at 350 °C for 30 min.

(b) RTP treated samples

The high-resolution spectra of Cu2p, S2p and Sb3d of our typical phase pure sample (CAS Cu-50 pre-annealed RTP 600 °C) are shown in Figure 3.25. The shown spectra are from the first etch level where the etching cycles were performed using 2 keV Ar$^+$ ions at a rate of 1.19 nm/s to remove any possible contaminants on the sample surface. The core-level spectrum of copper shows 3.25(a) the 2p
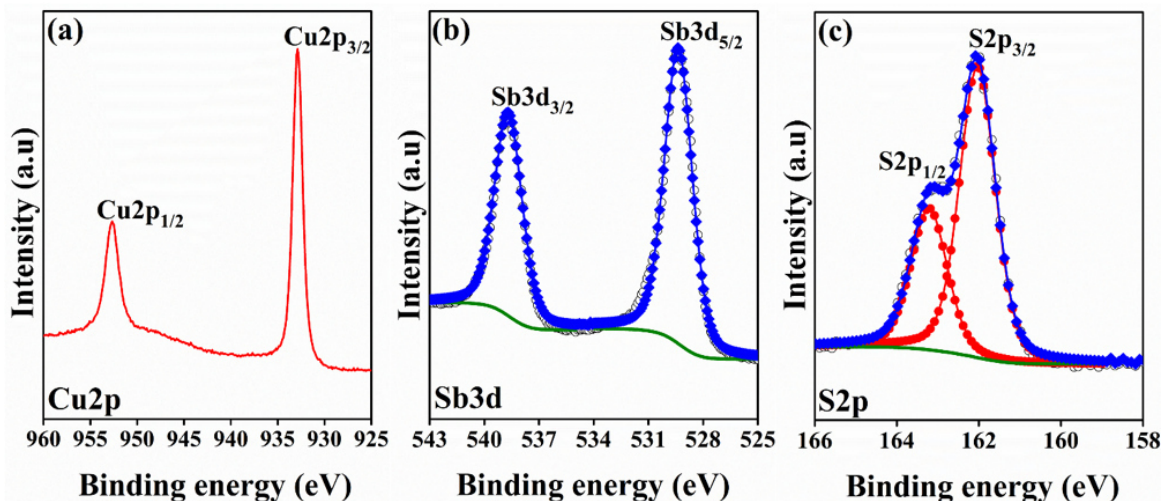
Figure 3.25: High-resolution XPS spectra of the core levels of (a) Cu 2p core level, (b) Sb3d core level and (c) S2p core level of CAS Cu-50 sample after Ar$^+$ ions etching of CuSbS$_2$ thin film formed by pre-annealed RTP at 600 °C for 5 min (CAS Cu-50 380-RTP 600).

doublet which constitutes Cu2p$_{3/2}$ and Cu2p$_{1/2}$ peaks due to spin-orbit coupling with respective binding energies of 932.68 and 952.38 eV separated by ΔE - 19.7 eV. These values are in good agreement with that of Cu$^+$ in CuSbS$_2$. The Sb3d core level spectrum and the deconvoluted peaks along with the resultant envelope are shown in Figure 3.25(b). From the figure, spin-orbit coupled Sb3d peaks at 529.9 eV (Sb3d$_{5/2}$) and 539.29 eV (Sb3d$_{3/2}$) concur with that from CuSbS$_2$ phase as reported in the previous studies. The deconvoluted peak of S2p at 161.9 eV (S2p$_{3/2}$) and 163.1 eV (S2p$_{1/2}$) with a separation of 1.2 eV inagreement with the reported range of B.E of S^{2-} state in CuSbS$_2$. Thus, the higher intense peak values of S2p and Sb3d along with that of Cu2p lines in correlation with our XRD results confirm the formation of CuSbS$_2$ as major phase.

The B.E profile montage and the respective composition analysis of the same sample are presented in Figure 3.26 [180] and Figure 3.27 [180] respectively. Analysis of the depth profile data showed the uniformity of the Cu, Sb and S elements throughout the depth of the film. In the case of CuSbS$_2$ samples formed by RTP at
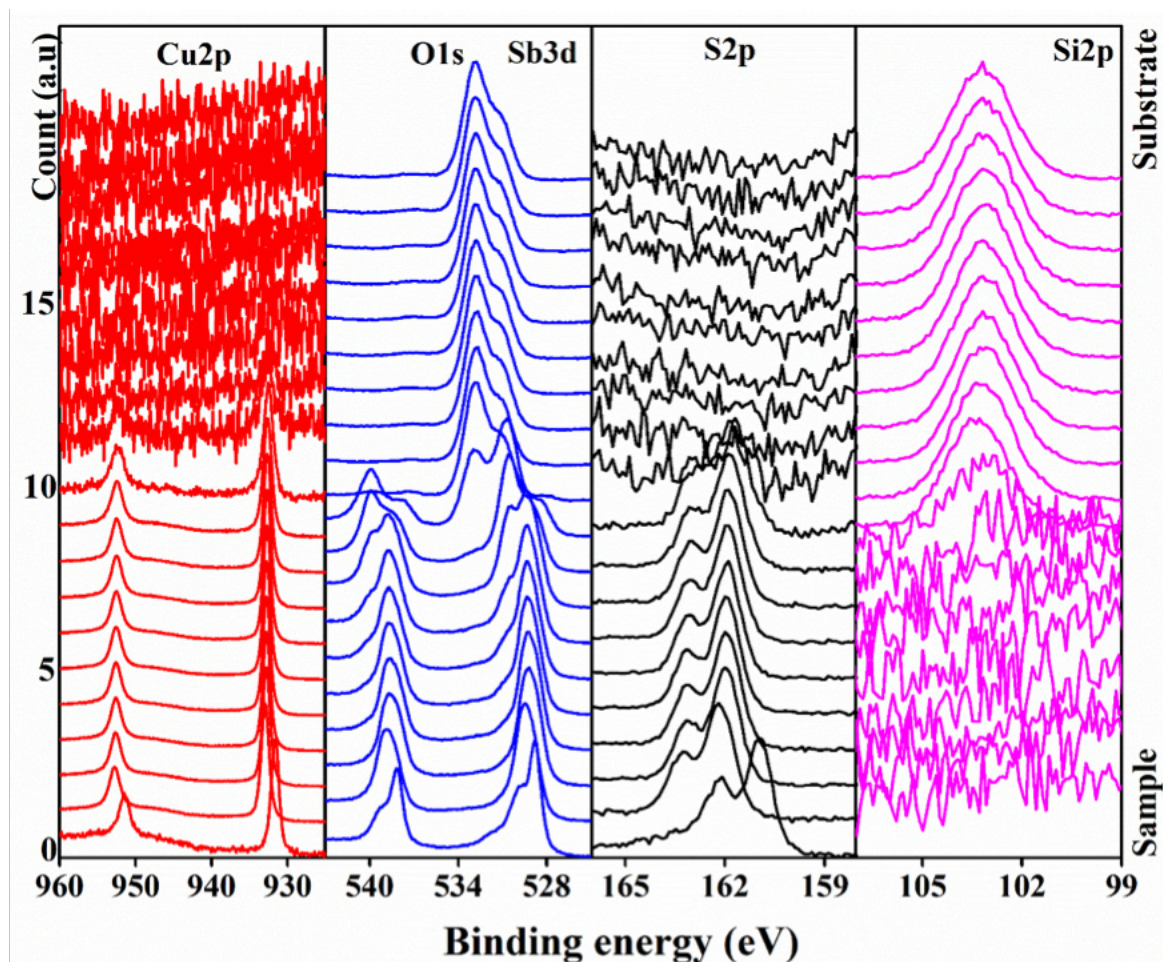
Figure 3.26: XPS depth profile of CuSbS$_2$ thin film formed by pre-annealed RTP at 600°C for 5 min (CAS Cu-50 380-RTP 600) (`https://doi.org/10.1016/j.solmat.2017.02.005`).

600 °C, the surface was antimony rich in composition. The formation of the ternary CuSbS$_2$ phase by the interlayer diffusion of Sb$_2$S$_3$ and Cu is clearly understood from the composition figures.

The high-resolution scans of the preferentially oriented films obtained by post heat treatment in RTP (glass/Sb$_2$S$_3$/Cu50/380 °C/RTP 625 °C 4.5 min, Mo/Sb$_2$S$_3$/Cu50/380 °C/RTP 400 °C 3 min) are shown in Figure 3.28 [190] and Figure 3.29 [190] respectively, where the data were collected from the 1st etched surface, in order to avoid the effect of any contaminations present on the sample surface. Elemental composition and the respective chemical states of CuSbS$_2$ samples formed at different
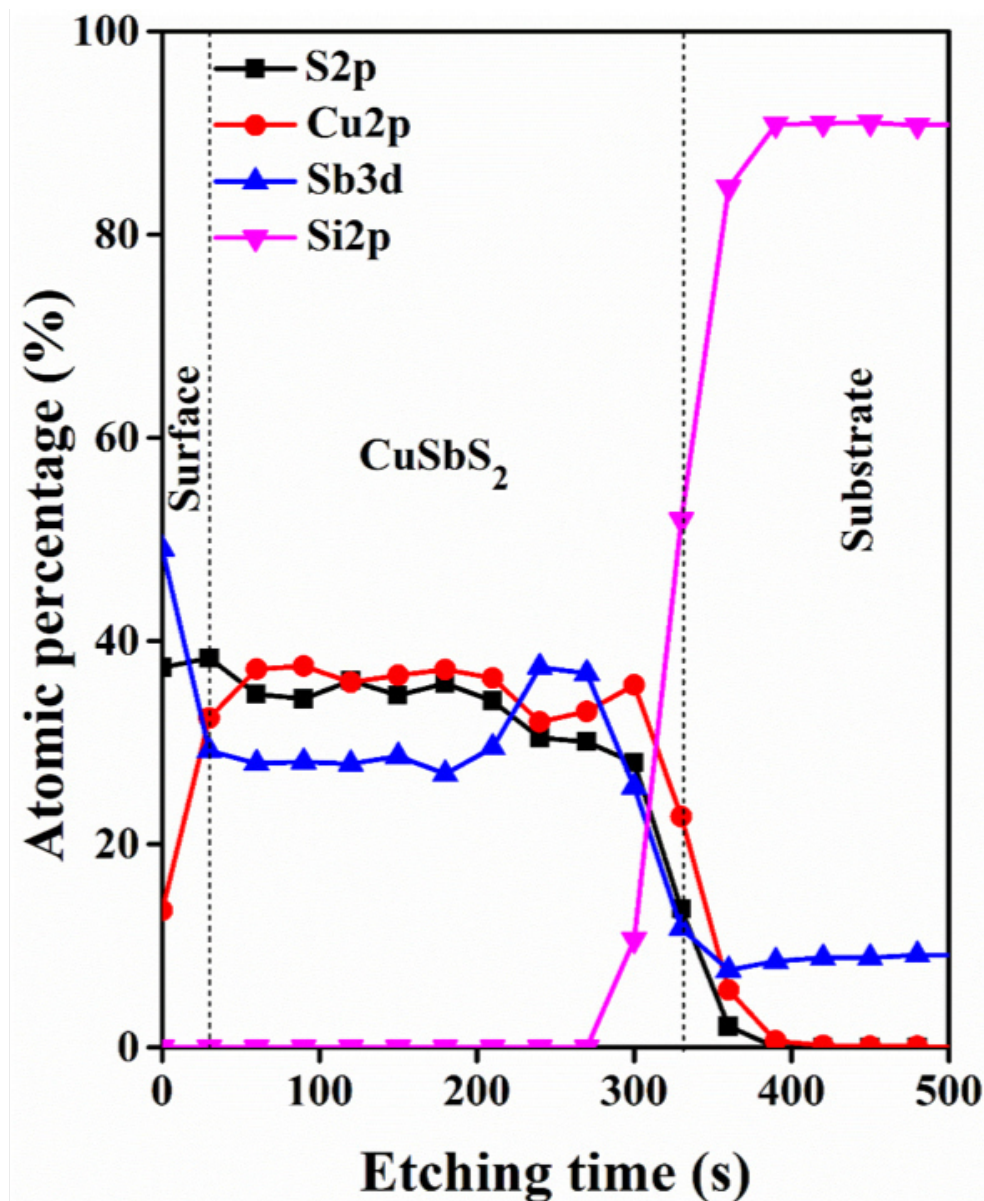
Figure 3.27: XPS profile montage of CuSbS$_2$ thin film formed by pre-annealed RTP at 600 °C for 5 min (CAS Cu-50 380-RTP 600) (`https://doi.org/10.1016/j.solmat.2017.02.005`).

conditions are summarized in Table 3.4. The B.E profile montage and the respective composition analysis of the same samples are presented in Figure 3.30.
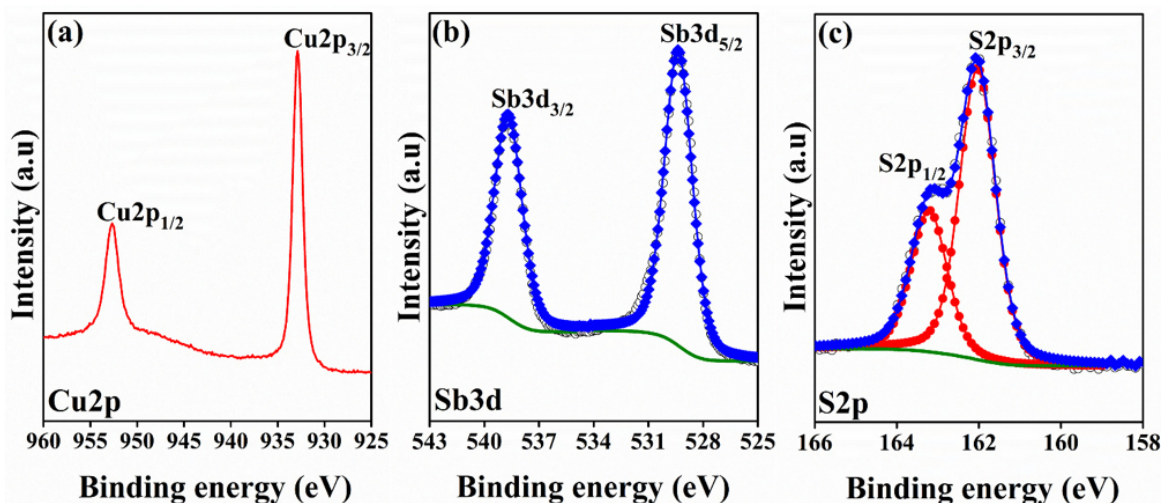
Figure 3.28: X-ray photoelectron spectroscopy of CuSbS$_2$ thin film on glass substrates pre-annealed RTP at 625 °C for 4 m 30 s after Ar$^+$ ion etching, (a) Cu2p core level (b) Sb3d core level (c) S2p core level. Reproduced with kind permission from Elsevier (`https://doi.org/10.1016/j.mssp.2018.11.007`).
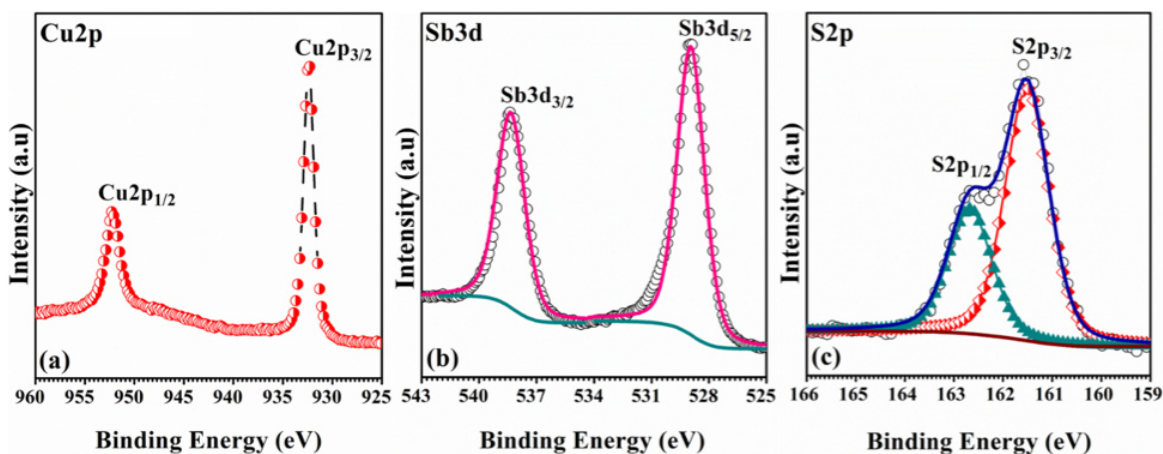
Figure 3.29: X-ray photoelectron spectroscopy of CuSbS$_2$ thin film Prepared on Mo substrates pre-annealed RTP at 400 °C for 3 m after Ar$^+$ ion etching, (a) Cu 2p core level (b) Sb3d core level (c) S2p core level. Reproduced with kind permission from Elsevier (`https://doi.org/10.1016/j.mssp.2018.11.007`).
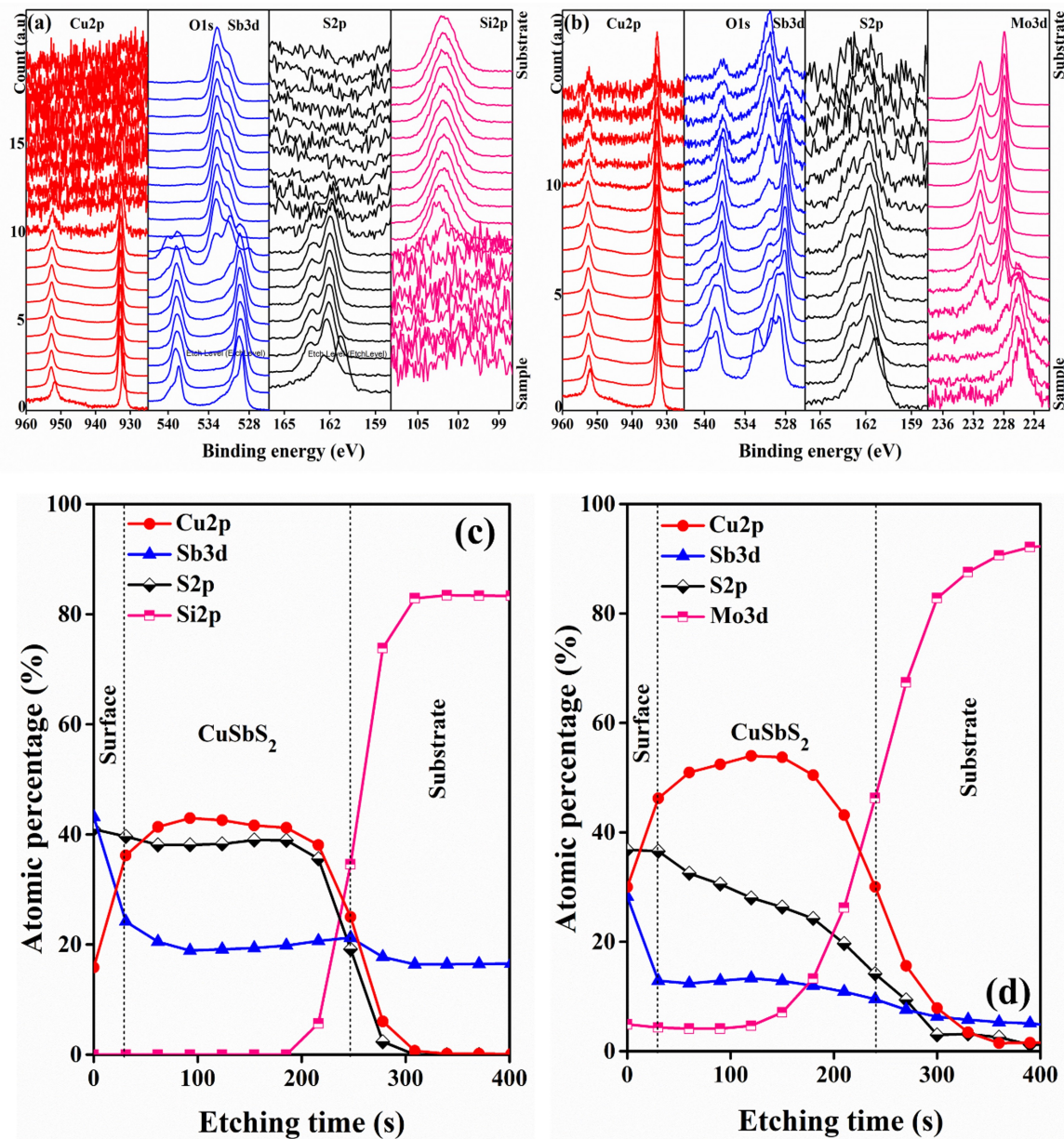
Figure 3.30: XPS depth profile (a) glass/CAS-50 pre annealed (380 °C 1 hr) RTP 625 °C 4 min 30 s (b) Mo/CAS-50 pre annealed (380 °C 45 min) RTP 400 °C 3 min and composition spectra of (c) glass/CAS-50 pre annealed (380 °C 1 hr) RTP 625 °C 4 min 30 s (d) Mo/CAS-50 pre annealed (380 °C 45 min) RTP 400 °C 3 min (https://doi.org/10.1016/j.mssp.2018.11.007).

Table 3.4: summary of elemental composition and the respective chemical states of $CuSbS_2$ samples formed at different conditions

Sample	High resolution $Cu2p_{3/2}$		High resolution $Sb3d_{5/2}$		High resolution $S2p_{3/2}$	
	Present work	Literature	Present work	Literature	Present work	Literature
CAS 75	932.9 eV	931.97 eV to	529.42 eV	529 eV to	162.21 eV	161.4 eV to
CAS 50	932.3eV	932.8 eV [86, 151, 166]	529 eV	530.6 eV [86, 151, 166]	161.51 eV	162.4 eV [86, 151, 166]

3.4.2.2   X-ray fluorescence spectroscopy (XRF)

Elemental composition of the Sb_2S_3 and CAS samples (where CBD of Sb_2S_3 at 25 °C for 4 h) were measured with a Fisherscope XUV-733 X-ray fluorescence (XRF) instrument and it is tabulated in the table given below:

Table 3.5: XRF measurements of Sb_2S_3, Sb_2S_3 with Cu varying thickness 5, 10, 20 and 50 nm.

Sample/ Precursor	Cu (%)	Sb (%)	S (%)	S/(Cu+Sb) (%)
Sb_2S_3		26.25	73.75	2.81
Sb_2S_3-Cu 5 nm	2.03	37.6	58.3	1.47
Sb_2S_3-Cu 10 nm	3.68	35.1	61.2	1.57
Sb_2S_3-Cu 20 nm	6.16	35.6	58.3	1.39
Sb_2S_3-Cu 50 nm	11.58	31.32	57.1	1.33

3.4.3   Morphology

(a) Scanning electron microscopy images: Vacuum oven annealed samples

The surface morphology and roughness of the CAS thin films are shown in the SEM images given in Figure 3.31, CAS thin films formed by heating 2 h Sb_2S_3
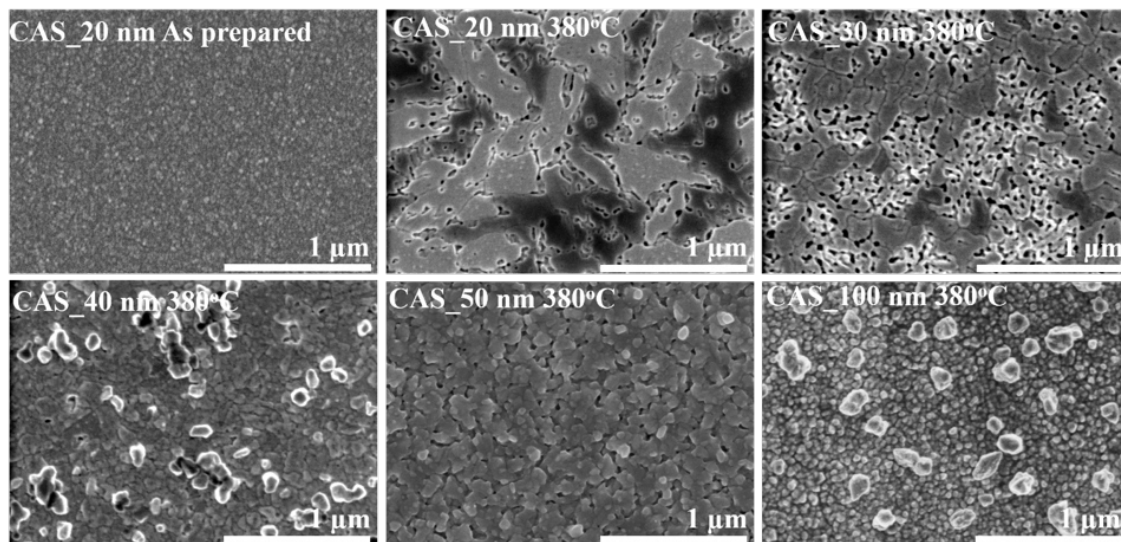
Figure 3.31: Scanning electron microscopy images for CuSbS$_2$ thin film formed by annealing glass/Sb$_2$S$_3$/Cu stacked layers with varying Cu thicknesses 20,30,40,50 and 100 nm (CAS Cu-20, CAS Cu-30, CAS Cu-40, CAS Cu-50 and CAS Cu-100) at 380 °C for 1 h in vacuum. SEM image of as prepared CAS Cu-20 is also included in the figure for reference.
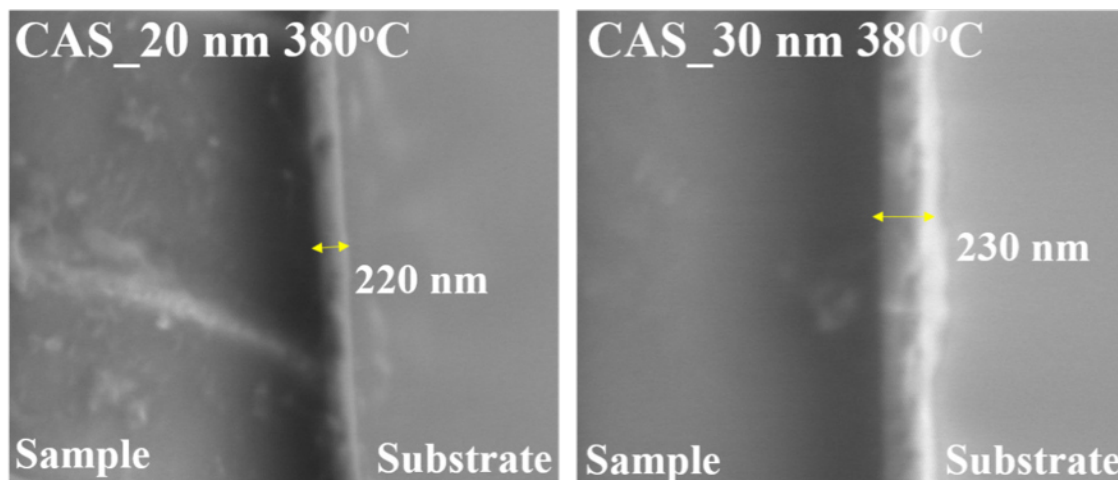
Figure 3.32: Cross-sectional scanning electron microscopy images for CuSbS$_2$ thin film formed by annealing glass/Sb$_2$S$_3$/Custacked layers with 20 nm Cu thickness (CAS Cu-20) at 380 °C for 1 h in vacuum.
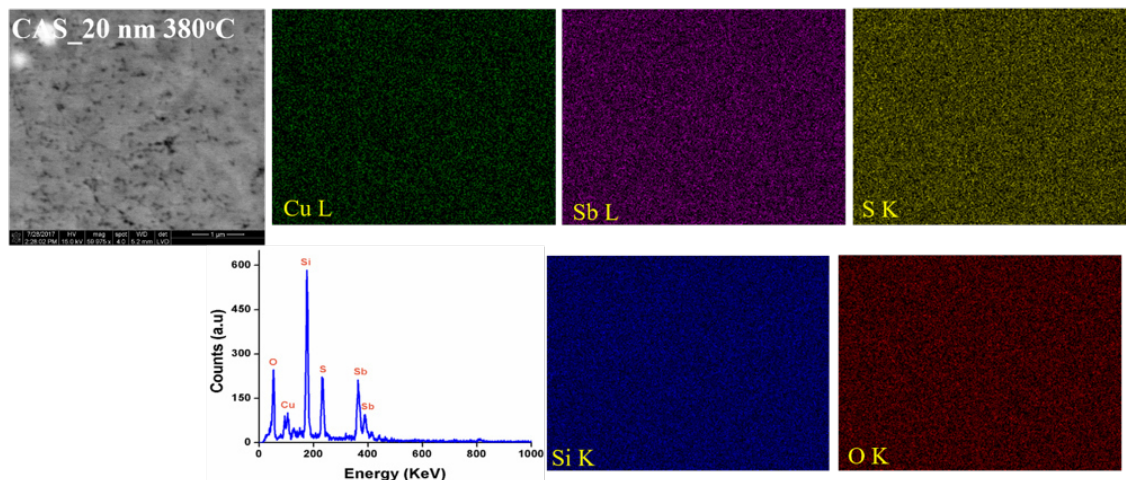
Figure 3.33: Scanning electron microscopy images, EDX, EDX mapping for CuSbS₂ thin film formed by annealing glass/Sb₂S₃/Custacked layers with 20 nm Cu thickness (CAS Cu-20) at 380 °C for 1 h in vacuum.
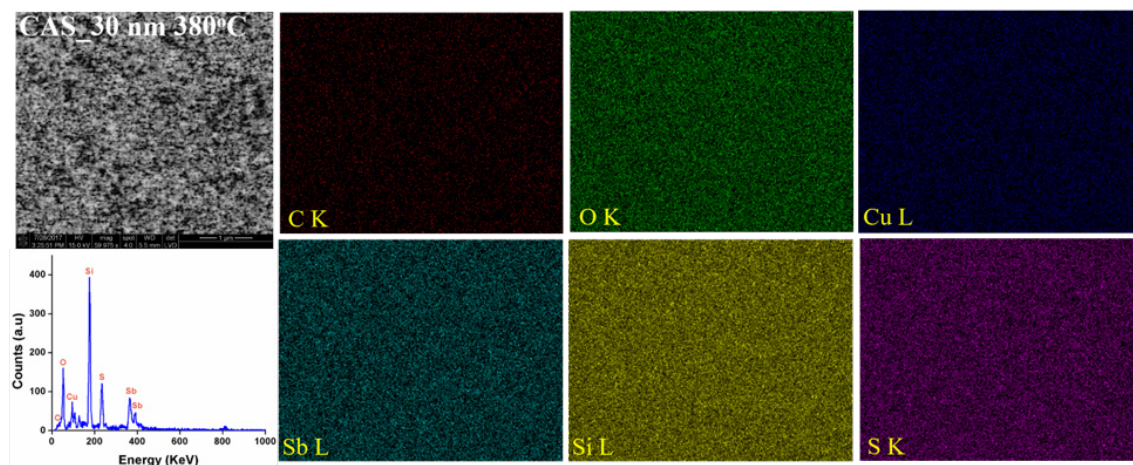
Figure 3.34: Scanning electron microscopy images, EDX, EDX mapping for CuSbS₂ thin film formed by annealing glass/Sb₂S₃/Custacked layers with 30 nm Cu thickness (CAS Cu-30) at 380 °C for 1 h in vacuum.

with varying Cu thicknesses from 20 nm to 100 nm. The surface morphology of the as prepared CAS 20 nm thin film is also included for reference. All the images were acquired by appling an acceleration voltage of 1 kV in the secondary electron mode and at the same magnification for easy comparison. As the Cu thickness is varied from 20 nm to 50 nm, all the CAS thin films show changes in their surface

morphology. CAS 20 nm thin film shows porous surface morphology composed of irregular shaped particles CAS 30 nm film exhibits a compact morphology with large coalescent grains. For CAS 40 nm film, bigger and compact grains with definite boundaries is formed, a distinct compared to the CAS 20 and 30 nm thin films. Coalescent and bigger grains evenly distributed on the surface with less voids is observed for CAS 50 nm sample. When the Cu thickness is further incrased to 100 nm, the film surface is finer grained compared to that of the CAS 50 nm thin films as seen in Figure 3.31. Thus, the CuSbS₂ films formed by varying Cu thickness showed very distinct morhologies compared to that of the as prepared CAS 20 nm film with surface comprised of relatively smaller spherical particles. Among the CAS thin films of different Cu thicknesses, the CAS 40 and 50 nm show relatively better surface morphologies for device applications where these thin films can be applied. These resuts also coincide with the XRD and Raman results 3.4.1.1. Average thickness of the CAS 20 and 30 nm thin films was measured from cross-section SEM images as shown in Figure 3.32, 220 nm and 230 nm respectively, no significant change in the film thickness. The average thicknesses of the films measured from cross-section SEM were comparable with the thickness measured using stylus profilometry of the same samples. Also as prepared Sb₂S₃ films sample was ∼200 nm in thickness. The thickness of the CAS thin films increased with increase in the Cu content.

Elemental composition and distribution of the CAS 20 and 30 samples were analyzed using SEM-EDX mapping. Figure 3.33 and Figure 3.34 show the corresponding analysis of the CAS 20 and 30 nm samples respectively (annealed at 380 °C for 1 h). From the EDX mapping of both samples, it can be seen that, Cu, Sb and S are uniformly distributed on the sample surface. The Si and O are either from the glass substrate or due to the exposure of the samples towards atmosphere. The EDX area scans of the samples also show that they are mainly constituted by Cu, Sb and S. Thus CAS with uniform elemental distribution is confirmed by the EDX area scans together with EDX mapping.
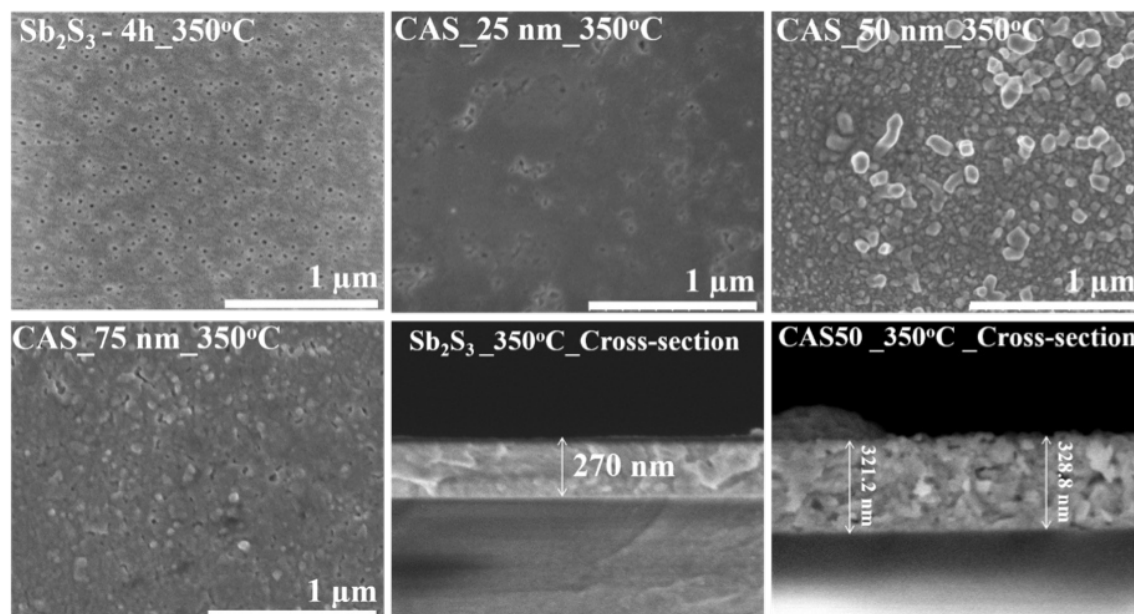
Figure 3.35: Scanning electron microscopy images for CuSbS$_2$ thin film formed by annealing glass/Sb$_2$S$_3$/Custacked layers with varying Cu thicknesses 25, 50 and 75 nm (CAS Cu-25, CAS Cu-50 and CAS Cu-75) at 350 °C for 30 min in vacuum where the Sb$_2$S$_3$ CBD was at 25 °C for 4 h. The SEM images of Sb$_2$S$_3$ thin films annealed at 350 °C for 30 min in vacuum oven. Cross-sectional Scanning electron micrographs for Sb$_2$S$_3$ and CAS-50 samples are also included in the same figure.

Surface morphology of the CAS thin films having varying Cu thicknesses deposited using 4 h Sb$_2$S$_3$ bath are presented in Figure 3.35 along with that of the Sb$_2$S$_3$ sample. Surface morphologies of the CAS thin films in this case are comparable with the morphologies of the similar Cu thickness CAS samples deposited using the 2 h Sb$_2$S$_3$ bath where the CAS 50 sample shows better surface morphology with bigger grains distributed uniformly on the surface. In contrast, the CAS 25 nm and CAS 75 nm samples (350 °C 30 min) show surfaces constituted by smaller grains and some voids. The Sb$_2$S$_3$ sample deposited from the 4 h bath shows a morphology having irregular shaped particles and many voids. The average thickness of the Sb$_2$S$_3$ sample and the CAS 50 nm sample are 270 nm and 325 nm respectively as measured from the SEM cross-section images.
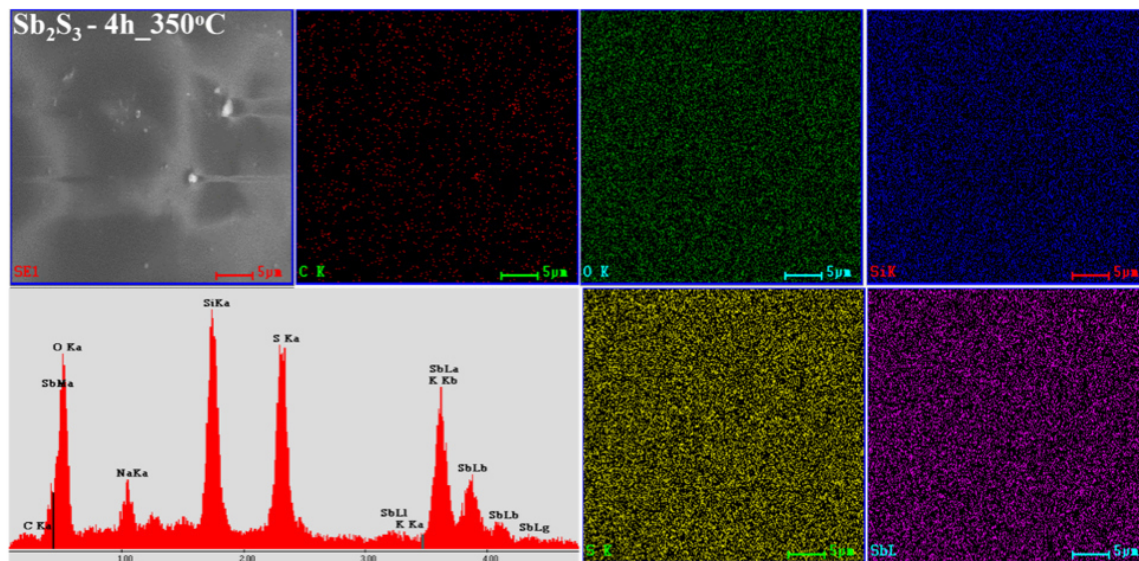
Figure 3.36: Scanning electron microscopy images, EDX, EDX mapping for CuSbS$_2$ thin films formed by annealing glass/Sb$_2$S$_3$ (4 h 25 °C) at 350 °C for 30 min in vacuum.
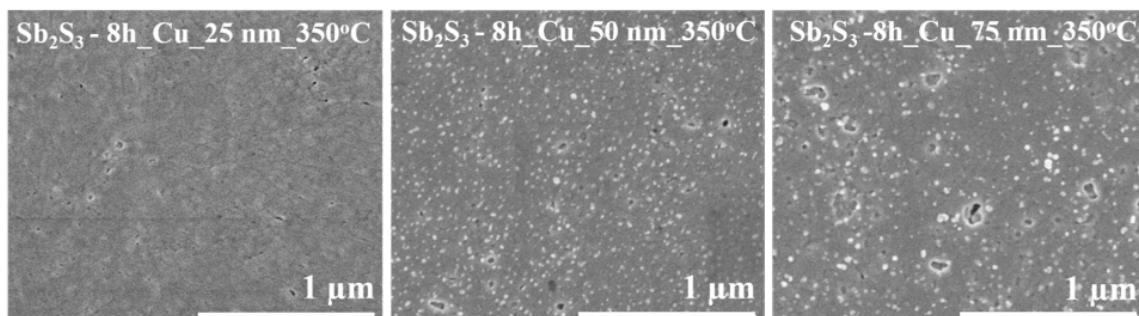
Figure 3.37: Scanning electron microscopy images for CuSbS$_2$ thin film formed by annealing glass/Sb$_2$S$_3$/Custacked layers with varying Cu thicknesses 25, 50 and 75 nm (CAS Cu-25, CAS, Cu-50 and CAS Cu-75) at 350 °C for 30 min in vacuum where the Sb$_2$S$_3$ CBD was at 25 °C for 8 h.

Figure 3.36 and Figure 3.37 present the EDX area scans and elemental mappings of Cu, Sb, S, Si and O of the Sb$_2$S$_3$ and CAS 50 nm samples. While Sb, S, Si and O were detected in both samples, in the case of the CAS 50 sample, presence of Cu is also observed as seen from the EDX area scans (The SEM images of the area selected for the scans and mapping are also included in both cases). All the
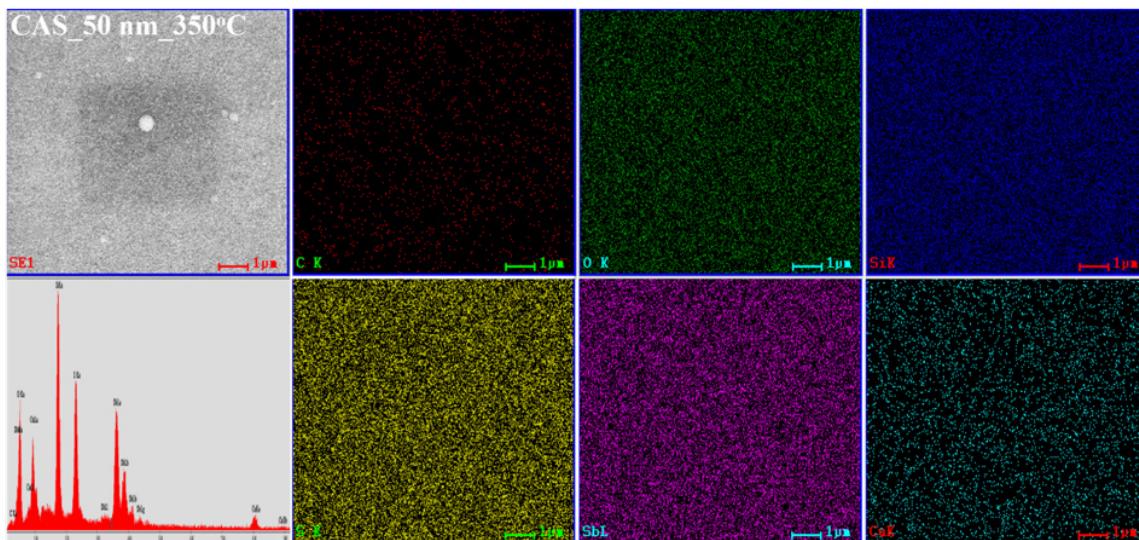
Figure 3.38: Scanning electron microscopy images, EDX, EDX mapping for CuSbS$_2$ thin film formed by annealing glass/Sb$_2$S$_3$-4h$_2$5 °C/Cu-50 nm (CAS-50) at 350 °C for 30 min in vacuum.

desired elements are distributed uniformly on the surface of the Sb$_2$S$_3$ and CAS 50 nm films as seen from the elemental mappings. SEM images of the CAS 50 and CAS 75 samples along with bare Sb$_2$S$_3$ deposited using 8 h bath are depicted in Figure 3.37. In the case of 8 h Sb$_2$S$_3$ bath, the CAS 50 and 75 samples possess a surface morphology having small and irregular shaped grains. In addition to this, some voids are also present on the sample surfaces in both cases. As the Sb$_2$S$_3$ is deposited from a long time CBD process, probably long time annealing is needed for these CAS films to improve the surface morphology for device applications. The surface of the pure Sb$_2$S$_3$ sample is composed of very small grains as observed from the Figure 3.38.

(b) Scanning electron microscopy images: RTP treated samples

The morphology of the CuSbS$_2$ thin films formed by annealing, preannealed RTP 600 °C and direct RTP 600 °C of CAS Cu-50 precursors is presented in Figure 3.39(a-d) [180] along with the as prepared precursor sample. The as prepared film

exhibits a compact morphology with relatively smaller spherical particles as seen in Figure 3.39(a). After annealing at 380°C, the morphology changes to irregular shaped particles distributed uniformly on the surface as evident from Figure 3.39(b). In the pre-annealed RTP 600 °C sample, the surface is composed of coalescent grains which are continuous and interconnected uniformly, as illustrated in Figure 3.39(d). For the direct RTP treated films, Figure 3.39(c) shows a better coalescence and more compact grains with well defined boundaries.
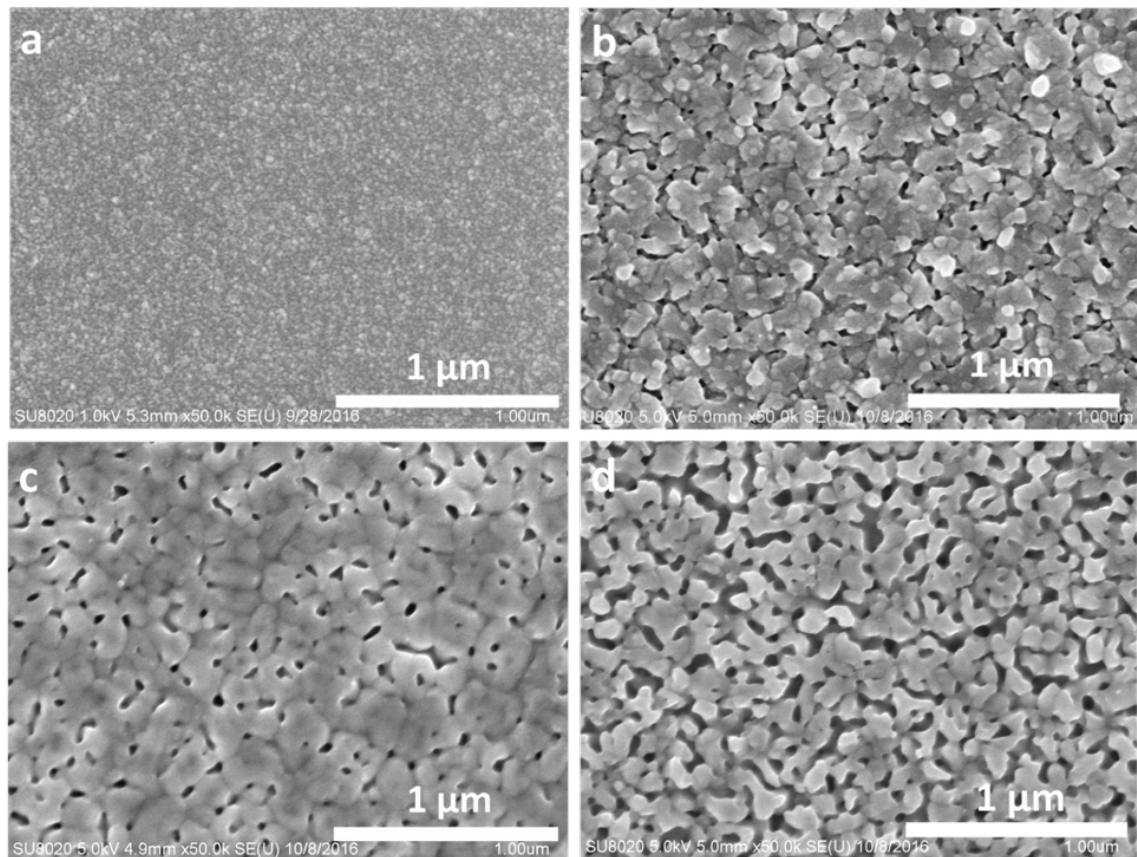
Figure 3.39: Scanning electron microscopy images for CuSbS₂ thin film (CAS Cu-50) (a) as prepared (b) annealed at 380 °C for 1 h in vacuum (c) RTP at 600 °C for 5 min (d) pre-annealed RTP at 600 °C for 5 min. Reproduced with kind permission from Elsevier (https://doi.org/10.1016/j.solmat.2017.02.005).

Morphology of CAS thin films formed by conventional vacuum oven annealing and pre-annealed RTP at 625°C (1,3,4 and 4.5 min) is given in Figure 3.40(a-e) [190]. Films annealed in vacuum oven show surface with irregular shaped small grains
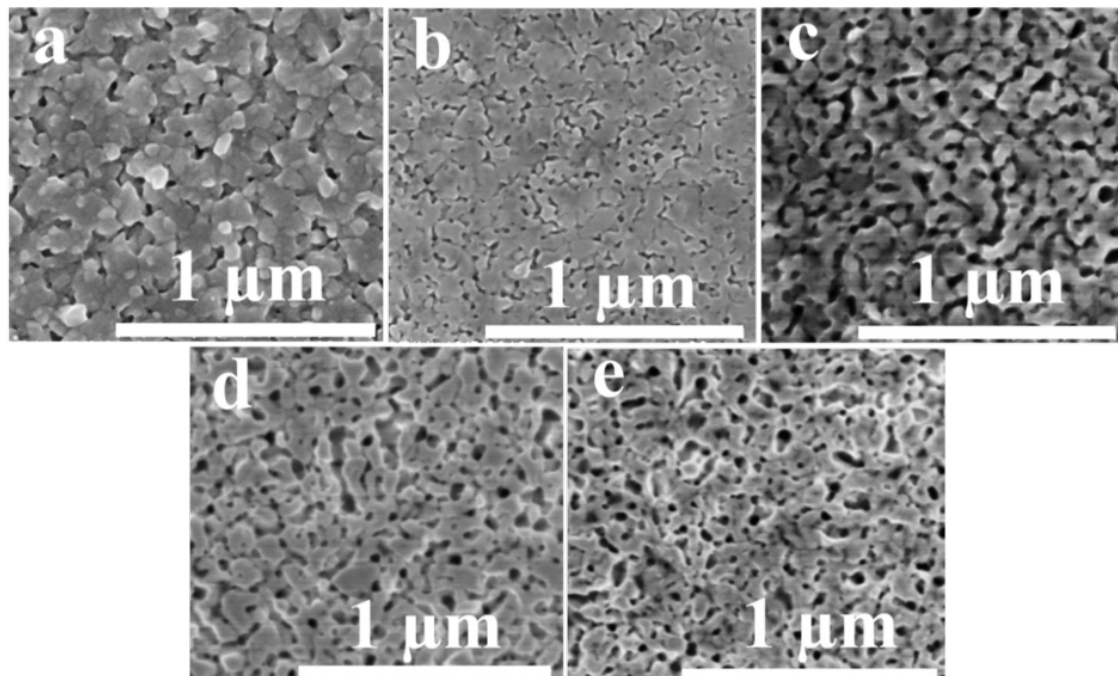
Figure 3.40: Scanning electron microscopy images of CAS films annealed in vacuum oven at 380 °C (a) pre-annealed RTP 625 °C for (b) 1 min (c) 3 min (d) 4 min (e) 4 min 30 second. Reproduced with kind permission from Elsevier `https://doi.org/10.1016/j.mssp.2018.11.007`).

(Figure 3.40a). pre-annealed film RTP at 625 °C for 1 minute improves the surface morphology due to the presence of uniformly distributed and bigger grains (Figure 3.40 b). By RTP for 3, 4 and 4 min 30 s (Figure 3.40 c, d and e) the morphology of films in changes to interconnected grains with significant porosity. Morphology of the CuSbS$_2$ films deposited on Mo substrates pre-annealed RTP at 375 and 400 °C for varying time is shown in Figure 3.41(a-f) [190] and Figure 3.42(a-f) [190]. CAS film deposited on Mo substrates annealed in conventional vacuum oven at 380 °C for 45 minutes also included for comparison. Particles are distributed homogeneously on surface of all the samples annealed conventionally and pre-annealed RTP at 375 and 400 °C. Only difference is the case of grain size and compactness. Pre-annealed RTP heated samples are compact with well-defined boundaries than conventionally annealed one.
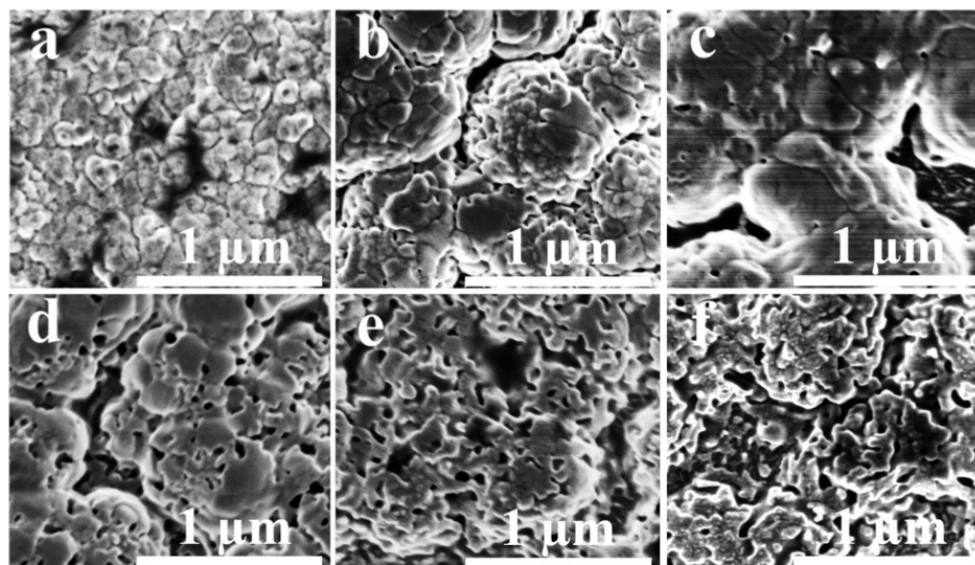
Figure 3.41: Scanning electron microscopy images of CAS films annealed in vacuum oven at 380 °C (a) pre-annealed RTP at 375 °C for (b) 1 min (c) 2 min (d) 3 min (e) 4 min (f) 5 min. Reproduced with kind permission from Elsevier `https://doi.org/10.1016/j.mssp.2018.11.007`).
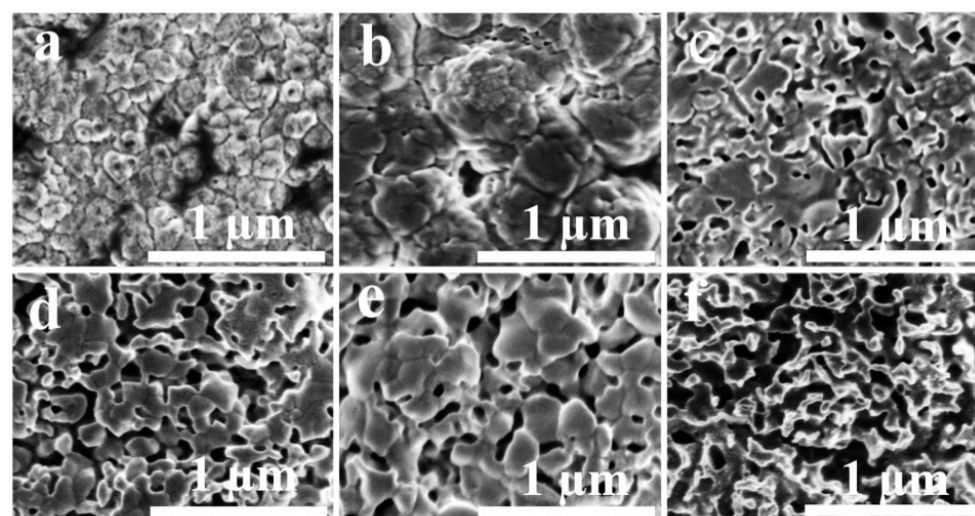
Figure 3.42: Scanning electron microscopy images of CAS films annealed in vacuum oven at 380 °C (a) pre-annealed RTP at 400 °C for (b) 1 min (c) 2 min (d) 3 min (e) 4 min (f) 5 min. Reproduced with kind permission from Elsevier (`https://doi.org/10.1016/j.mssp.2018.11.007`).

(c) Atomic Force Microscopy (AFM)

The surface morphology and roughness of all CAS films were investigated by atomic force microscopy (AFM) in contact mode. Figure 3.5 (a-c) and (d-f) [181] shows the 2D as well as 3D AFM images of CAS thin films CAS20, CAS30 and CAS40 respectively. As revealed in the figure, grain size the films increases gradually with the increase in Cu thickness from 20 to 40 nm. AFM images are taken by scanning an area of 2×2 μm . Roughness of the film surfaces calculated are 2.99 nm, 6.36 nm and 11.34 nm respectively for CAS 20, 30 and 40. Surface of the films appears as flat for the CAS 20 compared to other two whereas small grains appeared in CAS 30 film. For CAS 40 much bigger spherical grains are identified. Change in morphology of the films with varying Cu thickness is evident from SEM and AFM images.
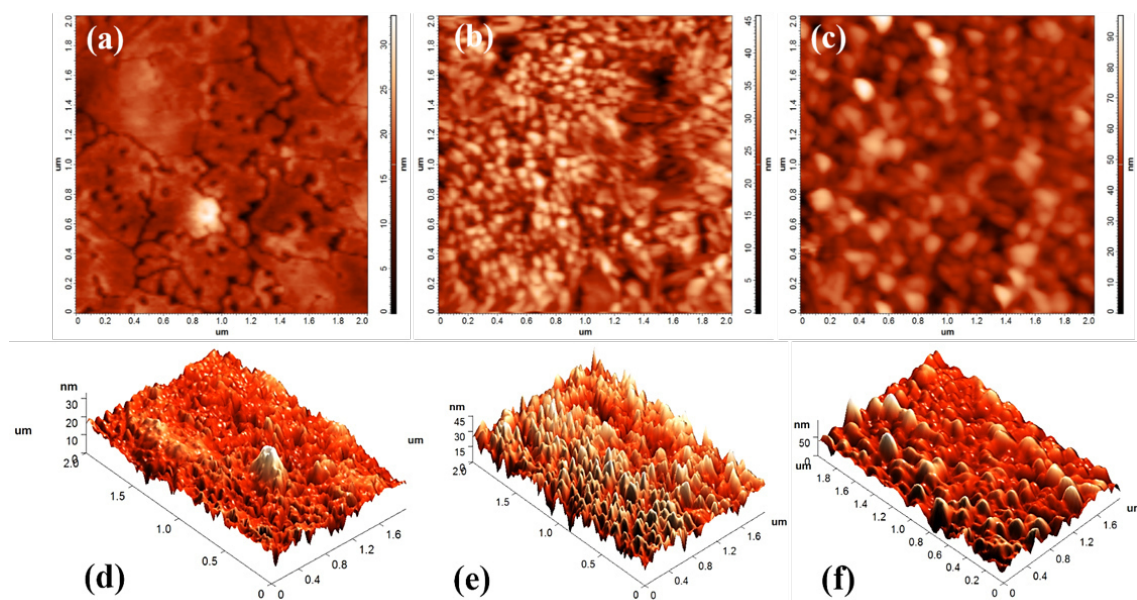
Figure 3.43: Atomic force micrographs (2D) for CuSbS$_2$ thin films with varying Cu thicknesses (a) CAS 20 (b) CAS 30 (c) CAS 40 and (d-f) their corresponding 3D images. Reproduced with kind permission from RSC advances (DOI: 10.1039/C8RA05662E).

3.4.4   Optical properties

(a) Conventionally annealed films
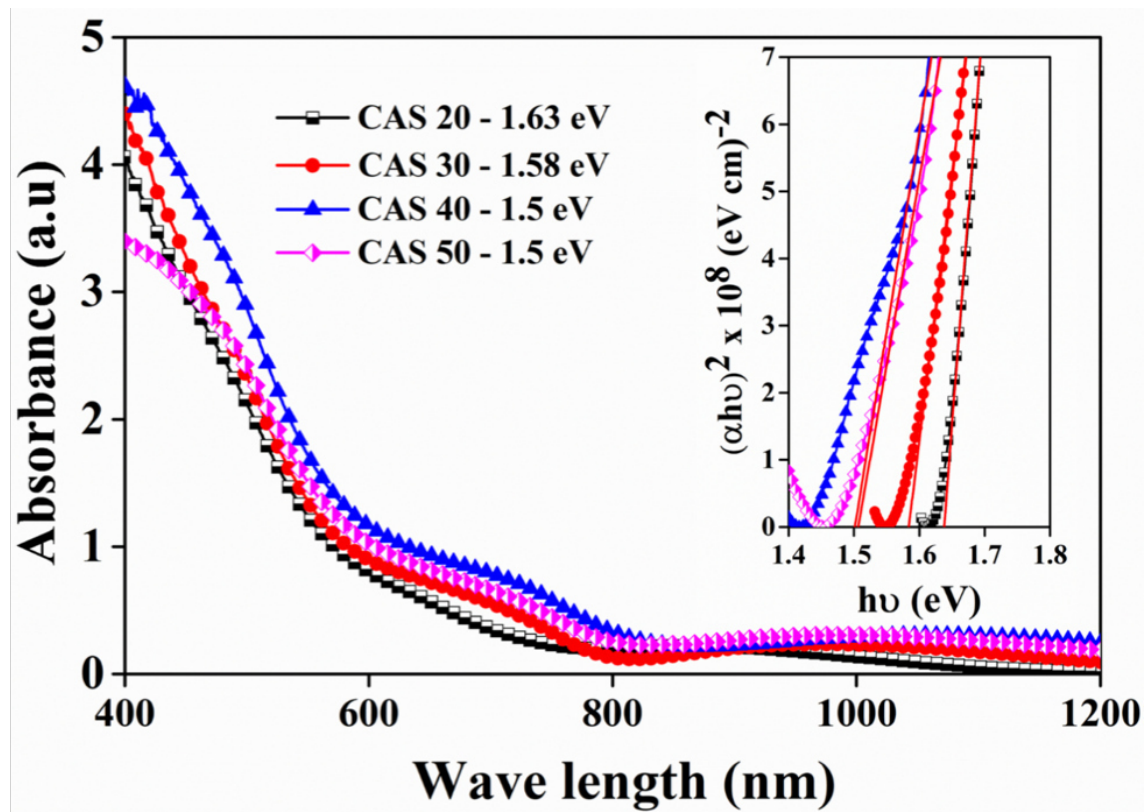
Figure 3.44: Optical absorption spectra of phase pure CAS thin films with varying Cu thicknesses 20, 30, 40 and 50 nm. Tauc plots for the evaluation of optical band gaps are given in the inset. Reproduced with kind permission from RSC advances (DOI: 10.1039/C8RA05662E).

The optical absorbance and energy bandgap of the CAS thin films deposited on glass substrates were determined using UV-Vis NIR spectrometer for the range of 400-1200 nm. Figure 3.44 [181]. shows the absorption spectra for CAS 20, 30, 40 and 50 thin films and their corresponding band gaps (inset). A broad, as well as strong absorbance in the range of 400 to 800 nm and its reduction at higher wavelength, is clear from the given spectra and the absorption coefficient of the prepared films were 10^5 cm^{-1}. Optical bandgap of the films were calculated using the Tauc plots
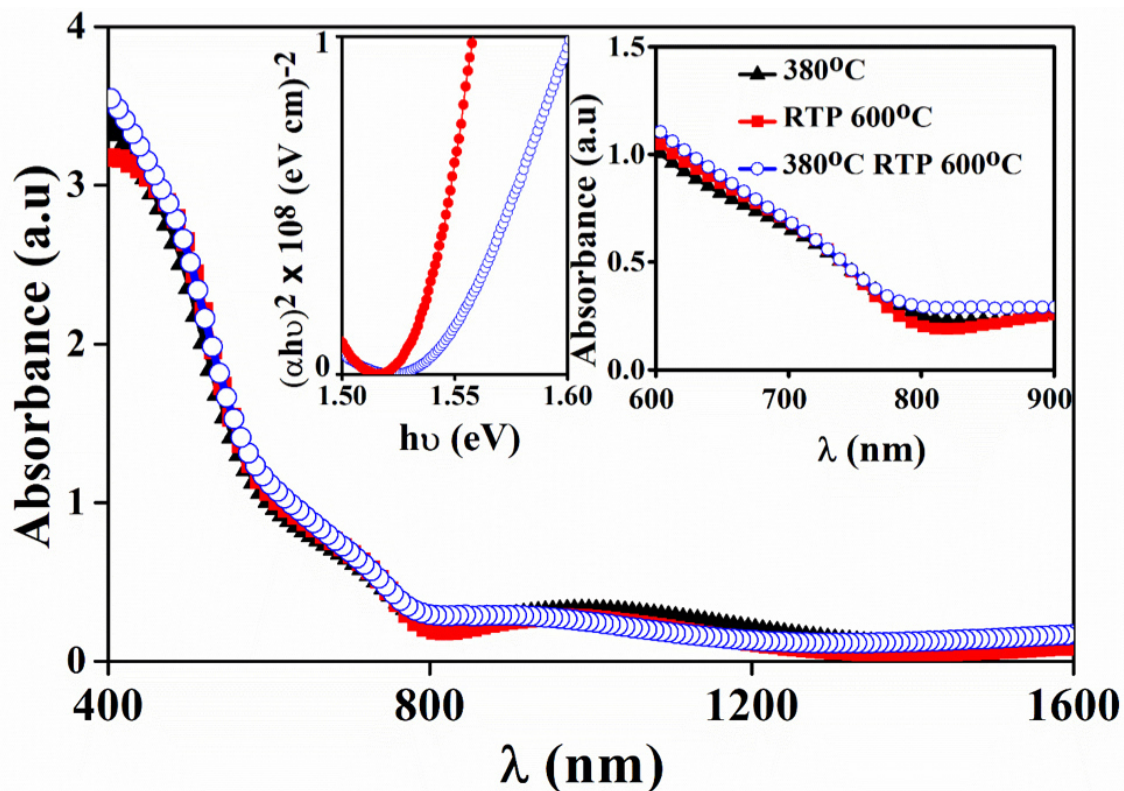
Figure 3.45: Optical absorption spectra of phase pure CuSbS₂ thin film (CAS Cu-50) formed at different conditions (a) pre-annealed RTP at 600 °C for 5 min. The region of onset of absorption and the Tauc plot for the evaluation of optical band gap are given in the inset. Reproduced with kind permission from Elsevier (`https://doi.org/10.1016/j.solmat.2017.02.005`).

based on the relation (section 3.3.7),

$$(\alpha h\nu\ )^n = A(h\nu - \mathrm{E}_g) \tag{3.8}$$

The plot of $(\alpha h\nu)^2$ vs $h\nu$ (Tauc plot) for the phase pure CuSbS₂ thin films yielding a good linear fit for n = 2 as given in the inset, implying direct optical absorption in these films. The bandgaps obtained for CAS 20, 30, 40 and 50 films are 1.63, 1.58 and 1.50 eV respectively [166]. The widest bandgap observed for 20 nm CAS film might be due to the higher content of unreacted Sb₂S₃. The higher electron-hole pair generation and potent absorption coefficient due to the direct bandgap make

these films suitable candidates for optoelectronic device applications [72] The direct band gap would also be beneficial for UV-NIR spectra detection.

(b) RTP treated films
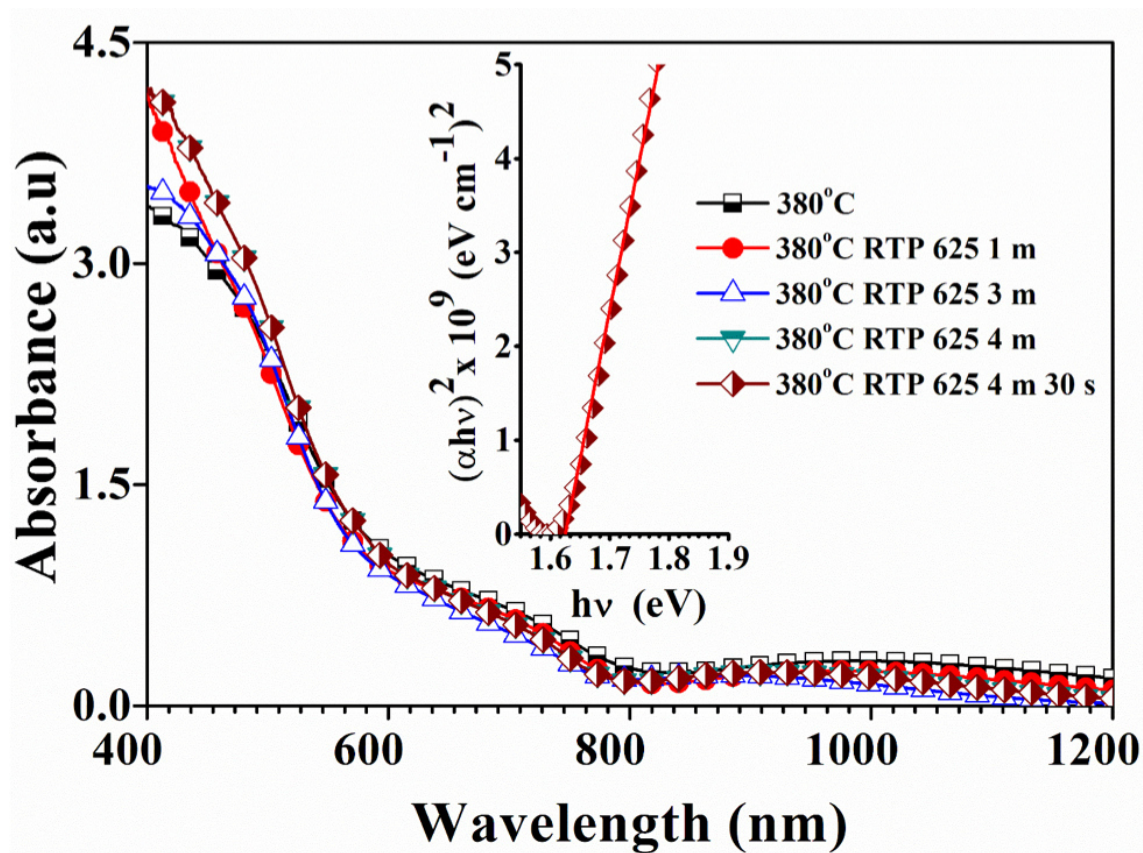
Figure 3.46: Optical absorption spectra of CuSbS₂ thin films deposited on glass substrates and the Tauc plot of the film pre-annealed RTP at 625 °C for 4 min 30 s. Reproduced with kind permission from Elsevier (`https://doi.org/10.1016/j.mssp.2018.11.007`).

Figure 3.45 [180] shows the absorbance spectra of typical phase pure CuSbS₂ thin films with Cu 50 nm (CAS Cu-50) formed by pre-annealed RTP and direct RTP. CAS Cu-50 annealed at 380 °C is also included in the same figure for comparison. All the films show good absorbance in the visible region. The energy range for plotting the band gaps was selected corresponding to the onset of absorption as shown in the inset. The band gap values were estimated from the extrapolation of linear region

of the plot to the hν axis. The E$_g$ values obtained for the films were 1.53 eV (RTP 600 °C), 1.54 eV (pre-annealed RTP 600 °C) which is in the reported range of values 1.5–1.6 eV [19,36] for CAS thin films. Also, the significant sub-bandgap can be observed in all the absorption spectra indicating the presence of high density of traps in the thin films.

Figure 3.46 [190] shows the absorbance spectra of CuSbS$_2$ thin films annealed in conventional vacuum oven at 380 °C and pre-annealed RTP at 625 °C for 4 min and 4 min 30 s in the wavelength range of 400-1200 nm. All the films showed good absorption in the visible region. The band gap of preferentially oriented sample (CAS 380 °C RTP 625 °C 4 min 30 s) is measured as specified earlier. As given in the inset of the graph, we plotted $(\alpha h\nu)^2$ vs hν and find the bang gap as 1.6 eV by extrapolating the linear fitting line to the X-axis, which is in the reported range of E$_g$ values for CuSbS$_2$ to be used as an absorber layer in solar cells.

3.4.5 Electrical properties

Based on the characterizations of the CAS thin films of varying Cu thicknesses, the CAS 50 sample was selected for the electrical properties measurement as it showed phase pure CuSbS$_2$ formation. The photocurrent response measurements were carried out for the CuSbS$_2$ thin films (CAS Cu-50) formed by annealing, pre-annealed RTP 600 °C and direct RTP 600 °C, as given in Figure 3.47 [180] . All the films exhibit photoconductivity, irrespective of the heat treatment carried out. The samples were illuminated using a halogen lamp with an illumination intensity of 500 realizing the photoconductivity measurements. For the measurements, a bias voltage of 10 V was applied between a pair of painted silver electrodes of equal dimensions and the current flowing through the sample was simultaneously measured in an interval of 20 s, first in the dark, followed by illuminating the sample and then again in dark. As the heating conditions were changed, for the given bias and keeping the electrode dimensions the same in all the samples, the dark current and the photocurrent showed an increase. The values of conductivity of the films undergone

direct RTP at 600 °C and pre-annealed RTP at 600 °C were in the order of 10^{-4} and 10^{-3} $(\Omega \text{cm})^{-1}$ respectively indicating that the pre-annealed RTP film was more conductive than the other. The higher conductivity for the pre-annealed RTP 600 °C film in this case can be attributed to its slightly higher crystallite size and the compact morphology with reduced grain boundaries as seen from the XRD and SEM results.

The photocurrent response measurements of CAS 50 films of randomly oriented growth (formed at 380 °C) and preferentially oriented growth (RTP at 625 °C 4½ min) were performed by illuminating the samples using the same halogen lamp of intensity 500 mW/m^2 and the corresponding measurements are depicted in Figure 3.48 [190]. From the zoomed data analysis from the figure indicated, it is revealed that, upon illumination, the increase in current is 0.25 μA for randomly oriented CAS film and 2.3 μA for the preferentially oriented film. Furthermore, for the oriented film, the dark current is one order higher than that of the randomly oriented sample.

The increase in the dark current in the highly oriented film can be attributed to increase in electrical conductivity due to the present larger grains in the preferentially oriented film and these results also agree with the XRD analysis. Further, the photocurrent response, photocurrent sensitivity and I-V curves of the preferentially oriented film were measured by illuminating the samples using different wavelength LEDs of 20 W as shown in Figure 3.49 [190]. Different wavelengths in the visible spectral region such as 450, 520, 620, 660, 740, 850, 940 nm and white light were selected for the illumination of the samples. A bias voltage of 10 V was applied for measuring the current under dark and illumination. First, the dark current was measured for 20 s and then under illumination for the next 20 s followed by another 20 s after the illumination turned off. The sample shows good photocurrent response under illumination using all the wavelengths as seen in Figure 3.49(a). The maximum photo response was obtained under illumination of the white light since white light consists photons of a range of wavelengths in the visible region which suggest that the film can be used to absorb solar light for PV device applications. After white light,
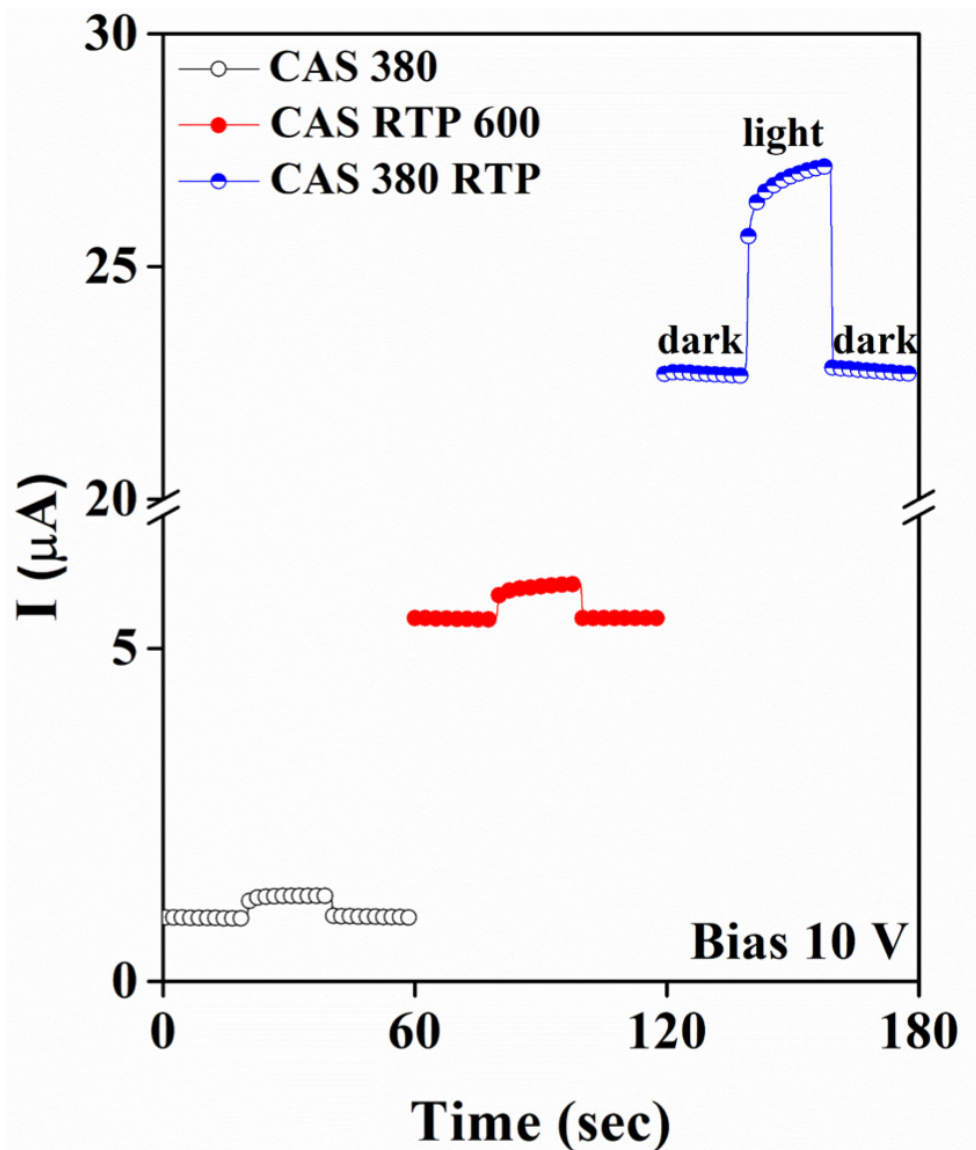
Figure 3.47: Photocurrent response curves for CuSbS₂ thin films (CAS Cu-50) formed at different conditions (a) annealed at 380 °C for 1 h in vacuum (b) RTP at 600 °C for 5 min (c) pre-annealed RTP at 600 °C for 5 min. Reproduced with kind permission from Elsevier (`https://doi.org/10.1016/j.solmat.2017.02.005`).

next higher photoresponse was observed for blue wavelength illumination due to the higher photon energies of this light compared to other wavelengths. Sensitivity of the CAS thin films towards different wavelength illuminations (Figure 3.49(b)) was calculated employing the equation [180],
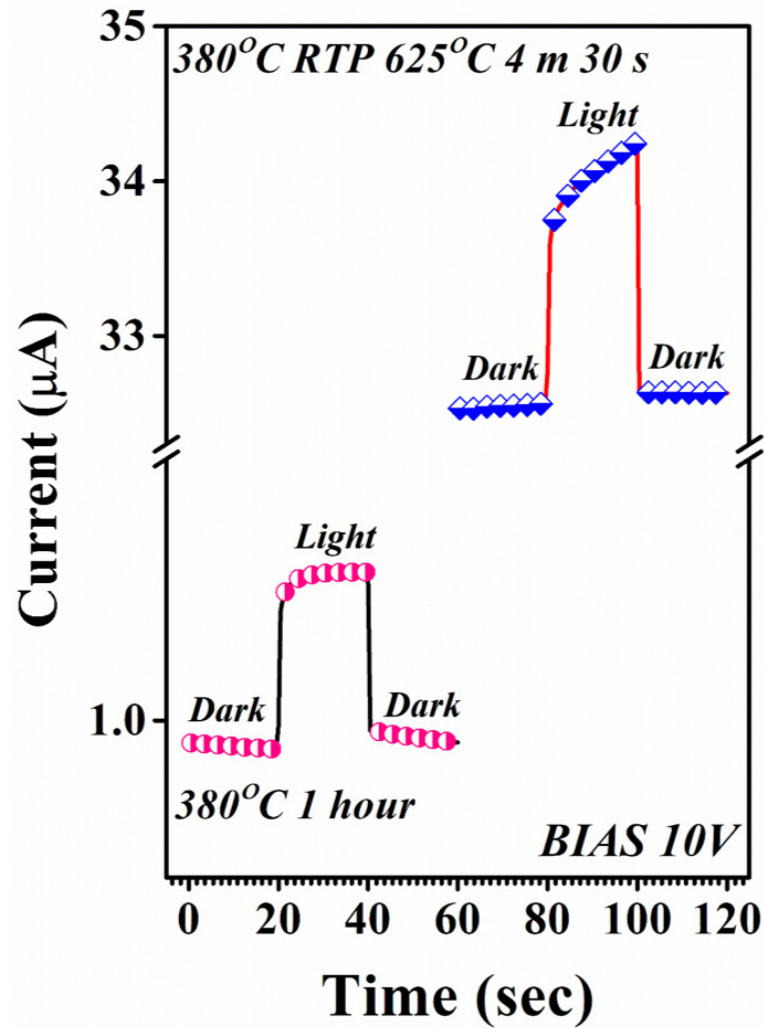
Figure 3.48: Photocurrent response curves of glass/CuSbS$_2$ thin films formed by annealed at 380 °C for 1 hour and pre-annealed RTP at 625 °C for 4 min 30 sec. Reproduced with kind permission from Elsevier (`https://doi.org/10.1016/j.mssp.2018.11.007`).

$$S(\%) = \frac{I_{ph} - I_d}{I_d} \times 100 \tag{3.9}$$

where I_{ph} is the photocurrent and I_d is the dark current. The estimated sensitivities were 16.19%, 12.85%, 11%, 9.05%, 7.62%, 7.62%, 3.33% and 0.47% respectively for white, 450, 520, 620, 660, 740, 850 and 940 nm wavelength illuminations.
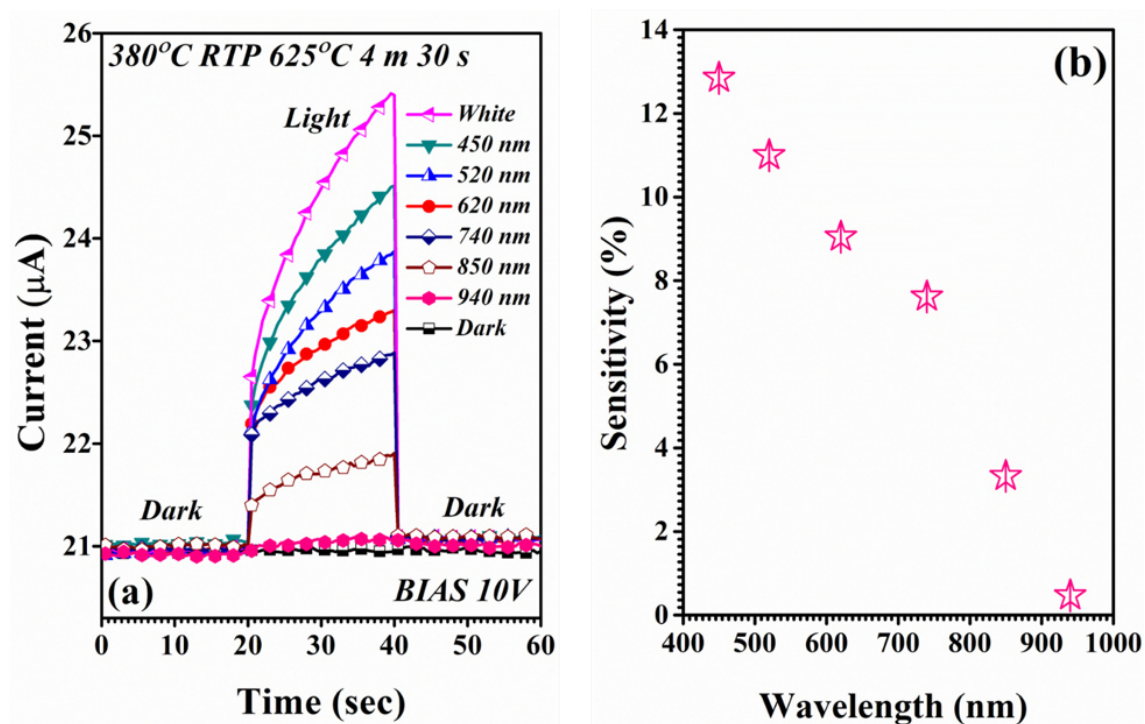
Figure 3.49: (a). Photo response of the pre-annealed RTP at 625 °C for 4 min 30 s film using LED sources having wavelength 450 nm, 520 nm, 620 nm, 660 nm and white light. Applied bias voltage: 10V and optical power of LED: 20 W (b). graph of sensitivity Vs wavelength. Reproduced with kind permission from Elsevier (https://doi.org/10.1016/j.mssp.2018.11.007).

The highest sensitivity was obtained under white light illumination as expected. The onset of increase in photosensitivity 800–700 nm indicates strong absorption supporting the band gap value of 1.6 eV as seen in Figure 3.49(b).

To study the photoconductive nature of the films deposited on Mo substrates, electrochemical measurements were also carried out. Two consecutive cycles were scanned in each measurement and the data recorded during the 2nd cycle is presented in each case. The respective cyclic voltammograms of CuSbS₂ thin films on Mo substrates (sample CAS 380 °C, CAS 380 °C RTP 400 °C 3 min) along with that of a bare substrate are presented in Figure 3.50 [190]. The bare Mo-substrate and sample CAS 380 °C showed relatively larger area (due to the higher width of the curves) enclosed by the voltammogram indicating higher capacitance value implying

more dielectric nature for these samples in comparison with that of CAS 380 °C RTP 400 °C 3 min sample, which was composed of highly oriented grains. This result is comparable with the better photoconductivity observed for the oriented films. In addition to that, the CAS films with oriented grain growth (CAS 380 °C RTP 400 °C 3 min) showed higher current at a specific voltage of 0.1 V which can be attributed to better electronic properties and slightly higher optical absorption in the blue region for such films. These results are in correlation with the previously discussed results where the pre-annealed sample showed better photo response and optical absorption. However, more investigations are needed for detailed analysis of the dielectric properties of CAS films formed at different conditions thereby exploring such materials for electrolysis reactions.

It is known from the literature that CuSbS$_2$ exists in orthorhombic form with layered structure consisting of covalently bonded quadruple layers perpendicular to c-axis ((001) plane)) bound together by van der Waals forces connecting Sb and S with a separation of ∼3.115 $\mathring{A}$. This layered structure plays an important role in better electrical properties exhibited by this compound. Moreover, copper antimony chalcogenides show possibility of crystallographic orientation of the layered structure in various ways with respect to the substrate especially in thin film form. The highly oriented layered structure can produce inert surfaces and reduce grain boundary recombination in 2D or 1D form. In our samples, the highly oriented grain growth along (103) plane with respect to the substrate surface can cause a tilt for the layered structure and the effect of such a structural characteristic on the electrical properties of the material is yet to be investigated in detail. By the present method of synthesis, CuSbS$_2$ was formed by interlayer diffusion and reaction between Sb$_2$S$_3$ and Cu during vacuum annealing for 1 h (pre-annealing). The complete reaction and compound formation occur during this process. But coalescence of fine grains resulting high grain growth/preferential orientation without change in composition can be achieved when such films are post treated by rapid thermal process (RTP) for 1–5 min. In our case, direct RTP without pre-annealing lead to either incomplete
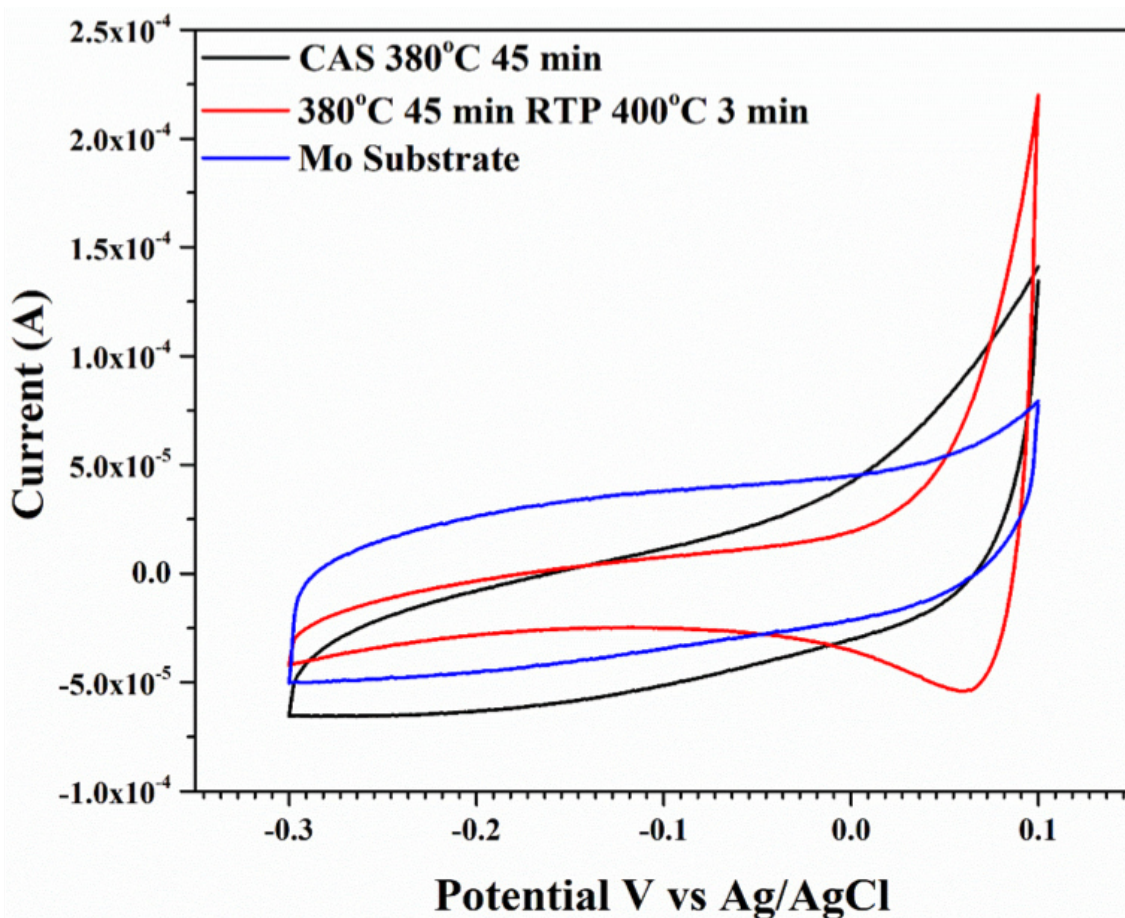
Figure 3.50: Cyclic voltammograms of CuSbS$_2$ thin films on Mo substrates. Electrolyte: 1 M KCl; Scanning speed: 50 mV s @1; Measured cycle: 2. Also, the voltammogram of a bare Mo-substrate measured under same conditions is included for comparison. Reproduced with kind permission from Elsevier (`https://doi.org/10.1016/j.mssp.2018.11.007`).

reaction between Sb$_2$S$_3$ and Cu or loss of material at the specified temperature range of 375–400 °C /625 °C depending on the nature of substrates used. In the field of photovoltaics device application, to achieve high production rate, cell fabrication time should be reduced. Further, the present work demonstrates the potential of employing rapid thermal processing to produce highly oriented grains in 2D or 1D structures to achieve fabrication of devices with reduced recombination leading to improved device performances.
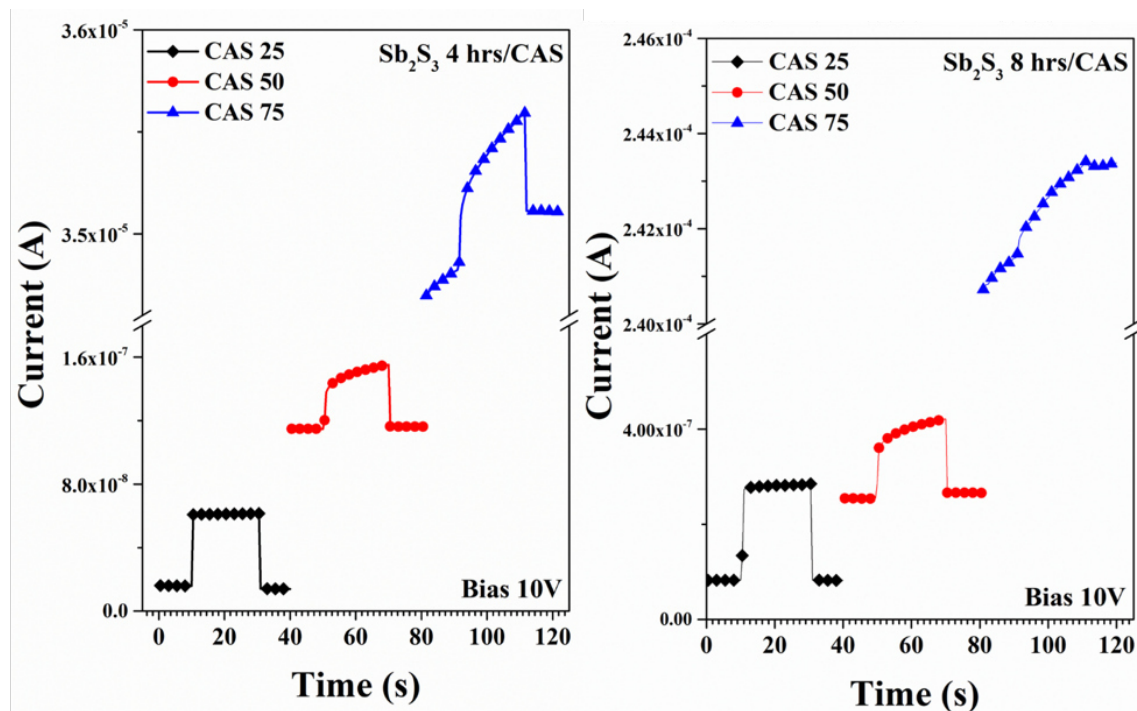
Figure 3.51: Photocurrent response curves for CuSbS₂ thin films (CAS Cu-25, CAS Cu-50, CAS Cu-75) formed by annealing glass/Sb₂S₃/Custack at 350 °C for 30 min in conventional vacuum oven where the Sb₂S₃ CBD bath was at room temperature for 4 and 8 h respectively.

The photocurrent response measurements of the CAS 25, 50 and 75 samples deposited using 4 h and 8 h CBD baths of Sb₂S₃ are presented in Figure 3.51. Similar like in the case of the previous conditions where the Sb₂S₃ bath was 2 h, here also, all the samples are photoconductive as evident from the increase in current upon illumination. In both cases, the CAS 75 sample shows slightly different photoresponse behavior where the photoconductivity is gradually increased upon illumination and then does not return to the ground state. This can be attributed to the higher Cu content and hence high conductivity of these films compared to the others.

Based on all the results discussed in this chapter, it can be concluded that, the structure, morphology, electrical and optical properties of the CAS thin films were strongly influenced by the Cu content, Sb₂S₃ bath duration and the post heat treatments (vacuum oven, RTP, pre-annealed RTP, temperature and time duration).

As one or more of the said parameters are varied, the resulted films exhibit variation in the properties opening up a way to modify their performance when integrated in real device applications. For instance, the phase pure CAS thin films showed an optical band gap of 1.5 eV indicating that these films can be strong candidates for PV applications. On the other hand, CAS samples having lesser Cu thicknesses showed conductivity and good photoresponse behavior suggesting that they can be used for effective photodetection application covering the entire Vis-NIR regions. Device applications based on the CAS thin films and the effect of different deposition parameters or post heat treatments on their performances are described in detail in the following chapter.

Chapter 4

$CuSbS_2$ BASED DEVICES: SOLAR CELLS AND PHOTODETECTOR

4.1 FABRICATION OF SOLAR CELLS AND PHOTODE-TECTORS

In this chapter, the application aspects of the $CuSbS_2$ thin films as solar cells and photodetectors are described in detail. Both solar cells and detectors were prepared using $CuSbS_2$ thin films formed at different conditions as attempts towards improving the performance of the fabricated devices. The solar cells were characterized using J-V curves and EQE measurements. The photodetectors were described in terms of their sensitivity, responsivity and cyclic stability. In both cases, the $CuSbS_2$ devices were also characterized in detail for their structure, elemental composition, and surface morphology using various characterization techniques.

4.1.1 Solar cells : glass/TCO/CdS/$CuSbS_2$/Ag

4.1.1.1 Deposition of CdS

Thin film of CdS was deposited on TCO/Glass by chemical bath deposition where the bath composition was cadmium chloride (10 ml), triethanolamine (5 ml), ammonium

hydroxide (10 ml), thiourea (10 ml) and deionized water (65 ml) [194]. The TCO samples were immersed in the bath at 70 °C for 20 min. The as-prepared CdS films were annealed in air at 400 °C for 30 min. The heat treatment of CdS buer layer in oxygen to produce a barrier against interlayer diusion CdS/CdTe solar cells (grain hardening), and thus to improve the device performance is already known [195].

4.1.1.2 Deposition of CuSbS$_2$ thin films

Thin films of antimony sulfide (Sb$_2$S$_3$) were deposited on CdS thin films annealed in air at 400 °C for 30 minutes by chemical bath deposition reported in the previous section (section number 3.2.1.2 explained CuSbS$_2$ synthesis procedure). The bath duration was varied from 2 h to 4 h, and then to 8 h. The as-deposited thin films were orange-yellow with good adhesion and of 200 nm in thickness. Thermal evaporation technique as explained before (section 3.2.1.3) was employed to deposit Cu layer of dierent thicknesses (50 and 75 nm) on Sb$_2$S$_3$ thin films. The evaporation process was carried out at high vacuum (10^{-6} Torr) at a rate of 2 $\overset{\circ}{A}$/s keeping the substrates rotating with 20 rpm speed.

4.1.1.3 Heat treatments

The PV structures of type glass/TCO/CdS/CuSbS$_2$ formed by heating the stacked layers at dierent conditions such as conventional annealing at 380 °C for 45 min, RTP at 400 °C for 5 min and pre-annealed RTP at 400 °C for 5 min. The PV structures of type glass/FTO/CdS/CuSbS$_2$ formed by annealing the stacked layers in the conventional vacuum oven at 350°C for 30 min. An ohmic contact of 0.25 cm^2 was made using silver paint (SPI supplies) to measure the current-voltage characteristics of the devices fabricated on ITO as well as FTO substrates. Schematic representation of the PV devices having p-n configuration is given below in Figure 4.1.
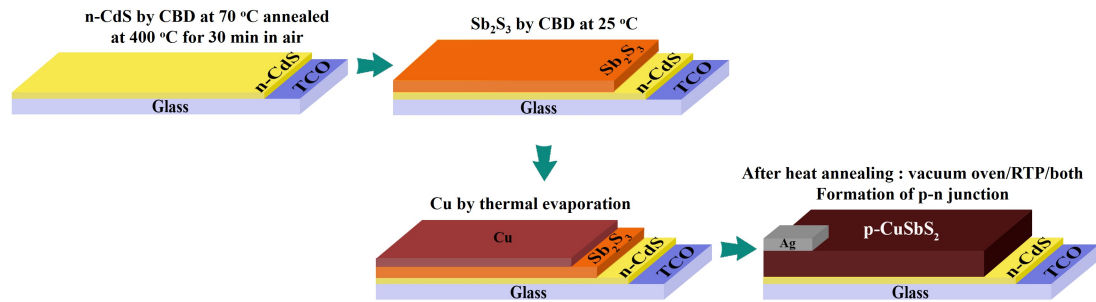
Figure 4.1: Superstrate p-n configuration of glass/TCO/(n)CdS/(p)CuSbS$_2$/Ag

4.1.2 Photodetector

CuSbS$_2$ thin films were deposited on cleaned glass substrates using combined CBD (2 h Sb$_2$S$_3$ bath) and thermal evaporation (Cu thicknesses 20, 30 and 40 nm) followed by a heat treatment in a conventional vacuum oven at 380 °C for 1 h. A pair of A$_g$ electrodes having equal dimensions (5×5 mm) were painted on the film surface using colloidal silver to use as the terminals in the two-point probe technique. A keithley picoammeter/ voltage source (Model No. 6487) was employed for applying the voltage through the painted electrodes and simultaneously measuring the current. The photoconductivity measurements were done using the same Keithley source while the sample was illuminated using a tungsten halogen lamp and under dark.

4.2 DEVICE CHARACTERIZATION

4.2.1 J-V Characteristics

Characterization of the PV devices was performed by measuring the I-V parameters of the cells using the same keithley picoammeter/ voltage source used for the electrical characterization of the CAS thin films. When the voltage and current density are plotted on the x and y axes respectively, the intersection on the x-axis gives the open-circuit voltage (V_{oc}) of the solar cell being measured while the intersection on the y-axis gives the short circuit current density (J_{sc}) which are two important parameters for evaluating the performance of the PV device. A typical experimental

set-up used for measuring the I-V characteristics of a solar cell under illumination is shown in Figure 4.2 [152]. The top and bottom electrodes of the device are used for the two-point measurement technique where the voltage and current are measured during the voltage sweep. The solar cell parameters such as efficiency and fill factor are then estimated using the obtained I-V characteristics of the cell. In this thesis, the contacts were made using silver paint to measure the J-V characteristics under dark and illumination. A solar simulator (Oriel) of intensity 100 mW/cm^2 under AM1.5 radiation was used as the illumination source.
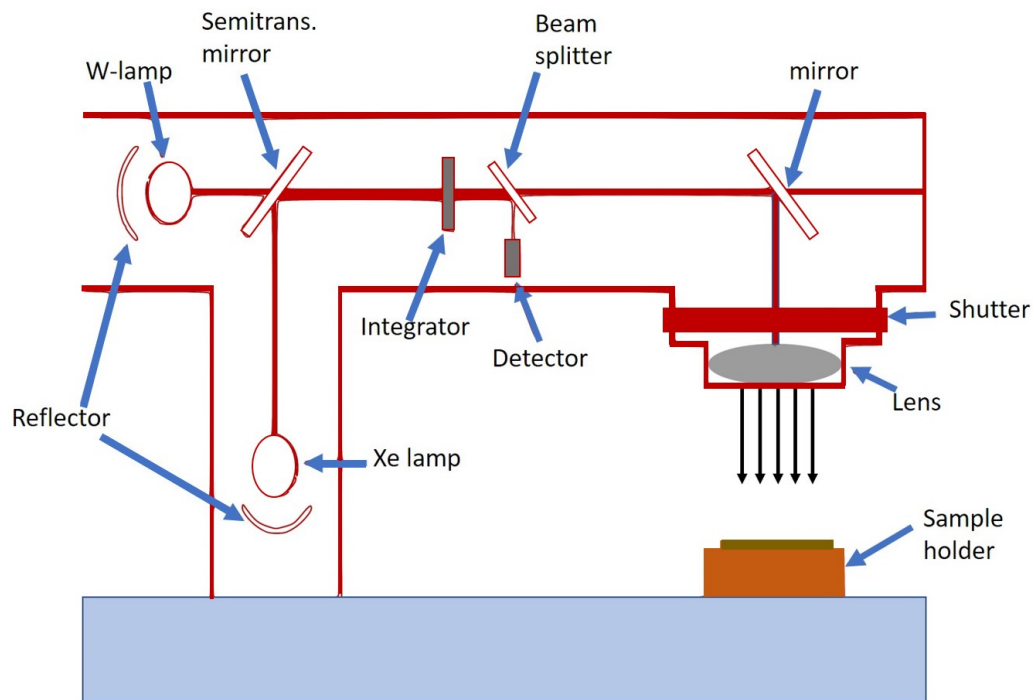
Figure 4.2: Schematic representation of solar simulator

4.2.2 EQE measurements

The behavior of a solar cell in a specific range of wavelengths was measured by means of its external quantum efficiency (EQE) [196]. The ratio between the number of incident photons and the number of charge carriers collected by solar cells is termed as the EQE of the PV device. The EQE was calculated using the spectral response of a solar cell where the spectral response is the ratio between the generated current

by the cell and the incident power. Spectral response is related to the EQE by the following equation:

$$EQE(\lambda) = \frac{hc}{q\lambda} \times SR \tag{4.1}$$

where c is the speed of light, h is the Planck's constant, q is the electronic charge and λ is the wavelength of light. In the present thesis, EQE measurement was done for the CAS based solar cells to evaluate and compare their device performances.

4.2.3 Photodetector characteristics

Evaluation of electrical properties as well as photoresponse measurements were done under the illumination from light-emitting diodes (LEDs) having wavelengths of 450, 620, 740 and 850 nm and optical power of 20 W using a picoammeter/voltage source meter (Keithley 6487). A pair of silver electrodes of 5 mm in length separated by 5 mm were painted using conductive silver paint (SPI® supplies) and dried on the sample surface for the photodetector characterization. The current-voltage measurements were carried out under dark as well as illumination for applied voltages from -5 to +5 V. Photoresponse switching behaviour of the CuSbS₂ thin films were measured at different applied potentials of 1, 3 and 5 V where the LED illumination was turned on and off at each 5th and 10th seconds respectively. Photodetection properties of CAS thin films for various intensities were measured by illuminating the samples using a diode-pumped continuous-wave laser of 532 nm with adjustable output power. The laser spot was expanded using a concave lens and the sample area excess of the electrode dimension was masked to avoid illumination. The same voltage source (Keithley 6487) used to apply voltage and simultaneously to measure current while the samples were illuminated by the laser. Laser output power was varied from 2 mW to 40 mW (2, 6, 10, 20, 30, and 40 mWs) during constant bias voltages 1, 3 and 5 V and photoresponse was measured for 20 s in dark, 20 s in light followed by another 20 s in dark.

4.3 RESULTS AND DISCUSSION

4.3.1 Photovoltaics

4.3.1.1 Effect of heat treatments : p-n configuration
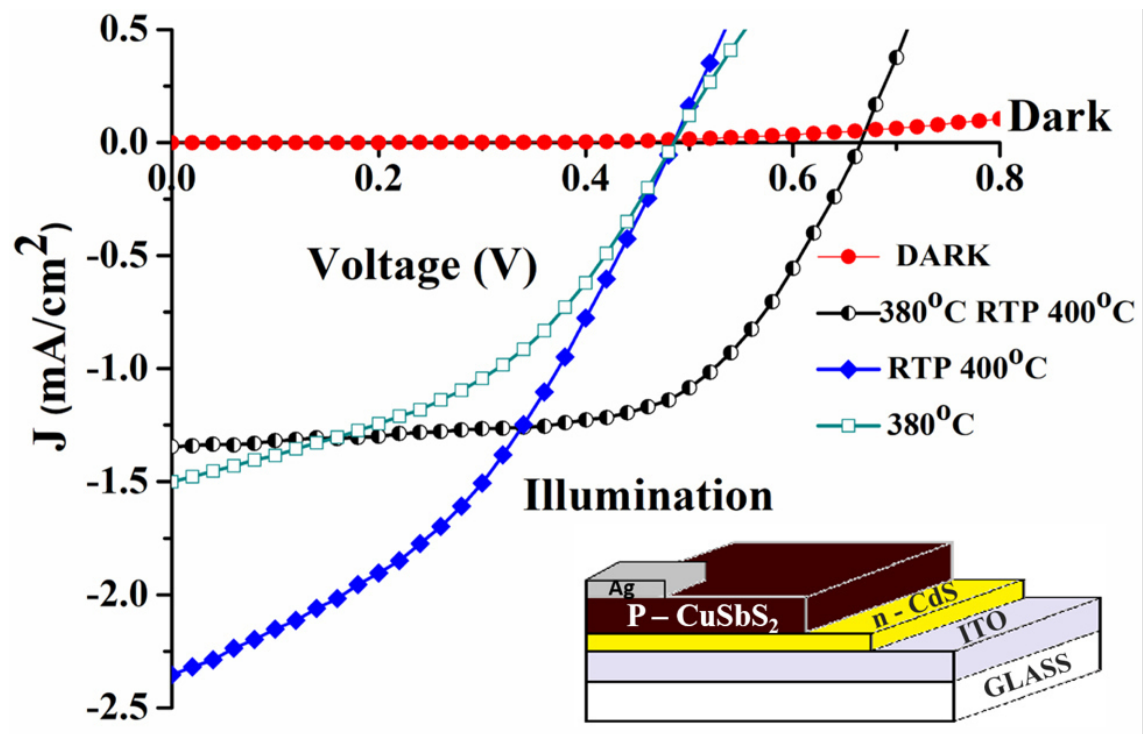
Figure 4.3: Evaluation of J-V characteristics of the glass/ITO/n-CdS/p-CuSbS₂ PV devices (using CAS Cu-50 film) fabricated at different conditions: annealing at 380°C for 45 min, RTP at 400°C for 5 min, pre-annealed RTP at 400°C for 5 min (schematic representation of the PV devices are also included in the figure). Reused with kind permission from Elsevier (`https://doi.org/10.1016/j.solmat.2017.02.005`).

Based on the property studies on the CAS thin films described in chapter 3, various photovoltaic structures using CAS Cu-50 thin films as an absorber and CdS thin films as window layers were prepared. Sequentially deposited glass/ITO/CdS/Sb₂S₃ /Cu layer structures of Cu 50 nm were annealed at dierent conditions to form PV junctions of type glass/ITO/n-CdS/p-CuSbS₂. The PV structures were formed by annealing at 380 °C for 45 min, RTP 400 °C for 5 min and pre-annealed at RTP 400

Table 4.1: Photovoltaic parameters of glass/ITO/n-CdS/p-CuSbS$_2$/Ag solar cells formed by annealing at 380 °C for 45 min, direct RTP at 400 °C for 5 minute and the pre-annealed RTP at 400 °C for 3 minutes (`https://doi.org/10.1016/j.solmat.2017.02.005`).

PV device (ITO/CdS/CuSbS$_2$)	V_{oc} (Volt)	J_{sc} (mA/cm^2)	FF	Efficiency (η) %
380 °C	0.49	1.50	0.43	0.31
RTP 400 °C	0.49	2.35	0.39	0.45
380 RTP 400 °C	0.67	1.35	0.61	0.6
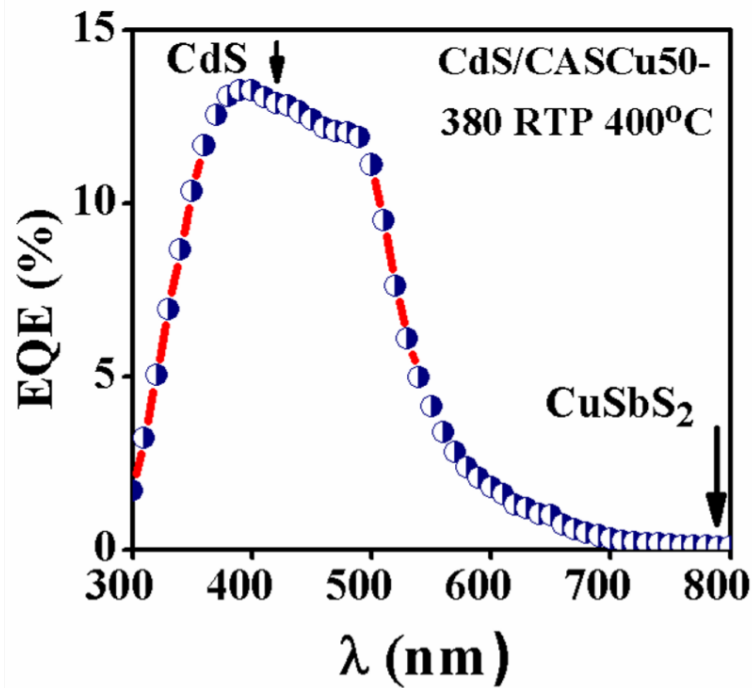
Figure 4.4: EQE measurement of glass/ITO/n-CdS/p-CuSbS$_2$ PV device pre-annealed RTP at 400 °C for 5 min. Reused with kind permission from Elsevier (`https://doi.org/10.1016/j.solmat.2017.02.005`).

°C for 5 min. When the device structures (glass/ITO/CdS/CuSbS$_2$) prepared on ITO were subjected to RTP above 400 °C, the samples evaporated. The J-V measurements were used for the characterization of the PV structures. Figure 4.3 [180]
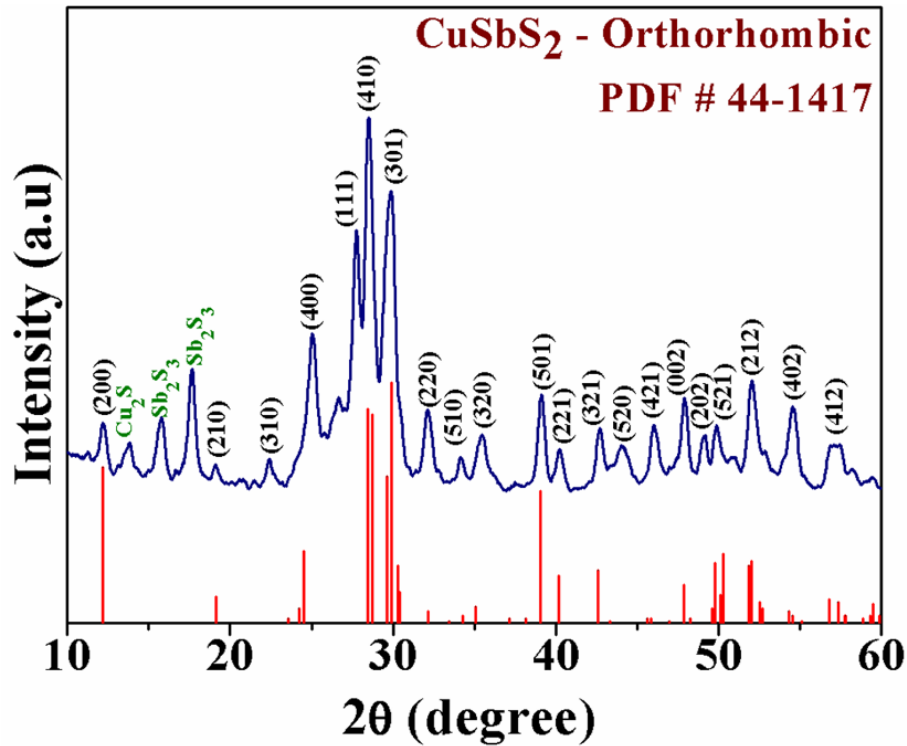
Figure 4.5: GIXRD of the of glass/ITO/n-CdS/p-CuSbS$_2$ PV device pre- annealed RTP at 400 °C for 5 min. Reused with kind permission from Elsevier (`https://doi.org/10.1016/j.solmat.2017.02.005`).

shows the J-V curves of the PV devices formed by various heat treatment. For the J-V measurements, the contacts were made of silver paint and the active device area was 25 mm². The photovoltaic device (glass/ITO/n-CdS/p-CuSbS$_2$) formed by annealing at 380 °C for 45 min, showed V_{oc}= 485 mV, J_{sc}= 1.5 mA/cm², FF = 0.4 and the conversion efficiency (η) = 0.3%. But the direct RTP grown device resulted in higher J_{sc}(2.3 mA/cm²) and η = 0.45% than those of the device formed by annealing. However, the pre-annealed RTP grown device showed an open-circuit voltage (V_{oc}) of 665 mV and a fill factor (FF) of 0.6, the highest values ever reported for CuSbS$_2$ based PV devices, establishing the perspective of CuSbS$_2$ for high efficiency PV devices. J_{sc} value for this device was 1.3 mA/cm² and the η = 0.6%, relatively lower values. The photovoltaic parameters of the same cells are tabulated below (Table 4.1).
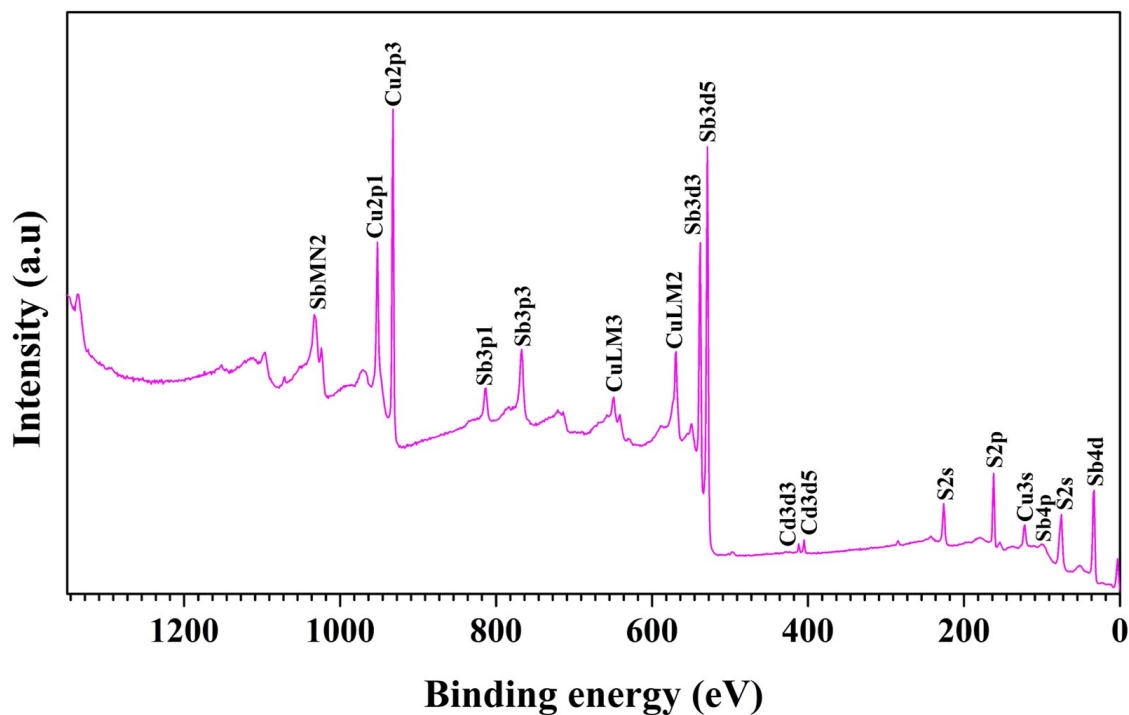
Figure 4.6: Survey spectrum of glass/ITO/n-CdS/p-CuSbS$_2$ PV device pre-annealed RTP at 400 °C for 5 min (after Ar$^+$ ion etching).
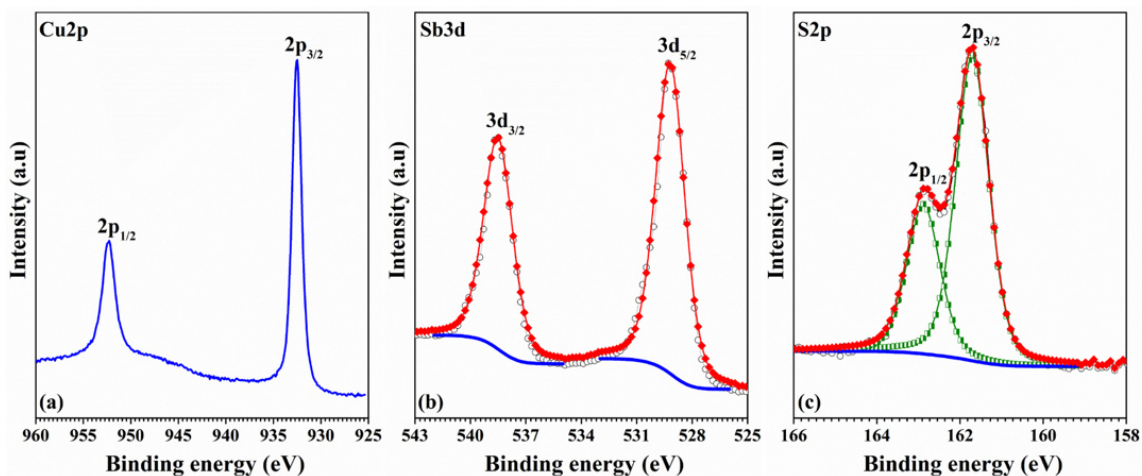
Figure 4.7: X-ray photoelectron spectroscopy of glass/ITO/n-CdS/p-CuSbS$_2$ PV device pre-annealed RTP at 400 °C for 5 min (after Ar$^+$ ion etching), (a) Cu2p core level (b) Sb3d core level (c) S2p core level.

External Quantum Efficiency (EQE) of the champion device formed by pre-annealed RTP is shown in Figure 4.4 [180]. A 300 nm thick CuSbS$_2$ absorber layer

can absorb almost 95% of the incident light owing to its higher absorption coefficient (10^5 cm^{-1}). Our champion cell shows J_{sc} value 1.3 mA/cm^2 which is in contrast to the data reported by NREL where the simulation data predicted a J_{sc} value of 15 mA/cm^2 for a 300 nm CuSbS$_2$ absorber layer assuming the standard photon flux values [85, 146]. From the given EQE data (Figure 4.4), 10 - 12% in the short wavelength region 400 - 500 nm which may be dominated by the optical absorption due to CdS. Our solar cell shows an EQE of less than 5% in the long-wavelength range which also contradicts the carrier generation by absorbing almost 95% of the incident light. The low J_{sc} in the range of 1.3 - 2.3 mA/cm^2 is in correlation with the low EQE of our PV devices. The lower EQE than expected implies a higher carrier recombination rate in and out of the space charge region. These observations demand further improvements in the CuSbS$_2$ absorber quality by reducing the grain boundaries and bulk defects including Cu$_2$S, Sb$_2$S$_3$ etc. Further requirement is to find appropriate ohmic contacts for such PV cells.

Figure 4.5 [180] shows the GIXRD patterns of champion device formed by pre-annealed RTP where the major peaks of the GIXRD pattern are identified as reflections of CuSbS$_2$, matching with that of the respective JCPDS data shown in the same figure. A few minor peaks of crystallized Sb$_2$S$_3$ and Cu$_2$S phases are also observed as marked in the figure. Such impurity phases are detrimental to the PV device as seen from the EQE curve. However, the major phase of the cell still remains as CuSbS$_2$ with a high order of crystallinity. Removing the Sb$_2$S$_3$ and Cu$_2$S impurity phases from the cell may probably help in increasing the conversion efficiency of the device.

The complete analysis of the elemental composition and their respective chemical states for the champion cell (glass/ITO/n-CdS/p-CuSbS$_2$) formed by pre-annealed RTP at 400 °C for 5 min were identified using the high-resolution spectra. The deconvolution of the high-resolution spectra was done by applying a shirley type background calculation. The survey spectrum and the high-resolution spectra of Cu2p, S2p and Sb3d of same sample recorded from the depth after first etching cycle at

a rate of 1.19 nm/s using 2 keV Ar$^+$ ions are presented in Figure 4.6 and Figure 4.7(a-c) respectively.
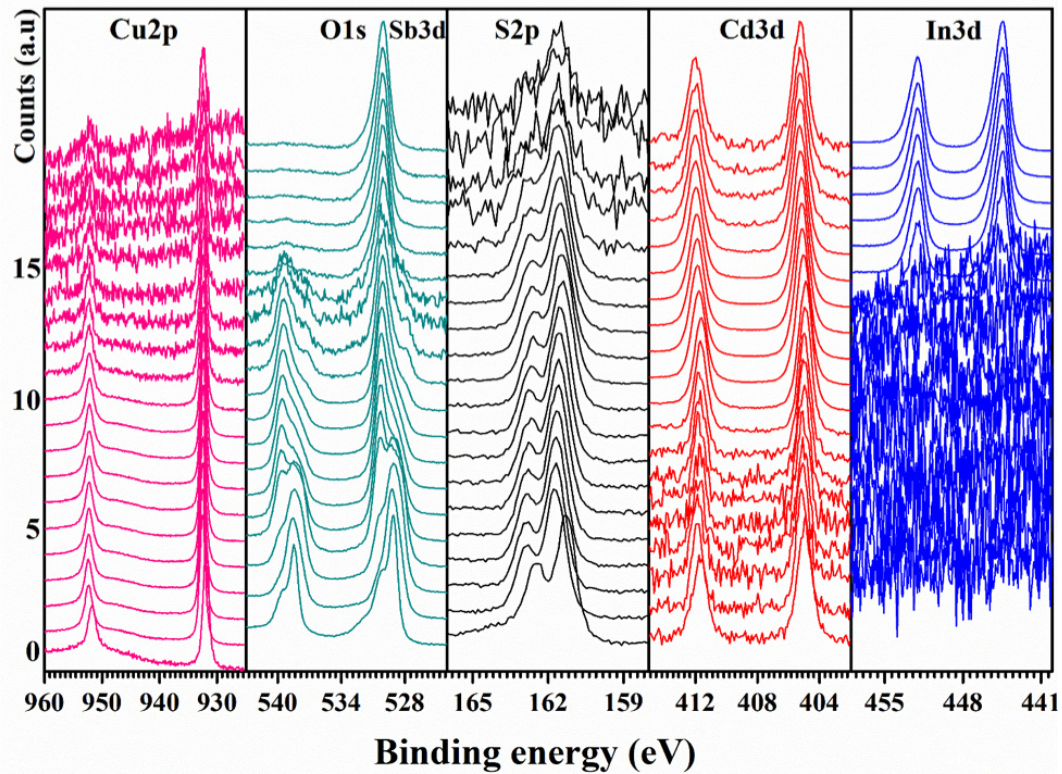
Figure 4.8: Depth profile of glass/ITO/n-CdS/p-CuSbS₂ PV device pre-annealed RTP at 400 °C for 5 min. (`https://doi.org/10.1016/j.solmat.2017.02.005`)

glass/ITO/n-CdS/p-CuSbS₂ sample consists only peaks corresponding to Sb, S and Cu as shown in Figure 4.6 confirming that, the sample was composed of only desired elements. For the detailed analysis, a narrow scan was done for Sb and S, after one cycle of etching using Ar$^+$ ions. Figure 4.7 shows the Cu2p, Sb3d and S2p spectra of the same sample. The Cu2p$_{3/2}$ and 2p$_{1/2}$ peaks possess binding energy values of 952.2 eV and 932.4 eV whereas the high-resolution spectrum of Sb is constituted by Sb3d$_{5/2}$ and Sb3d$_{3/2}$ located at 538.69 and 529.3 eV respectively. The 2p$_{3/2}$ and 2p$_{1/2}$ peaks from sulfur are observed at BE values of 162.9 and 161.7 eV. All the binding energies of the individual peaks from Sb, S and Cu match well with the previously reported BE values for the ternary CuSbS₂ system and therefore confirm the chemical composition of the deposited thin films [86, 151, 166]. Figure
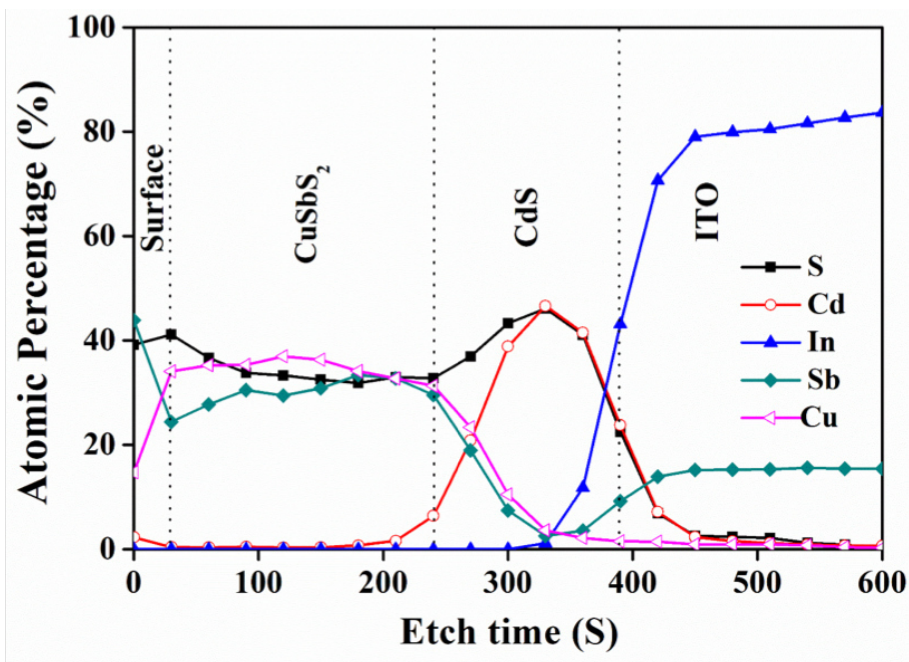
Figure 4.9: XPS profile montage of glass/ITO/n-CdS/p-CuSbS$_2$ PV device pre-annealed RTP at 400 °C for 5. Reused with kind permission from Elsevier (`https://doi.org/10.1016/j.solmat.2017.02.005`).

4.8 [180] and Figure 4.9 [180] shows the depth profile and composition montage by the XPS analysis of the PV device. Formation of CuSbS$_2$ absorber layer with uniformly distributed Cu, Sb and S and the interface of is clearly distinguished from the compositional analysis. In direct RTP CuSbS$_2$ samples, Sb deficient near surface layer implied the insufficient time for the interlayer diusion to achieve uniform composition, hence reducing the performance of the respective device (Figure 4.10). In the case of 380 °C annealed device, uniform composition was achieved (Figure 4.11). However, insufficient temperature may inhibit further grain growth. The morphology of the pre-annealed RTP sample is shown in Figure 4.12 [180]. Improved grain growth with less voids are observed for this resulted film. There for we can conclude that, in the case of combined process of annealing and RTP, uniform composition and higher grain growth may be promoted which in turn can cause devices with improved performance. However, the device surface likely to show low film density after the RTP which could also reduce the J_{sc} value of the PV devices due to poor
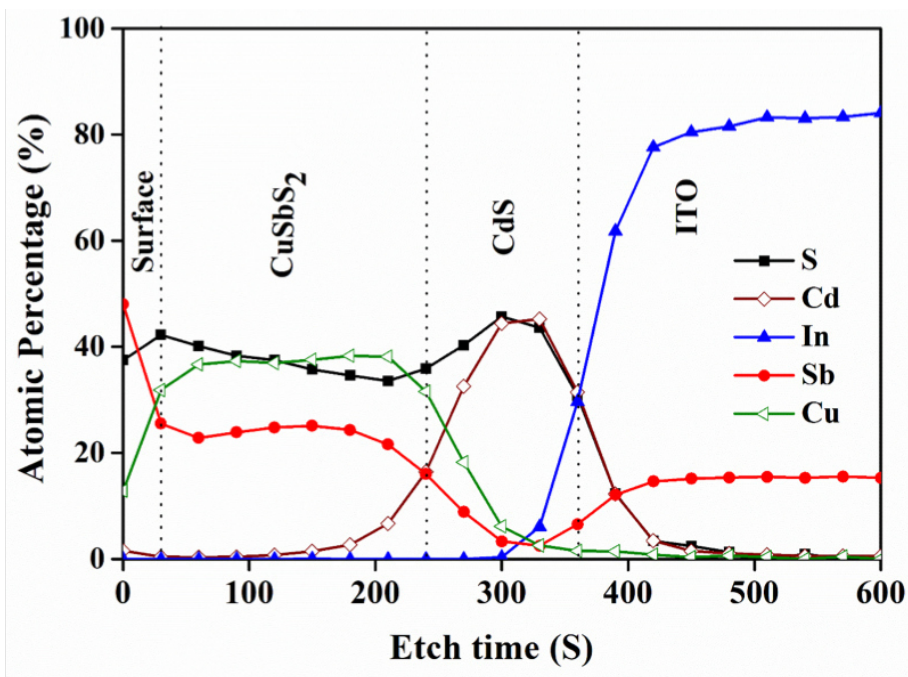
Figure 4.10: XPS profile montage of glass/ITO/n-CdS/p-CuSbS$_2$ PV device heated in RTP at 400 °C .
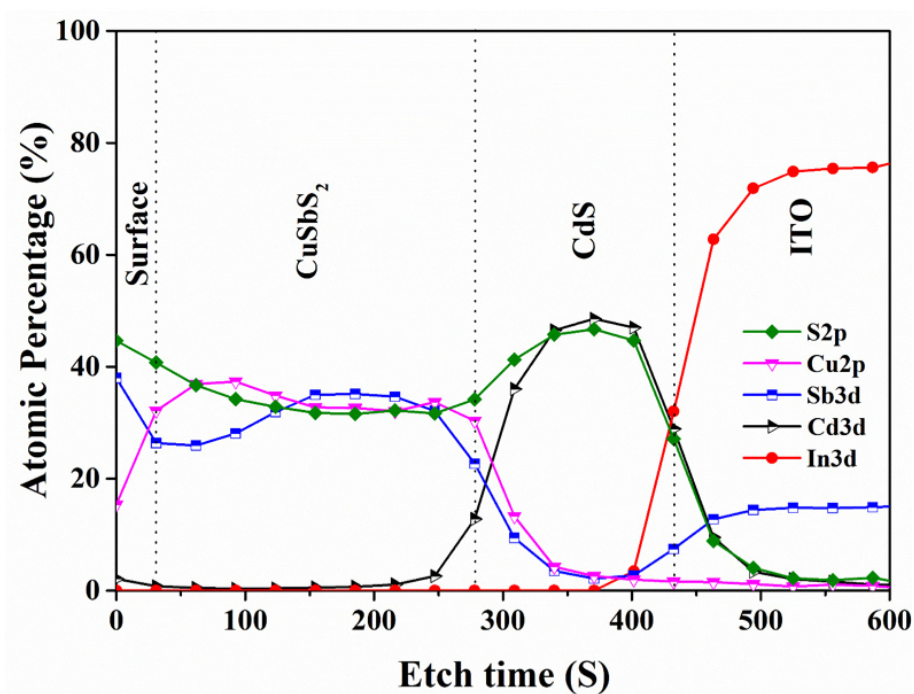
Figure 4.11: XPS profile montage of glass/ITO/n-CdS/p-CuSbS$_2$ PV device annealed at 380 °C for 45 min in conventional vacuum oven.
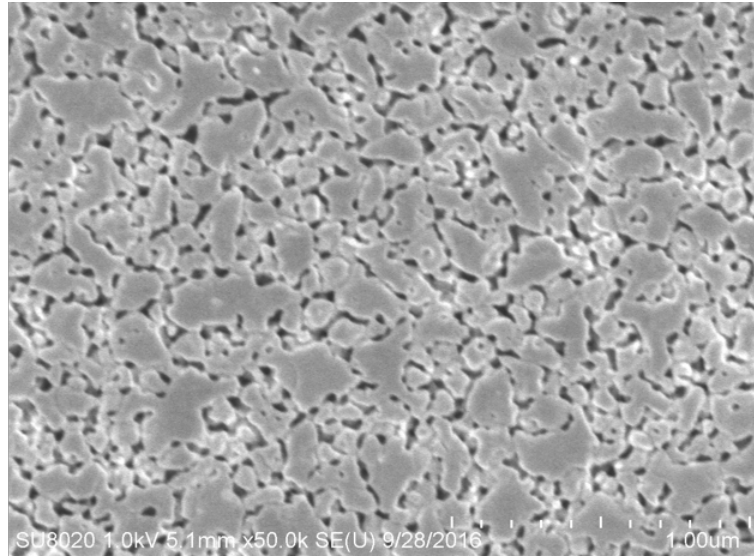
Figure 4.12: Scanning electron microscopy image of glass/ITO/n-CdS/p-CuSbS₂ PV device pre- annealed RTP at 400 °C for 5. Reused with kind permission from Elsevier (`https://doi.org/10.1016/j.solmat.2017.02.005`).

surface contacts.

4.3.1.2 Influence of Sb/Cu thickness

For further improvement of the solar cell properties, the thicknesses of the absorber layer were varied by Sb₂S₃ CBD duration (was changed from 2 to 4 and 8 h) while simultaneously varying the Cu layer thickness (25, 50 and 75 nm). Based on the property studies of these films (chapter 3), it is clearly evident that a Cu thickness of above 25 nm is necessary for the formation of the CuSbS₂ phase sacrificing the Sb₂S₃ phase. Based on these results, various photovoltaic structures using CAS Cu-50 and Cu -75 nm thin films (for both Sb₂S₃ CBD durations) as absorber and CdS thin films as window layers were prepared. Sequentially deposited glass/TCO/CdS/Sb₂S₃/Cu layer structures of Cu 50 nm and Cu 75 nm were annealed at conventional vacuum oven at 350 °C for 30 min to form PV junctions of type glass/TCO/n-CdS/p-CuSbS₂ . The J-V measurements were used for the characterization of the various PV structures. Figure 4.13 shows the J-V curves of the PV devices glass/ITO/n-
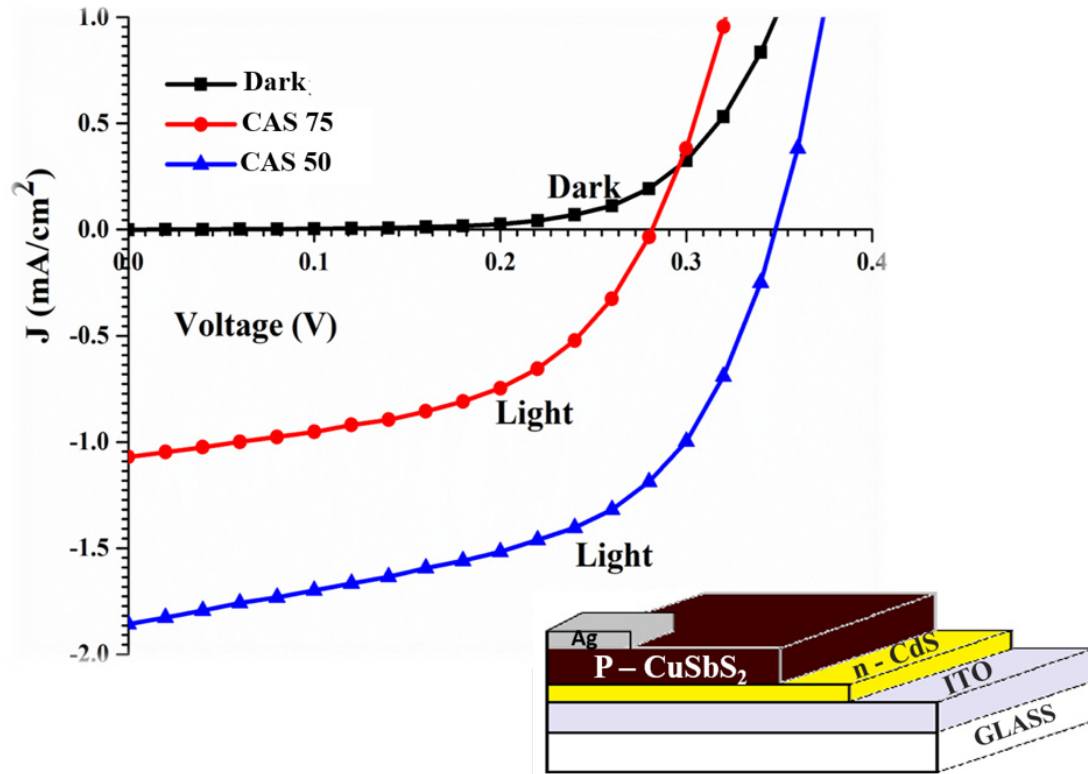
Figure 4.13: Evaluation of J-V characteristics of the glass/ITO/n-CdS/p-CuSbS$_2$ PV devices using CAS Cu-50 and Cu 75nm films fabricated by annealing at 350 °C for 30 min where the Sb$_2$S$_3$ layer thickness kept constant (CBD kept constant for 4 h).

CdS/p-CuSbS$_2$ annealed at 350 °C for 30 mins in vacuum oven (10^{-3} Torr) with varying Cu thickness: 50 and 75nm by keeping the CBD bath of Sb$_2$S$_3$ for 4 h at 25 °C. For the J-V measurements, the contacts were made of silver paint and the active device area was 25 mm^2. As seen in Figure 4.13, the PV device: glass/ITO/n-CdS/p-CuSbS$_2$ having Cu layer thickness of 50 nm showed better PV properties (V_{oc} : 0.348 V, J_{sc} : 1.86 mA/cm^2, FF : 0.58, η : 0.38%) than of CAS Cu 75 nm. The J-V curves of the PV devices glass/ITO/n-CdS/p-CuSbS$_2$ annealed at 350 °C for 30 mins in vacuum oven (10^{-3} Torr) with varying Cu thickness: 50 and 75nm by keeping the CBD bath of Sb$_2$S$_3$ for 8 h at 25 °C is shown in Figure 4.14. The PV device: glass/ITO/n-CdS/p-CuSbS$_2$ having Cu layer thickness of 50 nm showed V_{oc} : 0.261 V and J_{sc} : 0.7 mA/cm^2 for PV device having Cu layer thickness of 75
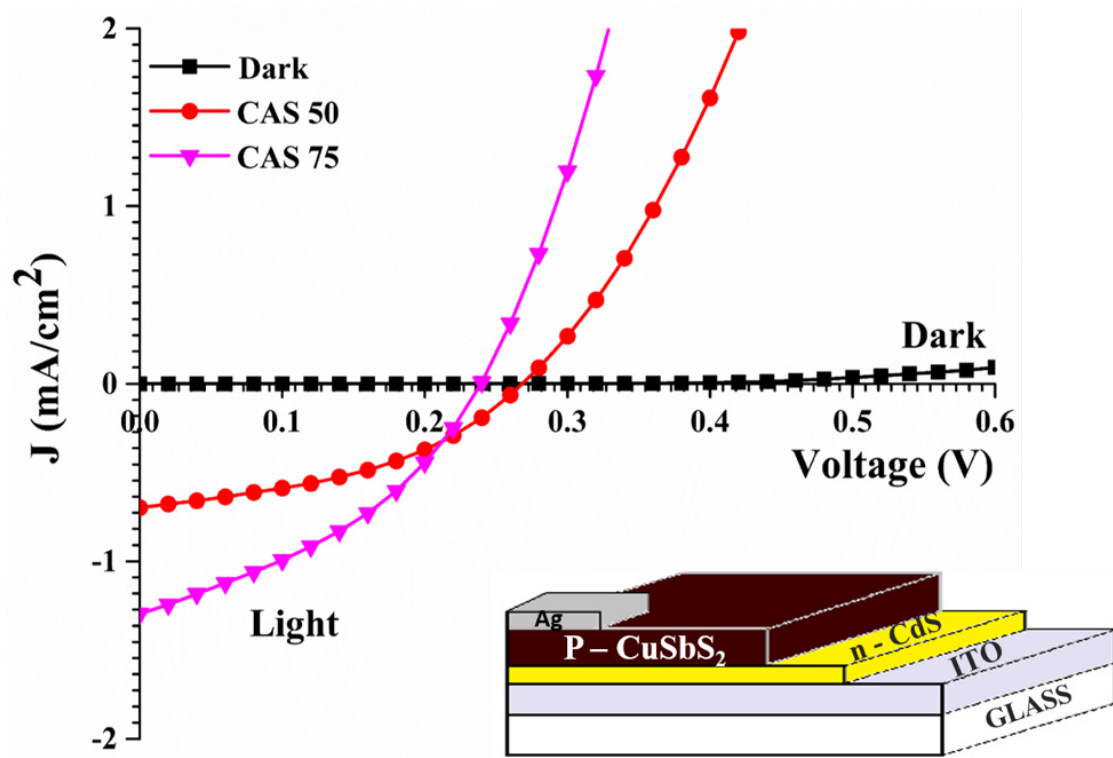
Figure 4.14: Evaluation of J-V characteristics of the glass/ITO/n-CdS/p-CuSbS$_2$ PV devices using CAS Cu-50 and Cu 75 nm films fabricated by annealing at 350 °C for 30 min where the Sb$_2$S$_3$ layer thickness kept constant (CBD kept constant for 8 h).

nm showed V_{oc} : 0.237 V and J_{sc} : 1.27 mA/cm^2. Based on the JV characteristics, the PV device: glass/ITO/n-CdS/p-CuSbS$_2$ having Cu layer thickness of 50 nm by keeping the CBD bath of Sb$_2$S$_3$ for 4 h at 25 °C were annealed at conventional vacuum oven at 350 °C for 30 minutes, showed better photovoltaic characteristics. Therefore, further characterization was done for the same one (best cell).

The GIXRD pattern of the best cell formed by annealing glass/ITO/n-CdS/p-CuSbS$_2$ (Cu layer thickness of 50 nm by keeping the CBD bath of Sb$_2$S$_3$ for 4 h at 25 °C) in conventional vacuum oven at 350 °C for 30 minutes is shown in Figure 4.15. As seen in the figure, the major peaks of the GIXRD pattern of the PV device are identified as reflections corresponding to the crystal planes of orthorhombic CuSbS$_2$, according to the JCPDS data shown in the same figure. In addition to this, a few

minor peaks of crystallized Sb_2S_3 and Cu_2S phases are also observed. Nevertheless, the major phase of the cell still remains as $CuSbS_2$ with a high order of crystallinity. These structural characterization results are comparable with that of the PV cell obtained by pre-annealed RTP technique.

Figure 4.15: GIXRD of the of glass/ITO/n-CdS/p-CuSbS₂ PV device using CAS Cu-50 film fabricated by annealing at 350 °C for 30 min where the Sb₂S₃ layer thickness kept constant (CBD kept constant for 4 h).

The complete analysis of the elemental composition and their respective chemical states for glass/ITO/n-CdS/p-CuSbS₂ cell formed by films annealed at 350°C for 30 min was identified using the high-resolution spectra. The high-resolution spectra of Cu2p, S2p and Sb3d of the cell recorded from the depth after first etching cycle are presented in Figure 4.16. The Cu2p spectrum shows a 2p doublet corresponding to 2p₃/₂ and 2p₁/₂ at B.E. values 952.1 and 931.8 eV respectively. Figure 4.16(a) and

Figure 4.16(b) illustrate spin-orbit coupled Sb3d major peaks at 538.6 eV (Sb3d$_{5/2}$) and 537.99 eV (Sb3d$_{3/2}$). The B.E of the sulfur peaks S2p$_{3/2}$ at 160.9 eV and S2p$_{1/2}$ at 162.1 eV is given as noted in Figure 4.16(c). All these B.Es are in is consistent with those reported for CuSbS$_2$thin films deposited on glass substrates reported on previous chapter.
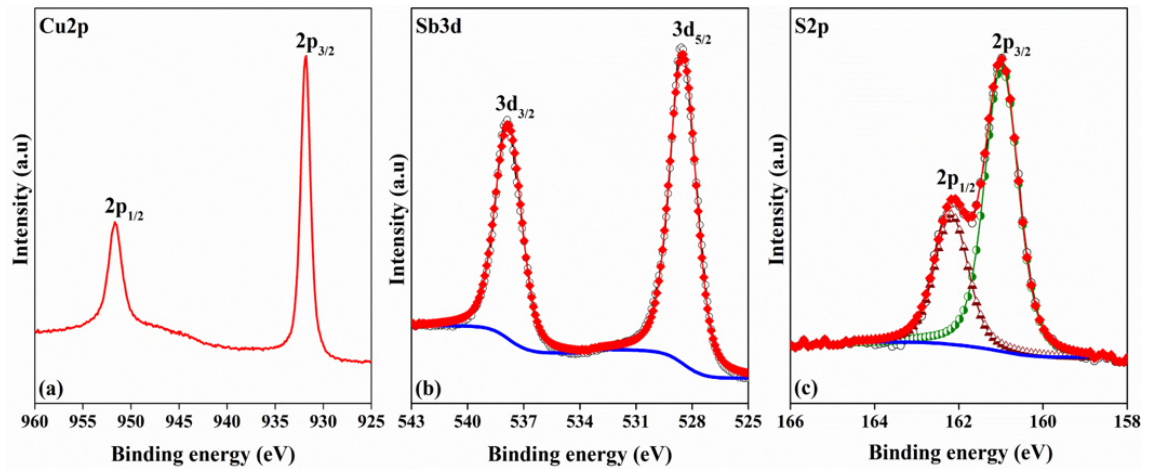
Figure 4.16: X-ray photoelectron spectroscopy of glass/ITO/n-CdS/p-CuSbS$_2$ PV device annealed at 350 °C for 30 min (after Ar$^+$ ion etching), (a) Cu2p core level (b) Sb3d core level (c) S2p core level.

The B.E profile montage and the respective composition analysis of the same sample is presented in Figure 4.17 and Figure 4.18. Analysis of the depth profile data showed uniformity of the Cu, Sb and S elements throughout the depth of the film. In analogous to the pre-annealed RTP cell (refer to Figure 4.8), here the diffusion of Cd into the whole sample is not observed as the compositional analysis does not show the presence of Cd until the etching time reaches around 300 s. On the other hand, diffusion of Cu into the underlying Sb$_2$S$_3$ layer during the annealing step accounts for the formation of the ternary CuSbS$_2$ phase. It can be easily identified from the Figure 4.18 that the sample is mainly constituted by CuSbS$_2$ above ITO/CdS layers from the strong signals from Sb, S and Cu.

The morphology of the glass/ITO/n-CdS/p-CuSbS$_2$ PV device fabricated by annealing at 350 °C for 30 min (Sb$_2$S$_3$ CBD bath for 4 h at 25 °C, Cu layer thicknesses
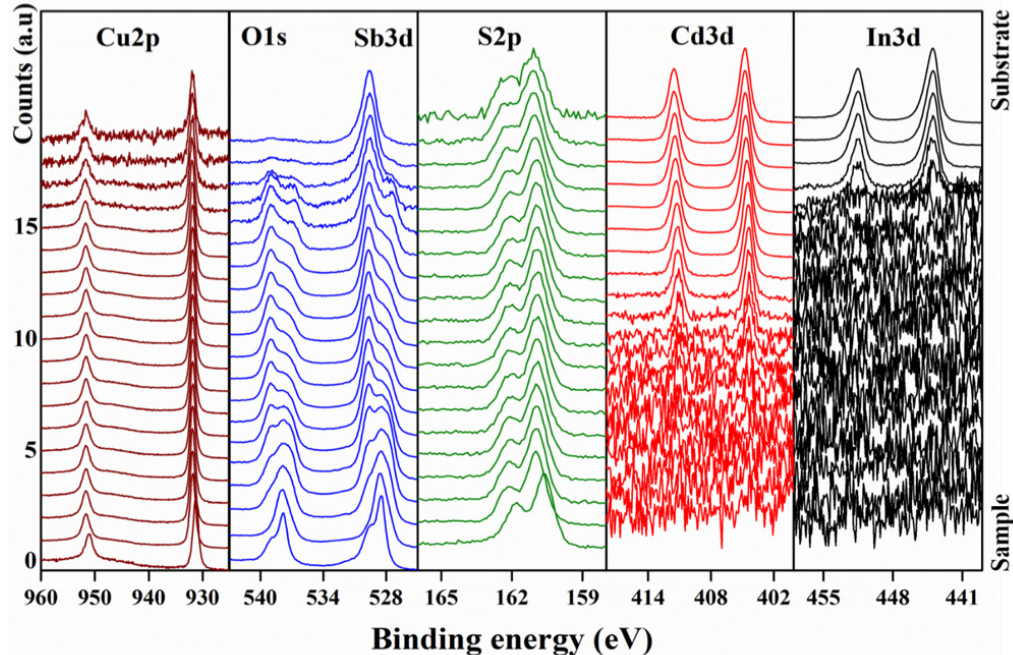
Figure 4.17: Depth profile of glass/ITO/n-CdS/p-CuSbS$_2$ PV device using CAS Cu-50 film fabricated by annealing at 350 °C for 30 min where the Sb$_2$S$_3$ layer thickness kept constant (CBD kept constant for 4 h).

50 nm) is shown in Figure 4.19. As seen in figure, the surface is composed of elongated grains which are continuous and interconnected uniformly. Bigger grains of irregular shapes occupy the majority of the surface area thereby forming lesser voids on the sample surface. Therefore we can conclude that, in the case of glass/ITO/n-CdS/p-CuSbS$_2$ PV device fabricated by annealing at 350 °C for 30 min (Sb$_2$S$_3$ CBD for 4 h at 25 °C, Cu 50 nm), uniform composition and enhanced grain growth are promoted which in turn may lead to devices with improved performance.

To study the effect of Cu layer thickness on the properties of PV devices, Sb$_2$S$_3$ CBD duration was kept constant for 4 h (since the better cell properties were observed for this condition) while simultaneously varying the Cu layer thickness. Figure 4.20 shows the J-V characteristics of the glass/ITO/n-CdS/p-CuSbS$_2$ PV devices using varying Cu thicknesses 5, 10, 20 and 50 nm fabricated by annealing at 350 °C for 30 min where the Sb$_2$S$_3$ layer thickness kept constant (CBD kept
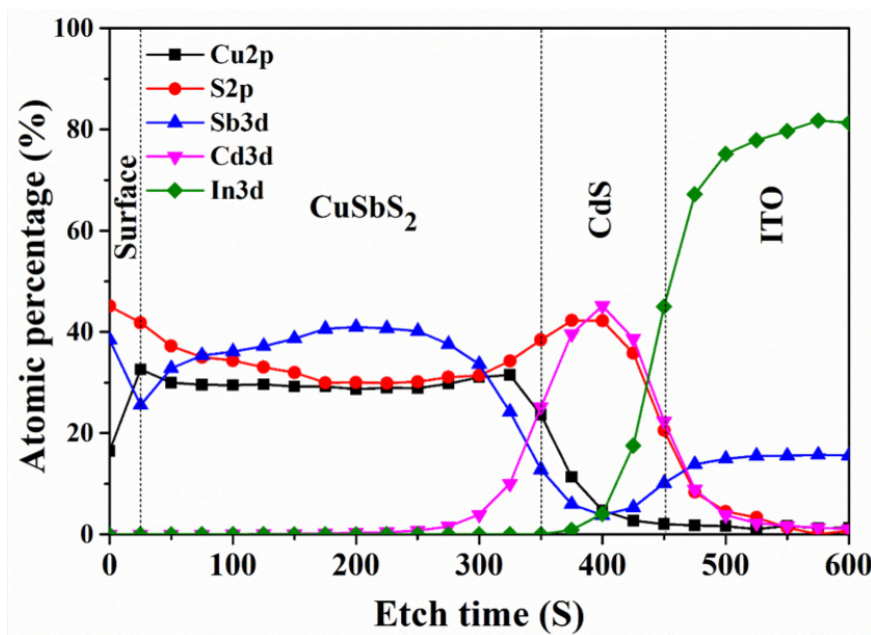
Figure 4.18: XPS profile montage of glass/ITO/n-CdS/p-CuSbS$_2$ device using CAS Cu-50 film by annealing at $350\,^{\circ}$C for 30 min where the Sb$_2$S$_3$ bath duration was for 4 h.
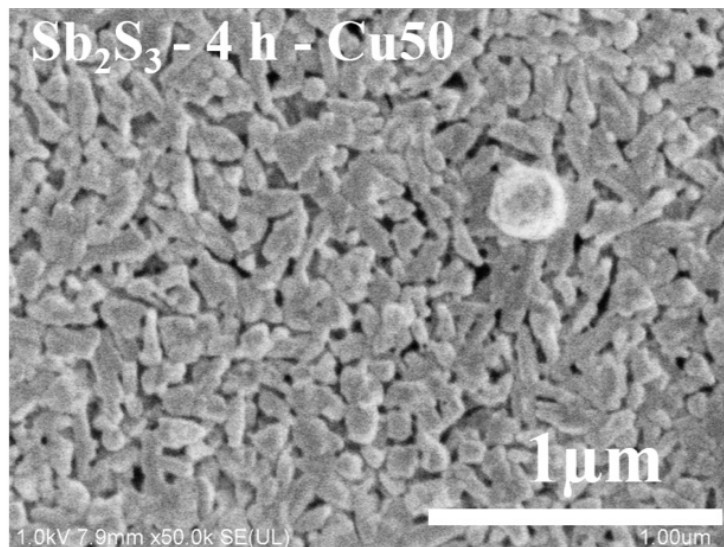
Figure 4.19: Scanning electron microscopy image of glass/ITO/n-CdS/p-CuSbS$_2$ PV device using CAS Cu-50 film fabricated by annealing at $350\,^{\circ}$C for 30 min where the Sb$_2$S$_3$ layer thickness kept constant (CBD kept constant for 4 h at $25\,^{\circ}$C).
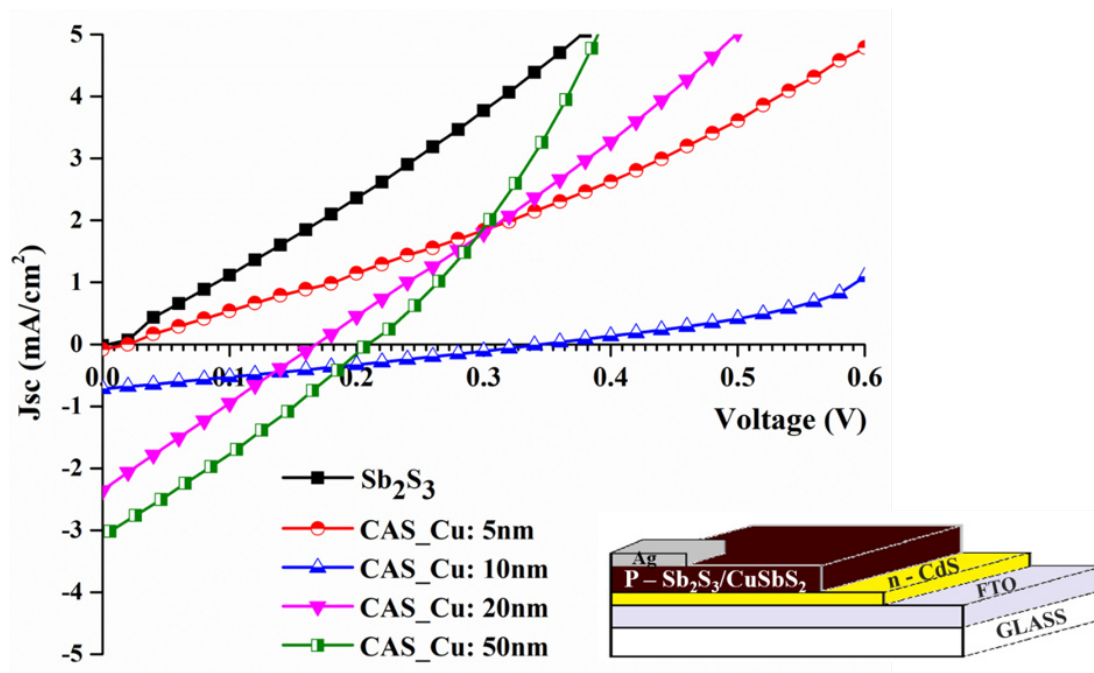
Figure 4.20: Evaluation of J-V characteristics of the glass/FTO/n-CdS/p-CuSbS$_2$ /Ag devices using varying Cu thicknesses 5, 10, 20 and 50 nm fabricated by annealing at 350 °C for 30 min where the Sb$_2$S$_3$ layer thickness kept constant (CBD kept constant for 4 h). J-V characteristics of glass/FTO/n-CdS/Sb$_2$S$_3$ is also included in the figure for reference.

constant for 4 h). J-V characteristics of glass/FTO/n-CdS/Sb$_2$S$_3$ is also included in the figure for comparison. For the J-V measurements, the contacts were made of silver paint and the active device area was 25 mm^2. Photovoltaic parameters of (glass/FTO/n-CdS/p-CuSbS$_2$/Ag) all solar cells are tabulated in Table 4.2. Among all cells, better PV properties were shown by glass/FTO/n-CdS/p-CuSbS$_2$/Ag with Cu 50 nm thickness V_{oc} : 0.207 V, J_{sc} : 3.0139 mA/cm^2, FF : 21.7% and efficiency (η) : 0.14%. External Quantum Efficiency (EQE) of the glass/FTO/n-CdS/Sb$_2$S$_3$ and glass/ITO/n-CdS/p-CuSbS$_2$ PV devices having various Cu thicknesses 5, 10, 20 and 50 nm fabricated by annealing at 350 °C for 30 min is shown in Figure 4.21.

As we observed in the case of the champion cell (EQE data (Figure 4.4)), here for glass/FTO/n-CdS/p-CuSbS$_2$/Ag with Cu 50 and 20 nm solar cells, EQE

Table 4.2: Photovoltaic parameters of glass/FTO/n-CdS/p-Sb$_2$S$_3$/Ag and glass/FTO/n-CdS/p-CuSbS$_2$/Ag solar cells with varying Cu thicknesses 5, 10, 20 and 50 nm formed by annealing at 350 °C for 30 min.

PV device (glass/FTO/CdS/Sb$_2$S$_3$/CuSbS$_2$)	V_{oc} (V)	J_{sc} (mA/cm^2)	FF
glass/FTO/CdS/Sb$_2$S$_3$	0.02	0.02	0.25
glass/FTO/CdS/CuSbS$_2$:Cu 5nm	0.02	0.05	0.26
glass/FTO/CdS/CuSbS$_2$:Cu 10nm	0.35	0.68	0.27
glass/FTO/CdS/CuSbS$_2$:Cu 20nm	0.17	2.37	0.25
glass/FTO/CdS/CuSbS$_2$:Cu 50nm	0.21	3.01	0.22

10 - 12% in the short wavelength region 400 - 500 nm which may be dominated by the optical absorption due to CdS. Our solar cell shows an EQE of less than 5% in the long-wavelength range which also contradicts the carrier generation by absorbing almost 95% of the incident light. As previously explained in the case of champion cell, further improvements in the CuSbS$_2$ absorber quality by reducing the grain boundaries and bulk defects including Cu$_2$S, Sb$_2$S$_3$ etc. as well as finding appropriate ohmic contacts for these desired PV devices are required to improve its PV properties.

X-ray photoelectron spectroscopy was employed to determine the elemental composition and chemical states using a typical survey and high-resolution spectral analyses of the glass/ITO/n-CdS/p-CuSbS$_2$ PV device using CAS Cu-50 film fabricated by annealing at 350 °C for 30 min where the Sb$_2$S$_3$ layer thickness was kept constant (CBD kept constant for 4 h at 25 °C). Low-resolution survey spectra recorded from 0 to 1350 eV were used for the elemental analysis of each sample whereas high-resolution spectra of Cu, Sb, and S were used for the chemical state analysis (Figure 4.22). An extremely small amount of carbon and oxygen presence was observed for the sample from the surface due to the surface contamination in the ambient atmosphere. After a small etch from the surface, this impurity presence
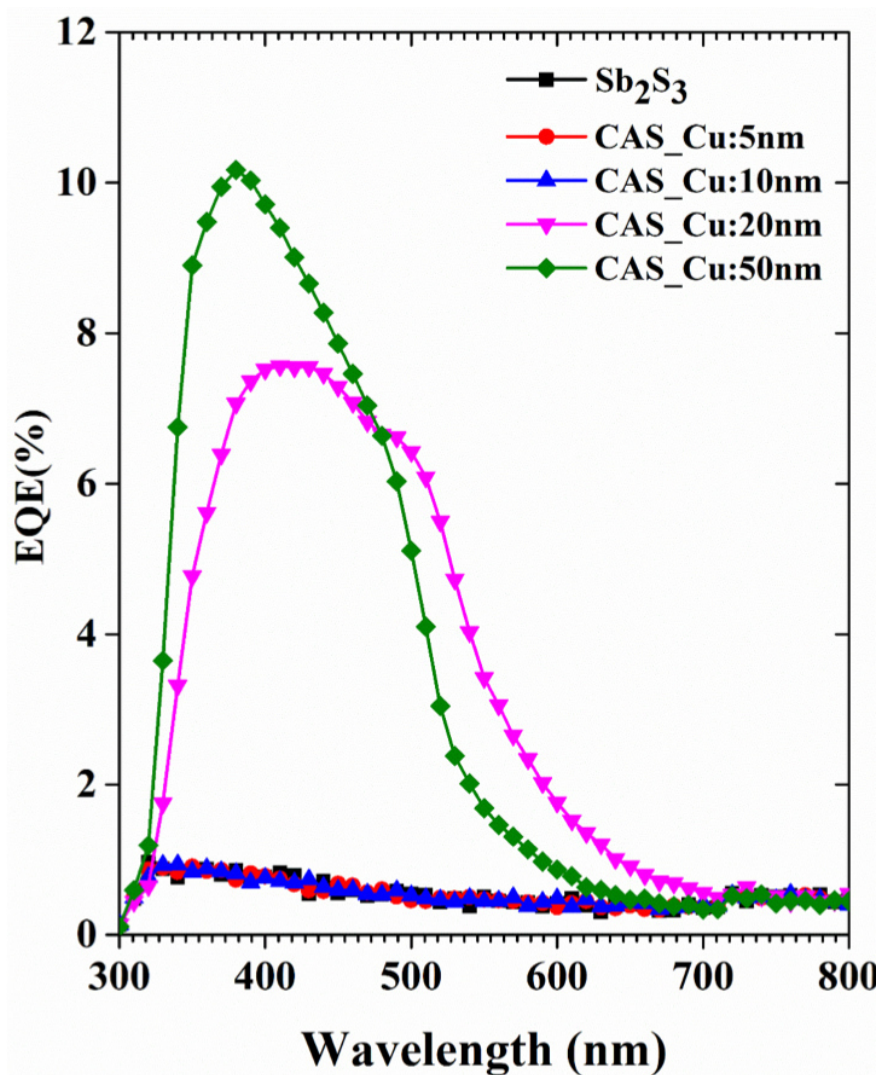
Figure 4.21: EQE measurement of glass/FTO/n-CdS/p-Sb$_2$S$_3$ and glass/ITO/n-CdS/p-CuSbS$_2$ PV devices using varying Cu thicknesses 5, 10, 20 and 50 nm fabricated by annealing at 350 °C for 30 min

was totally removed. The high-resolution scans of the same cell are shown in Figure 4.23, where the data were collected from the 1st etched surface, in order to avoid the effect of any contaminations present on the sample surface. The core-level spectrum of Cu shows a 2p doublet at binding energies 932.9 eV (2p$_{3/2}$) and 952.7 eV (2p$_{1/2}$) with a separation of 19.8 eV. Sb core level spectrum shows an excellent peak fitting with the major peaks at 529.42 eV (Sb3d$_{5/2}$) and 538.81 eV (Sb3d$_{3/2}$) (Figure 4.23(b)). The core level of sulfur showed major peaks of S2p$_{3/2}$ at 162.21 eV and
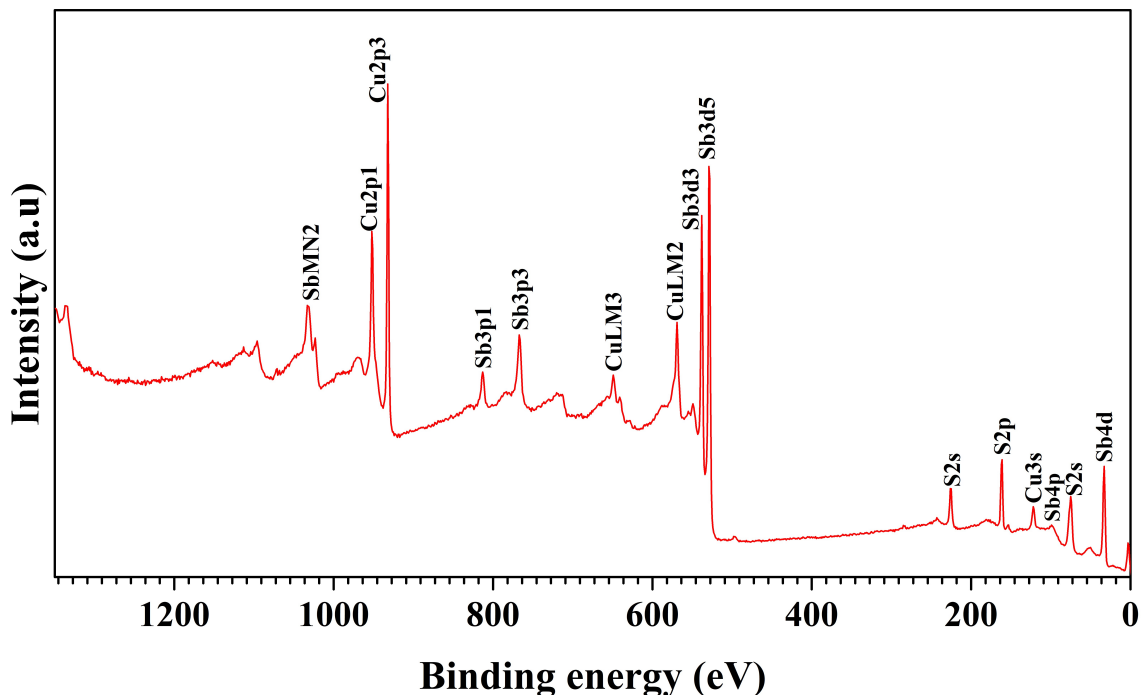
Figure 4.22: Survey spectrum of glass/FTO/n-CdS/p-CuSbS₂ PV device using CAS Cu-50 film fabricated by annealing at 350 °C for 30 min where the Sb₂S₃ layer thickness kept constant (CBD kept constant for 4 h at 25 °C).

S2p$_{1/2}$ at 163.33 eV with a separation of 1.12 eV. All the respective binding energy values of Sb, S and Cu are well matching with the previously reported BEs for the corresponding oxidation states of elements in CuSbS₂ thus confirming the formation of ternary CuSbS₂ phase [78, 152]. The B.E profile montage and the respective composition analysis of the same sample are presented in Figure 4.24 and Figure 4.25 respectively. Depth profile analysis showed the uniformity of the Cu, Sb and S elements throughout the depth of the film. In the case of CuSbS₂ samples formed by RTP at 600 °C, the surface was antimony rich in composition. The formation of the ternary CuSbS₂ phase by the interlayer diffusion of Sb₂S₃ and Cu is clearly indicated from the composition figures.

Figure 4.26 shows the SEM images together with the EDX elemental composition of glass/ITO/n-CdS/p-CuSbS₂ PV device using CAS Cu-50 film fabricated by
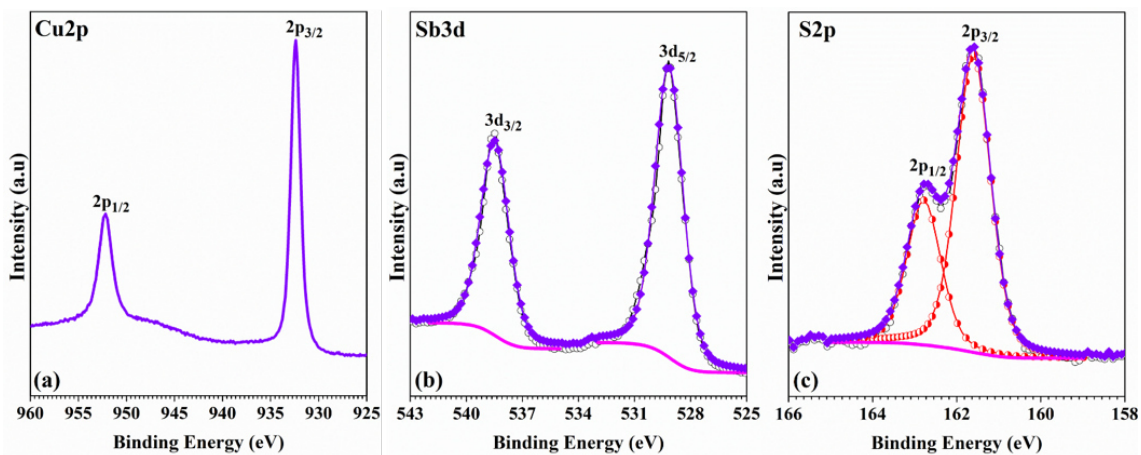
Figure 4.23: X-ray photoelectron spectroscopy of glass/FTO/n-CdS/p-CuSbS$_2$ PV device using CAS Cu-50 film fabricated by annealing at 350 °C for 30 min where the Sb$_2$S$_3$ layer thickness kept constant (CBD kept constant for 4 h at 25 °C) after Ar$^+$ ion etching, (a) Cu2p core level (b) Sb3d core level (c) S2p core level
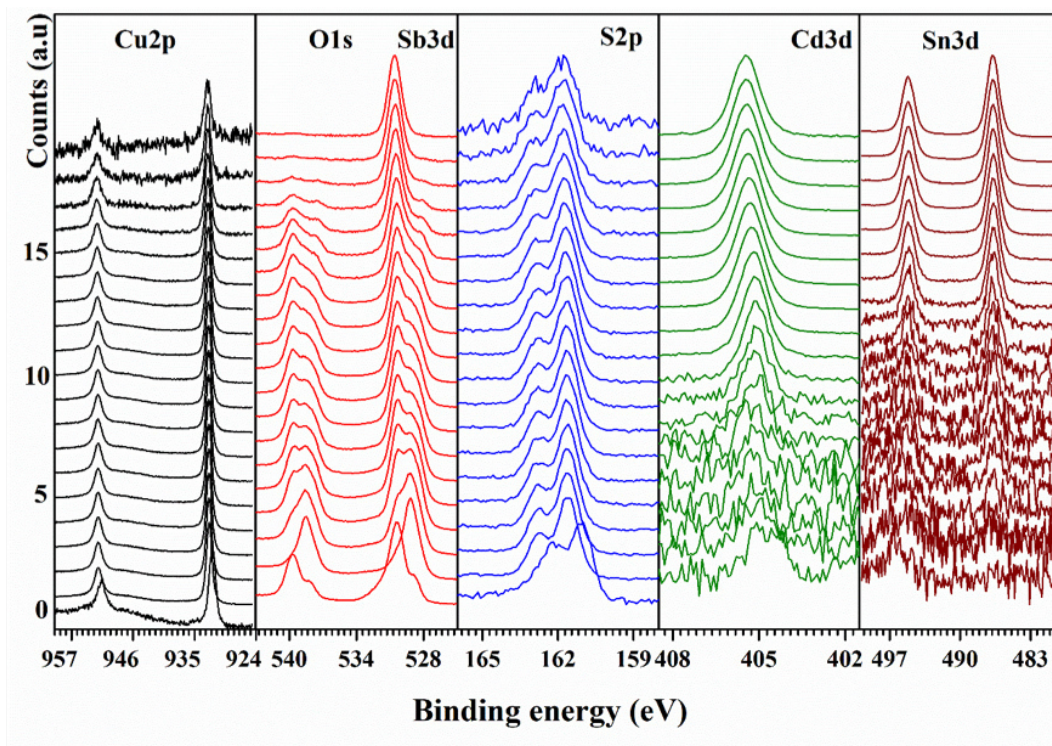
Figure 4.24: Depth profile of glass/ITO/n-CdS/p-CuSbS$_2$ PV device using CAS Cu-50 film fabricated by annealing at 350 °C for 30 min
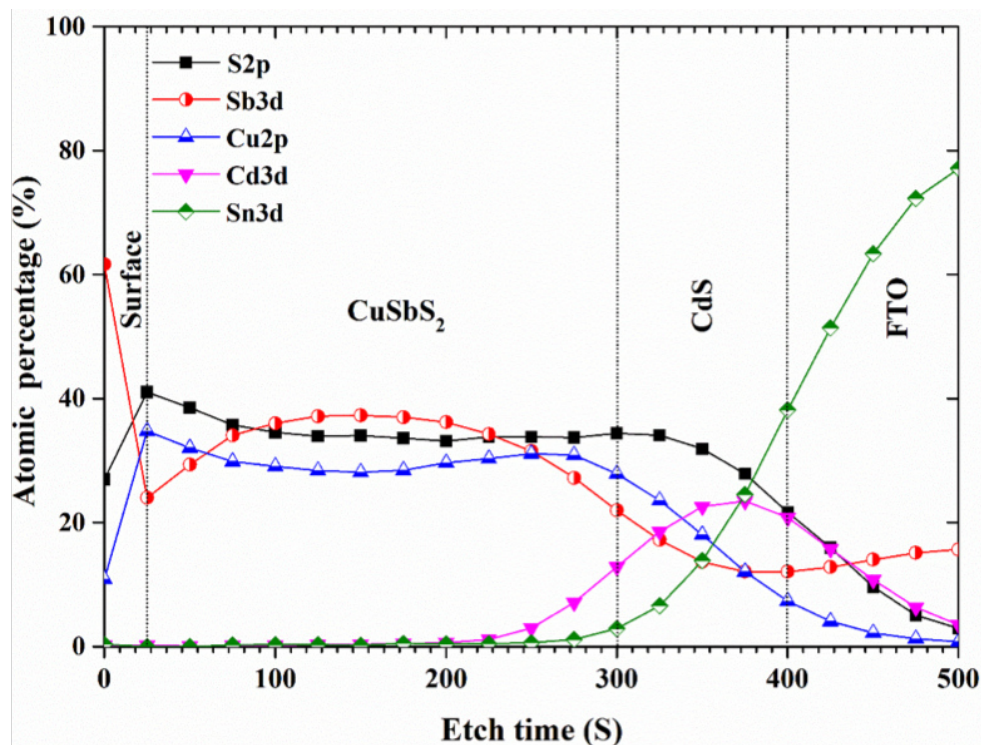
Figure 4.25: XPS profile montage of glass/FTO/n-CdS/p-CuSbS$_2$ PV device using CAS Cu-50 film fabricated by annealing at 350 °C for 30 min.
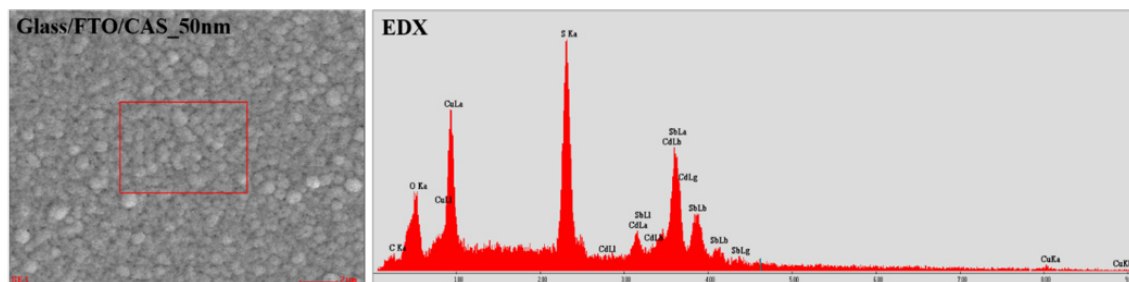
Figure 4.26: Scanning electron microscopy images and EDX elemental composition analysis of glass/FTO/n-CdS/p-CuSbS$_2$ PV device using CAS Cu-50 film fabricated by annealing at 350°C for 30 min where the Sb$_2$S$_3$ layer thickness kept constant (CBD kept constant for 4 h at 25 °C).

annealing at 350 °C for 30 min where the Sb$_2$S$_3$ layer thickness kept constant (CBD kept constant for 4 h at 25 °C). Spherical grains of different sizes constitute the surface morphology of these thin films with full surface coverage. The EDX spectrum of the same PV device was also collected to determine the elemental composition. The

major peaks in the EDX spectrum were corresponding to the characteristic X-rays of Sb, S, and Cu together with adventitious C and O indicating that the sample is composed of only the desired elements. The EDX elemental mapping of the solar cell (Figure 4.27) revealed the uniform distribution of each element such as Sb, S and Cu on the surface without any other impurities. Both the SEM images and EDX mapping data confirm the formation of the CuSbS$_2$ absorber layer in the PV device and its spherical uniform surface morphology.

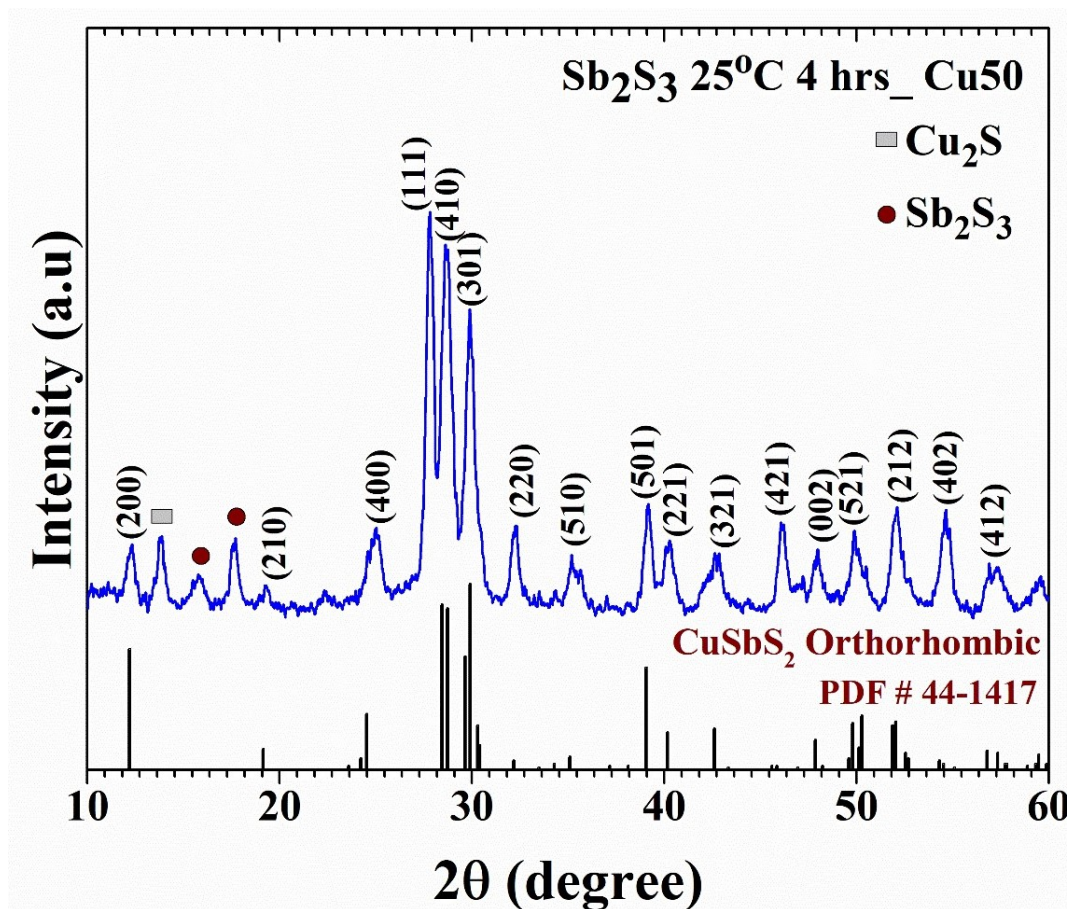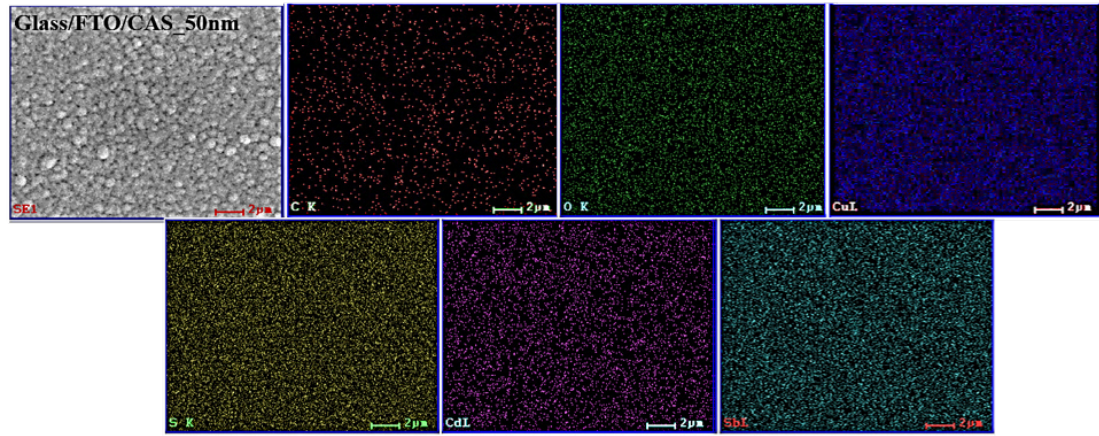Figure 4.27: EDX mapping for CuSbS$_2$ thin film formed analysis of glass/FTO/n-CdS/p-CuSbS$_2$ PV device using CAS Cu-50 film fabricated by annealing at 350 °C for 30 min where the Sb$_2$S$_3$ layer thickness kept constant (CBD kept constant for 4 h at 25 °C).

Superstrate p-i-n configuration

To further improve the photovoltaic parameters, a very thin intrinsic layer of Sb$_2$S$_3$ between n-CdS and p type CuSbS$_2$ was implemented. The advantage of introducing such an intrinsic layer between p and n layer is that it can widen electrostatic field region which enhances the photogenerated charge collection [197]. The p-i-n structure is preferable in devices using materials with short minority carrier diffusion length, improving J_{sc} and thus the efficiency [198].

The photovoltaic structures using CuSbS$_2$ as absorber material in a superstrate p-i-n configuration of glass/FTO/CdS/i-Sb$_2$S$_3$/CuSbS$_2$ is shown in Figure
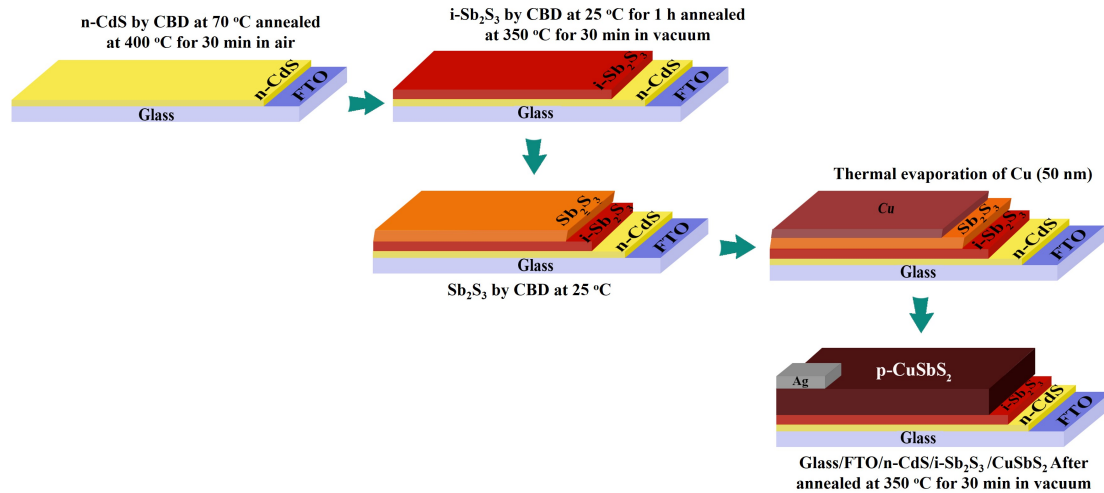
Figure 4.28: Superstrate p-i-n configuration of glass/SnO$_2$:F/(n)CdS/(i)Sb$_2$S$_3$/(p) CuSbS$_2$/Ag

4.28. Here, the window layer CdS were deposited as mentioned earlier (70 °C for 20 min). Sb$_2$S$_3$ Intrinsic layer was deposited over CdS coated FTO films by chemical bath deposition (25 °C for 1 h). The layered precursors of glass/FTO/CdS/Sb$_2$S$_3$ were annealed at 350°C for 1 h in conventional vacuum oven in order to form the crystalline phase of Sb$_2$S$_3$. From the previous results it was clearly observed that, among all the cells (p-n configuration : glass/FTO/n-CdS/p-CuSbS$_2$ which undergone just the conventional vacuum oven treatments) fabricated at different conditions, the one with 4 h Sb$_2$S$_3$ having Cu thickness 50 nm outperformed other PV devices. Hence, the same condition was selected for the fabrication of the absorber layer here in p-i-n configuration as well. The evaluation of the J-V curves under dark and illumination using the p-i-n junction configuration of glass/SnO$_2$:F/n-CdS/i-Sb$_2$S$_3$/p-CuSbS$_2$/Ag is shown in Figure 4.31. Same like in the case of PV devices having p-n configuration, For the J-V measurements, the contacts were made of silver paint where the active device area was 25 mm^2. As observed from the Figure 4.29, the PV device (glass/FTO/n-CdS/i-Sb$_2$S$_3$/p-CuSbS$_2$/Ag) formed by annealing at 350°C for 30 min showed V_{oc}= 483 mV, J_{sc}= 7.2 mA/cm^2, FF = 0.28 and the conversion efficiency (η) = 0.99%. Here, the increase in J_{sc} and thereby increase in efficiency is attributed to the use of an intrinsic layer in the device.
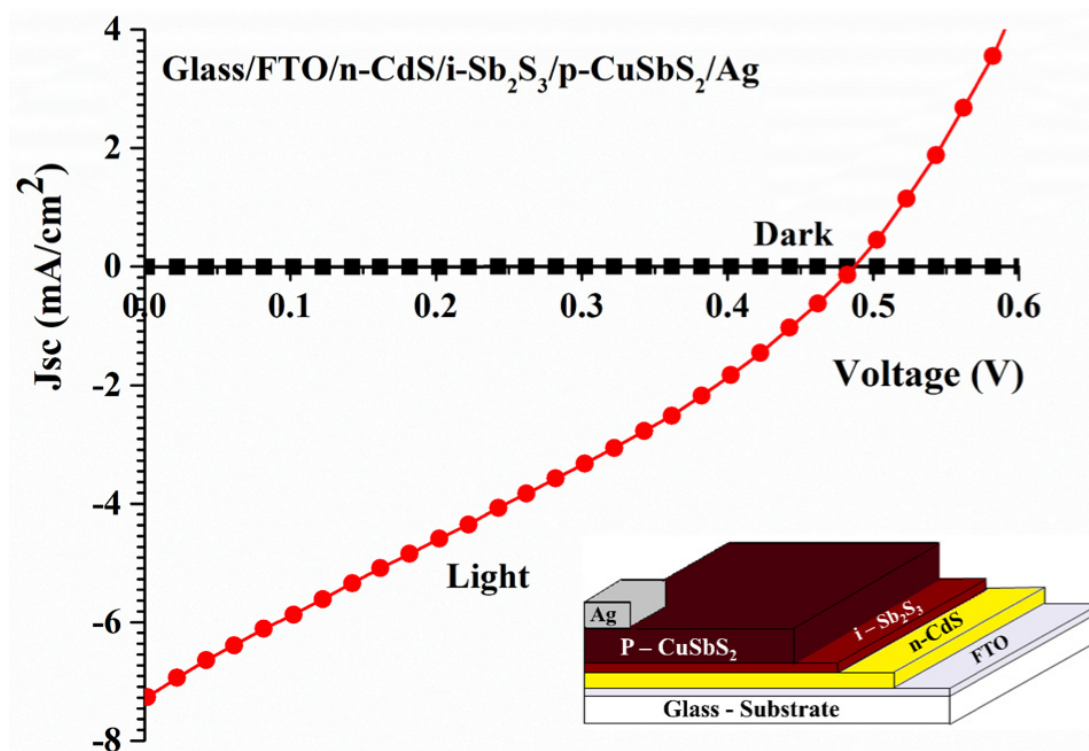
Figure 4.29: Glass/SnO$_2$:F/(n)CdS/(i)Sb$_2$S$_3$ /(p)CuSbS$_2$/Ag solar cells using CAS Cu-50 film fabricated by annealing at 350 °C for 30 min where the Sb$_2$S$_3$ layer thickness kept constant (CBD kept constant for 4 h at 25 °C).

X-ray photoelectron spectroscopy (XPS) analysis was carried out to estimate the complete analysis of the elemental composition and their respective chemical states for this cell (glass/FTO/n-CdS/i-Sb$_2$S$_3$/p-CuSbS$_2$) using the high-resolution spectra. Here also, the high-resolution spectra of Cu2p, S2p and Sb3d were recorded from the depth after the first etching cycle as presented in Figure 4.30(a), 4.30(b), and 4.30(c) respectively. As observed in Figure 4.30(a), B.E of Cu2p, Sb3d and S2pare in correlation with the repective energies in CuSbS$_2$ phase as described earlier. The layered structure of CuSbS$_2$/CdS/FTO is clear from the depth profile compositional analysis given in Figure 4.31.
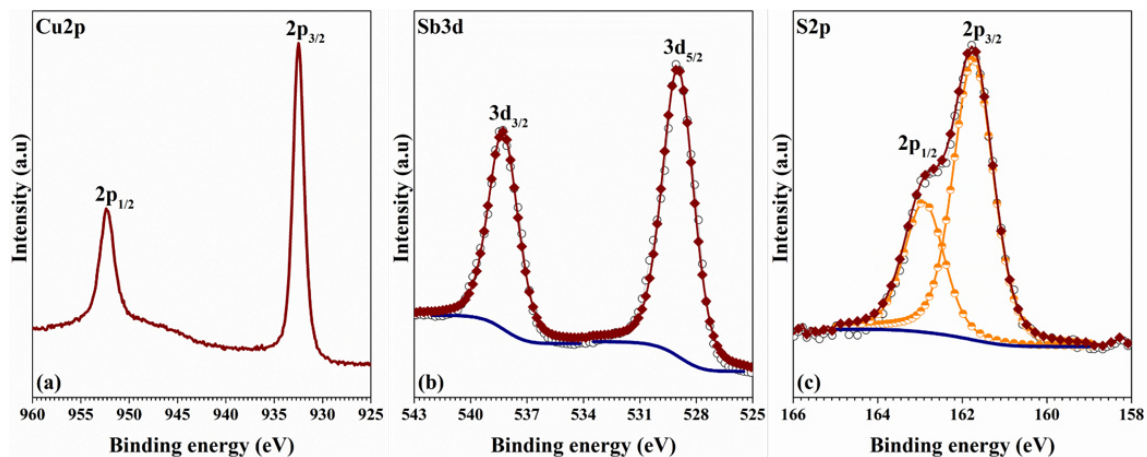
Figure 4.30: X-ray photoelectron spectroscopy of glass/SnO$_2$:F/n-CdS/i-Sb$_2$S$_3$/p-CuSbS$_2$ PV device using CAS Cu-50 film fabricated by annealing at 350 °C for 30 min after Ar$^+$ ion etching, (a) Cu2p core level (b) Sb3d core level (c) S2p core level
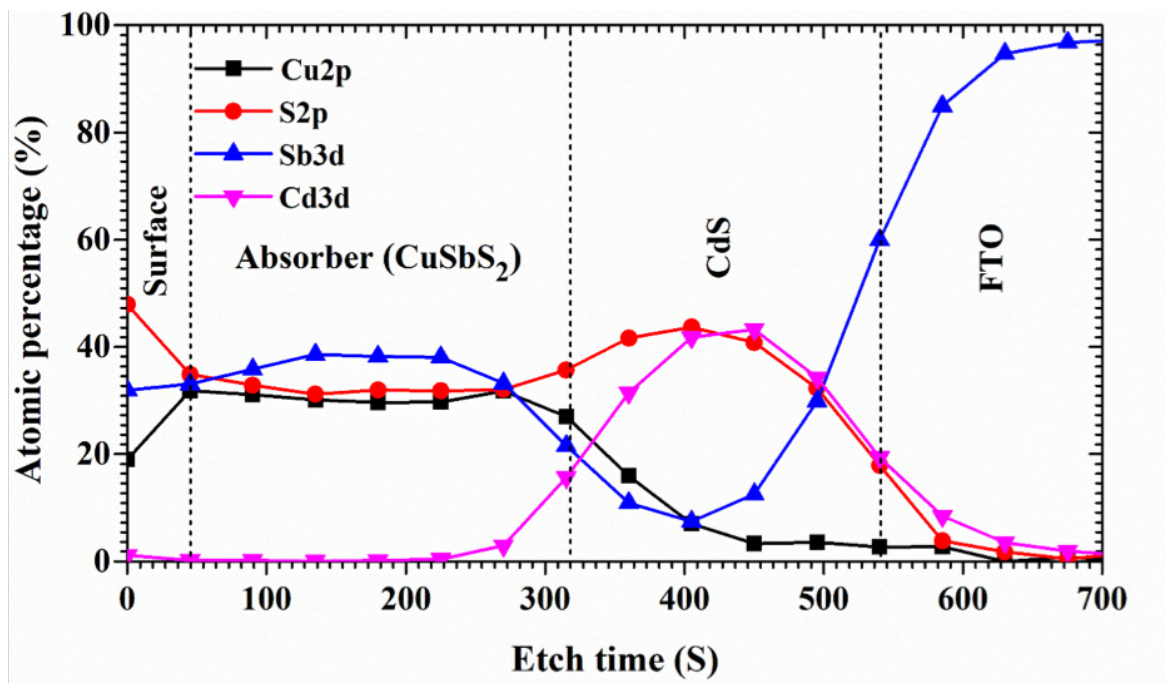
Figure 4.31: XPS profile montage of glass/SnO$_2$:F/n-CdS/i-Sb$_2$S$_3$/p-CuSbS$_2$ PV device using CAS Cu-50 film fabricated by annealing at 350 °C for 30 min

In conclusion based on all the above described results, the CuSbS$_2$ thin films (solar cells prepared on ITO using 2 h Sb$_2$S$_3$) formed were incorporated in photovoltaic structures of superstrate configuration: glass/TCO/CdS/CuSbS$_2$. The best photovoltaic parameters were V_{oc}= 0.665 V and FF = 0.62, the highest values ever reported for the CuSbS$_2$ based p-n junction solar cells, however, the J_{sc} was found to be low as 1.5 mA/cm^2. For further improvement of the J_{sc}, the Sb$_2$S$_3$ bath duration was increased to 4h and 8h simultaneously varying the Cu thickness in each case. Among the cells fabricated at different conditions, the one with 4 h Sb$_2$S$_3$ having Cu thickness 50 nm outperformed other PV devices in terms of J_{sc} even though the V_{oc} and FF of the same cell was not as high as that of the 2 h Sb$_2$S$_3$ based solar cell. Finally, a PV device was constituted in the p-i-n configuration using bare Sb$_2$S$_3$ as the intrinsic layer where the cell showed nearly 1% photoconversion efficiency which was much higher than the previously described PV devices. However, the synthesis of the CuSbS$_2$ thin films and thereafter the incorporation of the same in PV device application should be more optimized for making them suitable for practical use.

Table 2.1 summarizes some PV device configurations using CuSbS$_2$ or CuSbSe$_2$ as absorber materials. Among the various cell strcutures, Mo/CuSbS$_2$/CdS/i-ZnO/n-ZnO/Al showed the highest performance displaying a photoconversion efficiency of 3.22%. The V_{oc}, J_{sc} and FF values of the PV cell were 470 mV, 15.64 mA/cm^2 and 43.56% respectively. However a different configuration employing CuSbS$_2$ as Mo/CuSbS$_2$/CdS/i-ZnO/ITO/Al yielded open circuit voltage of 622 mV despite the lower conversion efficiency of the cell as 2.55% in comparison with the previous one. On the other hand, in the present work the highest conversion efficiency (0.6%) was achieved for the cell fabricated using pre-annealed RTP at 400 °C, but the V_{oc} of the same cell is found to be the highest ever reported for a CuSbS$_2$ based PV device up to date.

4.3.1.3 Electrical and photodetector properties

The current-voltage (I-V) characteristics of CuSbS$_2$ photodetector having varying Cu thicknesses (CAS 20, CAS 30, CAS 50) under dark, as well as illumination at different wavelength, LED for an applied voltage from -5V to +5V is shown in Figure 4.32 [181]. As shown in the figure, good symmetry of the I-V curves for all the films suggest better ohmic contact between the and CAS films. The photocurrent analysis under dark, as well as light at the same bias voltage, shows a significant increase in current with the illumination. CAS 40 and CAS 30 showed the highest current for the illumination wavelength of 450 nm which coincide with the optical results where the maximum absorption was in this wavelength range (Figure 3.44). These results are comparable with the work reported on flexible photodetector based on SnS thin films by Mahdi et al [199]. For the SnS photodetector illuminated by LED having wavelength of 380 nm showed better photocurrent rather than the LEDs with higher wavelengths (530, 750 and 850 nm) which is well matching with the current work. The SnS based photodetector exhibited a fast response, realiable photoresponse and high reproducibility with sensitivity for 380 nm as 2990 at an applied bias voltage of 3V. Sensitivity of the CAS thin films-based photodetector is almost one order less compared to the sensitivity of the SnS-based detectors. Nevertheless, they still offer promising photodetection properties in the entire UV and NIR regions.

Photoresponse of CAS 20, CAS 30 and CAS 40 samples at 1, 3 and 5 bias voltages under dark, as well as illumination using LEDs having wavelength of 450, 620, 740 and 850 nm at a cyclic interval of 5 sec, is shown in Figure 4.33, Figure 4.34 and Figure 4.35 respectively [181]. As observed in the previous results, CAS 40, as well as 30 films, show highest photocurrent for illumination having a wavelength of 460 nm. But CAS 20 shows better photocurrent for 740 nm. For all the samples, the photocurrent increases to a stable value under each bias voltage and reach back to its initial value as illumination is turned off, which shows the stability as well as reproducibility characteristics of the CAS photodetector. When we com-
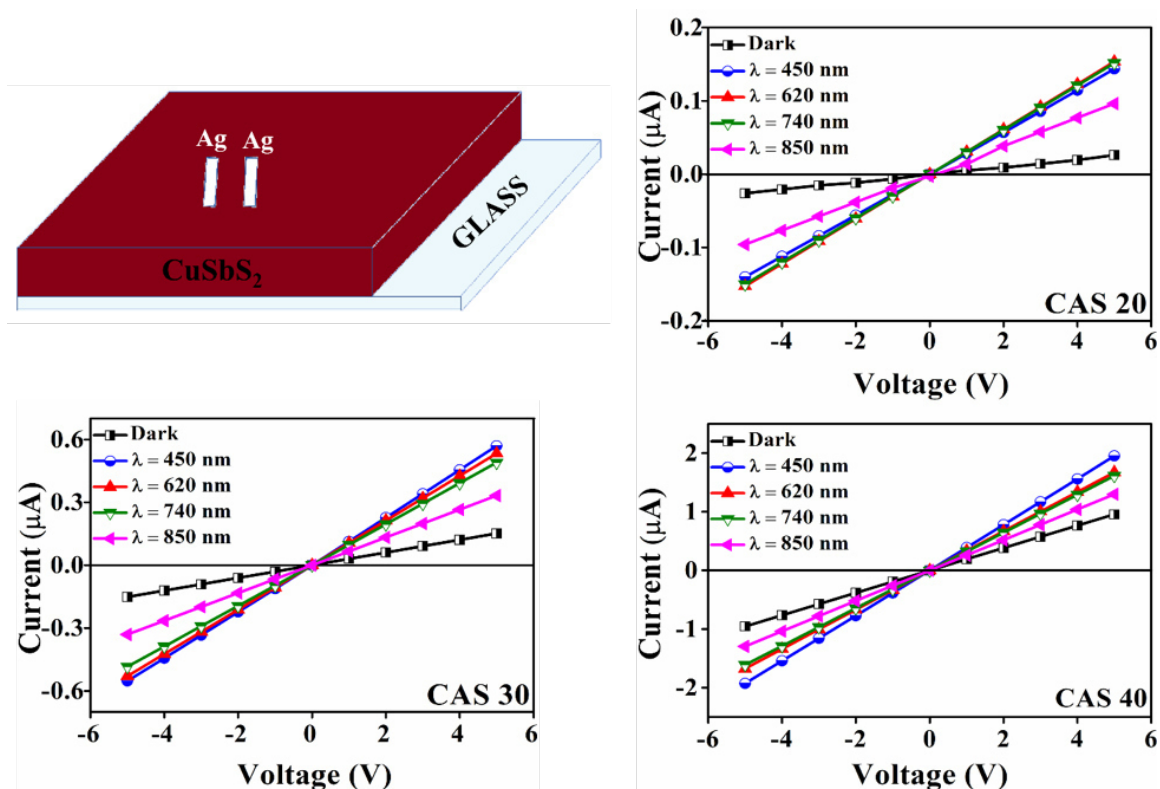
Figure 4.32: Schematic representation of the CAS photodetector device, the current voltage curves of the CAS 20, 30 and 40 photodetectors under dark and illumination with different wavelength LED's (450, 620, 740 and 850 nm) light. Reused with kind permission from RSC advances (`DOI:10.1039/C8RA05662E`).

pare the photoresponse of the CAS films in the present work with the first report on organic-inorganic photodetector based on CuSbS₂ nanocrystals, the fluctuation of photocurrent corresponds to the on/off switching is very fast in both cases, indicating a high photosensitivity [200]. The measure of change in conductivity of a sample upon illumination (photosensitivity) of the photodetectors are measured using equation 4.2 [199, 201] from both photoresponses using LEDs as well as the laser.

$$S(\%) = \frac{\Delta I_\lambda}{I_{dark}} \times 100 \tag{4.2}$$
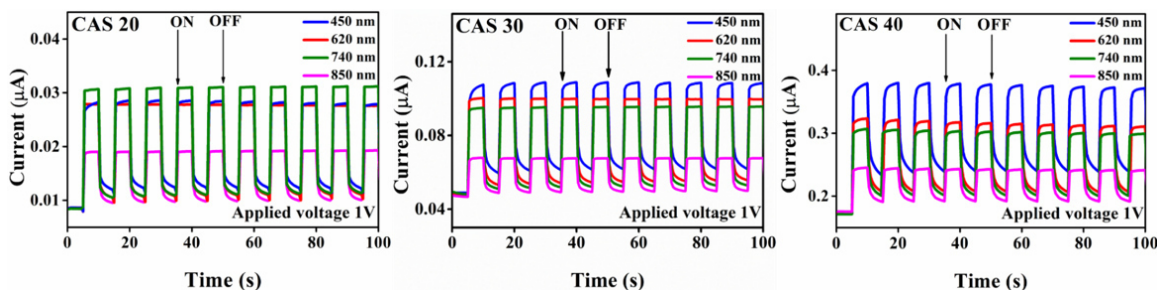
Figure 4.33: Photoresponse stability testing of CAS photodetector (CAS 20, CAS 30 and CAS 40) under illumination with LEDs having wavelengths 450, 620, 740 and 850 nm for bias voltage 1V. Reused with kind permission from RSC advances (DOI:10.1039/C8RA05662E)
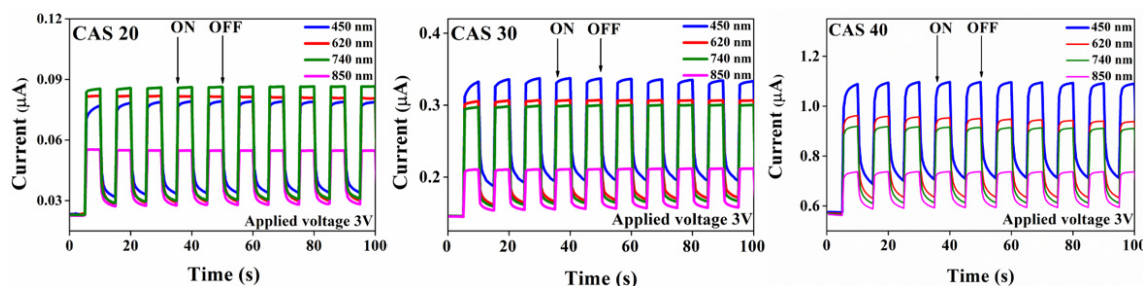
Figure 4.34: Photoresponse stability testing of CAS photodetector (CAS 20, CAS 30 and CAS 40) under illumination with LEDs having wavelengths 450, 620, 740 and 850 nm for bias voltage 3V. Reused with kind permission from RSC advances (DOI:10.1039/C8RA05662E).
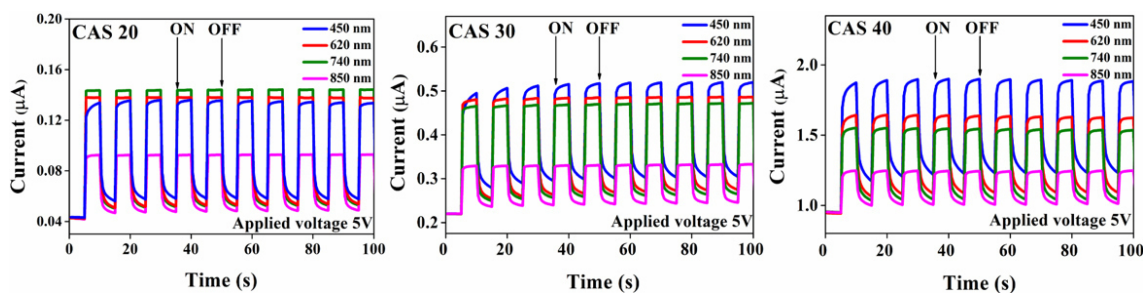
Figure 4.35: Photoresponse stability testing of CAS photodetector (CAS 20, CAS 30 and CAS 40) under illumination with LEDs having wavelengths 450, 620, 740 and 850 nm for bias voltage 5V. Reused with kind permission from RSC advances (DOI:10.1039/C8RA05662E).
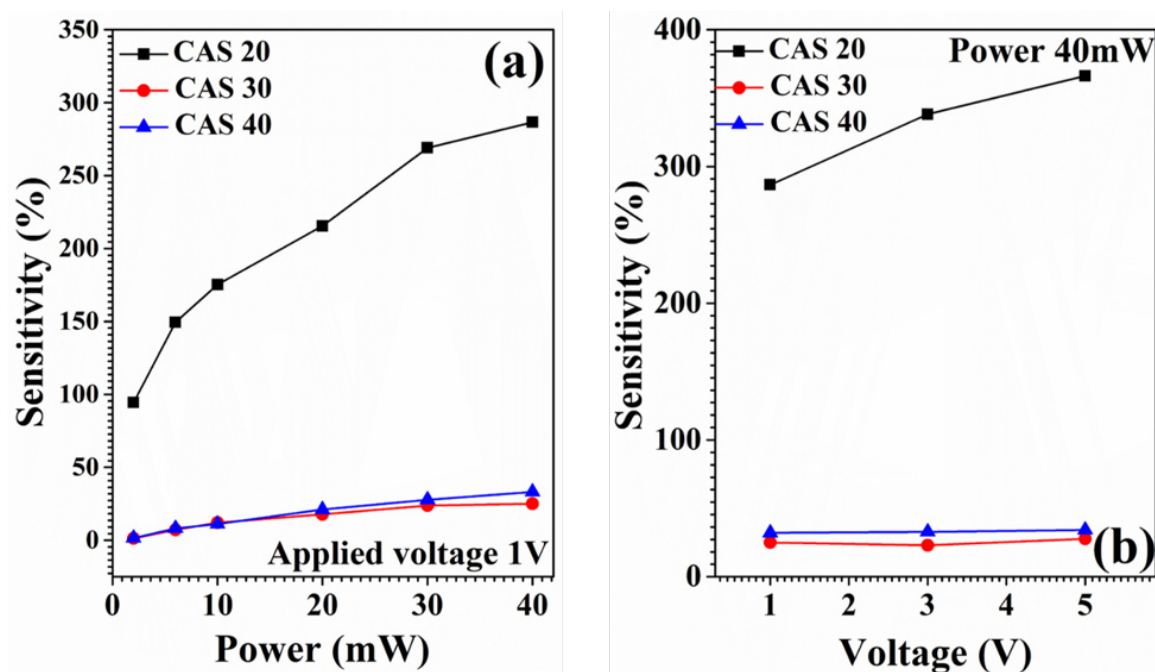
Figure 4.36: (a) Laser power vs sensitivity graphs of CAS 20, CAS 30 and CAS 40 samples at applied bias voltage 1V. (b) sensitivities of CAS 20, CAS 30 and CAS 40 samples for varying bias voltages (1, 3 and 5 V) for the laser power 40mW. Reused with kind permission from RSC advances (`DOI:10.1039/C8RA05662E`).

The corresponding values are shown in Table 4.3 and Table 4.4 for the applied bias voltage 1V, Table 4.5 and Table 4.6 for the applied bias voltage 3V, Table 4.7 and Table 4.8 for the applied bias voltage 5V respectively [181]. For the measurements using different wavelength LEDs, the highest sensitivity for the CAS20 sample is obtained for 740 nm whereas for CAS30 and CAS40 samples, blue light (450nm) showed highest sensitivities. Among all the samples, better sensitivity under all the wavelengths of illumination was recorded for CAS 20 film which might be due to the less conductivity of these films originated from the unreacted Sb$_2$S$_3$ as well as impurity phases. Sensitivity measurements corresponding to the illumination by green laser (532 nm) for different laser power (applied voltage 1V) as well as for different applied bias voltages (1V, 3V, and 5V) are presented in Figure 4.36(a) and Figure 4.36(b) [181].
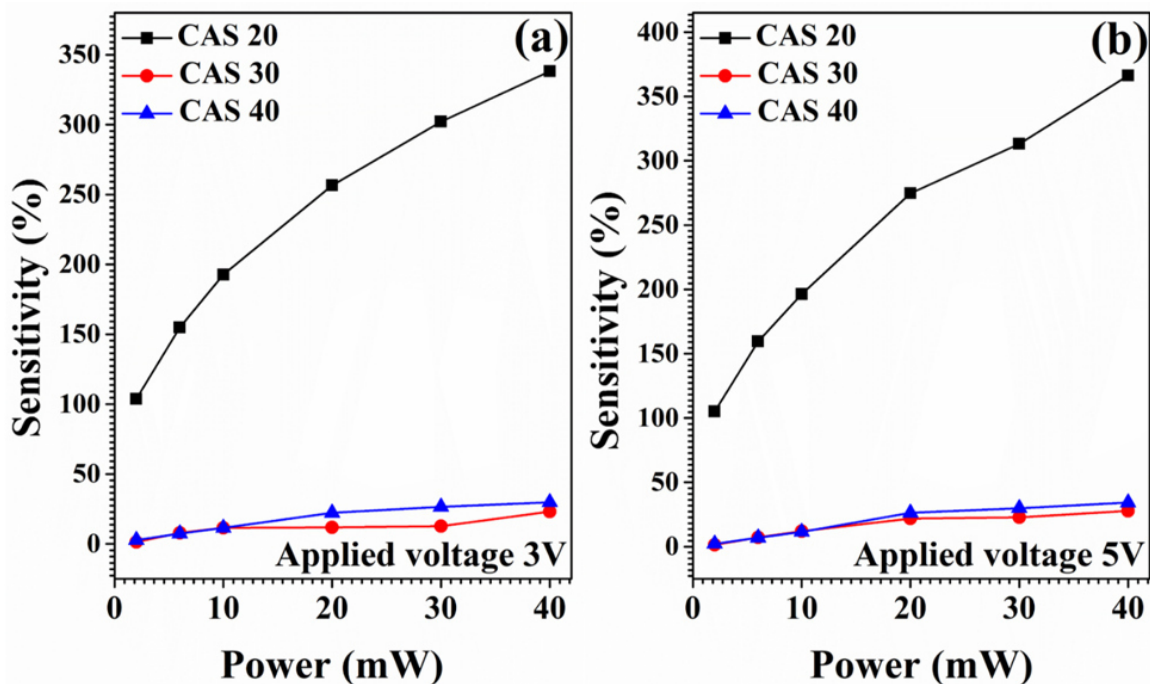
Figure 4.37: (a) Laser power vs sensitivity graphs of CAS 20, CAS 30 and CAS 40 samples at applied bias voltage 3V (b) Laser power vs sensitivity graphs of CAS 20, CAS 30 and CAS 40 samples at applied bias voltage 5V (DOI:10.1039/C8RA05662E).

Sensitivity measurements corresponding to the illumination by green laser (532 nm) for different laser power at two constant applied bias of 3V and 5V are shown in Figure 4.37(a and b) respectively [181]. In accordance with the measurements using LEDs, the highest sensitivities are recorded for the CAS 20 sample compared to CAS 30 and CAS 40, while illuminated using the laser. The sensitivity of all the three samples increases gradually with laser intensity. The amount of photocurrent generated per unit area per unit illumination intensity, responsivity (R) is calculated for for CAS 20, CAS 30 and CAS 40 from the photoresponse measurements using the following equation:

$$R = \frac{I_{light} - I_{dark}}{L_\lambda S} \tag{4.3}$$

Table 4.3: Sensitivity measurements of CAS 20, 30 and 40 using LEDs at applied voltage 1V. Reused with kind permission from RSC advances (DOI:10.1039/C8RA05662E).

Sample	Wavelength (nm)	I_{dark} (nA)	I_{light} (nA)	Sensitivity (%)
CAS 20	450	8.52	27.65	224.47
	620	8.53	27.86	226.56
	740	8.47	30.53	260.62
	850	8.51	18.90	122.14
CAS30	450	48.8	104.8	114.75
	620	48.07	99.79	107.59
	740	48.53	94.51	94.84
	850	46.93	67.5	43.92
CAS40	450	173.05	372.39	115.03
	620	172.82	321.08	85.55
	740	171.18	304.61	78.12
	850	175.29	243.87	39.42

where L_λ is the power density of the light source. The responsivity of the CAS detectors was calculated using equation (3) from the measurements done by laser illumination at applied voltages 1V, 3V, 5V, and the corresponding values are included in Table 4.4, Table 4.6 and Table 4.8 respectively. Highest responsivities were recorded for CAS 20 at the laser power of 2 mW, CAS 30 at 10 mW and CAS 40 at 6 mW respectively. All this electrical analysis is comparable with the reported work on hybrid photodetector based on CuSbS₂ [200] and the CAS film reported here. Among the fabricated photodetector configurations, the one having 20 nm CAS thin film outperformed others in terms of the device performance. This can be primarily attributed to the lower conductivity of these thin films in comparison with

Table 4.4: Sensitivity and responsivity measurements of CAS 20, CAS30 and CAS40 at various laser (532 nm) power density and applied voltage 1V. Reused with kind permission from RSC advances (`DOI:10.1039/C8RA05662E`).

Sample	Power density (mW/cm^2)	I_{dark} (nA)	I_{light} (nA)	Sensitivity (%)	Responsivity (AW^{-1}) *10^{-6}
CAS 20	0.8	3.95	7.68	94.43	19.05
	2.4	3.80	9.48	149.47	9.62
	3.9	3.88	10.68	175.25	6.91
	7.9	4.15	13.09	215.42	4.54
	11.8	3.94	14.55	269.03	3.59
	15.8	4.11	15.89	286.61	2.99
CAS30	0.8	71.4	72.3	1.26	4.57
	2.4	71.7	76.9	7.25	8.81
	3.9	71.6	80.3	12.15	8.84
	7.9	74.8	88.1	17.78	6.76
	11.8	74.9	92.7	23.76	6.03
	15.8	76.6	95.8	25.06	4.88
CAS40	0.8	196	199	1.53	15.24
	2.4	208	225	8.17	28.78
	3.9	215	239	11.16	24.38
	7.9	213	258	21.07	22.81
	11.8	212	271	27.78	19.97
	15.8	211	288	33.17	11.78

others due to the lower Cu content. The presence of unreacted Sb$_2$S$_3$ in the CAS 20 nm thin film might have also played a role in this case probably by contributing to the partial absorption of the incoming photons.

Table 4.5: Sensitivity measurements of CAS 20, 30 and 40 using LEDs at applied voltage 3V. Reused with kind permission from RSC advances (`DOI:10.1039/C8RA05662E`).

Sample	Wavelength (nm)	I_{dark} (nA)	I_{light} (nA)	Sensitivity (%)
CAS 20	450	23.31	74.79	220.85
	620	23.17	81.73	252.74
	740	22.97	84.84	269.35
	850	22.65	55.21	143.75
CAS 30	450	145.47	325.22	123.56
	620	145.30	303.68	109
	740	145.63	295.95	103.22
	850	145.04	210.61	45.21
CAS 40	450	575.04	1064.03	85.03
	620	570.93	952.79	66.88
	740	567.68	910.68	60.42
	850	564.34	730.13	29.36

Chalcogenide based binary, ternary and quaternary semiconductors and their composites have already proven to be suitable candidates for photodetector applications owing to its unique semiconducting properties. For instance, inorganic thin film visible light photodetector based on graphene on antimony sulfide was reported by Xiao et al. [202] and stable photoresponse was obtained even at zero bias voltage for the wavelength range 400-700 nm. In addition, CuInS₂ thin film and CuInSe₂ nanocrystals were also applied for light detection applications by various research groups [203, 204]. Hao et al. [200], reported the synthesis of a high-performance photodetector based on the hybrid film of CuSbS₂ nanocrystals and poly (3-hexylthiophene). Even though the constructed photodetector device had stable photodetection properties, better sensitivity was obtained in the infrared range.

Table 4.6: Sensitivity and responsivity measurements of CAS 20, 30 and 40 at various laser power and applied voltage 3V. Reused with kind permission from RSC advances (`10.1039/C8RA05662E`).

Sample	Power density (mW/cm^2)	I_{dark} (nA)	I_{light} (nA)	Sensitivity (%)	Responsivity (AW^{-1}) *10^{-5}
CAS 20	0.8	13.3	27.1	103.75	7.01
	2.4	13.5	34.4	154.81	3.54
	3.9	13.5	39.5	192.59	2.64
	7.9	13.8	49.2	256.52	1.80
	11.8	13.6	55.5	302.17	1.41
	15.8	13.3	59.6	338.23	1.17
CAS 30	0.8	213	216	1.41	1.52
	2.4	215	232	7.90	2.88
	3.9	219	244	11.41	2.54
	7.9	228	255	11.84	1.37
	11.8	229	258	12.36	0.98
	15.8	234	288	23.07	1.37
CAS 40	0.8	588	604	2.72	8.12
	2.4	631	676	7.30	7.67
	3.9	641	715	11.38	7.51
	7.9	636	777	22.16	7.16
	11.8	642	813	26.47	5.79
	15.8	651	845	29.80	4.93

In the present work the synthesized CAS thin films-based photodetectors exhibit reliable photodetection properties including the visible region as well as NIR regions. This study using CAS thin films as photodetecting devices promises a great future for this material in the field of optoelectronics as well where cost-effectiveness

Table 4.7: Sensitivity measurements of CAS 20, 30 and 40 using LEDs at applied voltage 5V. Reused with kind permission from RSC advances (`DOI:10.1039/C8RA05662E`).

Sample	Wavelength (nm)	I_{dark} (nA)	I_{light} (nA)	Sensitivity (%)
CAS 20	450	43.23	130.19	201.16
	620	42.55	137.85	223.85
	740	43.03	143.38	233.29
	850	42.37	91.82	116.71
CAS 30	450	220.15	478.31	117.27
	620	219.55	476.68	117.11
	740	219.74	461.96	110.23
	850	219.88	327.10	48.76
CAS 40	450	944.99	1823.82	93
	620	943.68	1617.62	71.42
	740	952.06	1534.40	61.17
	850	949.96	1236.11	30.12

and environment friendly nature of the constituent elements are of utmost importance. Earth abundancy of the elements in $CuSbS_2$ may also serve as an advantage when the devices based on this material has to be scaled up for commercial purpose. On the other hand, by precisely controlling the deposition parameters, one can get good control over the properties of the resulting $CuSbS_2$ thin films thereby opening a way to indirectly choose the operation conditions and performances of the fabricated devices based on $CuSbS_2$.

Table 4.8: Sensitivity and responsivity measurements of CAS 20, 30 and 40 at various laser power and applied voltage 5V. Reused with kind permission from RSC advances (DOI:10.1039/C8RA05662E).

Sample	Power density (mW/cm^2)	I_{dark} (nA)	I_{light} (nA)	Sensitivity (%)	Responsivity (AW^{-1}) *10^{-4}
CAS 20	0.8	23.7	48.6	105.06	1.26
	2.4	24.2	62.8	159.50	0.65
	3.9	24.2	71.7	196.28	0.48
	7.9	23.7	88.8	274.68	0.33
	11.8	24.3	100.5	313.16	0.26
	15.8	23.4	109.2	366.23	0.22
CAS 30	0.8	358	363	1.39	0.25
	2.4	358	384	7.26	0.44
	3.9	369	413	11.92	0.45
	7.9	366	446	21.85	0.41
	11.8	391	479	22.82	0.30
	15.8	386	493	27.72	0.27
CAS 40	0.8	979	1002	2.24	1.15
	2.4	1060	1134	6.98	1.25
	3.9	1066	1189	11.53	1.25
	7.9	1076	1359	26.30	1.44
	11.8	1090	1416	29.90	1.10
	15.8	1084	1455	34.22	0.94

CHAPTER 5

$CuSbSe_xS_{2-x}$ THIN FILMS: SYNTHESIS, CHARACTERIZATION AND DEVICE APPLICATIONS

In pursuit of improving the performance of $CuSbS_2$ /CdS PV structure, making solid solution with selenium to form a quaternary $CuSbSe_xS_{2-x}$ is explained in this chapter. One advantage of alloying with Se is that the band gap of the material shifts to 1.5 eV from 1.2 eV depending on the Se content incorporated which helps to absorb more solar light. Solar cells based on selenized CZTS and CIGS found to outperform the device performances displayed by bare CZTS and CIGS based PV devices. For instance, Wang et al. [205], achieved 12.6% conversion efficiency for a CZTSSe where the improved efficiency was attributed to the reduction of V_{oc} deficit. A hydrazine processed $Cu_2ZnSn(Se,S)_4$ exhibited comparable device properties to that of CIGSSe and $CuInSe_2$ based PV devices where the limiting factors were reported to be short minority carrier lifetime, dominant interface recombination, and high series resistance. CZTSSe-based solar cells fabricated using CZTS nanocrystals also showed a high total area power conversion efficiency of 7.2% [206]. On the other hand, a photoconversion efficiency of 15% was reported for a solar cell having CIGSSe as the absorber material which was obtained through a nanoparticle ink-based process of [207]. Motivated by these reports, we adopted this approach to

form CuSbSe$_X$S$_{2-X}$ films.

Here, Sb$_2$S$_3$ bath of 4 h was subjected to selenization process by a chemical method. We also report a systematical study by varying the Cu thickness from 5 to 50 nm for the selenized films. The properties of the quaternary CuSbSe$_X$S$_{2-X}$ are compared with that of Sb$_2$Se$_X$S$_{3-X}$ and CuSbS$_2$. The Sb$_2$Se$_X$S$_{3-X}$ thin films were prepared by heating glass/Sb$_2$S$_3$/Se and CuSbSe$_X$S$_{2-X}$ film were formed by heating glass/Sb$_2$S$_3$/Se/Cu layers. In both cases, the heating condition was by conventional annealing.

5.1 SYNTHESIS

5.1.1 Chemical deposition of Sb$_2$S$_3$

The chemical bath conditions were alike that used for the ternary CAS thin films (section 3.2.1.1). Briefly, in the typical process, the glass substrates were placed horizontally in a petri dish containing the solution of SbCl$_3$ and Na$_2$S$_2$O$_3$ and the solution mixture after well stirring was poured into it. The bath duration was 4 h in this case.

5.1.2 Selenization by chemical method

Sb$_2$S$_3$ layer coated glass substrates were dipped in a solution containing 7 ml of Na$_2$SeSO$_3$ (0.1 M), 40 ml of room temperature deionized water, and 1 ml acetic acid (25%). The selenium layer was deposited by one deposition for 1 h. 0.78 g of selenium powder (99.99% purity) and 4.5 g of Na$_2$S$_2$O$_3$ were dissolved in 100 ml deionized water at 90 °C for 3 h for preparing the Na$_2$SeSO$_3$ precursor solution [208, 209]. The selenium deposition was carried out over the Sb$_2$S$_3$layer before Cu deposition since the Sb$_2$S$_3$/Cu/Se layer formed impurity phase by reaction between Cu and Se during the heating stage.

5.1.3 Thermal evaporation of Cu

Cu thin films were deposited onto Sb$_2$S$_3$/Se coated glass substrates by means of thermal evaporation as explained in the last chapter (section 3.2.1.2). Different Cu thicknesses such as 5, 10, 20 and 50 nm were deposited on the glass/Sb$_2$S$_3$/Se layers.

5.1.4 Heat treatment

The Sb$_2$S$_3$/Se/Cu stacked layers were heaed at 350 °C in low vacuum (10^{-3} Torr) for 30 min in a conventioal vacuum furnace to form the quaternary CuSbSe$_X$S$_{2-X}$ through diffusion and reaction of the precursor layers. The selenium atoms were incorporated into the stack layers by Se thin film deposition by CBD forming a binary phase by reaction [210] and by diffusion-controlled reaction of metallic precursor by evaporation with selenium [211, 212]. In the present, to obtain the quaternary CuSbSe$_X$S$_{2-X}$ the glass/Sb$_2$S$_3$/Se/Cu stacked thin films were annealed.

5.2 FABRICATION OF SOLAR CELL

CuSbSe$_X$S$_{2-X}$ thin films were incorporated in PV structure glass/SnO$_2$:F/(n)CdS/ (p)CuSbSe$_X$S$_{2-X}$/Ag by the similar procedure described in the previous chapter. Only difference is that prior to copper evaporation, glass/SnO$_2$:F/CdS/Sb$_2$S$_3$ was coated with Se as mentioned above. The multilayer structure, glass/SnO$_2$:F/CdS/ Sb$_2$S$_3$/Se/Cu was heated at 350 °C for 30 min in low vacuum (4 $\times 10^{-3}$ Torr) (schematically represented Figure 5.1). Ohmic contacts were made using colloidal A$_g$(SPI supplies) for measuring the I-V characteristics of the fabricated PV devices. The contact area was 5 $\times$ 5 mm^2. The photovoltaic parameters of the prototypes were evaluated and thus the device performance.
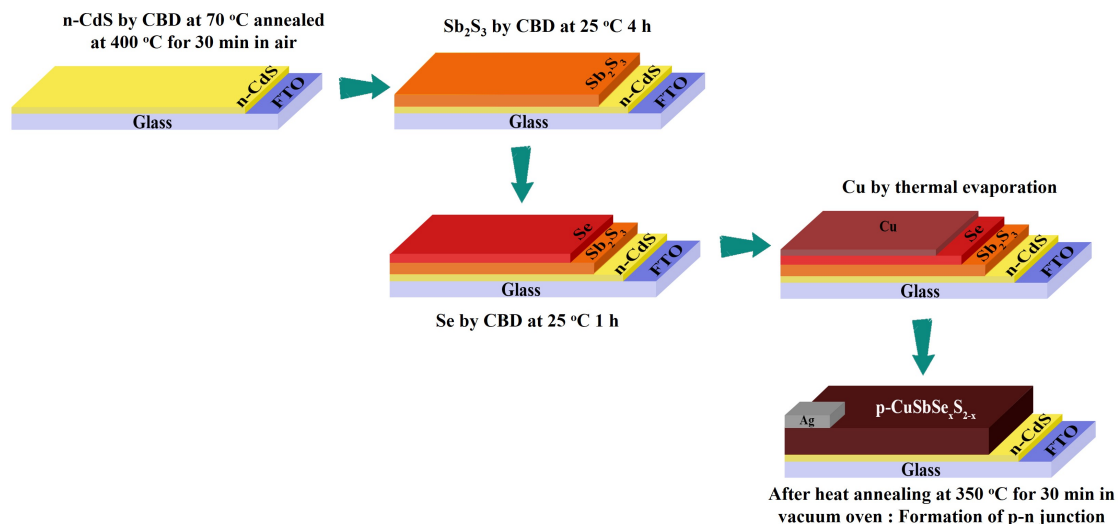
Figure 5.1: Superstrate p-n configuration of glass/SnO$_2$:F/(n)CdS/(p)CuSbSe$_X$ S$_{2-X}$/Ag

5.3   CHARACTERIZATION

The selenium contained thin films formed at different conditions were analyzed using different techniques such as XRD, XPS, XRF, Raman spectroscopy, SEM, EDX, and also evaluated their optoelectronic properties as elucidated in the previous chapters.

5.4   RESULTS AND DISCUSSION

5.4.1   Structure

Structural characteristics of the glass/Sb$_2$S$_3$/Se/Cu layers with varying Cu thicknesses from 5 to 50 nm together with that of glass/Sb$_2$S$_3$/Se were analyzed by grazing incidence X-ray diffraction analysis. Figure 5.2 shows the corresponding XRD patterns taken at an angle of incidence of 0.5$^{\mathrm{o}}$ as well as the standard JCPDS patterns for orthorhombic CuSbS$_2$ (PDF#44-1417) and stibnite Sb$_2$S$_3$ (PDF#42-1393). The glass/Sb$_2$S$_3$/Se/Cu layers having Cu thicknesses 5 and 10 nm present XRD patterns similar to that of the glass/Sb$_2$S$_3$/Se thin film as shown in the figure with major reflections from the (020), (120), (130), (211), (221), (240) and (501) crystal planes
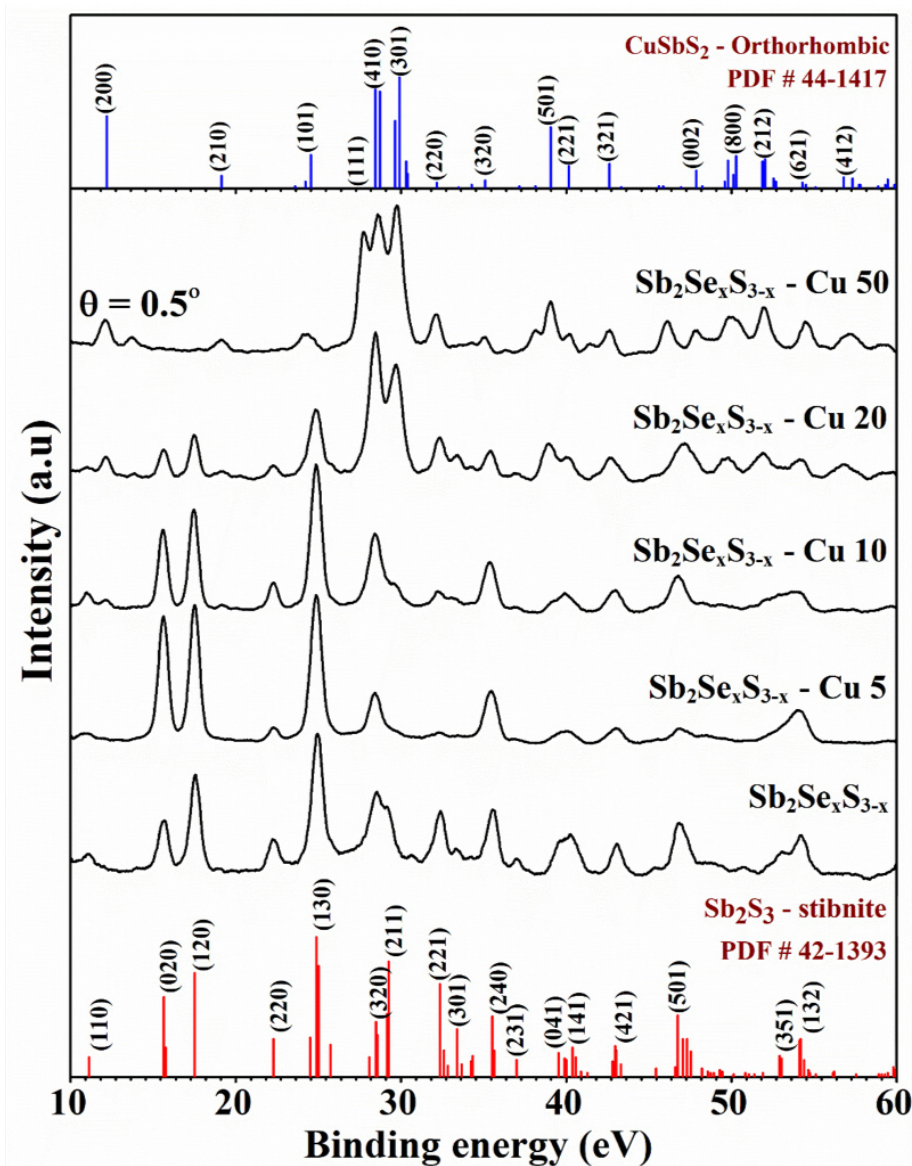
Figure 5.2: GIXRD patterns at $\theta = 0.5°$ for glass/Sb$_2$S$_3$/Se/Cu of varying Cu thicknesses 5, 10, 20 and 50 nm by keeping Sb$_2$S$_3$ and Se bath constant for 4 and 1 h respectively annealed at conventional vacuum oven at 350 °C for 30 min. GIXRD pattern of glass/Sb$_2$S$_3$/Se along with the standard pattern corresponding to Stibnite Sb$_2$S$_3$and orthorhombic CuSbS$_2$ (PDF#44–1417) are also included.

according to the standard JCPDS pattern of Sb$_2$S$_3$ having stibnite structure. Even though the glass/Sb$_2$S$_3$/Se/Cu (5 nm) thin film present similar XRD pattern as that of the film having 10 nm Cu, the CuSbS$_2$ formation has started as the Cu thickness
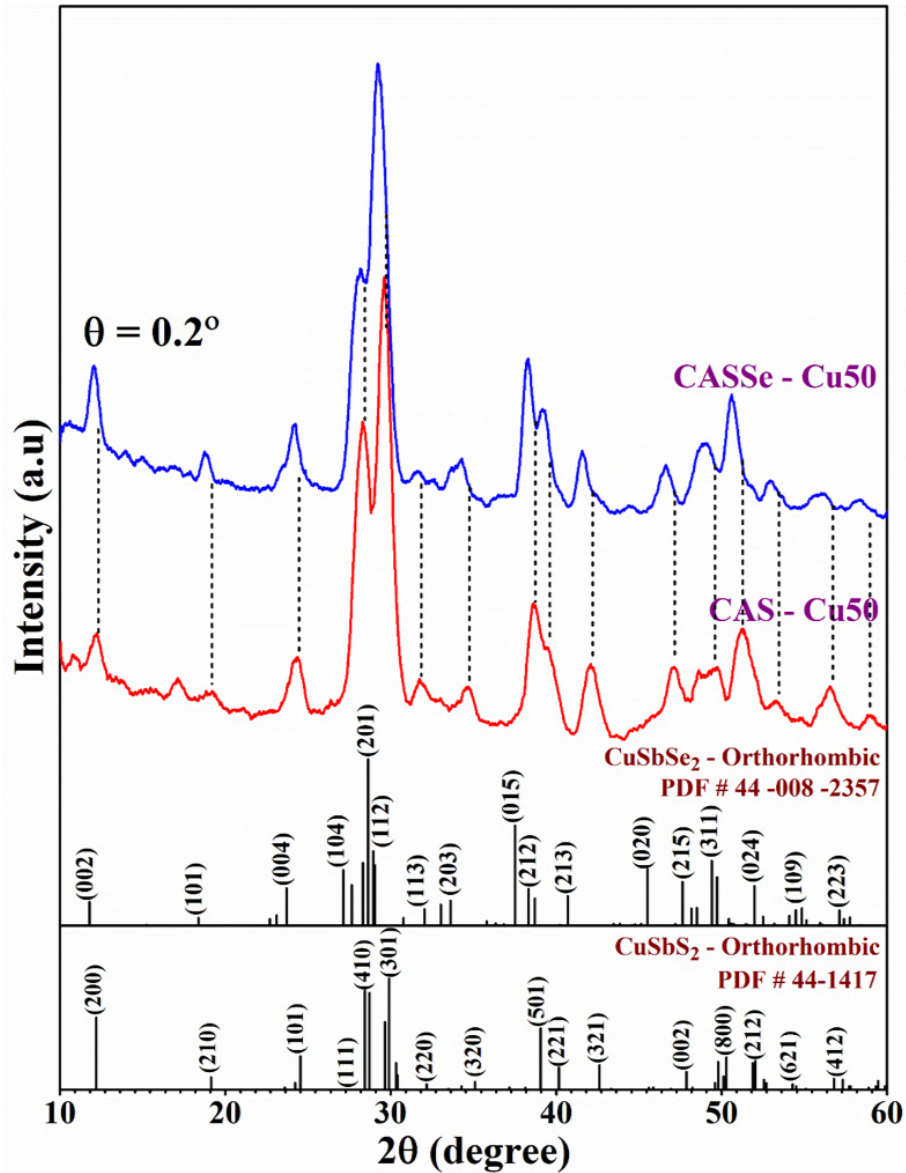
Figure 5.3: GIXRD patterns at $\theta = 0.2°$ for glass/Sb$_2$S$_3$/Cu and glass/Sb$_2$S$_3$/Se/Cu respectively annealed at conventional vacuum oven at 350 °C for 30 min. The standard pattern corresponding to orthorhombic CuSbS$_2$ (PDF#44–1417) and orthorhombic CuSbSe$_2$ (PDF#44–2357) are also included in the same figure for reference.

is increased from 5 to 10 nm. This is evidenced from the small peaks observed in the XRD pattern corresponding to the (200) and (220) crystal planes of orthorhombic CuSbS$_2$. As the Cu thickness is increased to 20 nm, the major phase detected is
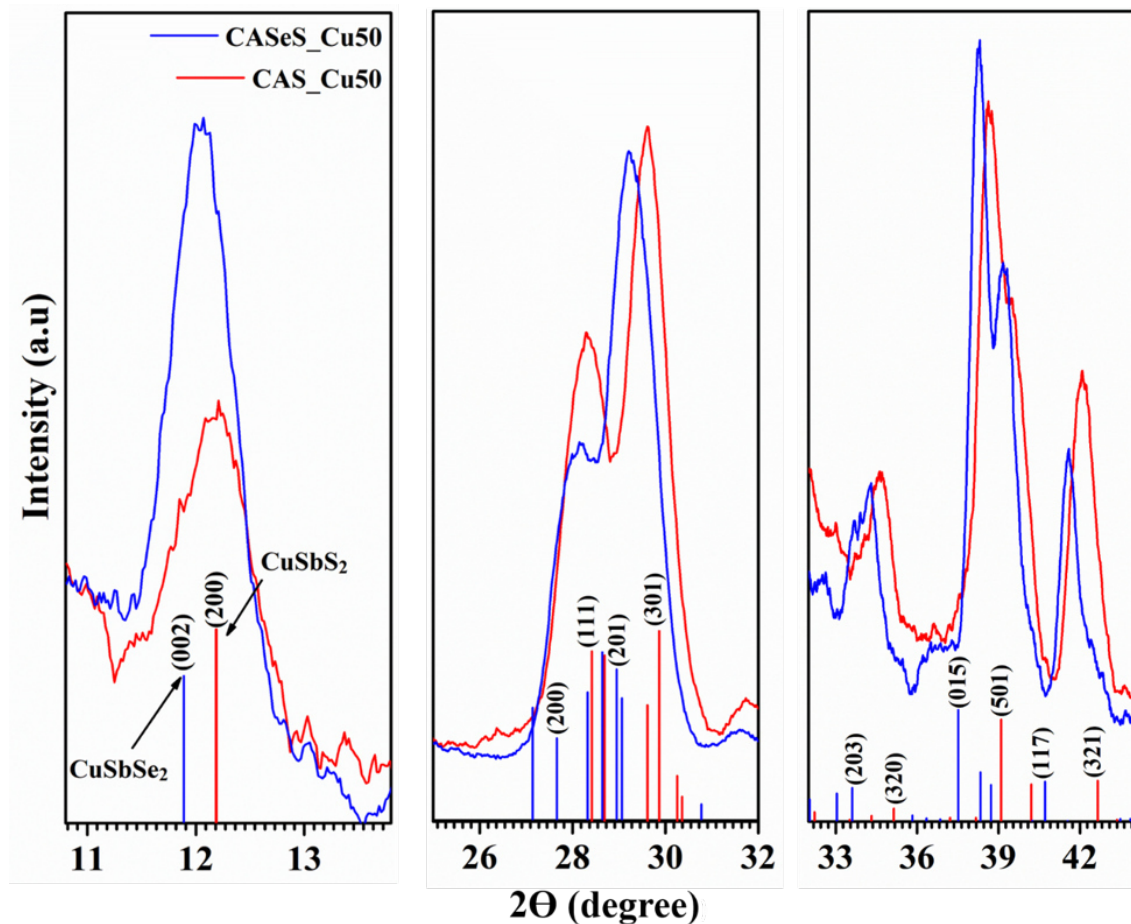
Figure 5.4: Shift of the GIXRD peaks at $\theta = 0.2°$ of glass/Sb$_2$S$_3$/Cu50 nm and glass/ Sb$_2$S$_3$/Se/Cu50 nm respectively annealed at 350 °C for 30 min.

CuSbS$_2$ and for 50 nm Cu sample phase pure CuSbS$_2$ can be observed. Since all the thin films were selenized, a small peak shift is expected with respect to that of pure Sb$_2$S$_3$ or CuSbS$_2$ phases. However, in this case, this peak shift is not clearly visible in the patterns. This may be due the suppression of the selenide peaks formed at the surface by the diffraction signals from the depth of the samples. To validate this, the XRD patterns of the glass/Sb$_2$S$_3$/Se/Cu and glass/Sb$_2$S$_3$/Cu layers were taken at angle of incidence of 0.2$^\text{o}$ and compared as shown in Figure 5.3. Standard JCPDS patterns of CuSbS$_2$ and CuSbSe$_2$ are also included in the same figure as references. The CuSbS$_2$ sample with 50 nm Cu shows the pattern of orthorhombic CuSbS$_2$ with preferential orientation along the (301) crystal plane. The same sample after

selenization also possess comparable pattern except with a slight shift of the peaks towards lower angle. On the other hand, the XRD pattern of the glass/Sb$_2$S$_3$/Se/Cu sample, not match with the JCPDS pattern for CuSbSe$_2$ excluding the possibility that CuSbSe$_2$ phase has formed by the selenization during heating in vacuum oven. This peak shift in the selenized samples indicate the formation of CuSbSe$_X$S$_{2-X}$ solid solution. In such a solid solution, fraction of the sulfur atoms in the CuSbS$_2$ lattice are substituted by Se atoms by which an increase in the lattice parameter owing to the larger atomic radius of Se atoms compared to that of S atoms. This effect is clearly depicted in Figure 5.4 which shows the zoomed version of the XRD patterns of the selenized and non-selenized samples. The formation of layered structure CuSbSe$_X$S$_{2-X}$ mesocrystals was reported by Ramasamy et al. where the XRD patterns that with increase of selenium content in CuSbSe$_X$S$_{2-X}$ showed a systematic shift in the diffraction peaks toward lower angles and which indicating the formation of a solid solution [119]. Takei et al. [82] prepared CuSb(S$_X$Se$_{1-X}$)$_2$ solid solution by mixing CuSbS$_2$ powder with CuSbSe$_2$ powder and post heating at 450 °C and analyzed the crystal structure by Rietveld refinement of XRD data. They found that the XRD peaks of the selenized samples were having intermediate positions compared to the peak positions of pure orthorhombic CuSbS$_2$ and CuSbSe$_2$. These XRD results are comparable with the results of the present study where a peak shift is noticed for the selenized samples which underlines the formation of the orthorhombic CuSbSe$_X$S$_{2-X}$.

Further analysis of the selenized films were done by Raman spectral studies. Figure 5.5 shows the Raman spectra of the glass/Sb$_2$S$_3$/Se/Cu with varying Cu thicknesses along with glass/Sb$_2$S$_3$/Se for comparison. The glass/Sb$_2$S$_3$/Se/Cu samples having Cu thicknesses 5 and 10 nm present almost similar spectra as that of selenized Sb$_2$S$_3$ sample exhibiting two weak Raman bands located at 274.5 and 300 cm^{-1}. As specified by Yun Liu et al [182] and Y A sorb et al. [183], Sb$_2$S$_3$ shows Raman active modes of A$_g$, A$_{1g}$, A$_{2g}$ and A$_{3g}$, B$_{1g}$, B$_{2g}$, and B$_{3g}$ at the wavenumbers 47.7, 50.8, 54.3, 69.1, 74.5, 99.1, 100,124.1,196.7, 208.2, 231.4, 241, 251, and 257.9
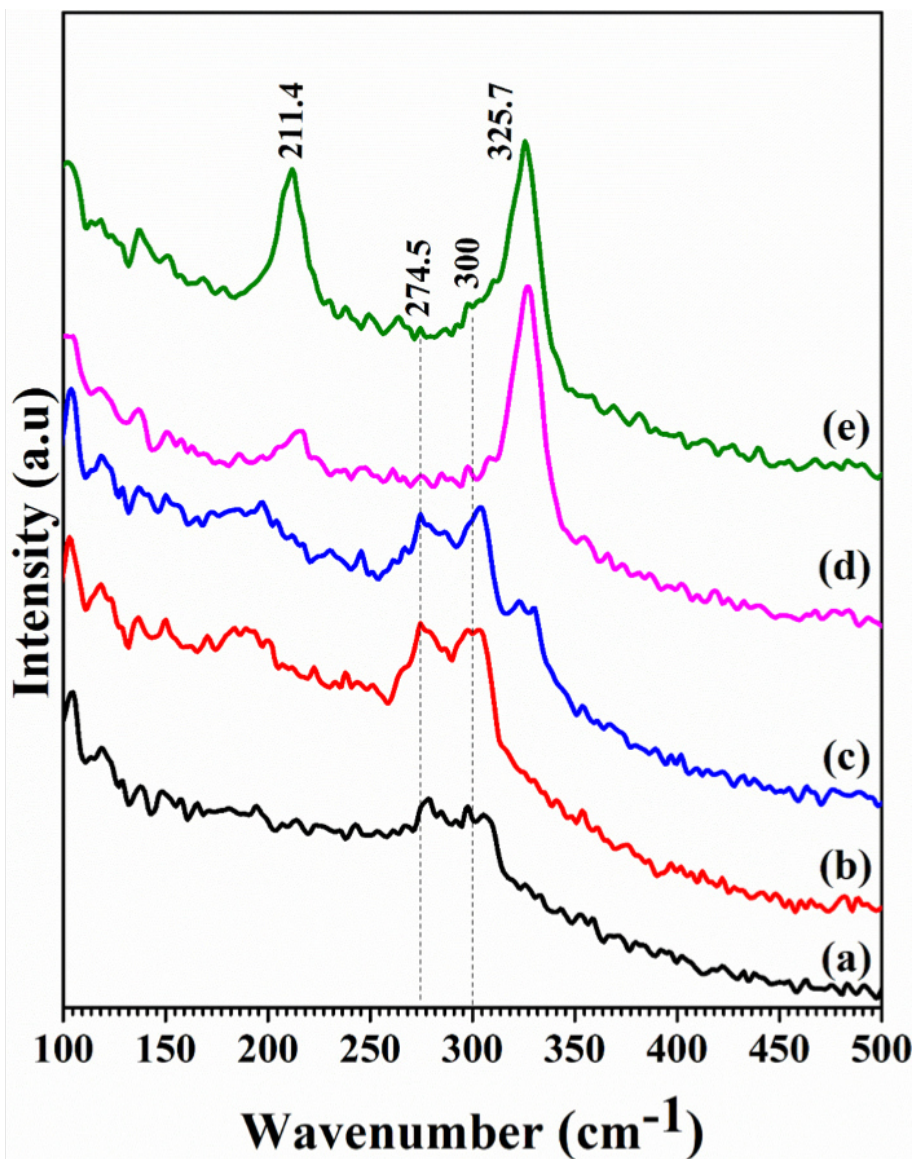
Figure 5.5: Raman spectra of glass/Sb$_2$S$_3$/Se/Cu of varying Cu thicknesses 5 (b), 10 (c), 20 (d) and 50 nm (e) by keeping Sb$_2$S$_3$and Se bath constant for 4 and 1 h respectively annealed at conventional vacuum oven at 350 °C for 30 min. Raman spectra of glass/Sb$_2$S$_3$/Se (a) is also included in the same figure for a reference.

cm^{-1}, 286 and 308 cm^{-1} and 314 cm^{-1} respectively. Here in the present spectra, the peaks are located at 274.5 and 300 cm^{-1} for antimony sulfide/Se films. The shift in Raman peaks of Sb$_2$S$_3$/Se peak compared to the bare Sb$_2$S$_3$ films (281 cm^{-1}, 303 cm^{-1} (given in chapter 3)) confirm the formation of Sb$_2$Se$_X$S$_{3-X}$ phase. As the Cu thickness in the sample is increased to 10 nm, a peak appeared at 325.7 cm^{-1}. As
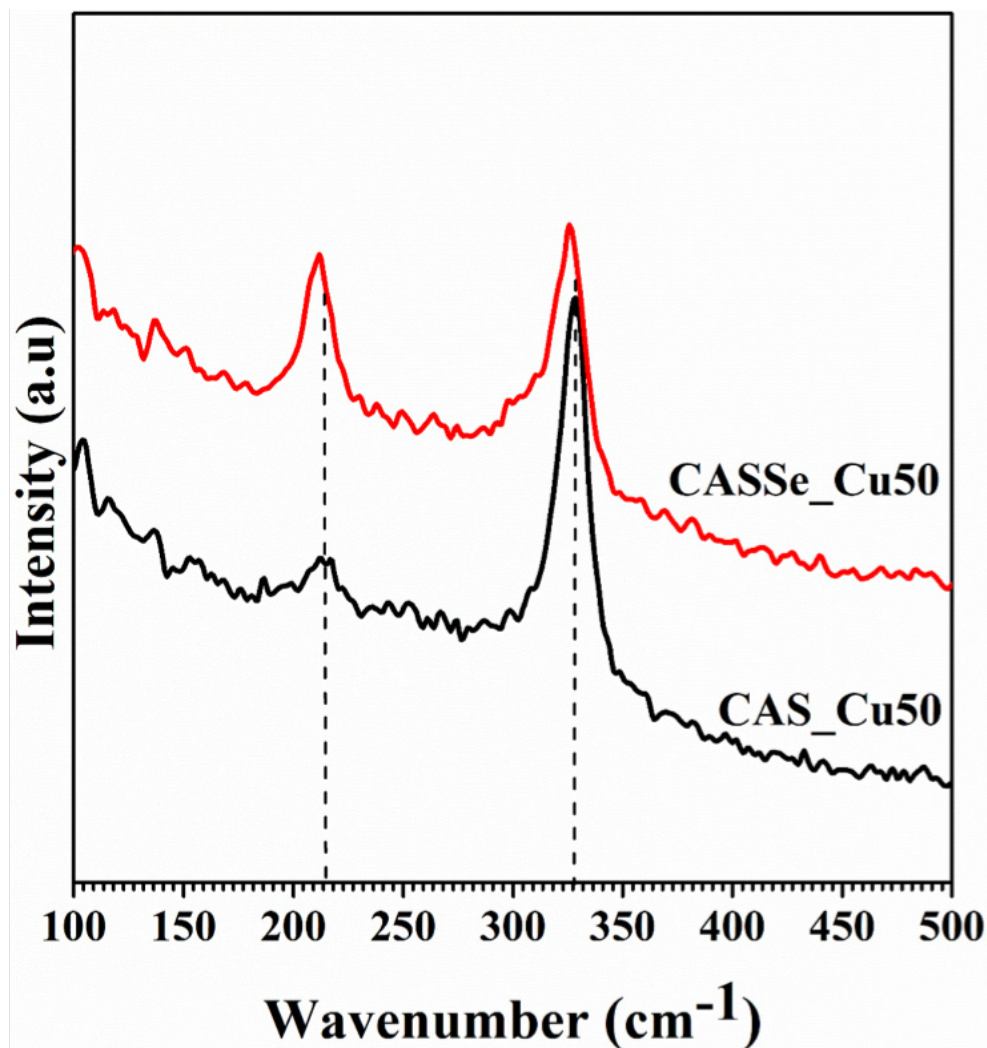
Figure 5.6: Raman spectra of glass/Sb$_2$S$_3$/Cu50 nm and glass/Sb$_2$S$_3$/Se/Cu50 nm respectively annealed at conventional vacuum oven at 350 °C for 30 min.

specified by Baker et al. [184] in a study on pressure induced structure transformation in orthorhombic CuSbS$_2$ (*pnma* space group), the Raman active zone-center vibrational modes can be described with four Raman active modes (A$_g$, B$_{1g}$, B$_{2g}$ and B$_{3g}$) and three infrared active modes (B$_{1u}$,B$_{2u}$,B$_{3u}$). The Raman spectrum for an unoriented CuSbS$_2$ sample at 532 nm excitation wave length published in RRUFF database [185] also supports the present findings. This implies that the ternary phase CuSbS$_2$ started to grow at Cu thickness 10 nm which is in good agreement with the observed XRD results for the same films. For the samples having Cu thickness 20

nm and 50 nm, two Raman bands are observed, one at 211.4 cm^{-1} and another one at 325.7 cm^{-1} which might be attributed to the CuSbSe$_X$S$_{2-X}$. This assumption is supported by the shift observed in the Raman bands of the selenized samples in comparison with the bare CuSbS$_2$ sample as shown in Figure 5.6. From Figure 5.6, it can be clearly seen that the peaks located around 211.4 and 325.7 cm^{-1} are slightly shifted towards smaller wavenumbers when the samples were undergone selenization. Jiří Sejkora et al. [213] recently reported a systematical study on the Raman spectra of CuSb(S,Se)$_2$ thin films. According to them, the vibratios at 330 and 314 cm^{-1} are corresponding to ν1 symmetric Sb–S stretching vibrations and modes at 220 and 180 cm^{-1} are ν1 symmetric Sb–Se stretching vibrations. Even though, the peak at 330 cm^{-1} is corresponding to the Sb-S stretching vibration, a shift in peak observed for the sample with Se concentration. Se rich samples showed a shift in peak towards the lower wavenumber 326 cm^{-1}. These results are comparable with our present study. Hence, together with the XRD analysis, the Raman analysis also confirms the formation of CuSbSe$_X$S$_{2-X}$ through successful selenization of CuSbS$_2$. The Raman peaks of Sb$_2$Se$_X$S$_{3-X}$ and CuSbSe$_X$S$_{2-X}$ thin films are tabulated in Table 5.1

Table 5.1: Raman peaks of Sb$_2$Se$_X$S$_{3-X}$ and CuSbSe$_X$S$_{2-X}$

Wave number (cm^{-1})	Compound	Vibrational modes
211.4	CuSbSe$_X$S$_{2-X}$	[184, 185, 213]
274.5	Sb$_2$Se$_X$S$_{3-X}$	[182, 183]
300	Sb$_2$Se$_X$S$_{3-X}$	[182, 183]
325.7	CuSbSe$_X$S$_{2-X}$	[184, 185, 213]

5.4.2   Chemical Composition

(a) X-ray photoelectron spectroscopy (XPS)

Figure 5.7 and 5.8 show the low-resolution survey spectra recorded from 0 to
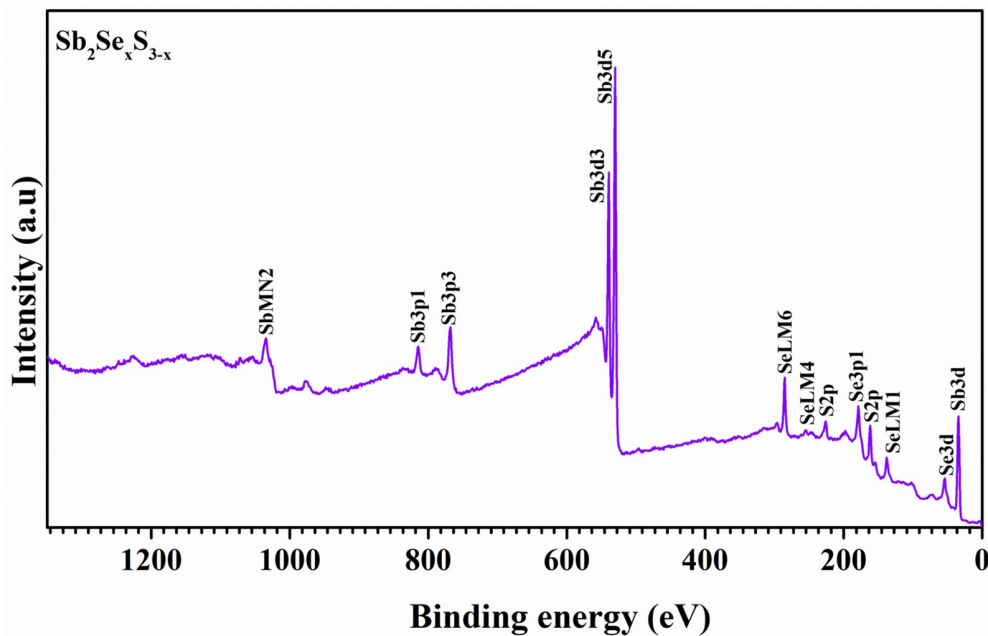
Figure 5.7: Survey spectrum of glass/Sb$_2$S$_3$/Se precursor thin film annealed at 350 °C for 30 min in vacuum oven.
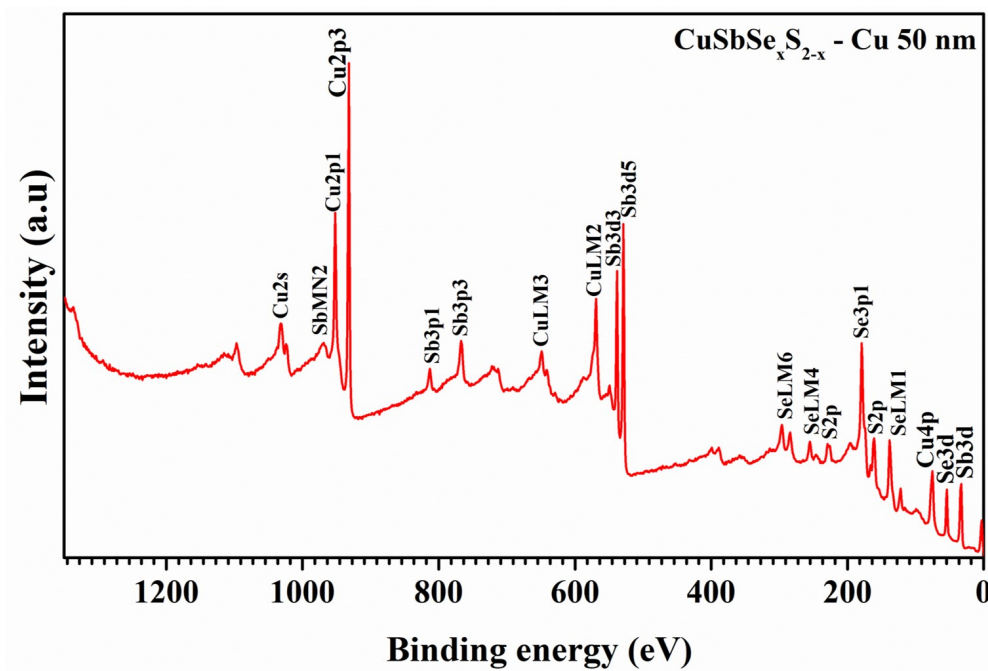
Figure 5.8: Survey spectrum of glass/Sb$_2$S$_3$/Se/Cu precursor thin film annealed at 350 °C for 30 min in vacuum oven.
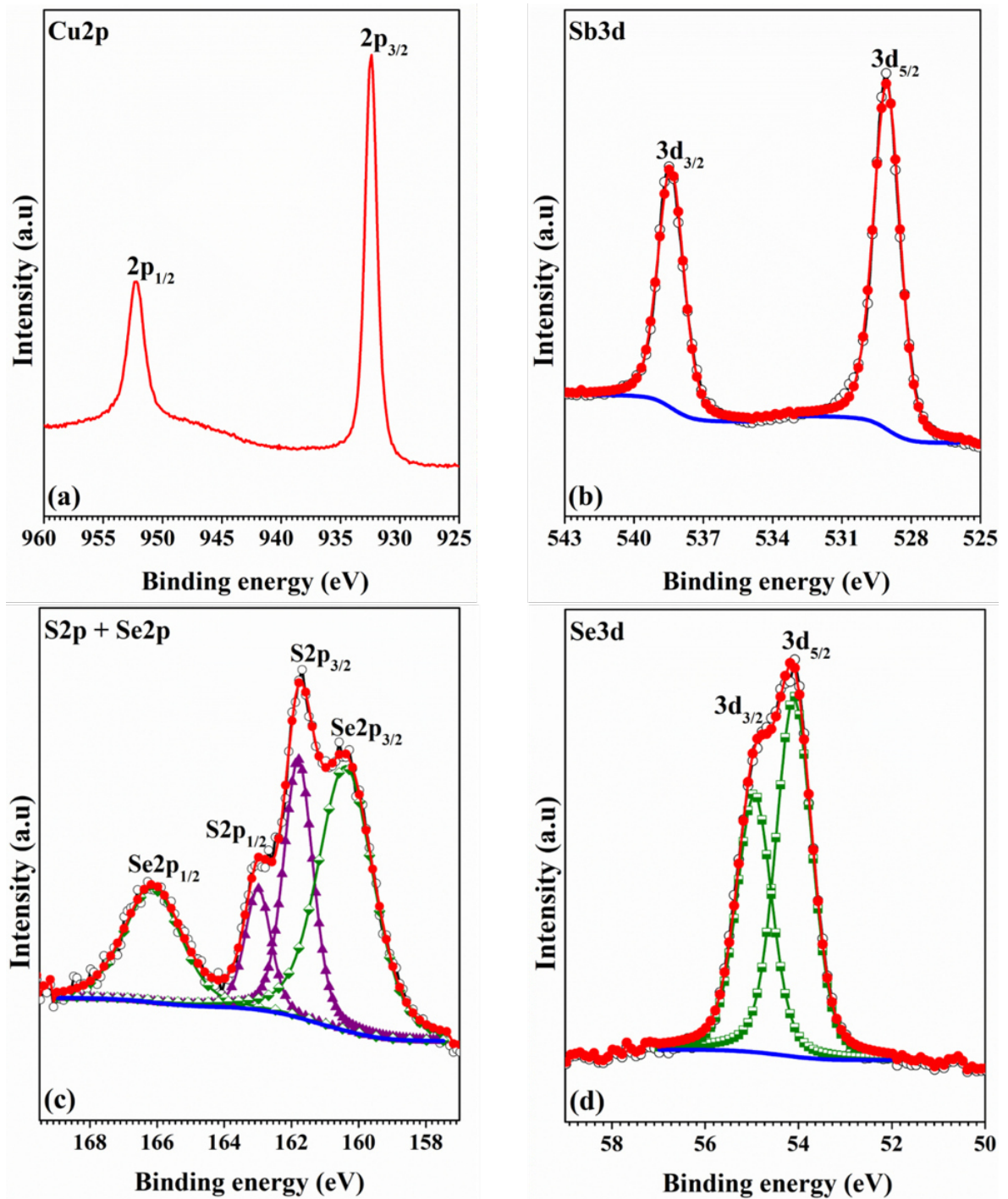
Figure 5.9: X-Ray photoelectron spectroscopy of Glass Sb$_2$S$_3$/Se/Cu precursor thin film annealed at 350 °C for 30 min in vacuum oven after Ar$^+$ ion etching, (a) Cu 2p core level (b) Sb 3d core level (c) S 2p core level (d) Se 3d core level.
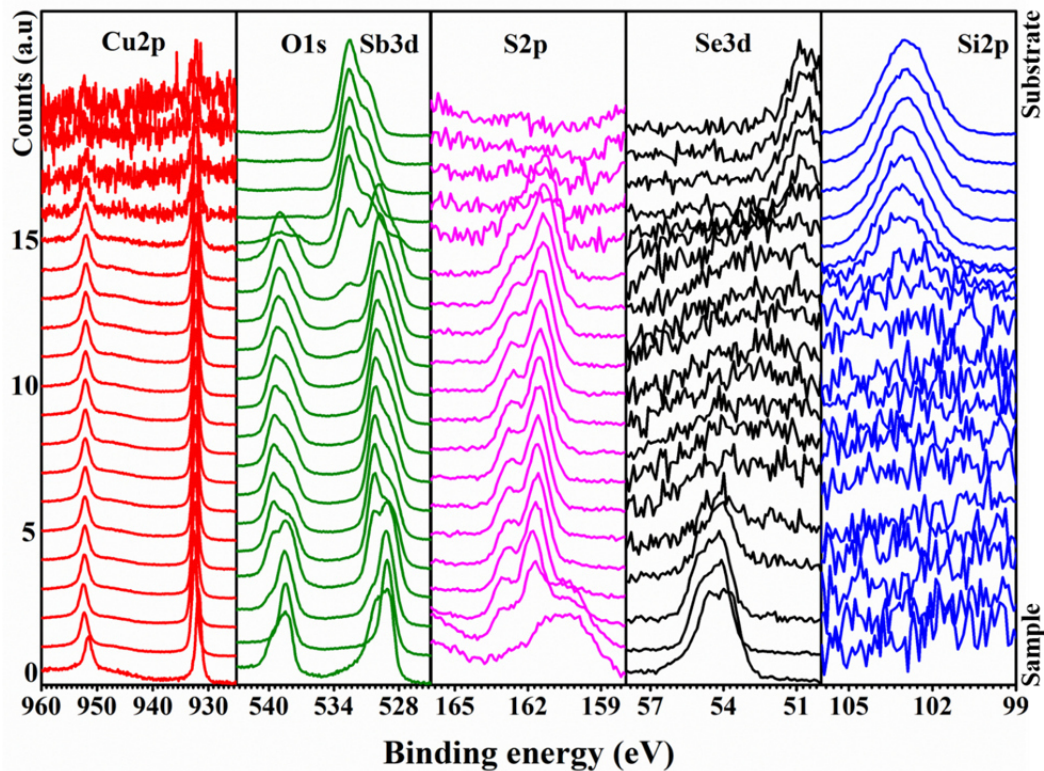
Figure 5.10: XPS depth profile of Glass Sb$_2$S$_3$/Se/Cu precursor thin film annealed at 350 °C for 30 min in vacuum.

1350 eV of glass/Sb$_2$S$_3$/Se, glass/Sb$_2$S$_3$/Se/Cu precursor thin films annealed at 350 °C for 30 min in vacuum oven after one cycle of etching using Ar$^+$ ions. Figure 5.9 (a-d) shows the high-resolution scans of Cu2p, S2p, Se3d and Sb3d respectively. Here, the Shirly method was used to compute the background of high-resolution scans of Cu2p, S2p, Se3d and Sb3d. Peaks from S2p, Se3d and Sb3d were deconvoluted using the Gaussian Lorentzian sum function. Figure 5.9(a) shows the core-level spectrum of copper 2p doublet which constitutes Cu2p$_{3/2}$ and Cu2p$_{1/2}$ peaks due to spin-orbit coupling with respective binding energies of 932.42 and 952.17 eV. The Sb3d core level spectrum and the deconvoluted peaks along with the resultant envelope are shown in Figure 5.9(b). From the figure, spin-orbit coupled Sb3d peaks at 529 eV (Sb3d$_{5/2}$) and 538.39 eV (Sb3d$_{3/2}$). In the case of Cu as well as Sb, the peaks were shifted lower energy comparing with the values reported for CuSbS$_2$ and this shift can be attributed to the formation of CuSbSe$_X$S$_{2-X}$ compound. Figure 5.9(c)
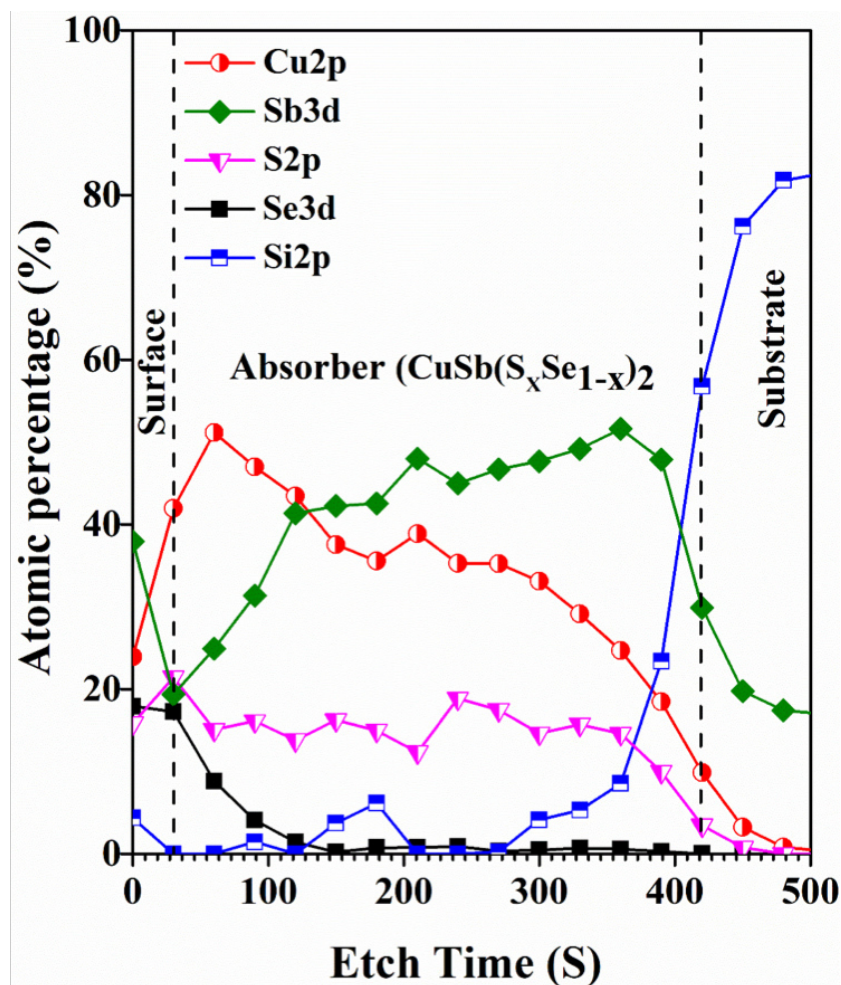
Figure 5.11: XPS profile montage of Glass Sb$_2$S$_3$/Se/Cu precursor thin film annealed at 350 °C for 30 min in vacuum.

shows the high-resolution spectrum scan for S2p. Two strong peaks at 161.7 eV and 162.9 eV with an energy separation of 1.2 eV were assigned to S2p$_{3/2}$ and S2p$_{1/2}$ respectively, where the extra peaks observed at 160.3 and 166.1 eV are assigned to Se2p$_{3/2}$ and Se2p$_{1/2}$ respectively. The high-resolution scan of Se3d is shown in Figure 5.9(d) where the two peaks are observed at 54.1 eV (Se3d$_{5/2}$) and 54.9 eV (Se3d$_{3/2}$) respectively. The formation of CuSbSe$_X$S$_{2-x}$ phase is clearly seen from the observable shift of Cu, Sb peaks and the binding energies of S, Se peaks, which are not corresponding any of their binaries. These results were in good agreement with that of the XRD and Raman analysis of the same sample.

The B.E profile montage and the respective composition analysis of the same sample is presented in Figure 5.10 and 5.11 respectively. Analysis of the depth profile data showed the uniformity of the Cu, Sb and S throughout the depth of the film. As observed from the Figure 5.10, the presence of selenium is only at the surface (up to the 5th etch level) due to the less duration of the deposition. The peak of Si was originated from the glass substrate.

(b) X-ray Fluorescence Spectroscopy (XRF)

Elemental composition of the glass/Sb$_2$S$_3$/Se and glass/Sb$_2$S$_3$/Se/Cu samples (where CBD of Sb$_2$S$_3$ at 25 °C for 4 h) annealed at 350 °C for 30 min in conventional vacuum oven were measured with a Fisherscope XUV-733 X-ray fluorescence (XRF) instrument and it is tabulated in the table given below.

Table 5.2: XRF measurements of Sb$_2$Se$_X$S$_{3-X}$, Sb$_2$S$_3$/Se with Cu thickness 5, 10, 20 and 50 nm.

Sample/Precursor	Cu (%)	Sb (%)	S (%)	Se (%)	Se/S (%)
Sb$_2$Se$_X$S$_{3-X}$		24.31	75.02	0.68	0.009
Sb$_2$S$_3$/Se_Cu 5 nm	0.807	39.4	59	0.79	0.013
Sb$_2$S$_3$/Se_Cu 10 nm	3.13	32.96	62.84	1.07	0.017
Sb$_2$S$_3$/Se_Cu 20 nm	5.62	30.6	62.7	1.08	0.017
Sb$_2$S$_3$/Se_Cu 50 nm	12.89	29.75	54.86	2.48	0.045

5.4.3 Morphology

Morphology, cross section SEM and EDX spectrum of the glass/Sb$_2$S$_3$/Se precursor thin film annealed at 350 °C for 30 min. are presented in Figure 5.12. The actual surface morphology of the selenized Sb$_2$S$_3$ sample is hard to determine from the SEM image as no particular grain morphology can be identified. However, some big spherical particles are present on the surface as indicated by the difference in the
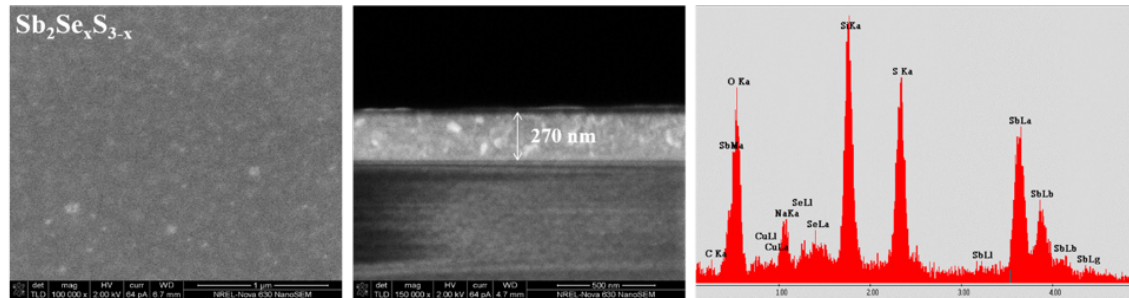
Figure 5.12: Scanning electron microscopy images, cross-sectional scanning electron micrographs and EDX for Sb$_2$Se$_X$S$_{3-X}$ thin films formed by annealing glass/Sb$_2$S$_3$/Se at 350 °C for 30 min.
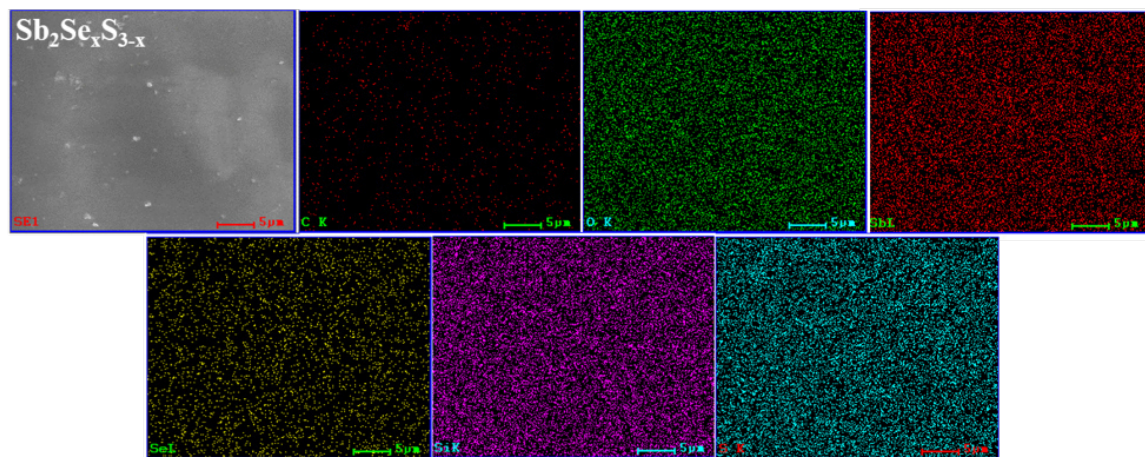
Figure 5.13: Scanning electron microscopy images and EDX mapping for Sb$_2$Se$_X$S$_{3-X}$ thin films formed by annealing glass/Sb$_2$S$_3$/Se at 350 °C for 30 min.

contrast. The cross-section image of the same was taken for determining the average thickness of the sample. The antimony sulfide sample after undergone selenization process shows thickness of around 270 nm as marked in the Figure. To confirm the elemental composition of the sample, EDX analysis was performed and the major elements detected were Sb, S, O, C, Se, Na and Si. Sb, S and Se are originated from the sample and O, C, Si from the substrate. Nevertheless, the EDX pattern confirmed that the sample was constituted by only the desired elements. Moreover, in addition to the XRD, XPS and Raman analyses, the EDX analysis also evidence the successful selenization of the Sb$_2$S$_3$ samples. Figure 5.13 depicts the SEM surface
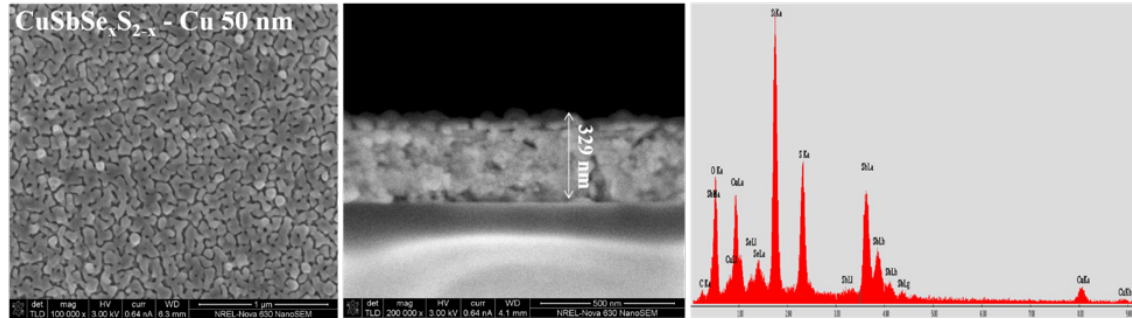
Figure 5.14: Scanning electron microscopy images, cross-sectional Scanning electron micrographs and EDX for CuSbSe$_X$S$_{2-X}$ thin films formed by annealing glass/Sb$_2$S$_3$/Se/Cu at 350 °C for 30 min.
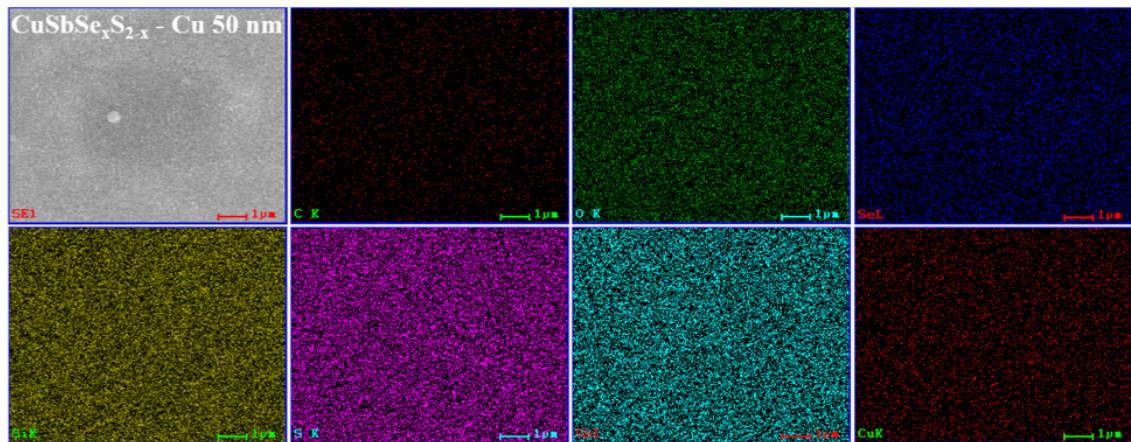
Figure 5.15: Scanning electron microscopy images and EDX mapping for CuSbSe$_X$S$_{2-X}$ thin films formed by annealing glass/Sb$_2$S$_3$/Se/Cu at 350 °C for 30 min.

morphology and elemental mapping of the Sb$_2$Se$_X$S$_{3-X}$ sample. From the elemental mapping of C, O, Cu, Se, Si, S and Sb, the uniform distribution of the elements on the sample surface can be clearly noticed.

Surface morphology, cross-section SEM image and EDX pattern of the CuSbSe$_X$S$_{2-X}$ thin film sample having 50 nm Cu thickness is presented in Figure 5.14. The CuSbS$_2$ sample after selenization, the surface of the films consists irregular shaped grains having well defined boundaries as seen in the image. Thickness of the CuSbSe$_X$S$_{2-X}$ layer was measured as 329 nm from the SEM cross-section analysis.

The EDX pattern of the CuSbSe$_X$S$_{2-X}$ sample also consists the peaks corresponding to the same elements as that in the Sb$_2$Se$_X$S$_{3-X}$ with the addition of the peaks corresponding to Cu.

Elemental mapping of the CuSbSe$_X$S$_{2-X}$ thin film sample formed by annealing the glass/Sb$_2$S$_3$/Se/Cu at 350 °C for 30 minutes shows the distribution of all desired elements on the sample surface as shown in Figure 5.15. Uniform distribution of Cu, Sb, S and Se can be seen from the EDX mapping.

5.4.4 Optical properties

Optical properties of the selenized Sb$_2$S$_3$, CuSbS$_2$ sample having 50 nm Cu and the pristine CuSbS$_2$ sample were measured using UV-Vis spectroscopy. Optical absorption spectra, transmittance and reflectance were measured using the glass substrates as references in the spectrophotometer. Sb$_2$S$_3$ and CuSbS$_2$ samples after selenization shows distinct absorption spectra as shown in Figure 5.16 where the absorption is higher for the CuSbSe$_X$S$_{2-X}$ thin film sample compared to the Sb$_2$Se$_X$S$_{3-X}$. Difference in the absorption between both samples is significant especially in the longer wavelength regions. Optical band gap of the selenized Sb$_2$S$_3$ and CuSbS$_2$ samples were calculated employing Tauc plot relation as shown in Figure 5.16. The Sb$_2$Se$_X$S$_{3-X}$ sample shows an optical band gap of 1.83 eV while the CuSbSe$_X$S$_{2-X}$ exhibits a much lower energy bang gap as 1.55 eV. Optical transmittance and reflectance of both these films are also presented in Figure 5.17. Both films show an average transmittance above 50% in the near infrared region whereas it decreases gradually as the wavelength of light is decreased. On the other hand, both samples display different reflectance behavior. The emerging quaternary CuSbSe$_X$S$_{2-X}$ material shows much lower reflectance compared to the Sb$_2$Se$_X$S$_{3-X}$. This also underlines the higher absorption of light in the CuSbSe$_X$S$_{2-X}$ as both thin film samples show similar kind of transmittance spectra.
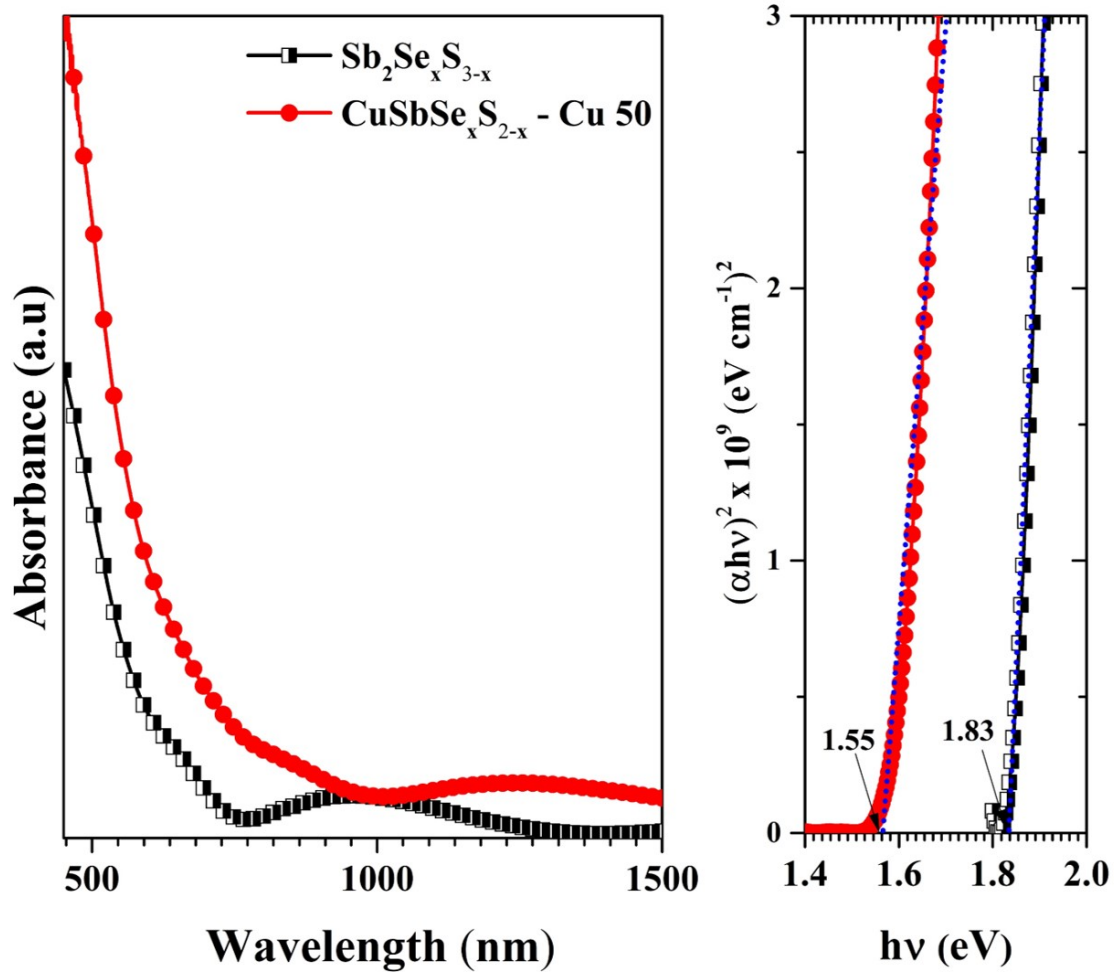
Figure 5.16: Optical absorption spectra and evaluation of optical band gap for Sb$_2$ Se$_X$S$_{3-X}$ and CuSbSe$_X$S$_{2-X}$ thin films formed by annealing glass/Sb$_2$S$_3$ /Se, glass/Sb$_2$S$_3$/Se/Cu50 nm at 350 °C for 30 min.

For better understanding, the optical properties of the CuSbSe$_X$S$_{2-X}$ sample is compared with that of the CuSbS$_2$ sample as shown in Figure 5.18. In this case also, it is evident that the selenized CuSbS$_2$ sample has higher absorption than the other. However, optical band gap of both these samples fall in the same range as 1.55 and 1.57 eV respectively for CuSbSe$_X$S$_{2-X}$ and CuSbS$_2$. This slight variation of band gap maybe due to the formation of the quaternary phase only on the surface of the sample. A slightly lower optical band gap for the selenized sample suggests that it can perform similar or better than CuSbS$_2$ thin films when integrated in
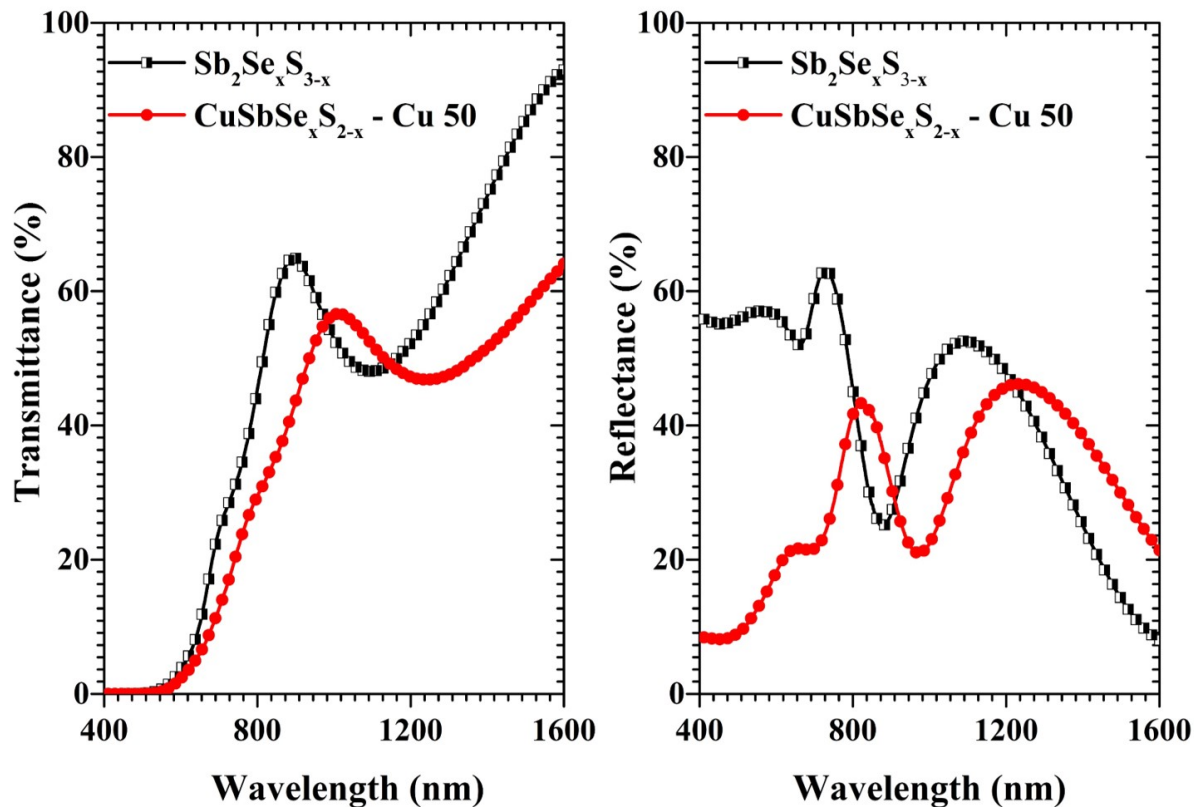
Figure 5.17: Transmittance (T) Spectra, Reflectance (R) spectra for Sb$_2$Se$_X$S$_{3-X}$ and CuSbSe$_X$S$_{2-X}$ thin films formed by annealing glass/Sb$_2$S$_3$/Se, glass/Sb$_2$S$_3$/Se/Cu50 nm at 350 °C for 30 min.

photovoltaic device applications. Optical properties of the CuSbSe$_X$S$_{2-X}$ thin films in general found to be better than both Sb$_2$Se$_X$S$_{3-X}$ as well as CuSbS$_2$ samples. This emerging quaternary material therefore can be used for applications including opto-electronics and photovoltaics. In the case of CuSbSe$_X$S$_{2-X}$ thin films were fabricated following the similar procedure as that in this thesis work, two different transitions were observed, one at 1.4 and another one at 1.2 eV [152]. In that case, the optical transition occurred at 1.4 eV was corresponding to the CuSbSe$_X$S$_{2-X}$ solid solution whereas the one at 1.2 eV was attributed to the Cu$_2$S impurity phase as reported by Colombara et al. [67] and Klimov et al [214].
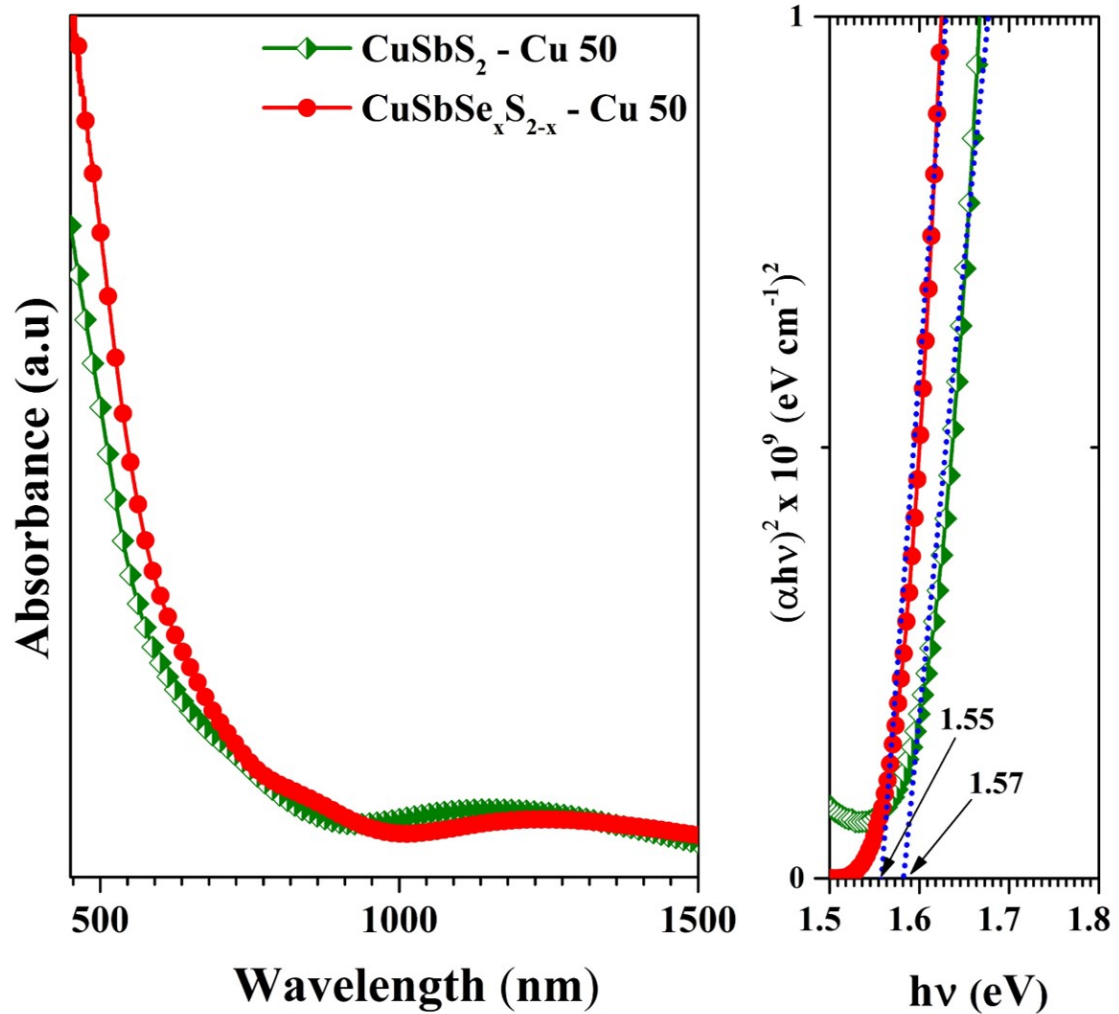
Figure 5.18: Optical absorption spectra and evaluation of optical band gap for CuSbS$_2$ and CuSbSe$_X$S$_{2-X}$ thin films formed by annealing glass/Sb$_2$S$_3$/Cu, glass/Sb$_2$S$_3$/Se/Cu50 nm at 350 °C for 30 min.

5.4.5   Electrical properties

Electrical properties of the Sb$_2$Se$_X$S$_{3-X}$ and CuSbSe$_X$S$_{2-X}$ thin films were analyzed by measuring the I-V curves and photoconductivity and compared both with that of bare CuSbS$_2$ thin films. Figure 5.19 shows the I-V curves of the Sb$_2$Se$_X$S$_{3-X}$, CuSbSe$_X$S$_{2-X}$ and CuSbS$_2$ thin films. From the figure, all the three thin films show an ohmic type behavior irrespective of the thin film forming condition/different pre-
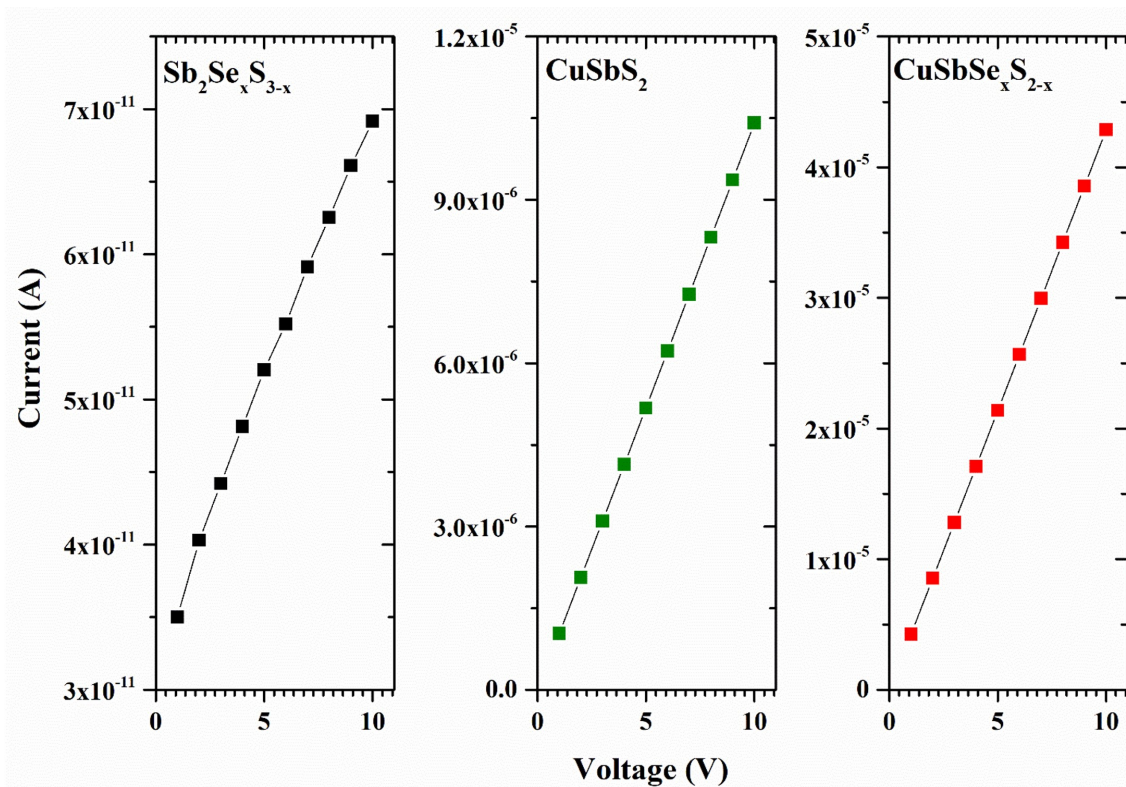
Figure 5.19: Current (I) - Voltage (V) characteristics of for Sb$_2$Se$_X$S$_{3-X}$, CuSbS$_2$, CuSbSe$_X$S$_{2-X}$ thin films formed by annealing - glass/Sb$_2$S$_3$/Se, glass/Sb$_2$S$_3$/Se/Cu50 nm and glass/Sb$_2$S$_3$/Cu at 350 °C for 30 min.

cursor layers used. However, a notable difference on the order of measured current can be observed where the Sb$_2$Se$_X$S$_{3-X}$ exhibits lower conductivity in comparison with both CuSbSe$_X$S$_{2-X}$ and CuSbS$_2$ thin films. Photoconductivity measurements were done by illuminating the thin film precursor layers using a halogen lamp and simultaneously measuring the current for evalutaing the opto-electronic properties of these films. Photoresponse measurements of Sb$_2$Se$_X$S$_{3-X}$, and CuSbSe$_X$S$_{2-X}$ samples are depicted in Figure 5.20 a bias voltage of 10 V is applied. The dark conducitivity of the CuSbSe$_X$S$_{2-X}$ thin film is almost 5 orders of magnitude higher compared to the dark conductivity of the glass/Sb$_2$S$_3$/Se thin film as seen from the y-axis of the photoresponse measurement curves. However, in both cases, the measured current shows a significant increase upon illumination due to the additional charge generation in these thin films and then again decrease as soon as the illumi-
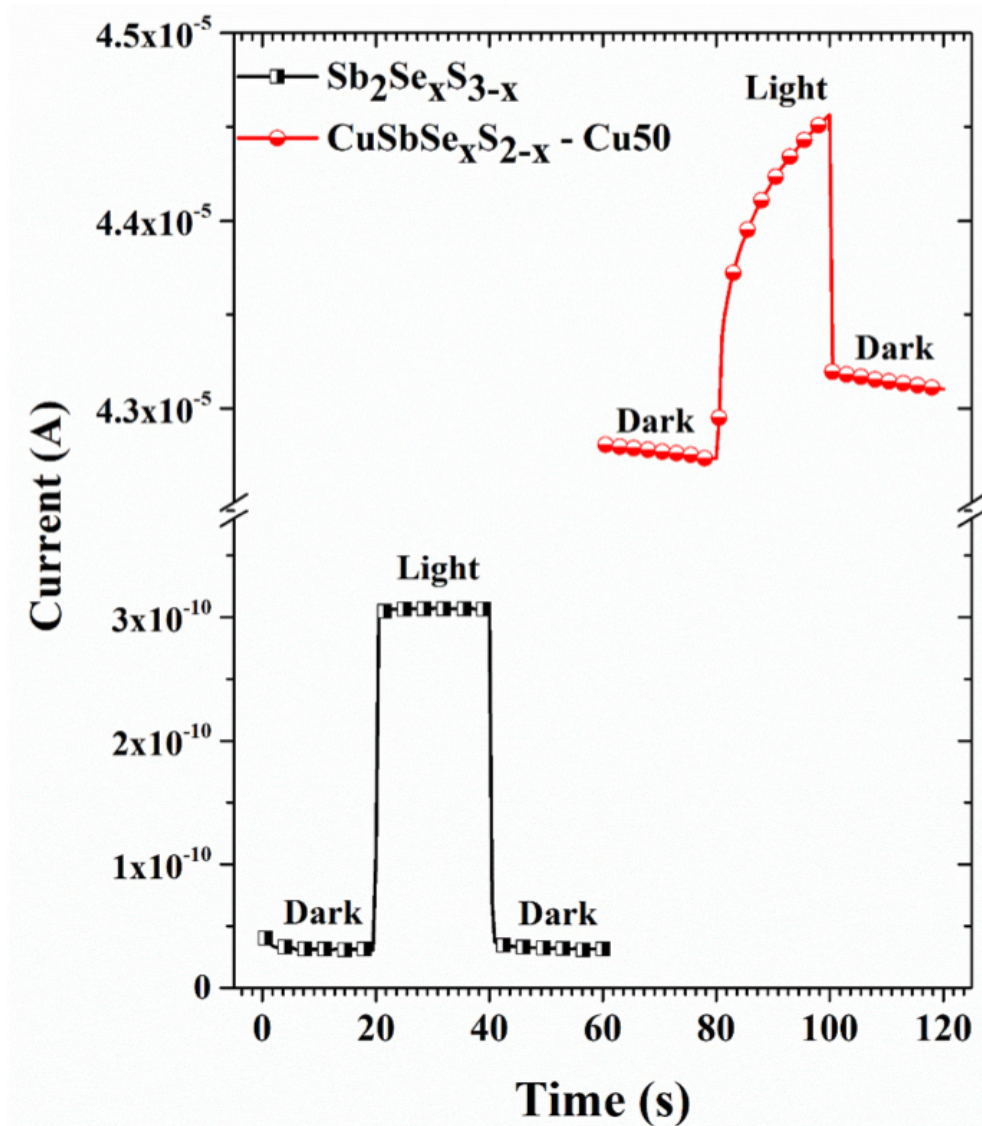
Figure 5.20: Photocurrent response curves for Sb$_2$Se$_X$S$_{3-X}$ and CuSbSe$_X$S$_{2-X}$ thin films formed by annealing glass/Sb$_2$S$_3$/Se, glass/Sb$_2$S$_3$/Se/Cu50 nm at 350 °C for 30 min.

nation is turned off. In the present experiment, for each sample, the current was measured first for 20 sec in dark followed by 20 s under illumination using a halogen lamp and then again another 20 s in dark. The photocurrent switch immeadiately as the ilumination is either turned on or off. One major difference between the photoresponse measurements of the Sb$_2$Se$_X$S$_{3-x}$ and CuSbSe$_X$S$_{2-x}$ samples is that, in the case of the CuSbSe$_X$S$_{2-x}$ thin film, the photo generated current does not come back
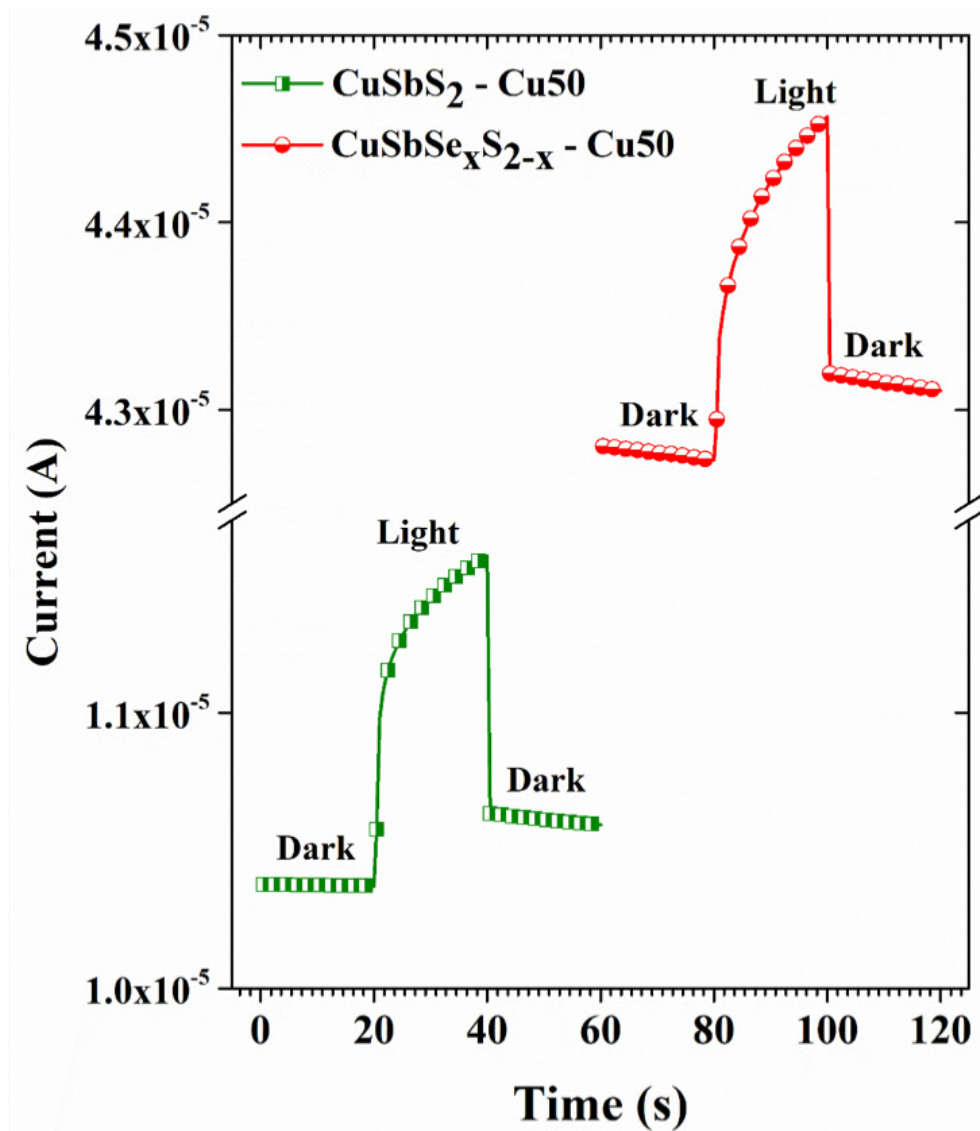
Figure 5.21: Photocurrent response curves for CuSbS$_2$ and CuSbSe$_X$S$_{2-X}$ thin films formed by annealing glass/Sb$_2$S$_3$/Cu, glass/Sb$_2$S$_3$/Se/Cu50 nm at 350 °C for 30 min.

to the ground state within the measured time interval in contrast to the Sb$_2$Se$_X$S$_{3-x}$ layer where the current comes back to the initial state immediately after turning the illumination off. This could be attributed to the higher density of defects in the CuSbSe$_X$S$_{2-X}$ thin films than the other and hence the generated charge carriers are trapped inside these defects which delay the recombination process [152]. Figure 5.21 displays the photoresponse comparison between the bare CuSbS$_2$ and CuSbSe$_X$S$_{2-X}$ thin films where the selenized sample shows an enhanced photoresponse compared

to the other. However, the shape of the photoresponse curves in both cases remain the same. This indicates that the CuSbS$_2$ sample after selenization may effectively replace the Sb$_2$Se$_X$S$_{3-X}$ or the CuSbS$_2$ samples for different applications owing to its better opto-electronic properties. To determine and compare the photovoltaic parameters of the CuSbSe$_X$S$_{2-X}$ thin films, they were tested as absorber layers in solar cells and the results are described in the following section.

5.4.6   Device properties

(a) J-V Characteristics
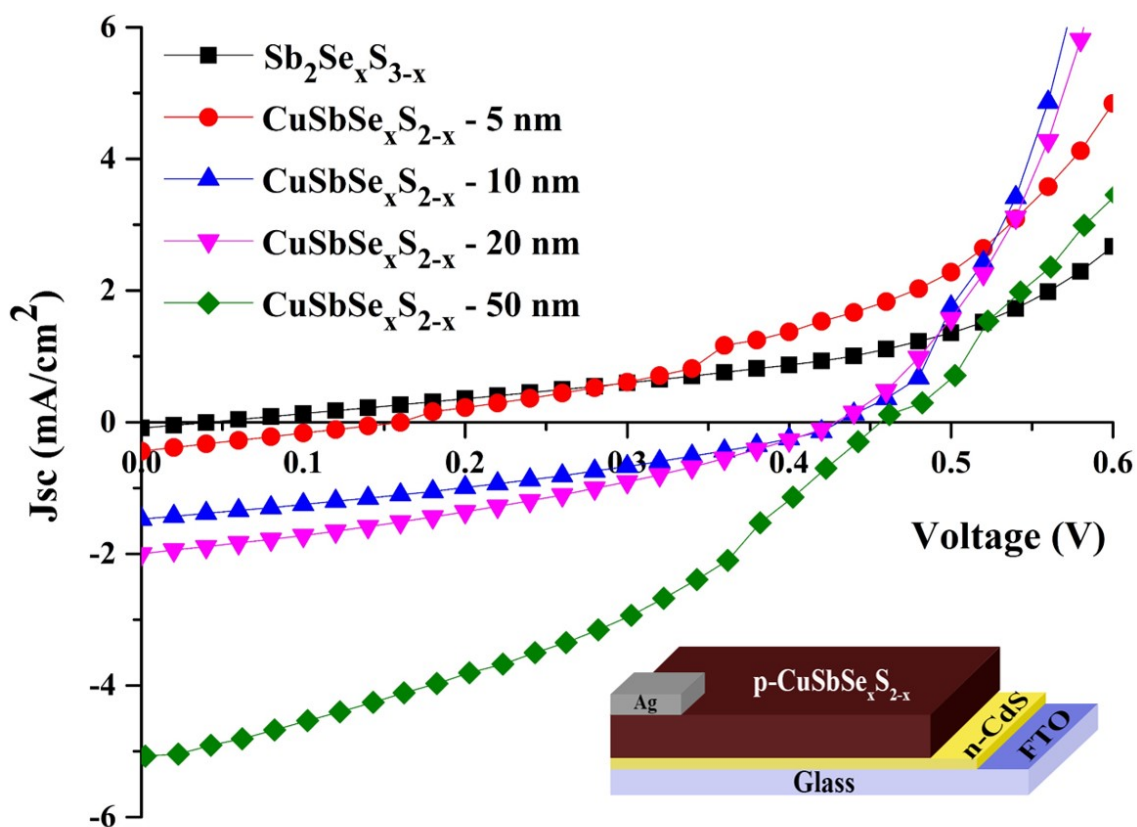
Figure 5.22: Evaluation of J-V characteristics of the glass/FTO/n-CdS/p-Sb$_2$Se$_X$ S$_{3-X}$, glass/FTO/n-CdS/p-PV devices (using Cu-5, 10, 20 and 50 nm film).

Device properties of the Sb$_2$Se$_X$S$_{3-X}$ and CuSbSe$_X$S$_{2-X}$ having Cu thicknesses 5, 10, 20 or 50 nm were tested by integrating these layers as absorber lay-

ers in solar cells in the substrate configuration glass/FTO/n-CdS/p-Sb$_2$Se$_X$S$_{3-X}$ [or CuSbSe$_X$S$_{2-x}$]. The corresponding J-V measurements for the solar cells under an illumination from a solar simulator of otput power density 100 mW/cm^2 are depicted in Figure 5.22. It can be easily identified that the solar cell with having a Cu thickness of 50 nm outperforms all others in terms of device performnace (indicated by the green curve in Figure 5.22). This can be directly correlated with the enhanced properties of the film as described in the previous sections of the chapter. A trend can be noticed in the device properties of the films where the glass/FTO/n-CdS/p-Sb$_2$Se$_X$S$_{3-X}$ shows the lowest solar cell efficiency and then gradually increases with the Cu thickness in the glass/FTO/n-CdS/p-CuSbSe$_X$S$_{2-X}$ layers. The solar cell efficiencies correspnding to the different samples are tabulated in the Table 5.3

Table 5.3: Photovoltaic parameters of and glass/FTO/n-CdS/p-CuSbSe$_X$S$_{2-X}$/Ag solar cells with varying Cu thicknesses 5, 10, 20 and 50 nm formed by annealing at 350 °C for 30 min

PV device (glass/FTO/CdS/Sb$_2$S$_3$/Se/Cu/Ag)	V_{oc} (Volt)	J_{sc} (mA/cm^2)	FF	Efficiency η (%)
glass/FTO/CdS/Sb$_2$S$_3$/Se	0.06	0.06	0.25	0.001
glass/FTO/CdS/Sb$_2$S$_3$/Se/Cu : Cu 5nm	0.16	0.43	0.25	0.02
glass/FTO/CdS/Sb$_2$S$_3$/Se/Cu : Cu 10nm	0.43	1.44	0.34	0.21
glass/FTO/CdS/Sb$_2$S$_3$/Se/Cu : Cu 20nm	0.43	1.97	0.34	0.29
glass/FTO/CdS/Sb$_2$S$_3$/Se/Cu : Cu 50nm	0.46	5.08	0.38	0.91

Efficiency of the cell having CuSbSe$_X$S$_{2-X}$-Cu50 nm as the absorber layer presents a photoconversion efficiency of 0.91% which is much higher compared to a similar solar cell configuration but having the bare CuSbS$_2$ as the absorber material (chapter 4). External Quantum Efficiency (EQE) of the glass/FTO/n-CdS/Sb$_2$S$_3$/Se and glass/FTO/n-CdS/p-Sb$_2$S$_3$/Se/Cu PV devices using varying Cu thicknesses 5, 10, 20 and 50 nm fabricated by annealing at 350 °C for 30 min are shown in Figure 5.23(a). As observed in the given figure, the better EQE curves were observed for the

glass/FTO/n-CdS/p-CuSbSe$_X$S$_{2-X}$ with Cu 50 nm thickness. 10-21% EQE were observed in the wavelength region of 350-550 nm which is comparably higher than that glass/FTO/n-CdS/p-CuSbS$_2$ with Cu 50 nm thickness (Figure 5.23(b)). Hence, the seleneziation of the CuSbS$_2$ layers could be a very important step towards the high performance photovoltaic devices as required by the current and future scenarios incorporating a material having earth abundant constituents.
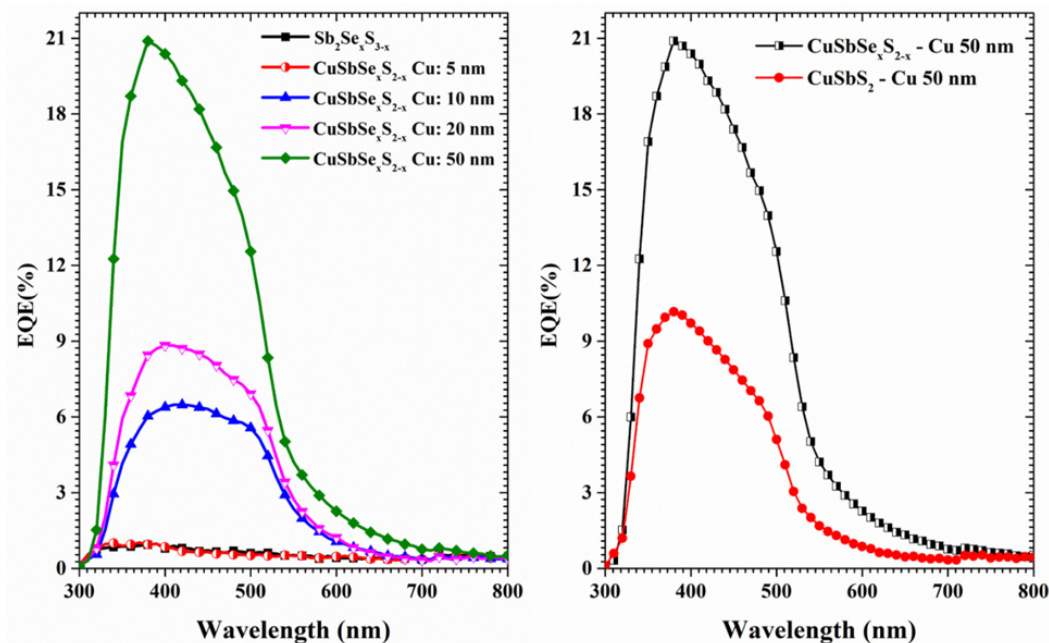
Figure 5.23: EQE measurement of (a) glass/FTO/n-CdS/p-Sb$_2$Se$_X$S$_{3-X}$, glass/FTO/n-CdS/p-CuSbSe$_X$S$_{2-X}$PV devices using varying Cu thicknesses 5, 10, 20 and 50 nm fabricated by annealing at 350 °C for 30 min (b) EQE measurements of glass/FTO/n-CdS/p-CuSbSe$_X$S$_{2-X}$ and glass/FTO/n-CdS/p-CuSbS$_2$ for comparison.

The high-resolution spectra and depth profile by the XPS analysis of the PV device (glass/FTO/n-CdS/p-/Sb$_2$S$_3$/Se/Cu 50 nm at 350 °C for 30 min) shown in Figure 5.24 and 5.25 respectively. Here, the high-resolution spectra of Cu2p, S2p and Sb3d are presented in Figure 5.24(a), 5.24(b), and 5.24(c). The core level spectrum of copper shows the 2p doublet which constitutes Cu2p$_{3/2}$ and Cu2p$_{1/2}$ peaks due to spin orbit coupling with respective binding energies of 932.2 and 952.2 eV which do
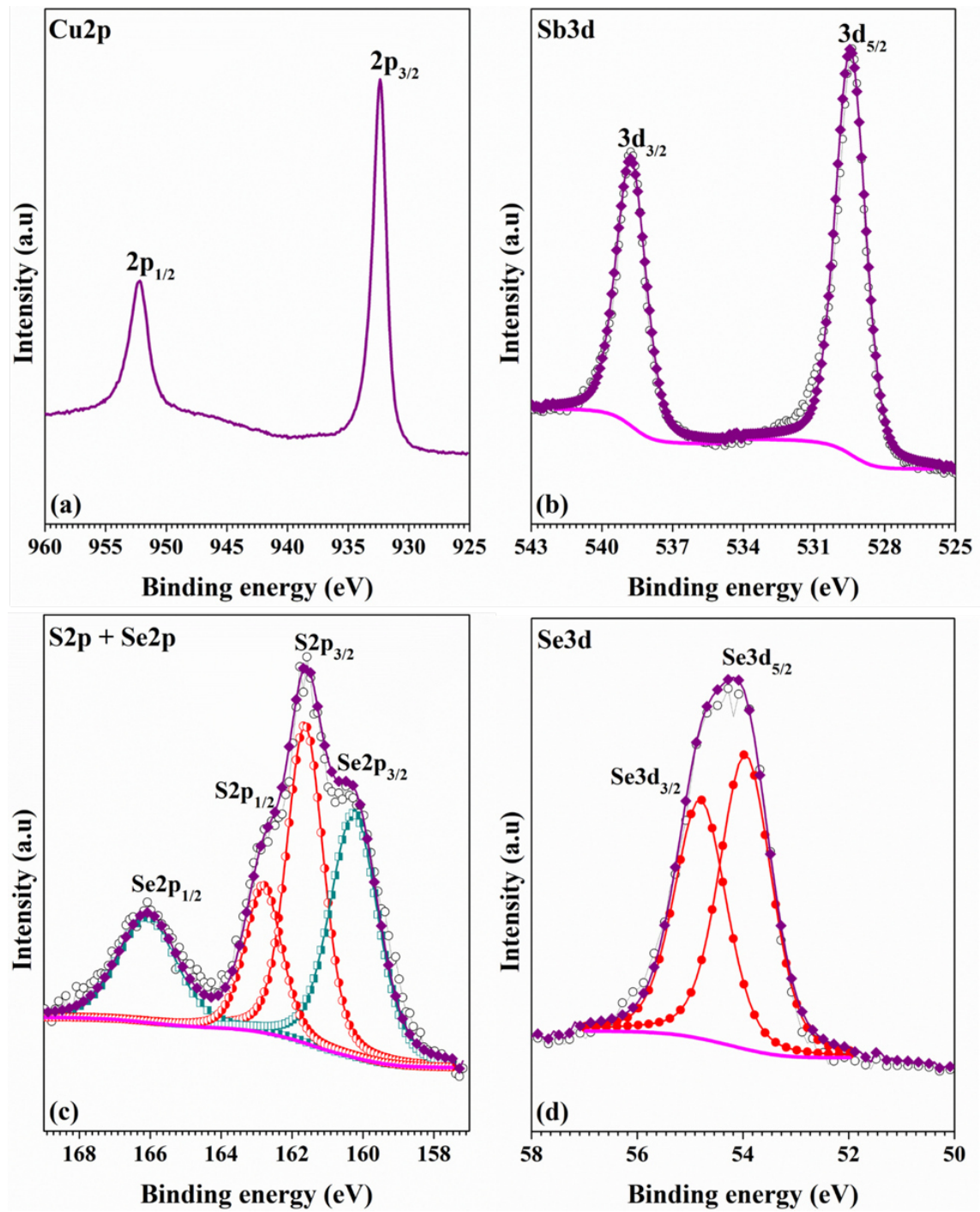
Figure 5.24: X-ray photoelectron spectroscopy of glass/FTO/CuSbSe$_X$S$_{2-X}$-Cu 50 nm precursor thin film annealed at 350 °C for 30 min in vacuum oven after Ar$^+$ ion etching, (a) Cu2p core level (b) Sb3d core level (c) S2p core level (d) Se3d core level.
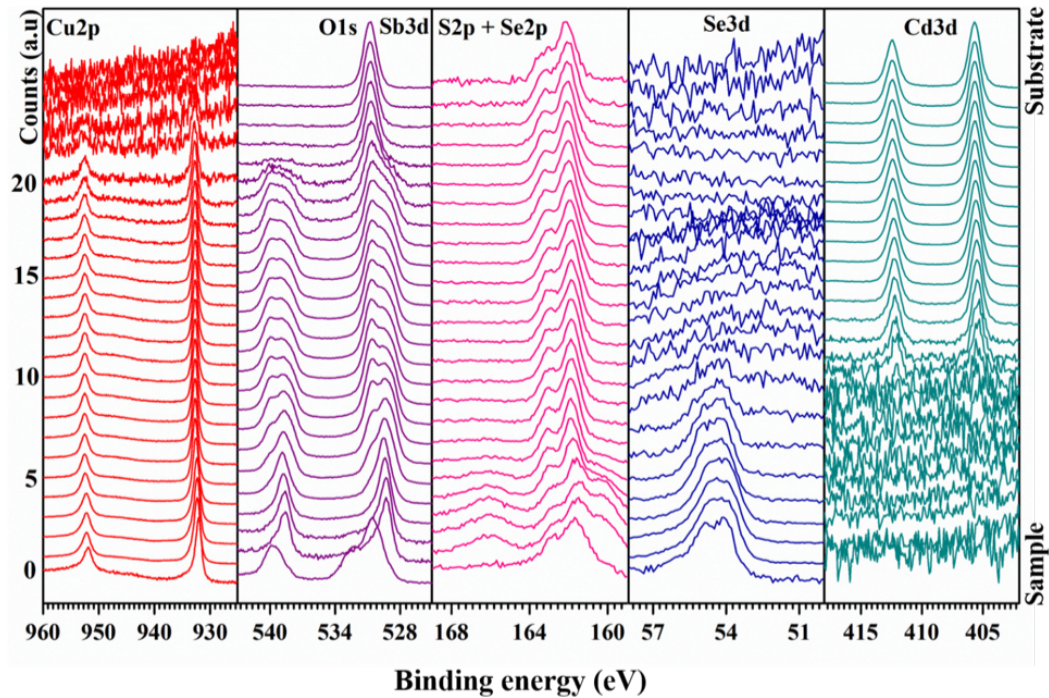
Figure 5.25: XPS depth profile of glass/FTO/CuSbSe$_X$S$_{2-X}$-Cu 50 nm.

not match with the formation of CuSbS$_2$ or elemental Cu, implying the formation of new quaternary compound, since there is no XPS reports are available for this compound. The Sb3d core level spectrum and the deconvoluted 3d peaks at 529.3 eV (Sb3d$_{5/2}$) and 538.69 eV (Sb3d$_{3/2}$) (Figure 5.24(b)). In the case of Cu as well as Sb, the peaks were shifted lower energy comparing with the values reported for CuSbS$_2$ and this shift can be attributed to the formation of compound. The observed peak values of Cu and Sb for this present cells are well matching with the observed Cu and Sb peak position for the glass/Sb$_2$S$_3$/Se/Cu_50 film and which supports the formation of the quaternary phase. The high-resolution spectra scan for S2p, Figure 5.24(c) shows two strong peaks at 161.6 eV and 162.8 eV with an energy separation of 1.2 eV were assigned to S2p$_{3/2}$ and S2p$_{1/2}$ respectively, along with that a Se2p$_{3/2}$ and Se2p$_{1/2}$ core levels are present in the analysis region of S2pcore levels, and these peaks located at 160.2 eV and 166.1 eV respectively do not corresponds to a compound containing selenium. The high-resolution scan of Se3d is shown in Figure 5.8(d) where the two peaks are observed at 54.1 eV (Se3d$_{5/2}$) and 54.9 eV (Se3d$_{3/2}$)

respectively, which do not match with any selenium compound reported. Combining our results of the B.E values of Cu2p, Sb3d , S2p, Se3p and Se3d core levels and the phases detected in our XRD results, the formation of can be concluded. The depth profile analysis of the same cell is given in Figure 5.25. The uniformity of the Cu, Sb, S and Se elements throughout the depth of the film is clearly seen in this figure. From this analysis it is also observed that the presence of selenium is only in the surface of the thin film (up to 5th etch level), which means the complete reaction of Se with other elements are occur only at the surface of the sample and these results is in good agreement with that of the XRD results obtained for the same film prepared on the glass substrates.
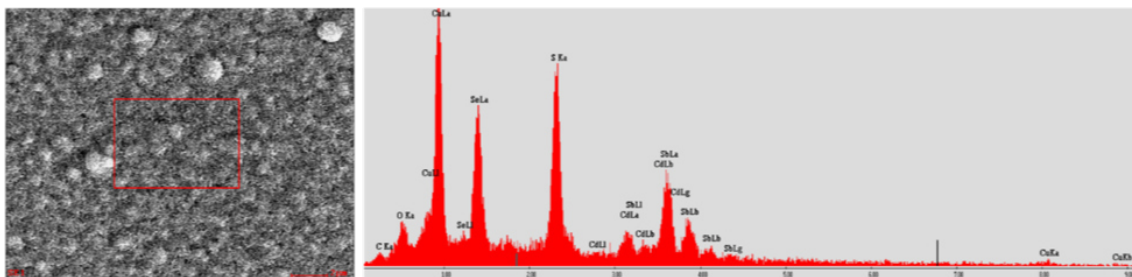
Figure 5.26: Scanning electron microscopy images and EDX for glass/FTO/n-CdS/p-CuSbSe$_X$S$_{2-X}$ formed by annealing glass/FTO/CdS/Sb$_2$S$_3$/Se/Cu_50 nm at 350 °C for 30 min.

Surface morphology and EDX analysis of the solar cell, glass/FTO/CdS/CuSb Se$_X$S$_{2-X}$-Cu50 nm is presented in Figure 5.26. As seen from the image, the CuSbS$_2$ sample after selenization possess totally different surface morphology compared to that of the bare CuSbS$_2$ sample (Chapter 4, Figure 4.26). The surface of the films consists irregular shaped grains having well defined boundaries as seen in the image. The EDX analysis of the sample also collected to determine the elemental composition. The major peaks in the EDX analysis were corresponding to the characteristic X-rays of Sb, S, Se and Cu together with adventitious C and O indicating that the sample is composed of only the desired elements (5.27). The EDX elemental mapping of the solar cell revealed the uniform distribution of each element such as Sb, S, Se and Cu on the surface without any other impurities. SEM images and EDX
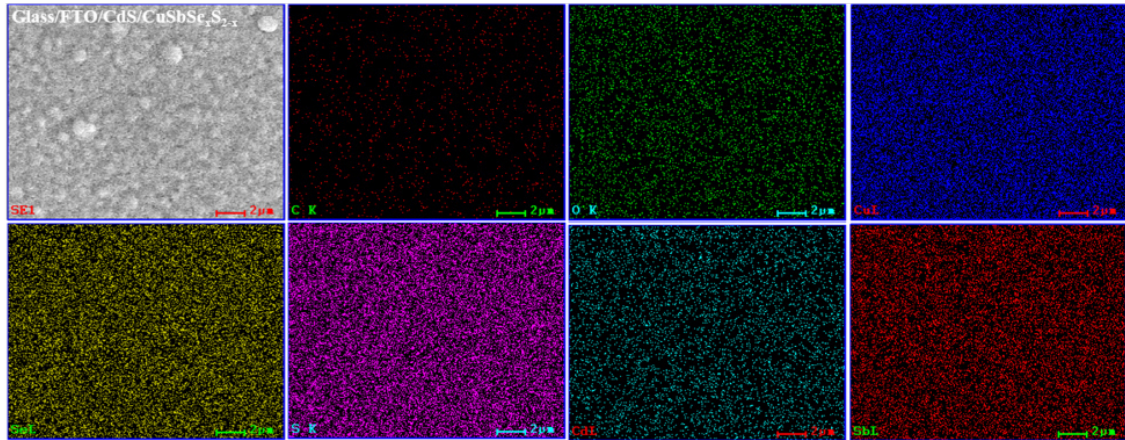
Figure 5.27: Scanning electron microscopy images and EDX mapping for glass/FTO/ n-CdS/p-CuSbSe$_X$S$_{2-X}$ formed by annealing glass/FTO/CdS/Sb$_2$S$_3$ /Se/ Cu_50 nm at 350 °C for 30 min.

mapping data confirm the formation of the absorber layer in the PV device.

In conclusion, we have synthesized thin films by depositing selenium over glass/Sb$_2$S$_3$ layers followed by Cu evaporation and heat treatments. The structure, morphology, elemental composition, chemical state, optical, electrical and optoelectronic properties were studied in detail using various characterization techniques. While XRD and Raman analyses confirmed the formation of the thin films identified from the peak shift compared to the bare CuSbS$_2$ analysis of different thin film properties revealed that the CuSbSe$_X$S$_{2-X}$ performs better than CuSbS$_2$ in terms of electrical conductivity and optical absorption. Analysis of the effect of different Cu thickness led to the finding that Cu 50 nm is an appropriate Cu thickness for better thin film characteristics. Based on the results obtained, the CuSbSe$_X$S$_{2-X}$ were finally tested as absorber layers in solar cell prototypes where it showed enhanced performance in comparison with both CuSbS$_2$ as well as Sb$_2$Se$_X$S$_{3-X}$ thin films. The improved efficiency of the cells having the structure glass/FTO/n-CdS/p-CuSbSe$_X$S$_{2-X}$ could be directly attributed to the properties of the layers. It was found that the selenization step plays an important role in altering the characteristics of the CuSbS$_2$ thin films and thereby making it a better choice for PV device

applications. However, more work is needed in this direction to further optimize the selenization stage and thereby enhancing more the solar cell charateristics incorporating these thin film layers.

Chapter 6

CONCLUSIONS

This thesis presents the synthesis and characterization of copper antimony sulfide ($CuSbS_2$) and copper antimony selenosulfide $CuSbSe_XS_{2-X}$ thin films by combined chemical bath deposition (CBD) and thermal evaporation followed by heat treatments as well as their application in the field of photovoltaics and photodetectors. For synthesis of thin film precursors, chemical bath deposition technique to deposit Sb_2S_3 thin films on which the Cu layer was evaporated. The effects of Sb_2S_3/Cu layer thicknesses and the type of heat treatments such as Rapid Thermal Processing (RTP), conventional vacuum oven annealing or both and at different temperatures as well as durations on the formation of phase pure $CuSbS_2$ phase were studied in detail. In summary,

- A systematic study on the growth of $CuSbS_2$ thin films on glass substrates for conventional annealing (380 °C for 1 h) by varying Cu content (1-100 nm) for a given Sb_2S_3 (25 °C for 2 h) layer thickness of 200 nm.

- Analysis of the thin films formed at different conditions using various characterization techniques to determine their crystalline structure, morphology, elemental composition, chemical state, and photo - physical properties.

- For a given Sb_2S_3 thickness (200 nm), Cu 50 nm was effective for the formation of orthorhombic $CuSbS_2$.

185

- Formation of $CuSbS_2$ along with Cu_2S (minor presence of binary) by conventional annealing (350 - 380 °C , 30 - 60 min) due to slow heating and cooling.

- Removal of binary phases to form phase pure $CuSbS_2$ on glass substrates by RTP above 500 °C due to instantaneous heat supply.

- Highly oriented $CuSbS_2$ growth on glass by conventional annealing followed by RTP (pre-annealed RTP)above 600 °C .

- Photoconductive $CuSbS_2$ films with crystallite size (15-20 nm) with optical band gap values 1.5 - 1.6 eV.

- The $CuSbS_2$ thin films were incorporated in photovoltaic structures of superstrate p-n configuration: glass/ITO/n-CdS/p-$CuSbS_2$. Both conventionally annealed and the direct RTP devices showed PV effect with typical parameters of V_{oc}= 485 mV, J_{sc}= 1.5-2.3 mA/cm^2, FF = 0.4 and the conversion eciency (η) = 0.3%.

- The PV devices formed by pre-annealed RTP grown device showed an open-circuit voltage (V_{oc}) of **665 mV** and a fill factor (FF) of **0.6**, the highest values ever reported for $CuSbS_2$ based PV devices establishing the perspective of $CuSbS_2$ for high eciency PV devices. J_{sc}value for this device was 1.3 mA/cm^{2}and the η = 0.6%, relatively lower values.

- The $CuSbS_2$ thin films formed at two different conditions were incorporated in photovoltaic structures of superstrate p-n configuration: glass/FTO/n-CdS/p-$CuSbS_2$. Among the cells fabricated at different conditions, the one with 4 h Sb_2S_3having Cu thickness 50 nm outperformed other PV devices in terms of J_{sc}(3 mA/cm^2).

- PV devices with p-i-n configuration glass/FTO/n-CdS/i-Sb_2S_3/p-$CuSbS_2$/Ag using bare Sb_2S_3(25 °C 1 h annealed conventionally at 350 °C for 30 mins) as the intrinsic layer and e the cell showed improved performance V_{oc}= **483 mV,** J_{sc}= **7.2 mA/cm^2, FF = 0.28 and conversion eciency nearly 1%**

- Synthesis of $CuSbSe_XS_{2-X}$ thin films by dipping glass/Sb_2S_3 in sodium seleno-sulfate solution forllowed by Cu evaporation and heat treatment at $350\,°C$ for 30 min in conventional vacuum oven.

- The structure, morphology, elemental composition, chemical state, optical, electrical and opto-electronic properties were studied in detail using various characterization techniques. XRD and Raman analyses confirmed the formation of the $CuSbSe_XS_{2-X}$ thin films identified from the peak shift compared to the bare $CuSbS_2$.

- Improved optical absorption and electrical conductivity of $CuSbSe_XS_{2-X}$ thin films compared to that of $CuSbS_2$ films.

- Glass/FTO/n-CdS/p-$CuSbSe_XS_{2-X}$/Ag devices showed PV parameters $V_{oc}=$ 462 mV, $J_{sc}=$ 5.07 mA/cm^2, FF = 0.38 and the conversion eciency of 0.91%.

- The selenization step plays an important role in altering the characteristics of the $CuSbS_2$ thin films and thereby making it a better choice for PV device applications.

- For the first time ever, explored the capability of the $CuSbS_2$ as a photodetector for a wide range of wavelengths (Vis to NIR region). We found that $CuSbS_2$ has great potential as a photodetector as well owing to its high sensitivity towards detection of different wavelengths.

- Photoresponse measurements of all the samples were recorded as a function of incident light wavelength using LEDs as well as function of incident light intensity using a laser. All the samples showed stable, reproducible photodetector properties with high sensitivity and responsivity even at a low applied bias voltage. This study can help in cost effective production of photodetector devices using environment friendly materials with selective wavelength detection properties at low cost in large area.

In general, the study delivers a thorough understanding on the structure, morphology and photophysical properties of the emerging ternary and quaternary $CuSbS_2$ and $CuSbSe_XS_{2-X}$ thin films and how these properties can be altered simply by adjusting the deposition parameters. The work inspires research towards fabrication of photovoltaic and opto-electronic devices using earth abundant, cost-effective and low-toxic semiconductor thin film materials. For any further optimization of the thin film properties and thereby enhancement in the device performance either by following the same synthetic route or by different methods, this study can serve as an initial step.

REFERENCES

[1] McLamb, "E. energy." https://www.ecology.com/2011/09/06/fossil-fuels-renewable-energy-resources/, 2011.

[2] G. Kanniah, *Fossil fuels*, 2010. `https://www.studentenergy.org/topics/fossil-fuels`.

[3] M. Hannah Ritchie, *Fossil Fuels*, 2017. `https://ourworldindata.org/fossil-fuels`.

[4] C. Nunez, *Global warming solutions, explained*, 2019. `https://www.nationalgeographic.com/environment/global-warming/global-warming-solutions/`.

[5] A. G. Chmielewski, "Environmental effects of fossil fuel combustion," *Interaction: Energy/Environment*, 1999.

[6] A. H. Eldin, M. Refaey, and A. Farghly, "A review on photovoltaic solar energy technology and its efficiency," in *17th international middle-east power system conference (mepcon'15), at mansoura university, egypt*, pp. 1–7, 2015.

[7] P. G. V. Sampaio and M. O. A. González, "Photovoltaic solar energy: Conceptual framework," *Renewable and Sustainable Energy Reviews*, vol. 74, pp. 590–601, 2017.

[8] T. history of Solar, *energy*, 2014. `https://www1.eere.energy.gov/solar/pdfs/solar_timeline.pd`.

[9] L. M. Fraas, "History of solar cell development," in *Low-Cost Solar Electric Power*, pp. 1–12, Springer, 2014.

[10] A. L. H. of Solar Cells, *A Little History of Solar Cells*, 11. `https://ocw.tudelft.nl/wp-content/uploads/solar_energy_section_11.pdf`.

[11] A. Blakers, N. Zin, K. R. McIntosh, and K. Fong, "High efficiency silicon solar cells," *Energy Procedia*, vol. 33, pp. 1–10, 2013.

[12] R. . G. S. Report, *R. Renewables 2017 Global Status Report 2017*, 2017. `www.ren21.net/wp-content/uploads/2017/06/GSR2017_Full-Report.pdf`, `www.ren21.net/wp-content/uploads/2017/03/GFR-Full-Report-2017.pdf`.

[13] M. C. T. Bahaa E. A. Saleh, *Fundamentals of Photonics*, 1991. `https://onlinelibrary.wiley.com/doi/book/10.1002/0471213748`.

[14] V. Chmill, *Radiation tests of semiconductor detectors*. PhD thesis, KTH, 2006.

[15] I. P. Mathews, "High-efficiency photovoltaics through mechanically stacked integration of solar cells based on the inp lattice constant," 2014.

[16] D. G. Diso, *Research and development of CdTe based thin film PV solar cells*. PhD thesis, Sheffield Hallam University, 2011.

[17] J. Nelson, *The physics of solar cells*. World Scientific Publishing Company, 2003.

[18] S. Fonash, *Solar cell device physics*. Elsevier, 2012.

[19] S. M. Sze and K. K. Ng, *Physics of semiconductor devices*. John Wiley & Sons, 2006.

[20] R. H. Bube, "Photovoltaic materials, series on properties of semiconductor materials, vol. 1.," 1998.

[21] A. Izadian, A. Pourtaherian, and S. Motahari, "Basic model and governing equation of solar cells used in power and control applications," in *2012 IEEE Energy Conversion Congress and Exposition (ECCE)*, pp. 1483–1488, IEEE, 2012.

[22] M. T. Boyd, S. A. Klein, D. T. Reindl, and B. P. Dougherty, "Evaluation and validation of equivalent circuit photovoltaic solar cell performance models," *Journal of solar energy engineering*, vol. 133, no. 2, p. 021005, 2011.

[23] J. Cubas, S. Pindado, and C. De Manuel, "Explicit expressions for solar panel equivalent circuit parameters based on analytical formulation and the lambert w-function," *Energies*, vol. 7, no. 7, pp. 4098–4115, 2014.

[24] S. S. Hegedus and A. Luque, "Status, trends, challenges and the bright future of solar electricity from photovoltaics," *Handbook of photovoltaic science and engineering*, pp. 1–43, 2003.

[25] R. C. Hsu, C.-T. Liu, W.-Y. Chen, H.-I. Hsieh, and H.-L. Wang, "A reinforcement learning-based maximum power point tracking method for photovoltaic array," *International Journal of Photoenergy*, vol. 2015, 2015.

[26] U. Gangopadhyay, S. Jana, and S. Das, "State of art of solar photovoltaic technology," in *Conference Papers in Science*, vol. 2013, Hindawi, 2013.

[27] Y. Kuang, M. Di Vece, J. K. Rath, L. van Dijk, and R. E. Schropp, "Elongated nanostructures for radial junction solar cells," *Reports on Progress in Physics*, vol. 76, no. 10, p. 106502, 2013.

[28] M. Mrinalini, N. Islavath, S. Prasanthkumar, and L. Giribabu, "Stipulating low production cost solar cells all set to retail. . . !," *The Chemical Record*, vol. 19, no. 2-3, pp. 661–674, 2019.

[29] T. D. Lee and A. U. Ebong, "A review of thin film solar cell technologies and challenges," *Renewable and Sustainable Energy Reviews*, vol. 70, pp. 1286–1297, 2017.

[30] J. Liu, Y. Yao, S. Xiao, and X. Gu, "Review of status developments of high-efficiency crystalline silicon solar cells," *Journal of Physics D: Applied Physics*, vol. 51, no. 12, p. 123001, 2018.

[31] H. Charles Jr and A. Ariotedjo, "Review of amorphous and polycrystalline thin film silicon solar cell performance parameters," *Solar Energy*, vol. 24, pp. 329–339, 1980.

[32] T. D. Lee and A. Ebong, "Thin film solar technologies: a review," in *2015 12th International Conference on High-capacity Optical Networks and Enabling/Emerging Technologies (HONET)*, pp. 1–10, IEEE, 2015.

[33] S. Guha, J. Yang, and B. Yan, "High efficiency multi-junction thin film silicon cells incorporating nanocrystalline silicon," *Solar Energy Materials and Solar Cells*, vol. 119, pp. 1–11, 2013.

[34] J. Yang, A. Banerjee, and S. Guha, "Triple-junction amorphous silicon alloy solar cell with 14.6% initial and 13.0% stable conversion efficiencies," *Applied Physics Letters*, vol. 70, no. 22, pp. 2975–2977, 1997.

[35] S. Kim, J.-W. Chung, H. Lee, J. Park, Y. Heo, and H.-M. Lee, "Remarkable progress in thin-film silicon solar cells using high-efficiency triple-junction technology," *Solar Energy Materials and Solar Cells*, vol. 119, pp. 26–35, 2013.

[36] Z. Fang, X. C. Wang, H. C. Wu, and C. Z. Zhao, "Achievements and challenges of CdS/CdTe solar cells," *International Journal of Photoenergy*, vol. 2011, 2011.

[37] D. Bonnet and H. Rabenhorst, "New results on the development of a thin-film p-CdTe-n-CdS heterojunction solar cell," in *Photovoltaic Specialists Conference, 9 th, Silver Spring, Md*, pp. 129–132, 1972.

[38] N. Nakayama, H. Matsumoto, K. Yamaguchi, S. Ikegami, and Y. Hioki, "Ceramic thin film cdte solar cell," *Japanese Journal of Applied Physics*, vol. 15, no. 11, p. 2281, 1976.

[39] P. V. Meyers, "Design of a thin film cdte solar cell," *Solar Cells*, vol. 23, no. 1-2, pp. 59–67, 1988.

[40] K. Mitchell, C. Eberspacher, F. Cohen, J. Avery, G. Duran, and W. Bottenberg, "Progress towards high efficiency thin film CdTe solar cells," *Solar cells*, vol. 23, no. 1-2, pp. 49–57, 1988.

[41] X. Wu, J. Keane, R. Dhere, C. DeHart, D. Albin, A. Duda, T. Gessert, S. Asher, D. Levi, and P. Sheldon, "16.5%-efficient CdS/CdTe polycrystalline thin-film solar cell," in *Proceedings of the 17th European photovoltaic solar energy conference*, vol. 995, James & James Ltd.: London, 2001.

[42] X. Wu, R. Dhere, D. Albin, T. Gessert, C. DeHart, J. Keane, A. Duda, T. Coutts, S. Asher, D. Levi, *et al.*, "High-efficiency CTO/ZTO/CdS/CdTe polycrystalline thin-film solar cells," tech. rep., National Renewable Energy Lab., Golden, CO.(US), 2001.

[43] F. Solar, "First solar hits record 22.1% conversion efficiency for cdte solar cell," 2016.

[44] J. Fischer, J. K. Larsen, J. Guillot, Y. Aida, T. Eisenbarth, D. Regesch, V. Depredurand, N. Fevre, S. Siebentritt, and P. J. Dale, "Composition dependent characterization of copper indium diselenide thin film solar cells synthesized from electrodeposited binary selenide precursor stacks," *Solar Energy Materials and Solar Cells*, vol. 126, pp. 88–95, 2014.

[45] S. Rampino, N. Armani, F. Bissoli, M. Bronzoni, D. Calestani, M. Calicchio, N. Delmonte, E. Gilioli, E. Gombia, R. Mosca, *et al.*, "15% efficient $Cu(In,Ga)Se_2$ solar cells obtained by low-temperature pulsed electron deposition," *Applied Physics Letters*, vol. 101, no. 13, p. 132107, 2012.

[46] T. Nakada, "CIGS-based thin film solar cells and modules: Unique material properties," *Electronic Materials Letters*, vol. 8, no. 2, pp. 179–185, 2012.

[47] A. Romeo, M. Terheggen, D. Abou-Ras, D. Bätzner, F.-J. Haug, M. Kälin, D. Rudmann, and A. Tiwari, "Development of thin-film Cu(In,Ga)Se$_2$ and CdTe solar cells," *Progress in Photovoltaics: Research and Applications*, vol. 12, no. 2-3, pp. 93–111, 2004.

[48] J. Guillemoles, "The puzzle of Cu(In,Ga)Se$_2$(CIGS) solar cells stability," *Thin Solid Films*, vol. 403, pp. 405–409, 2002.

[49] J. Srour, M. Badawi, F. El Haj Hassan, and A. Postnikov, "Crystal structure and energy bands of (Ga/In)Se and Cu(In,Ga)Se$_2$ semiconductors in comparison," *physica status solidi (b)*, vol. 253, no. 8, pp. 1472–1475, 2016.

[50] J. Ramanujam and U. P. Singh, "Copper indium gallium selenide based solar cells–a review," *Energy & Environmental Science*, vol. 10, no. 6, pp. 1306–1319, 2017.

[51] R. Mickelsen and W. S. Chen, "High photocurrent polycrystalline thin-film CdS/CuInSe$_2$ solar cella," *Applied Physics Letters*, vol. 36, no. 5, pp. 371–373, 1980.

[52] Y. Tang, "Copper indium gallium selenide thin film solar cells," *Nanostructured Solar Cells*, pp. 183–200, 2017.

[53] NREL, *Best Research-Cell Efficiency Chart*, 2019. `https://www.nrel.gov/pv/cell-efficiency.html`.

[54] D. J. Lewis, P. Kevin, O. Bakr, C. A. Muryn, M. A. Malik, and P. O'Brien, "Routes to tin chalcogenide materials as thin films or nanoparticles: a potentially important class of semiconductor for sustainable solar energy conversion," *Inorganic Chemistry Frontiers*, vol. 1, no. 8, pp. 577–598, 2014.

[55] R. Hall, R. Birkmire, J. Phillips, and J. Meakin, "Thin-film polycrystalline Cu$_2$S/Cd$_{1-X}$ Zn$_X$S solar cells of 10% efficiency," *Applied Physics Letters*, vol. 38, no. 11, pp. 925–926, 1981.

[56] J. G. Radich, R. Dwyer, and P. V. Kamat, "Cu_2S reduced graphene oxide composite for high-efficiency quantum dot solar cells. overcoming the redox limitations of S2–/S n 2–at the counter electrode," *The Journal of Physical Chemistry Letters*, vol. 2, no. 19, pp. 2453–2460, 2011.

[57] A. Lokhande, R. Chalapathy, M. He, E. Jo, M. Gang, S. Pawar, C. Lokhande, and J. H. Kim, "Development of Cu_2SnS_3 (cts) thin film solar cells by physical techniques: A status review," *Solar Energy Materials and Solar Cells*, vol. 153, pp. 84–107, 2016.

[58] D. Cao, C. Wang, F. Zheng, W. Dong, L. Fang, and M. Shen, "High-efficiency ferroelectric-film solar cells with an n-type Cu2O cathode buffer layer," *Nano letters*, vol. 12, no. 6, pp. 2803–2809, 2012.

[59] B. Li, H. Cao, G. Yin, Y. Lu, and J. Yin, "Cu2o@reduced graphene oxide composite for removal of contaminants from water and supercapacitors," *Journal of Materials Chemistry*, vol. 21, no. 29, pp. 10645–10648, 2011.

[60] S.-J. Moon, Y. Itzhaik, J.-H. Yum, S. M. Zakeeruddin, G. Hodes, and M. Gratzel, "Sb_2S_3-based mesoscopic solar cell using an organic hole conductor," *The Journal of Physical Chemistry Letters*, vol. 1, no. 10, pp. 1524–1527, 2010.

[61] B. Krishnan, A. Arato, E. Cardenas, T. D. Roy, and G. Castillo, "On the structure, morphology, and optical properties of chemical bath deposited Sb_2S_3 thin films," *Applied Surface Science*, vol. 254, no. 10, pp. 3200–3206, 2008.

[62] M. Minbashi, A. Ghobadi, M. Ehsani, H. R. Dizaji, and N. Memarian, "Simulation of high efficiency SnS-based solar cells with SCAPS," *Solar Energy*, vol. 176, pp. 520–525, 2018.

[63] K. R. Reddy, N. K. Reddy, and R. Miles, "Photovoltaic properties of SnS based solar cells," *Solar energy materials and solar cells*, vol. 90, no. 18-19, pp. 3041–3046, 2006.

[64] L. Luo, W. Luan, B. Yuan, C. Zhang, and L. Jin, "High efficient and stable solid solar cell: based on FeS$_2$ nanocrystals and p3ht: PCBM," *Energy Procedia*, vol. 75, pp. 2181–2186, 2015.

[65] J. Puthussery, S. Seefeld, N. Berry, M. Gibbs, and M. Law, "Colloidal iron pyrite (FeS2) nanocrystal inks for thin-film photovoltaics," *Journal of the American Chemical Society*, vol. 133, no. 4, pp. 716–719, 2010.

[66] B. Rezig, H. Dahman, and M. Kenzari, "Iron pyrite FeS2 for flexible solar cells," *Renewable Energy*, vol. 2, no. 2, pp. 125–128, 1992.

[67] D. Colombara, L. M. Peter, K. D. Rogers, J. D. Painter, and S. Roncallo, "Formation of CuSbS$_2$ and CuSbSe$_2$ thin films via chalcogenisation of Sb–Cu metal precursors," *Thin Solid Films*, vol. 519, no. 21, pp. 7438–7443, 2011.

[68] C. Garza, S. Shaji, A. Arato, E. P. Tijerina, G. A. Castillo, T. D. Roy, and B. Krishnan, "p-type CuSbS$_2$ thin films by thermal diffusion of copper into Sb$_2$S$_3$," *Solar Energy Materials and Solar Cells*, vol. 95, no. 8, pp. 2001–2005, 2011.

[69] T. A. Berhe, W.-N. Su, C.-H. Chen, C.-J. Pan, J.-H. Cheng, H.-M. Chen, M.-C. Tsai, L.-Y. Chen, A. A. Dubale, and B.-J. Hwang, "Organometal halide perovskite solar cells: degradation and stability," *Energy & Environmental Science*, vol. 9, no. 2, pp. 323–356, 2016.

[70] N.-G. Park, "Organometal perovskite light absorbers toward a 20% efficiency low-cost solid-state mesoscopic solar cell," *The Journal of Physical Chemistry Letters*, vol. 4, no. 15, pp. 2423–2429, 2013.

[71] S. Banu, Y. Cho, K. Kim, S. K. Ahn, J. S. Cho, J. Gwak, and A. Cho, "Effect of cu content in CuSbS$_2$ thin films using hybrid inks: Their photovoltaic properties and defect characteristics," *Solar Energy Materials and Solar Cells*, vol. 189, pp. 214–223, 2019.

[72] M. Medina-Montes, O. Vieyra-Brito, N. R. Mathews, and X. Mathew, "Development of sputtered $CuSbS_2$ thin films grown by sequential deposition of binary sulfides," *Semiconductor Science and Technology*, vol. 33, no. 5, p. 055004, 2018.

[73] Y. Zhang, J. Huang, C. Yan, K. Sun, X. Cui, F. Liu, Z. Liu, X. Zhang, X. Liu, J. A. Stride, *et al.*, "High open-circuit voltage $CuSbS_2$ solar cells achieved through the formation of epitaxial growth of $CdS/CuSbS_2$ hetero-interface by post-annealing treatment," *Progress in Photovoltaics: Research and Applications*, vol. 27, no. 1, pp. 37–43, 2019.

[74] A. Nagaoka, M. Takeuchi, K. Yoshino, S. Ikeda, S. Yasui, T. Taniyama, and K. Nishioka, "Growth of $CuSbS_2$ single crystal as an environmentally friendly thermoelectric material," *physica status solidi (a)*, p. 1800861, 2019.

[75] F. W. de Souza Lucas and A. Zakutayev, "Research update: Emerging chalcostibite absorbers for thin-film solar cells," *APL Materials*, vol. 6, no. 8, p. 084501, 2018.

[76] A. Zakutayev, "Brief review of emerging photovoltaic absorbers," *Current Opinion in Green and Sustainable Chemistry*, vol. 4, pp. 8–15, 2017.

[77] U. S. D. of the Interior, *USGS 2014. U.S. Geological Survey: Mineral commodity summaries*, 2014. `https://www.usgs.gov/centers/nmic/mineral-commodity-summaries`.

[78] B. Krishnan, S. Shaji, and R. E. Ornelas, "Progress in development of copper antimony sulfide thin films as an alternative material for solar energy harvesting," *Journal of Materials Science: Materials in Electronics*, vol. 26, no. 7, pp. 4770–4781, 2015.

[79] F. W. de Souza Lucas, A. W. Welch, L. L. Baranowski, P. C. Dippo, H. Hempel, T. Unold, R. Eichberger, B. Blank, U. Rau, L. H. Mascaro, *et al.*, "Effects of thermochemical treatment on $CuSbS_2$ photovoltaic absorber quality and solar

cell reproducibility," *The Journal of Physical Chemistry C*, vol. 120, no. 33, pp. 18377–18385, 2016.

[80] A. W. Welch, L. L. Baranowski, P. Zawadzki, C. DeHart, S. Johnston, S. Lany, C. A. Wolden, and A. Zakutayev, "Accelerated development of CuSbS2 thin film photovoltaic device prototypes," *Progress in Photovoltaics: Research and Applications*, vol. 24, no. 7, pp. 929–939, 2016.

[81] Y. C. Choi, E. J. Yeom, T. K. Ahn, and S. I. Seok, "CuSbS$_2$-sensitized inorganic–organic heterojunction solar cells fabricated using a metal–thiourea complex solution," *Angewandte Chemie International Edition*, vol. 54, no. 13, pp. 4005–4009, 2015.

[82] K. Takei, T. Maeda, and T. Wada, "Crystallographic and optical properties of CuSbS$_2$ and CuSb (S$_{1-X}$Se$_X$)$_2$ solid solution," *Thin Solid Films*, vol. 582, pp. 263–268, 2015.

[83] B. John, G. G. Silvena, S. Hussain, M. S. Kumar, and A. L. Rajesh, "Surfactant-mediated solvothermal synthesis of CuSbS$_2$ nanoparticles as p-type absorber material," *Indian Journal of Physics*, vol. 93, no. 2, pp. 185–195, 2019.

[84] M. Birkett, C. N. Savory, M. K. Rajpalke, W. M. Linhart, T. J. Whittles, J. T. Gibbon, A. W. Welch, I. Z. Mitrovic, A. Zakutayev, D. O. Scanlon, *et al.*, "Band gap temperature-dependence and exciton-like state in copper antimony sulphide, CuSbS$_2$," *APL Materials*, vol. 6, no. 8, p. 084904, 2018.

[85] A. W. Welch, P. P. Zawadzki, S. Lany, C. A. Wolden, and A. Zakutayev, "Self-regulated growth and tunable properties of CuSbS2 solar absorbers," *Solar Energy Materials and Solar Cells*, vol. 132, pp. 499–506, 2015.

[86] B. Yang, L. Wang, J. Han, Y. Zhou, H. Song, S. Chen, J. Zhong, L. Lv, D. Niu, and J. Tang, "CuSbS$_2$ as a promising earth-abundant photovoltaic

absorber material: a combined theoretical and experimental study," *Chemistry of Materials*, vol. 26, no. 10, pp. 3135–3143, 2014.

[87] A. W. Welch, *CuSb(S,Se)$_2$ thin film heterojunction photovoltaic devices.* PhD thesis, Colorado School of Mines. Arthur Lakes Library, 2015.

[88] S. Banu, S. J. Ahn, S. K. Ahn, K. Yoon, and A. Cho, "Fabrication and characterization of cost-efficient CuSbS$_2$ thin film solar cells using hybrid inks," *Solar Energy Materials and Solar Cells*, vol. 151, pp. 14–23, 2016.

[89] M. Wang, G. Yue, X. Fan, and P. Yan, "Properties and characterization of Cu$_3$SbS$_3$ nanowires synthesized by solvothermal route," *Journal of Crystal Growth*, vol. 310, no. 12, pp. 3062–3066, 2008.

[90] B. Du, R. Zhang, M. Liu, K. Chen, H. Zhang, and M. J. Reece, "Crystal structure and improved thermoelectric performance of iron stabilized cubic Cu$_3$SbS$_3$ compound," *Journal of Materials Chemistry C*, vol. 7, no. 2, pp. 394–404, 2019.

[91] N. Bouaniza, N. Hosni, and H. Maghraoui-Meherzi, "Structural and optical properties of Cu$_3$SbS$_3$ thin film deposited by chemical bath deposition along with the degradation of methylene blue," *Surface and Coatings Technology*, vol. 333, pp. 195–200, 2018.

[92] J. Kavinchan, E. Saksornchai, S. Thongtem, and T. Thongtem, "One-step microwave assisted synthesis of copper antimony sulphide (Cu$_3$SbS$_4$) nanostructures: optical property and formation mechanism study," *Chalcogenide Letters*, vol. 15, no. 12, pp. 599–604, 2018.

[93] C. Tablero, "Electronic property analysis of o-doped Cu$_3$SbS$_3$," *Solar Energy Materials and Solar Cells*, vol. 104, pp. 180–184, 2012.

[94] A. Hussain, R. Ahmed, N. Ali, A. Shaari, J.-T. Luo, and Y. Q. Fu, "Characterization of Cu$_3$SbS$_3$ thin films grown by thermally diffusing cu2s and Sb$_2$S$_3$ layers," *Surface and Coatings Technology*, vol. 319, pp. 294–300, 2017.

[95] A. Pfitzner, M. Evain, and V. Petricek, "$Cu_{12}Sb_4S_{13}$: A temperature-dependent structure investigation," *Acta Crystallographica Section B: Structural Science*, vol. 53, no. 3, pp. 337–345, 1997.

[96] L. Wang, B. Yang, Z. Xia, M. Leng, Y. Zhou, D.-J. Xue, J. Zhong, L. Gao, H. Song, and J. Tang, "Synthesis and characterization of hydrazine solution processed $Cu_{12}Sb_4S_{13}$ film," *Solar Energy Materials and Solar Cells*, vol. 144, pp. 33–39, 2016.

[97] K. Chen, J. Zhou, W. Chen, P. Zhou, F. He, and Y. Liu, "Size-dependent synthesis of $Cu_{12}Sb_4S_{13}$ nanocrystals with bandgap tunability," *Particle & Particle Systems Characterization*, vol. 32, no. 11, pp. 999–1005, 2015.

[98] J.-H. Pi, S.-G. Kwak, S.-Y. Kim, G.-E. Lee, and I.-H. Kim, "Thermal stability and mechanical properties of thermoelectric tetrahedrite $Cu_{12}Sb_4S_{13}$," *Journal of Electronic Materials*, vol. 48, no. 4, pp. 1991–1997, 2019.

[99] S.-Y. Kim, S.-G. Kwak, J.-H. Pi, G.-E. Lee, and I.-H. Kim, "Preparation of tetrahedrite $Cu_{12}Sb_4S_{13}$ by mechanical alloying and hot pressing," *Journal of Electronic Materials*, vol. 48, no. 4, pp. 1857–1863, 2019.

[100] J. Van Embden, K. Latham, N. W. Duffy, and Y. Tachibana, "Near-infrared absorbing $Cu_{12}Sb_4S_{13}$ and Cu_3SbS_4 nanocrystals: synthesis, characterization, and photoelectrochemistry," *Journal of the American Chemical Society*, vol. 135, no. 31, pp. 11562–11571, 2013.

[101] E. J. Skoug, J. D. Cain, D. T. Morelli, M. Kirkham, P. Majsztrik, and E. Lara-Curzio, "Lattice thermal conductivity of the Cu_3SbSe_4-Cu_3SbS_4 solid solution," *Journal of Applied Physics*, vol. 110, no. 2, p. 023501, 2011.

[102] U. Chalapathi, B. Poornaprakash, and S.-H. Park, "Growth and properties of Cu_3SbS_4 thin films prepared by a two-stage process for solar cell applications," *Ceramics International*, vol. 43, no. 6, pp. 5229–5235, 2017.

[103] G. Han, J. W. Lee, and J. Kim, "Fabrication and characterization of Cu_3SbS_4 solar cell with Cd-free buffer," *Journal of the Korean Physical Society*, vol. 73, no. 11, pp. 1794–1798, 2018.

[104] G. H. Albuquerque, K.-J. Kim, J. I. Lopez, A. Devaraj, S. Manandhar, Y.-S. Liu, J. Guo, C.-H. Chang, and G. S. Herman, "Multimodal characterization of solution-processed Cu_3SbS_4 absorbers for thin film solar cells," *Journal of Materials Chemistry A*, vol. 6, no. 18, pp. 8682–8692, 2018.

[105] M. Kumar and C. Persson, "$CuSbS_2$ and $CuBiS_2$ as potential absorber materials for thin-film solar cells," *Journal of Renewable and Sustainable Energy*, vol. 5, no. 3, p. 031616, 2013.

[106] A. W. Welch, L. L. Baranowski, P. Zawadzki, S. Lany, C. A. Wolden, and A. Zakutayev, "$CuSbSe_2$ photovoltaic devices with 3% efficiency," *Applied Physics Express*, vol. 8, no. 8, p. 082301, 2015.

[107] L. Yu, R. S. Kokenyesi, D. A. Keszler, and A. Zunger, "Inverse design of high absorption thin-film photovoltaic materials," *Advanced Energy Materials*, vol. 3, no. 1, pp. 43–48, 2013.

[108] D.-J. Xue, B. Yang, Z.-K. Yuan, G. Wang, X. Liu, Y. Zhou, L. Hu, D. Pan, S. Chen, and J. Tang, "$CuSbSe_2$ as a potential photovoltaic absorber material: Studies from theory to experiment," *Advanced Energy Materials*, vol. 5, no. 23, p. 1501203, 2015.

[109] E. Ismailova, L. Mashadieva, I. Bakhtiyarly, and M. Babanly, "Phase equilibria in the Cu_2Se-SnSe - $CuSbSe_2$ system," *Russian Journal of Inorganic Chemistry*, vol. 64, no. 6, pp. 801–809, 2019.

[110] A. S. Kshirsagar and P. K. Khanna, "Reaction tailoring for synthesis of phase-pure nanocrystals of $AgInSe_2$, Cu_3SbSe_3 and $CuSbSe_2$," *ChemistrySelect*, vol. 3, no. 10, pp. 2854–2866, 2018.

[111] C. Wang, B. Yang, R. Ding, W. Chen, R. Kondrotas, Y. Zhao, S. Lu, Z. Li, and J. Tang, "Reactive close-spaced sublimation processed $CuSbSe_2$ thin films and their photovoltaic application," *APL Materials*, vol. 6, no. 8, p. 084801, 2018.

[112] K. J. Tiwari, "Growth and study of $Cu_2ZnSnSe_4$ $CuSbSe_2$ and Sb_2Se_3 thin films for solar cell application and device studies based on Sb_2Se_3 thin films," 2018.

[113] M. Eriksen, "Creation of thin film $CuSbSe_2$ through closed space vapor transportdeposition," 2018.

[114] S. Rampino, F. Pattini, M. Bronzoni, M. Mazzer, M. Sidoli, G. Spaggiari, and E. Gilioli, "$CuSbSe_2$ thin film solar cells with~ 4% conversion efficiency grown by low-temperature pulsed electron deposition," *Solar Energy Materials and Solar Cells*, vol. 185, pp. 86–96, 2018.

[115] H. Salehi *et al.*, "Ab-initio study of electronic, optical, dynamic and thermoelectric properties of $CuSbX_2$ (X= S, Se) compounds," *Journal of Optoelectronical Nanostructures*, vol. 3, no. 2, pp. 53–64, 2018.

[116] N. Alsaleh, *Mechanisms of Enhanced Thermoelectricity in Chalcogenides*. PhD thesis, 2018.

[117] K. J. Tiwari, V. Vinod, A. Subrahmanyam, and P. Malar, "Growth and characterization of chalcostibite $CuSbSe_2$ thin films for photovoltaic application," *Applied Surface Science*, vol. 418, pp. 216–224, 2017.

[118] J. T. Dufton, A. Walsh, P. M. Panchmatia, L. M. Peter, D. Colombara, and M. S. Islam, "Structural and electronic properties of $CuSbS_2$ and $CuBiS_2$: potential absorber materials for thin-film solar cells," *Physical Chemistry Chemical Physics*, vol. 14, no. 20, pp. 7229–7233, 2012.

[119] K. Ramasamy, R. K. Gupta, S. Palchoudhury, S. Ivanov, and A. Gupta, "Layer-structured copper antimony chalcogenides ($CuSbSe_XS_{2-X}$): Stable electrode

materials for supercapacitors," *Chemistry of Materials*, vol. 27, no. 1, pp. 379–386, 2014.

[120] B. A. Collins, Z. Li, J. R. Tumbleston, E. Gann, C. R. McNeill, and H. Ade, "Absolute measurement of domain composition and nanoscale size distribution explains performance in ptb7: Pc71bm solar cells," *Advanced Energy Materials*, vol. 3, no. 1, pp. 65–74, 2013.

[121] M. R. De Guire, L. P. Bauermann, H. Parikh, and J. Bill, "Chemical bath deposition," in *Chemical Solution Deposition of Functional Oxide Thin Films*, pp. 319–339, Springer, 2013.

[122] D. Mugle and G. Jadhav, "Short review on chemical bath deposition of thin film and characterization," in *AIP Conference Proceedings*, vol. 1728, p. 020597, AIP Publishing, 2016.

[123] R. Khatri and A. Patel, "A comprehensive review on chemical bath deposited ZnS thin film,"

[124] C. L. McCarthy, P. Cottingham, K. Abuyen, E. C. Schueller, S. P. Culver, and R. L. Brutchey, "Earth abundant $CuSbS_2$ thin films solution processed from thiol–amine mixtures," *Journal of Materials Chemistry C*, vol. 4, no. 26, pp. 6230–6233, 2016.

[125] F. Loranca-Ramos, C. Diliegros-Godines, R. S. González, and M. Pal, "Structural, optical and electrical properties of copper antimony sulfide thin films grown by a citrate-assisted single chemical bath deposition," *Applied Surface Science*, vol. 427, pp. 1099–1106, 2018.

[126] Y. Rodrıguez-Lazcano, M. Nair, and P. Nair, "$CuSbS_2$ thin film formed through annealing chemically deposited Sb_2S_3-CuS thin films," *Journal of Crystal Growth*, vol. 223, no. 3, pp. 399–406, 2001.

[127] C. Macías, S. Lugo, Á. Benítez, I. López, B. Kharissov, A. Vázquez, and Y. Peña, "Thin film solar cell based on $CuSbS_2$ absorber prepared by chemical

bath deposition (CBD)," *Materials Research Bulletin*, vol. 87, pp. 161–166, 2017.

[128] P. Doshi, J. Moschner, J. Jeong, A. Rohatgi, R. Singh, and S. Narayanan, "Characterization and application of rapid thermal oxide surface passivation for the highest efficiency RTP silicon solar cells," in *Conference Record of the Twenty Sixth IEEE Photovoltaic Specialists Conference-1997*, pp. 87–90, IEEE, 1997.

[129] M. Tyona, "A theoritical study on spin coating technique," *Advances in materials Research*, vol. 2, no. 4, pp. 195–208, 2013.

[130] E. Spooner, *spin coating film thickness*, 2019. `https://www.ossila.com/pages/spin-coating-film-thickness`.

[131] A. K. Alves, C. P. Bergmann, and F. A. Berutti, "Spray pyrolysis," in *Novel Synthesis and Characterization of Nanostructured Materials*, pp. 23–30, Springer, 2013.

[132] O. Malik, F. J. De La Hidalga-Wade, and R. R. Amador, "Spray pyrolysis processing for optoelectronic applications," *Pyrolysis*, p. 197, 2017.

[133] D. Perednis and L. J. Gauckler, "Thin film deposition using spray pyrolysis," *Journal of electroceramics*, vol. 14, no. 2, pp. 103–111, 2005.

[134] S. Manolache and A. Duta, "The influence of the spray deposition parameters in the photovoltaic response of the three-dimensional (3d) solar cell: Tco/dense tio2/$CuSbS_2$/graphite," *Journal of optoelectronics and advanced materials*, vol. 9, no. 10, pp. 3219–3222, 2007.

[135] I. Popovici and A. Duta, "Tailoring the composition and properties of sprayed $CuSbS_2$ thin films by using polymeric additives," *International Journal of Photoenergy*, vol. 2012, 2012.

[136] S. Thiruvenkadam and A. L. Rajesh, "Effect of temperature on structural and optical properties of spray pyrolysed $CuSbS_2$ thin films for photovoltaic applications," *International Journal of Scientific & Engineering Research*, vol. 5, no. 1, 2014.

[137] J. A. Ramos Aquino, D. L. Rodriguez Vela, S. Shaji, D. A. Avellaneda, and B. Krishnan, "Spray pyrolysed thin films of copper antimony sulfide as photovoltaic absorber," *physica status solidi (c)*, vol. 13, no. 1, pp. 24–29, 2016.

[138] A. Ray, "Electrodeposition of thin films for low-cost solar cells," *Electroplating of Nanostructures*, 2015.

[139] A. R. F. Logan G. Kiefer, D. o. M. S. Taylor D. Sparks, and S. L. C. U. Engineering, The University of Utah, *Electroplating of Thin Films*, 2019. `https://www.jove.com/science-education/10489/electroplating-of-thin-films`.

[140] W. Septina, S. Ikeda, Y. Iga, T. Harada, and M. Matsumura, "Thin film solar cell based on $CuSbS_2$ absorber fabricated from an electrochemically deposited metal stack," *Thin Solid Films*, vol. 550, pp. 700–704, 2014.

[141] A. Rastogi and N. Janardhana, "Properties of $CuSbS_2$ thin films electrodeposited from ionic liquids as p-type absorber for photovoltaic solar cells," *Thin Solid Films*, vol. 565, pp. 285–292, 2014.

[142] M. E. Edley, B. Opasanont, J. T. Conley, H. Tran, S. Y. Smolin, S. Li, A. D. Dillon, A. T. Fafarman, and J. B. Baxter, "Solution processed $CuSbS_2$ films for solar cell applications," *Thin Solid Films*, vol. 646, pp. 180–189, 2018.

[143] D. Tang, J. Yang, F. Liu, Y. Lai, J. Li, and Y. Liu, "Growth and characterization of $CuSbSe_2$ thin films prepared by electrodeposition," *Electrochimica Acta*, vol. 76, pp. 480–486, 2012.

[144] J. Vossen and J. O'Neill Jr, "Rf sputtering processes," tech. rep., RCA Labs., Princeton, NJ, 1968.

[145] P. J. Kelly and R. D. Arnell, "Magnetron sputtering: a review of recent developments and applications," *Vacuum*, vol. 56, no. 3, pp. 159–172, 2000.

[146] A. W. Welch, L. L. Baranowski, P. Zawadzki, C. DeHart, S. Johnston, S. Lany, C. A. Wolden, and A. Zakutayev, "Accelerated development of CuSbS2 thin film photovoltaic device prototypes," *Progress in Photovoltaics: Research and Applications*, vol. 24, no. 7, pp. 929–939, 2016.

[147] L. I. Soliman, A. M. A. El Soad, H. A. Zayed, and S. A. El Ghfar, "Structural and electrical properties of $CuSbTe_2$, $CuSbSe_2$ and $CuSbS_2$ chalcogenide this films," *FIZIKA A*, vol. 11, no. 4, pp. 139–152, 2002.

[148] A. Rabhi, M. Kanzari, and B. Rezig, "Optical and structural properties of $CuSbS_2$ thin films grown by thermal evaporation method," *Thin Solid Films*, vol. 517, no. 7, pp. 2477–2480, 2009.

[149] A. Rabhi and M. Kanzari, "Effect of air annealing on $CuSbS_2$ thin film grown by vacuum thermal evaporation," *Chalcogenide Letters*, vol. 8, no. 4, pp. 255–262, 2011.

[150] R. Suriakarthick, V. N. Kumar, T. Shyju, and R. Gopalakrishnan, "Effect of substrate temperature on copper antimony sulphide thin films from thermal evaporation," *Journal of Alloys and Compounds*, vol. 651, pp. 423–433, 2015.

[151] R. Ornelas-Acosta, D. Avellaneda, S. Shaji, G. Castillo, T. D. Roy, and B. Krishnan, "$CuSbS_2$ thin films by heating Sb_2S_3/Cu layers for pv applications," *Journal of Materials Science: Materials in Electronics*, vol. 25, no. 10, pp. 4356–4362, 2014.

[152] M. C. R. E. O. Acosta, *"Thin films of Cu, In and Sb chalcogenides as photovoltaic absorbers*, 2015. `http://eprints.uanl.mx/9269/1/1080215110.pdf`.

[153] U. Chalapathi, B. Poornaprakash, C.-H. Ahn, and S.-H. Park, "Two-stage processed $CuSbS_2$ thin films for photovoltaics: Effect of cu/sb ratio," *Ceramics International*, vol. 44, no. 12, pp. 14844–14849, 2018.

[154] H. Fukuda, *Rapid thermal processing for future semiconductor devices*. Elsevier, 2003.

[155] F. Roozeboom and N. Parekh, "Rapid thermal processing systems: A review with emphasis on temperature control," *Journal of Vacuum Science & Technology B: Microelectronics Processing and Phenomena*, vol. 8, no. 6, pp. 1249–1259, 1990.

[156] R. Kulkarni and A. Shaligram, "Modelling, simulation and design optimization of rapid thermal processing system," *IETE Technical Review*, vol. 15, no. 1-2, pp. 123–129, 1998.

[157] V. Y. Kireev and A. Tsimbalov, "Rapid thermal processing: a new step forward in microelectronics technologies," *Russian Microelectronics*, vol. 30, no. 4, pp. 225–235, 2001.

[158] R. Singh, "Rapid isothermal processing," *Journal of Applied Physics*, vol. 63, no. 8, pp. R59–R114, 1988.

[159] F. Roozeboom, "Temperature control and system design aspects in rapid thermal processing," *MRS Online Proceedings Library Archive*, vol. 224, 1991.

[160] H. Park, T. Yoon, and O. Kim, "Optimal control of rapid thermal processing systems by empirical reduction of modes," *Industrial & engineering chemistry research*, vol. 38, no. 10, pp. 3964–3975, 1999.

[161] D. Colombara, L. M. Peter, K. D. Rogers, J. D. Painter, and S. Roncallo, "Formation of $CuSbS_2$ and $CuSbSe_2$ thin films via chalcogenisation of sb-cu metal precursors," *Thin Solid Films*, vol. 519, no. 21, pp. 7438–7443, 2011.

[162] E. Peccerillo, J. Major, L. Phillips, R. Treharne, T. J. Whittles, V. Dhanak, D. Halliday, and K. Durose, "Characterization of sulfurized $CuSbS_2$ thin films for pv applications," in *2014 IEEE 40th Photovoltaic Specialist Conference (PVSC)*, pp. 0266–0269, IEEE, 2014.

[163] R. Ornelas-Acosta, S. Shaji, D. Avellaneda, G. Castillo, T. D. Roy, and B. Krishnan, "Thin films of copper antimony sulfide: a photovoltaic absorber material," *Materials Research Bulletin*, vol. 61, pp. 215–225, 2015.

[164] S. Ikeda, Y. Iga, W. Septina, T. Harada, and M. Matsumura, "$CuSbS_2$-based thin film solar cells prepared from electrodeposited metallic stacks composed of cu and sb layers," in *2013 IEEE 39th Photovoltaic Specialists Conference (PVSC)*, pp. 2598–2601, IEEE, 2013.

[165] T. Minemoto, T. Matsui, H. Takakura, Y. Hamakawa, T. Negami, Y. Hashimoto, T. Uenoyama, and M. Kitagawa, "Theoretical analysis of the effect of conduction band offset of window/cis layers on performance of CIS solar cells using device simulation," *Solar Energy Materials and Solar Cells*, vol. 67, no. 1-4, pp. 83–88, 2001.

[166] T. J. Whittles, T. D. Veal, C. N. Savory, A. W. Welch, F. W. de Souza Lucas, J. T. Gibbon, M. Birkett, R. J. Potter, D. O. Scanlon, A. Zakutayev, *et al.*, "Core levels, band alignments, and valence-band states in $CuSbS_2$ for solar cell applications," *ACS applied materials & interfaces*, vol. 9, no. 48, pp. 41916–41926, 2017.

[167] M. Nair, Y. Pena, J. Campos, V. Garcia, and P. Nair, "Chemically deposited Sb_2S_3 and Sb_2S_3-cus thin films," *Journal of The Electrochemical Society*, vol. 145, no. 6, pp. 2113–2120, 1998.

[168] V. Vinayakumar, S. Shaji, D. Avellaneda, T. D. Roy, G. Castillo, J. Martinez, and B. Krishnan, "$CuSbS_2$ thin films by rapid thermal processing of Sb_2S_3-Cu stack layers for photovoltaic application," *Solar Energy Materials and Solar Cells*, vol. 164, pp. 19–27, 2017.

[169] E. N. Kaufmann, "Characterization of materials, 2 volume set," *Characterization of Materials, 2 Volume Set, by Elton N. Kaufmann (Editor), pp. 1392. ISBN 0-471-26882-8. Wiley-VCH, January 2003.*, p. 1392, 2003.

[170] M. C. George, "Asm handbook: Volume 10: Materials characterization," 1998.

[171] R. L. McCreery, *Raman spectroscopy for chemical analysis*, vol. 225. John Wiley & Sons, 2005.

[172] J. Wolstenholme and J. Watts, *An Introduction to Surface Analysis by XPS and AES*. J. Wiley & sons, 2003.

[173] J. Chastain, "Handbook of x-ray photoelectron spectroscopy," *Perkin-Elmer Corporation*, vol. 40, p. 221, 1992.

[174] H. Günzler and A. Williams, "Handbook of analytical techniques," *Evolution*, vol. 1, pp. 1–2, 2001.

[175] B. Beckhoff, B. Kanngießer, N. Langhoff, R. Wedell, and H. Wolff, *Handbook of practical X-ray fluorescence analysis*. Springer Science & Business Media, 2007.

[176] S. J. B. Reed, *Electron microprobe analysis and scanning electron microscopy in geology*. Cambridge University Press, 2005.

[177] P. C. Braga and D. Ricci, *Atomic force microscopy: biomedical methods and applications*, vol. 242. Springer Science & Business Media, 2004.

[178] J. Solé, L. Bausa, and D. Jaque, *An introduction to the optical spectroscopy of inorganic solids*. John Wiley & Sons, 2005.

[179] R. Bube, "Photoconductivity of solids, john wiley & sons," *New York*, 1960.

[180] V. Vinayakumar, S. Shaji, D. Avellaneda, T. D. Roy, G. Castillo, J. Martinez, and B. Krishnan, "CuSbS$_2$ thin films by rapid thermal processing of Sb$_2$S$_3$-Cu stack layers for photovoltaic application," *Solar Energy Materials and Solar Cells*, vol. 164, pp. 19–27, 2017.

[181] V. Vinayakumar, S. Shaji, D. Avellaneda, J. Aguilar-Martínez, and B. Krishnan, "Copper antimony sulfide thin films for visible to near infrared photodetector applications," *RSC advances*, vol. 8, no. 54, pp. 31055–31065, 2018.

[182] Y. Liu, K. T. E. Chua, T. C. Sum, and C. K. Gan, "First-principles study of the lattice dynamics of Sb_2S_3," *Physical Chemistry Chemical Physics*, vol. 16, no. 1, pp. 345–350, 2014.

[183] Y. Sorb, V. Rajaji, P. Malavi, U. Subbarao, P. Halappa, S. C. Peter, S. Karmakar, and C. Narayana, "Pressure-induced electronic topological transition in Sb_2S_3," *Journal of Physics: Condensed Matter*, vol. 28, no. 1, p. 015602, 2015.

[184] J. Baker, R. S. Kumar, D. Sneed, A. Connolly, Y. Zhang, N. Velisavljevic, J. Paladugu, M. Pravica, C. Chen, A. Cornelius, *et al.*, "Pressure induced structural transitions in $CuSbS_2$ and $CuSbSe_2$ thermoelectric compounds," *Journal of Alloys and Compounds*, vol. 643, pp. 186–194, 2015.

[185] R. S. Data, *RRUFF*, 2019. `http://rruff.info/`.

[186] R. A. Garcia, C. M. Avendaño, M. Pal, F. P. Delgado, and N. R. Mathews, "Antimony sulfide (Sb_2S_3) thin films by pulse electrodeposition: Effect of thermal treatment on structural, optical and electrical properties," *Materials Science in Semiconductor Processing*, vol. 44, pp. 91–100, 2016.

[187] P. Makreski, G. Petruševski, S. Ugarković, and G. Jovanovski, "Laser-induced transformation of stibnite (Sb_2S_3) and other structurally related salts," *Vibrational Spectroscopy*, vol. 68, pp. 177–182, 2013.

[188] M. Hart and A. Evans, "Rapid thermal processing in semiconductor technology," *Semiconductor Science and Technology*, vol. 3, no. 5, p. 421, 1988.

[189] K. Siemer, J. Klaer, I. Luck, J. Bruns, R. Klenk, and D. Bräunig, "Efficient $cuins_2$ solar cells from a rapid thermal process (rtp)," *Solar Energy Materials and Solar Cells*, vol. 67, no. 1-4, pp. 159–166, 2001.

[190] V. Vinayakumar, S. Shaji, D. Avellaneda, J. A. Martinez, and B. Krishnan, "Highly oriented $CuSbS_2$ thin films by rapid thermal processing of pre-annealed

Sb_2S_3-Cu layers for PV applications," *Materials Science in Semiconductor Processing*, vol. 91, pp. 81–89, 2019.

[191] K. A. John, R. R. Philip, P. Sajan, and T. Manju, "In situ crystallization of highly conducting and transparent ITO thin films deposited by RF magnetron sputtering," *Vacuum*, vol. 132, pp. 91–94, 2016.

[192] G. Zoppi, K. Durose, S. Irvine, and V. Barrioz, "Grain and crystal texture properties of absorber layers in MOCVD-grown CdTe/CdS solar cells," *Semiconductor science and technology*, vol. 21, no. 6, p. 763, 2006.

[193] H. Liu, J. Xie, P. Liu, and B. Dai, "Effect of Cu+/Cu2+ ratio on the catalytic behavior of anhydrous nieuwland catalyst during dimerization of acetylene," *Catalysts*, vol. 6, no. 8, p. 120, 2016.

[194] G. Gonzalez, B. Krishnan, D. Avellaneda, G. A. Castillo, T. D. Roy, and S. Shaji, "Modification of optical and electrical properties of chemical bath deposited cds using plasma treatments," *Thin Solid Films*, vol. 519, no. 21, pp. 7587–7591, 2011.

[195] X. Mathew, J. S. Cruz, D. R. Coronado, A. R. Millán, G. C. Segura, E. R. Morales, O. S. Martínez, C. C. Garcia, and E. P. Landa, "CdS thin film post-annealing and Te–S interdiffusion in a CdTe/CdS solar cell," *Solar Energy*, vol. 86, no. 4, pp. 1023–1028, 2012.

[196] W. Ananda, "External quantum efficiency measurement of solar cell," in *2017 15th International Conference on Quality in Research (QiR): International Symposium on Electrical and Computer Engineering*, pp. 450–456, IEEE, 2017.

[197] K. W. Böer, *Survey of Semiconductor Physics: Volume II Barriers, Junctions, Surfaces, and Devices.* Springer Science & Business Media, 2012.

[198] A. Luque and S. Hegedus, *Handbook of photovoltaic science and engineering.* John Wiley & Sons, 2011.

[199] M. S. Mahdi, K. Ibrahim, A. Hmood, N. M. Ahmed, S. A. Azzez, and F. I. Mustafa, "A highly sensitive flexible SnS thin film photodetector in the ultraviolet to near infrared prepared by chemical bath deposition," *RSC Advances*, vol. 6, no. 116, pp. 114980–114988, 2016.

[200] M. Hao, Y. Liu, F. Zhou, L. Jiang, F. Liu, and J. Li, "$CuSbS_2$ nanocrystals applying in organic–inorganic hybrid photodetectors," *ECS Solid State Letters*, vol. 3, no. 9, pp. Q41–Q43, 2014.

[201] T. S. Reddy and M. S. Kumar, "Co-evaporated SnS thin films for visible light photodetector applications," *RSC Advances*, vol. 6, no. 98, pp. 95680–95692, 2016.

[202] Y. Xiao, C. Li, X. Tan, L. Zhang, Y. Zhong, and H. Zhu, "Full-inorganic thin film solar cell and photodetector based on "graphene-on-antimony sulfide" heterostructure," *Solar RRL*, vol. 1, no. 12, p. 1700135, 2017.

[203] S. Bulyarsky, L. Vostretsova, and S. Gavrilov, "Photodetectors based on $CuInS_2$," *Semiconductors*, vol. 50, no. 1, pp. 106–111, 2016.

[204] R. Guo, T. Shen, and J. Tian, "Broadband hybrid organic/$CuInSe_2$ quantum dot photodetectors," *Journal of Materials Chemistry C*, vol. 6, no. 10, pp. 2573–2579, 2018.

[205] W. Wang, M. T. Winkler, O. Gunawan, T. Gokmen, T. K. Todorov, Y. Zhu, and D. B. Mitzi, "Device characteristics of CZTSSe thin-film solar cells with 12.6% efficiency," *Advanced Energy Materials*, vol. 4, no. 7, p. 1301465, 2014.

[206] Q. Guo, G. M. Ford, W.-C. Yang, B. C. Walker, E. A. Stach, H. W. Hillhouse, and R. Agrawal, "Fabrication of 7.2% efficient CZTSSe solar cells using CZTS nanocrystals," *Journal of the American Chemical Society*, vol. 132, no. 49, pp. 17384–17386, 2010.

[207] T. K. Todorov, O. Gunawan, T. Gokmen, and D. B. Mitzi, "Solution-processed Cu (In,Ga)(S,Se)2 absorber yielding a 15.2% efficient solar cell," *Progress in Photovoltaics: Research and Applications*, vol. 21, no. 1, pp. 82–87, 2013.

[208] K. Bindu, M. Lakshmi, S. Bini, C. S. Kartha, K. Vijayakumar, T. Abe, and Y. Kashiwaba, "Amorphous selenium thin films prepared using chemical bath deposition: optimization of the deposition process and characterization," *Semiconductor science and technology*, vol. 17, no. 3, p. 270, 2002.

[209] K. Bindu, C. S. Kartha, K. Vijayakumar, T. Abe, and Y. Kashiwaba, "$CuInSe_2$ thin film preparation through a new selenisation process using chemical bath deposited selenium," *Solar Energy Materials and Solar Cells*, vol. 79, no. 1, pp. 67–79, 2003.

[210] J. González, S. Shaji, D. Avellaneda, G. Castillo, T. D. Roy, and B. Krishnan, "Photovoltaic structures using $AgSb(S_XSe_{1-X})_2$ thin films as absorber," *Applied Physics A*, vol. 116, no. 4, pp. 2095–2105, 2014.

[211] D. Dwyer, I. Repins, H. Efstathiadis, and P. Haldar, "Selenization of co-sputtered CuInAl precursor films," *Solar Energy Materials and Solar Cells*, vol. 94, no. 3, pp. 598–605, 2010.

[212] S. Martín and C. Guillén, "Study of the chalcopyrite $Cu(In,Al)Se_2$ crystalline growth by selenization of different evaporated precursors ratios," *Journal of Crystal Growth*, vol. 336, no. 1, pp. 82–88, 2011.

[213] J. Sejkora, E. Buixaderas, P. Škácha, and J. Plášil, "Micro-raman spectroscopy of natural members along $CuSbS_2$-$CuSbSe_2$ join," *Journal of Raman Spectroscopy*, vol. 49, no. 8, pp. 1364–1372, 2018.

[214] V. Klimov, P. Haring Bolivar, H. Kurz, V. Karavanskii, V. Krasovskii, and Y. Korkishko, "Linear and nonlinear transmission of Cu_XS quantum dots," *Applied physics letters*, vol. 67, no. 5, pp. 653–655, 1995.